UNIVERSITÀ DI PARMA

UNIVERSITA' DEGLI STUDI DI PARMA

DOTTORATO DI RICERCA IN
SCIENZE DELLA TERRA

CICLO XXXII

Development of tight anticlines in platform carbonates at the toe of transpressional thrust wedges: structural and paleofluid constraints from the Pag anticline, External Dinarides (Croatia)

Coordinatore:
Chiar.mo Prof. Fulvio Celico

Tutor:
Chiar.mo Prof. Fabrizio Storti

Co-Tutor:
Prof. Andrea Bistacchi

Dottorando:
Andrea Succo

Anno 2016/2018

"Sognava rocce alte, spazi aperti e cielo sopra la testa. Senza, era triste."

M.C.

The research presented in this thesis was carried out at:

Dipartimento di Scienze Chimiche, della Vita e della Sostenibilità Ambientale

Università di Parma

Parco Area delle Scienze, 11/a

Plesso Geologico

43124 Parma

and

Dipartimento di Scienze dell'Ambiente e della Terra

Università degli Studi di Milano-Bicocca

Piazza della Scienze 1 e 4,

20126 Milano

ABSTRACT

The long term evolution of orogenic wedges is characterized by complex interactions between tectonics, gravity, and surface processes. In the external sectors of fold-and-thrust belts, deformation involves interaction between folding and faulting in long-lasting deformation sequences. Describing and quantifying kinematic evolutions and fluid-rocks interaction processes is fundamental for understanding long-lived deformation processes involved in fold-and-thrust belts. At wedge toes, low amounts of deformation are expected and predicted by strain and kinematic models. However, multiple syn-orogenic contractional pulses and possible stress field variations, mechanical and stratigraphic properties of deformed successions, and fluid circulations at shallow crustal levels, may dramatically increase the complexity and intensity of deformation developed in the frontal parts of foreland thrust-and-fold belts. A better understanding of the relative role of these different factors to determine fold complexity at thrust wedge toes has important academic and economical implications.

A world-class example of long-lasting contractional orogeny is provided by the Dinarides and, in particular, their frontal sector (i.e., External Dinarides), which offers outstanding exposures where studying the interplay between deformation, stratigraphy, and fluid-rock interactions in folded and faulted carbonate platform rocks. This Ph.D. thesis investigates on deformation structures developed during folding on a fault-related anticline involving a tight carbonate platform succession. Research was performed by a multidisciplinary approach to study the structural architecture and kinematic evolution of the anticline, the interaction between contractional folding and strike-slip faulting, and the role played by misoriented inherited faults on folding. Paleo-fluid evolution is also taken into account to better understand deformation structure timing and palaehydrological evolution, and the influence of deformation elements on fluid circulation through the anticline.

The case study of the Pag anticline (External Dinarides, Croatia) allowed investigating on a shallow-depth detachment fold developed in proximal surface conditions at the toe of the late-Eocene Dinarides thrust wedge. Despite its structural position, the Pag anticline is characterized by high-structural complexity, including a non-cylindrical box fold geometry dissected by a pair of major overstepping conjugate forethrust and backthrust, and strongly compartmentalized by two sets of high-angle strike-slip faults, both striking oblique to the fold axis. The presence of a

thin-skinned inherited fault system, oriented almost perpendicular to the fold axis, plays a major role during late-stage of transpressional folding. Fold evolution is characterized by the interaction between contractional and right-lateral strike-slip deformations since the early stages of layer-parallel shortening and folding. Palaehydrological evidence from structural diagenesis of folding- and faulting-related veins indicates that most of the long-lasting evolution of deformation progressed in "bedset confined" conditions, strongly influenced by stratigraphic-related eogenetic fluids, characterized by a meteoric signature and very slowly moving along pre-existing deformation structures. Only in the later stages, during fold tightening and compartmentalizaton, strike-slip fault zones and reactivated pre-tightening structures acted as fluid-conduits, triggering meteoric fluid circulation, showing the same isotopic signature through each stratigraphic unit. This suggests that the major hydrological connectivity for mineralizing fluid was reached during the latest stages of folding. Fault-controlled de-dolomitization processes occurred, recrystallizing fault-related dolomite bodies formed before folding. To conclude, this case study offered an outstanding opportunity to investigate and document folding-related deformation, fold evolution and architecture, and fluid circulation that occurred at the toe of the Dinarides foreland thrust-and-fold belt, involving platform carbonate rocks.

NOTES FOR THE READER

This manuscript is composed of different chapters, which are organized as follows:

1) GENERAL INTRODUCTION

Short introduction about tectonics and sedimentation processes in the Dinarides collisional orogen, introduction to mechanical stratigraphy and fold-related deformation, and research objectives.

2) GEOLOGICAL MAP OF THE PAG ANTICLINE

Description of the stratigraphy and tectono-stratigraphic evolution of the Pag anticline (Croatia), developed at very shallow crustal levels, at the toe of the Dinarides orogenic wedge.

3) CALCAREOUS NANNOFOSSIL BIOSTRATIGRAPHY

Dating the age of turbidite deposits of the Pag thrust-top foreland basin, which allowed us to constraining the timing of folding and obtaining paleoenvironmental indications.

4) INHERITED EXTENSIONAL FAULTS

Structural description and kinematic model of pre-folding inherited extensional fault zones passively rotated in the Pag anticline. This feature allowed us to investigate the role of thin-skin extensional features involved in contractional structures.

5) THE PAG ANTICLINE

The Pag anticline case study, its structural architecture and kinematic evolution, with a specific focus on fault-fold interaction and paleofluid evolution, and their interaction with mechanical stratigraphy.

6) GENERAL CONCLUSIONS

Final chapter highlighting the major outcomes of the present work.

BIBLIOGRAPHY

Comprehensive list of references cited in previous chapters.

Research activities have been carried out within the framework of the SEFRAC project, which was founded by ENI S.p.a., and involved the University of Parma (Italy), the University of Milano-Bicocca (Italy), and the TU Delft University of Technology (Netherlands). The project started in late 2017 and had the purpose to provide a better understanding of fracture geometry, attributes and drivers, in platform carbonates rocks. Moreover, an additional target of the project was to set up a combined methodology to collect and describe the natural fracture system in the field, by a multiscale and multidisciplinary approach, and to build an "atlas of fracturing *facies*" as reference interactive catalogue of naturally fractured field analogues.

Research activities in the Pag anticline were supported by ENI Exploration & Production. Moreover, Marco Meda and Luca Clemenzi, from the GEBA research team of ENI, actively participated to the project.

RIASSUNTO

L'evoluzione a lungo termine di catene orogeniche è contraddistinta da complesse interazioni tra processi tettonici, gravitativi and processi di superficie. Nei settori esterni di catene a pieghe e sovrascorrimenti, la deformazione comporta l'interazione tra piegamento e fagliazione durante evoluzione deformativa multistadiale. La descrizione e quantificazione dell'evoluzione cinematica e dei processi d'interazione fluido-roccia è fondamentale per la comprensione dei processi deformativi che avvengo nelle catene a pieghe e sovrascorrimenti. Al fronte della catena, moderate intensità di deformazione sono attese e predette dai modelli cinematici e deformativi. Tuttavia, pulsi multipli contrazionali durante l'evoluzione della catena e possibili variazione del campo di stress, proprietà meccaniche e stratigrafiche delle unità deformate e la circolazione di fluidi in condizioni crostali superficiali, possono aumentare drammaticamente l'intensità di deformazione sviluppatasi nelle porzioni frontali di una catena a pieghe e sovrascorrimenti. Una migliore comprensione del relativo ruolo di questi differenti fattori nel determinare una maggiore complessità strutturale al fronte della catena ha importanti implicazioni accademiche ed economiche.

Un tipico esempio di catena contrazionale sono le Dinaridi e, in particolare, il loro settore esterno (Dinaridi Esterne), le quali offrono esposizioni eccezionali dove studiare le interazioni tra deformazione, stratigrafia e interazioni fluido-roccia in carbonati di piattaforma piegati e fagliati. Questa tesi di Dottorato ha l'obbiettivo di investigare le strutture deformative sviluppatesi durante il piegamento di una anticlinale che coinvolge una successione di rocce carbonatiche fortemente cementate. La ricerca è stata condotta tramite un approccio multidisciplinare analizzando l'architettura strutturale ed evoluzione cinematica dell'anticlinale, le interazioni tra piegamento l'attività di faglie transcorrenti e il ruolo di faglie estensionali ereditate sul piegamento. L'evoluzione dei paleo-fluidi è stata analizzata per comprendere l'evoluzione delle strutture strutture deformative, paleo-idrologica e l'influenza degli elementi deformativi sulla circolazione di fluidi nell'anticlinale.

Il caso di studio dell'anticlinale di Pag (Dinaridi Esterne, Croazia) permette di investigare lo sviluppo di una piega da detachment formatasi in condizione relativamente superficiali in posizione frontale di prisma dinarico tado-eocenico. Nonostante la sua posizione strutturale, la piega è caratterizzata da un'elevata complessità strutturale di stili deformativi, tra cui una geometria non-cilindrica di tipo "box-fold" dissecata da una coppia di sovrascorrimenti e retro-sovrascorrimenti coniugati e fortemente

compartimentalizzata di zone di faglia transcorrenti ad alto anglo oblique rispetto all'asse della piega. La presenza di faglie estensionali ereditate, sub-perpendicolari all'asse della piega, influenza fortemente l'evoluzione plicativa durante gli stadi tardivi a carattere transpressivo. L'evoluzione dell'anticlinale è caratterizzata dall'interazione tra deformazione contrazionale e trascorrente fin dagli stadi iniziali di layer-parallel shortening e piegamento. Evidenze paleo-idrologiche sulla base di dati diagenetico-strutturali su vene associate al piegamento ed alle faglie transcorrenti, suggeriscono che la maggior parte dell'evoluzione deformativa sia avvenuta in condizioni idrauliche di tipo "strato confinato", fortemente influenzate dalla re-circolazione di fluidi eogenetici e quindi condizionata dalle varie unità stratigrafiche con fluidi connati di tipo meteorico-freatico. Solo negli stadi tardivi, principalmente durante l'amplificazione e compartimentalizzazione della piega, le zone di faglia transcorrenti e la riattivazione di strutture precedenti, guidano la circolazione di fluidi meteorici che presentano la stessa firma isotopica in tutte le unità stratigrafiche deformate. In questi stadi evolutivi si raggiunge la maggior connettività tra il reticolo di strutture deformative. Questo suggerisce che la maggiore connettività idrologica pe fluidi mineralizzanti è stata raggiunta durante gli stadi tardivi del piegamento. Inoltre, de-dolomitizzazione selettiva lungo le zone di faglia avviene durante la circolazione di questi fluidi meteorici tardivi, ricristallizzando corpi di dolomia precedenti il piegamento. Per concludere, questo caso di studio offre un'intrigante opportunità di investigare la deformazione associata a pieghe, di documentare l'architettura strutturale e l'evoluzione tettonica e architetturale e dei paleo-fluidi nei settori esterni della catena dinarica in rocce carbonatiche.

NOTE PER IL LETTORE

Questo manoscritto è organizzato in diversi capitoli, secondo l'ordine seguente:

1) GENERAL INTRODUCTION

Breve introduzione sui processi di tettonica e sedimentazione nel prisma collisionale Dinarico, introduzione sulla problematica della stratigrafia meccanica e delle strutture deformative associate a pieghe e, infine, sugli obiettivi della ricerca.

2) GEOLOGICAL MAP OF THE PAG ANTICLINE

Descrizione della stratigrafia e dell'evoluzione tettono-stratigrafica dell'anticlinale di Pag (Croazia), che si è sviluppata a livelli strutturali superficiali e nella porzione frontale del prisma orogenico dinarico.

3) CALCAREOUS NANNOFOSSIL BIOSTRATIGRAPHY

Datazione dell'età dei depositi torbiditici del bacino di thrust-top Pag, la quale consente di vincolare l'età del piegamento e di ottenere indicazioni paleoambientali del contesto deposizionale.

4) INHERITED EXTENSIONAL FAULTS

Descrizione strutturale e modello cinematico di zone di faglia estensionale ereditate pre-piegamenteo e passivamente ruotate nell'anticlinale di Pag. La loro individuazione e presenza permette di investigare il ruolo strutture estensionali relativamente pellicolari coinvolte in strutture contrazionali.

5) THE PAG ANTICLINE

Caso di studio dell'anticlinale di Pag, nel quale si sviluppa la sua architettura strutturale ed evoluzione cinematica, con dettaglio sull'interazione faglie-pieghe durante il piegamento, sull'evoluzione e circolazione di paleo-fluidi durante e post-piegamento e sulle interazioni e ruolo della stratigrafia meccanica.

6) GENERAL CONCLUSIONS

Capitolo finale in cui vengono evidenziate le conclusioni generali di questo lavoro.

BIBLIOGRAPHY

Lista dei riferimenti bibliografici citati in tutti i precedenti capitoli

L’attività di ricerca si è svolta nell’ambito di progetto SEFRAC, finanziato dalla compagnia petrolifera ENI S.p.a., ed ha coinvolto l’Università di Parma (Italia), l’Università deglii Studi di Milano Bicocca (Italia) e TU Delft University of Technology (Olanda). Il progetto ha avuto inizio nel verso la fine del 2017 ed ha avuto come principale obiettivo quello di fornire un’analisi comprensiva sulle geometrie, attributi e “drivers” del network di fratture, in rocce di piattaforma carbonatica. Ulteriore target addizionale del progetto è stato quello di impostare e testare una metodologia combinata di campionamento a descrizione di sistemi naturali fratturati in affioramento, tramite un approccio multiscala e multidisciplinare, e di progettare e costruire, rendendolo operativo su piattaforma intranet ENI, un “atlante della facies di fratturazione “come catalogo interattivo di analoghi affioranti.

L’attività di ricerca sull’anticlinale di Pag è stata supportata da ENI divisione Esplorazione e Produzione. Inoltre, Marco Meda e Luca Clemenzi del team di ricerca GEBA, hanno attivamente partecipato al progetto.

ACKNOWLEDGMENTS

This Thesis results from three years of geological research as well as professional and personal growth. This project allowed me to work in a research team, to collaborate with industry personnel, to carry out extensive fieldwork, and to attend workshops, short courses, conferences, and meetings. This gave me a chance to meet a lot of new people and to exchange with them ideas and knowledge.

First of all, I'm strongly indebted with my tutor, Prof. Fabrizio Storti, for his great scientific and moral support and advice, and constructive criticism. I do want to thank you for your contributions and continuous motivations until the end of my Ph.D., thus allowing me to significantly progress as a person and a scientist. I would also like to thank my co-tutor, Prof. Andrea Bistacchi, which is a very eclectic and ingenious scientist. Its contributions to promote new ideas, to support fieldwork activities, and also to criticize some of my initial work were fundamental during these years. Immeasurable thanks to Dr. Silvia Mittempergher, for her foundamental contribution, moral support, and constructive suggestions. We carried out together intense fieldwork in Pag, and I really appreciated your help during field and laboratory work. Your great support, ideas, and enthusiasm were essential for me to complete my work in Pag.

I'm grateful to Prof. Andrea Festa and Prof. Stefano Tavani for their constructive and thorough reviews, from which this work has greatly benefited.

In these three years that I spent in Parma, I appreciated a lot the warm and friendly environment that characterizes the NEXT Research Group. Many thanks to everybody in the group, namely Fabrizio Balsamo, Alessio Lucca, Luigi Berio, Silvia Brizzi, Silvia Cortinovis and Mattia Pizzati. For the professional and human support that I received from you.

All people involved in the SEFRAC Team, and Marco Meda and Luca Clemenzi from ENI, are greatly acknowledged for sharing ideas, views, and advice, and for the friendly environment that was created since the beginning of the project. Discussions with Giovanni Bertotti and Pierre-Olivier Bruna, in fact helped optimizing fieldwork and understanding the large-scale fold structure and fracture timing. Thanks also to Roberto Fantoni, ENI, for helpful suggestions on the Adriatic realm.

I'm strongly indebted to Luca Barchi, Cristian Cavozzi, Andrea Comelli, and Enrico Maria Selmo for their constant technical support and for providing thin sections, rock porosity data, and carbon and oxygen isotope data.

Many many thanks to my mother and my father, and to the other family members for their support and interest in my activity. Immeasurable thanks to Silvia, who supported me both in difficult and successful moments during these three years. Thanks to my "mentor" Mario for supporting me in everything and last but not least, many thanks to Luigi and my other "alpine" friends, hoping for new climbing adventures.

CONTENTS

CHAPTER 1.

GENERAL INTRODUCTION

1.1 INTRODUCTION

The geometry and evolution of orogens are commonly controlled by processes of lower crustal accretion associated with a gradual migration of deformation and exhumation towards foreland sectors (e.g. Faccenna et al., 2014). In the upper part of fold and thrust belts, deformation involves interaction between folding and faulting in long-lasting deformation sequences (Tavani et al., 2015). Describing and quantifying tectonic and kinematic evolutions and fluid-rocks interaction processes is of fundamental importance for properly framing deformation patterns in fold and thrust belts, especially near their toes, where low amounts of strain are expected. This Ph.D. Thesis deals with the development of tight anticlines in platform carbonate rocks, at the toe of transpressional orogenic wedges. A world-class example of long-lasting compressional to transpressional orogeny is provided by the Dinarides and, in particular, their frontal sector (i.e., External Dinarides), which provides well-exposed areas where effectively investigate on deformation, stratigraphy, and fluid-rock interactions in folded and faulted carbonate platform rocks. The Pag anticline, located at the toe of the transpressional External Dinarides thrust-wedge, provides the case study of this research work, aimed at unraveling folding processes, interaction between faults and fold, fluid-rocks interaction, and mechanical stratigraphy on driving deformation localization in a long-lasting multi-step fold deformation pathway. The case study is investigated by a multidisciplinary approach that includes: analysis of the large-scale structures, detailed geological and structural mapping; meso- and micro-structural analysis; petrographic and geochemical analysis of fold- and fault-related veins; stratigraphic and biostratigraphic analysis.

1.2 THE DINARIC OROGEN

The Alpine-Carpathian-Dinaridic orogenic system that encircles the Pannonian Basin, is a part of a much larger Circum-Mediterranean orogenic system (**Figure 1.1**), which includes tectonic units derived from the dismembering of the Adriatic microplate, European continental plate, and Neotethys Ocean, incorporated into thrust systems of different polarity (e.g. Schmid et al., 2008; Ustaszewski et al., 2008). The Western and Eastern Alps, and Carpathians thrust systems, face the European foreland, while the Southern Alps, and the Dinaridic thrust systems, face the Adriatic foreland (e.g. Ustaszewski et al., 2008).

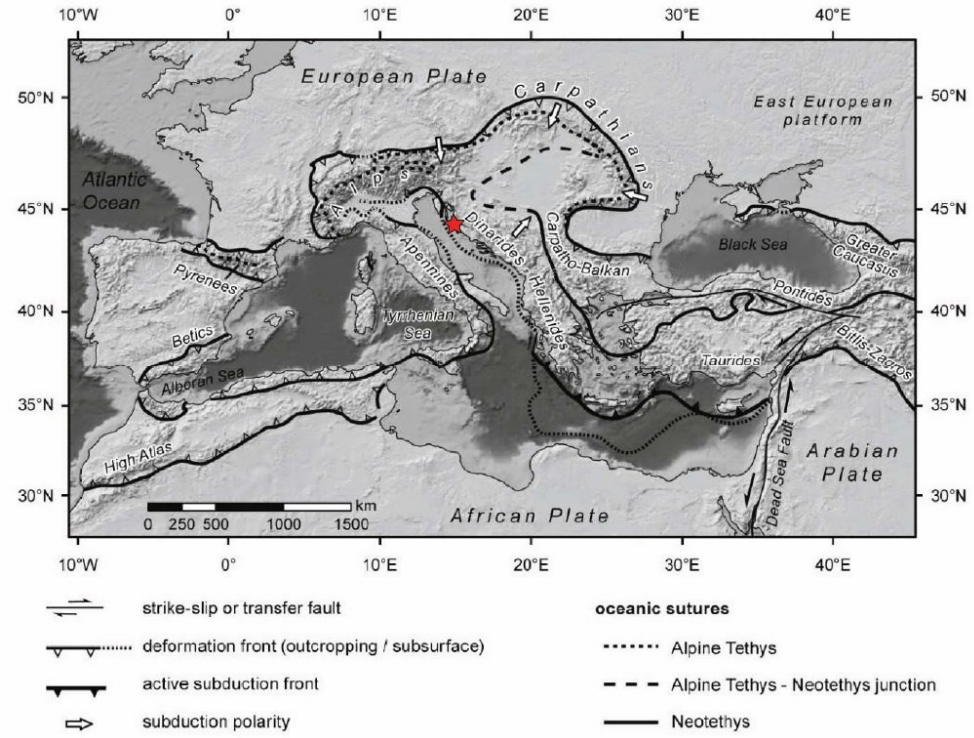

Figure 1.1 - Position of the Dinarides within the European Alpine system, with the suture zones of the Alpine Tethys and Neotethys and the major deformation fronts also shown. The red star indicates the position of the study area in the frontal sector of the Dinarides. Modified from Ustaszewski et al., 2008.

1.2.1 *The overall tectonic architecture*

The Dinarides are a c. 700 km long, NW-striking mountain belt located along the NE Adriatic coast and connecting the Southern Calcareous Alps to the north, with the Albanides and Hellenides-Taurides belts to the south. (Pamić et al., 1998; Vlahović et al., 2012). This orogenic belt derives from the alpine orogeny and deformed thick sedimentary successions of Carboniferous to Quaternary age.

The evolution of the Dinarides was controlled by a number of tectonic events within the Alpine orogenic cycle (between Late-Permian to Oligocene). However, the main imprint was tectonic uplift and formation of an imbricated nappe system during Late Eocene to Oligocene times, which resulted in the "present-day" Dinarides fold-and-thrust belt (Pamić et al., 1998). The orogenic belt is composed by several tectonic units that are derived from both the Adriatic Microplate to the SW (present-day coordinate system), and its contact zone with the European plate to the NE (Tari, 2002, with references).

According to Vlahović et al. (2005, with references) and Schmid et al (2008, with references), the Dinarides orogenic system can be subdivided into two main tectonostratigraphic domains (**Figure 1.2**):

i) Outer or Karst Dinarides, i.e., the External Dinaridic Platform, composed by the tectonic units of the Dalmatian Zone, Budva-Cukali Zone, and High Karst Unit;

ii) Internal Dinarides, i.e., Internal Dinaridic Platform that is composed by the tectonic units of the Pre-Karst and Bosnian Flysch Unit, the thrust sheets of East Bosnian-Drumitor, Drina-Ivanjica and Jadar-Kopaonik, Ophiolites obducted on Adria Margin, and the Sava Zone, which resembles the Cenozoic suture between Dinarides and Tisza-Dacia Mega-Unit.

Outer or Karst Dinarides (**Figure 1.2**) are mainly composed of an impressively thick carbonate succession deposited on the Adriatic Carbonate Platform (AdCP hereafter). Carbonate sedimentation started "*sensu-lato*" already in Carboniferous, Late Permian and Triassic times. However, "*sensu-stricto*", most of the carbonate succession was deposited on AdCP during Jurassic and Cretaceous times (Velić et al. 2003; Vlahović et al., 2005; Vlahović et al., 2012 with references). Overall, the carbonate succession that was built over about 250 Ma (with a total thickness of c. 8 km) in relatively stable shallow-marine environments. Outer Dinarides expose also some deepwater sediments deposited in narrow deep-water troughs (e.g Budva Zone; **Figure 1.2**; Korbar, 2009).

The area of Internal Dinarides tectonostratigraphic unit, located between Outer Dinarides and Pannonian Basin, is mainly composed of a deep-water succession deposited on the passive margin of the Adria Microplate (Korbar, 2009; Schmid et al., 2008; Vlahović et al., 2012). Accordingly, it is composed of passive continental margin carbonate-clastic series, deep-water sediments of ophiolitic complexes, ophiolitic mélange units, flysch-like, and bimodal magmatic and metamorphic rocks that compose formations within the Sava Suture Zone (**Figure 1.2**; Pamić et al., 1998; Schmid et al., 2008 with references).

1.2.2 *Tectonics and sedimentation in the Dinarides orogen*

The Dinarides orogen started its evolution with the opening of a northern branch of the Neotethys Ocean (e.g., Stampfli & Borel, 2002; Schmid et al., 2008) during Middle Triassic times, which also triggered the formation of the Budva graben in the external parts of the SE-Dinarides. This graben was

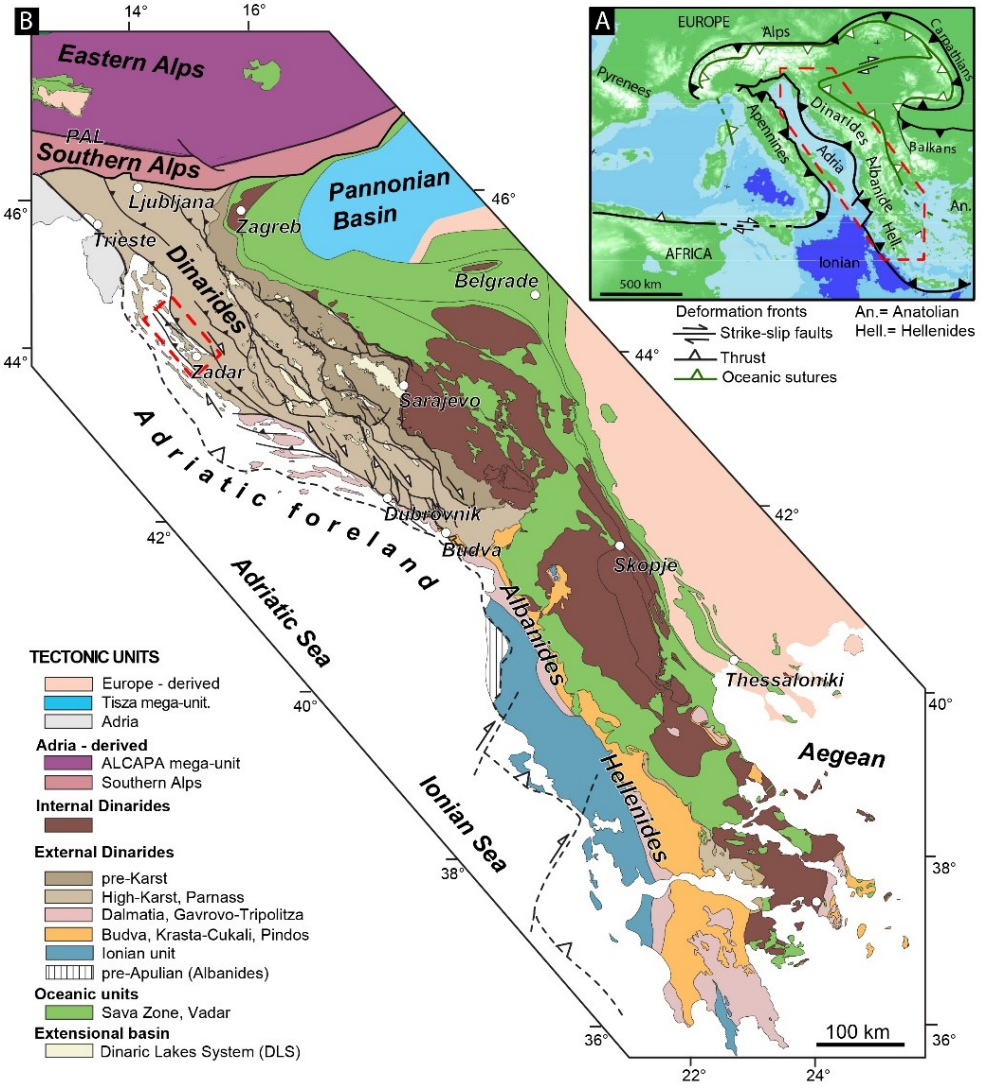

Figure 1.2 - Tectonic map of the external parts of the Dinarides, Albanides, and Hellenides, as well as the neighboring parts of Pannonian Basin, Southern, and Eastern Alps (modified from Schmid et al., 2008, 2011). The red dotted polygon is the location of the study area. The map in the upper right corner is the localization of the tectonic map in the larger European orogenic context. PAL = Peri – Adriatic Lineament.

gradually filled with deep marine carbonates, whereas in the remainder of the external Dinarides, only shallow-water carbonate sedimentation took place (Dimitrijević, 1997; Vlahovic et al., 2005). During late Early Jurassic times, shallow water deposition continued in the Adriatic carbonate platform, while it was separated by intervening deep marine basins to the north and south (Vlahović et al., 2005). The shallow marine platform carbonates continued to be deposited in the platform areas of the Dinarides until Eocene times (Cosović et al., 1994). These platform carbonates were

alternated with intra-platform deep marine troughs, which were filled with deep marine turbidites (e.g. Korbar et al., 2001; Tišljar et al., 1998). Within the internal parts of the Dinarides, carbonate platform deposition was interrupted by sedimentation of deep-marine turbidites during Kimmeridgian times (i.e. Vranduk Flysch), which continued with thickest deposition during uppermost Cretaceous times (i.e. the Ugar and Durmitor flysches; Mikes et al., 2008).

The main tectonic units in the Dinarides formed in response to a Cretaceous – Oligocene phase of NE-SW oriented contraction, created by the convergence between Europe- and Adriatic-derived units (e.g. Dimitrijević, 1997; Schmid et al., 2008). SW-vergent thrusting gradually migrated towards the external parts of the Dinarides (Aubouin et al., 1970; Dimitrijević, 2001). The last phase of orogenic deformation was associated with the deposition of late Eocene clastic turbidites and late Eocene - Oligocene coarse conglomeratic molasses deposits (the Promina Beds) near thrust contacts and inside the basins (Mrinjek, 1993; Zupanič & Babić, 2011). This was followed by generalized early – middle Miocene extension as a result of orogenic collapse and slab retreat, which created the Miocene Dinarides Lake System (**Figure 1.3**; Andrić et al., 2017; Harzhauser et al., 2011; Mandic et al., 2012). In these basins, late Oligocene – early Miocene continental to shallow-marine lacustrine contractional flexural deposition was followed by an early – middle Miocene asymmetric extension featuring coarse clastic deposits, and by an upper Miocene continental alluvial to deltaic deposition that was partly coeval with the late-stage inversion of the basin (Andrić et al., 2017; Hrvatović, 2006).

This phase of extension affected the entire Dinarides and provide critical stratigraphic constraints to a post-middle Miocene phase of contraction, driven by the N- to NE-ward indentation of the Adriatic microplate (Pinter et al., 2005; Ustaszewski et al., 2008). This deformation is also associated with an observed present-day slab in the far external Dinarides, as indicated by large-scale high-velocity anomalies along them (Šumanovac et al., 2017; Šumanovac & Dudjak, 2016; Ustaszewski et al., 2008).

1.2.3 *The Adriatic Carbonate Platform (AdCP)*

Tectonic and sedimentary evolution of the Karst Dinarides is genetically linked with that of the AdCP (**Figure 1.4**), formed on the Adria Microplate as a vast and relatively stable shallow-marine area (Vlahović et al., 2012) of about c. 80-200 km wide and nearly 700 km long, i.e. one of the largest Mesozoic carbonate platforms (**Figure 1.4**) in the Perimediterranean region.

The onset of AdCP formation was characterized by Middle Triassic volcanism i.e., continental rifting that, due to extension and formation of deep normal faults, enabled break-up of the Adria Microplate (Pamić et al., 1998) and formation of the isolated carbonate Southern Tethyan Megaplatform within the area of the future AdCP (Vlahović et al., 2005). The authors point out that in Middle/Late Triassic to Lower Jurassic times, AdCP was very broad and characterized by mostly continuous shallow-marine carbonate deposition including Upper Triassic Hauptdolomit and Lower Jurassic limestones (e.g. Lithiotid limestone).

In middle to late Early Jurassic times, the Southern Tethyan Megaplatform was dismembered into several other carbonate platforms (e.g., Apenninic and Apulian) isolated by deeper marine areas (e.g., Adriatic Basin, Ionian and Belluno basins, Lagonero Basin, and Slovenian and Bosnian troughs; Vlahović et al., 2005 with references therein). A common feature of these Mesozoic carbonate platforms was the dominant shallow marine carbonate deposition due to gradual subsidence, with periods of emergence due to either extensional tectonics and eustatic changes. Environments ranged from peritidal through shallow subtidal–lagoons, restricted inner platforms, high-energy tidal bars, beach and shoreface to reefal–perireefal areas, with carbonate slope deposits in the areas of drowned platform and intraplatform troughs (Tišljar et al., 2002; Vlahović et al., 2005 with references). Besides tectonic activity that formed shallow intraplatform trough (e.g. Gorski Kotar area), dominant shallow-marine depositional rates were influenced by environment energy and global events, i.e., anoxic events (OAE- see Valhović et al., 2005 and references therein), which resulted in specific lithotype deposition and depositional cycles from high energy oolitic limestones to heavily bioturbated limestones. Accordingly, during the 125 Myr of the AdCP's existence, trough Late-Triassic, Jurassic and Cretaceous times the thickness of deposited limestone and dolostone reached between 3500 and 5000 m.

Completion of AdCP deposition was characterized by regional emergence through Late Cretaceous and Palaeogene times, with syn-sedimentary compressional tectonic deformations, which driven turbiditic foreland and thrust-top basin depositions of Eocene flysch strata in a newly formed basin above either Late Cretaceous rudist rich carbonates or Eocene foraminiferal limestone. (Vlahović et al., 2005). The final tectonic uplift of the Dinarides started in Late Eocene to Oligocene times (Dinaric phase of the Southern Alps; see Schmid et al. 2008 for details) with formation of the Outer Dinaridic thrust nappe systems, e.g., Dalmatian Zone and High Karst Unit, and deposition of clastic-carbonate sediments i.e., Promina marls, calcarenites, and conglomerates and Jelar i.e. Velebit carbonate breccias.

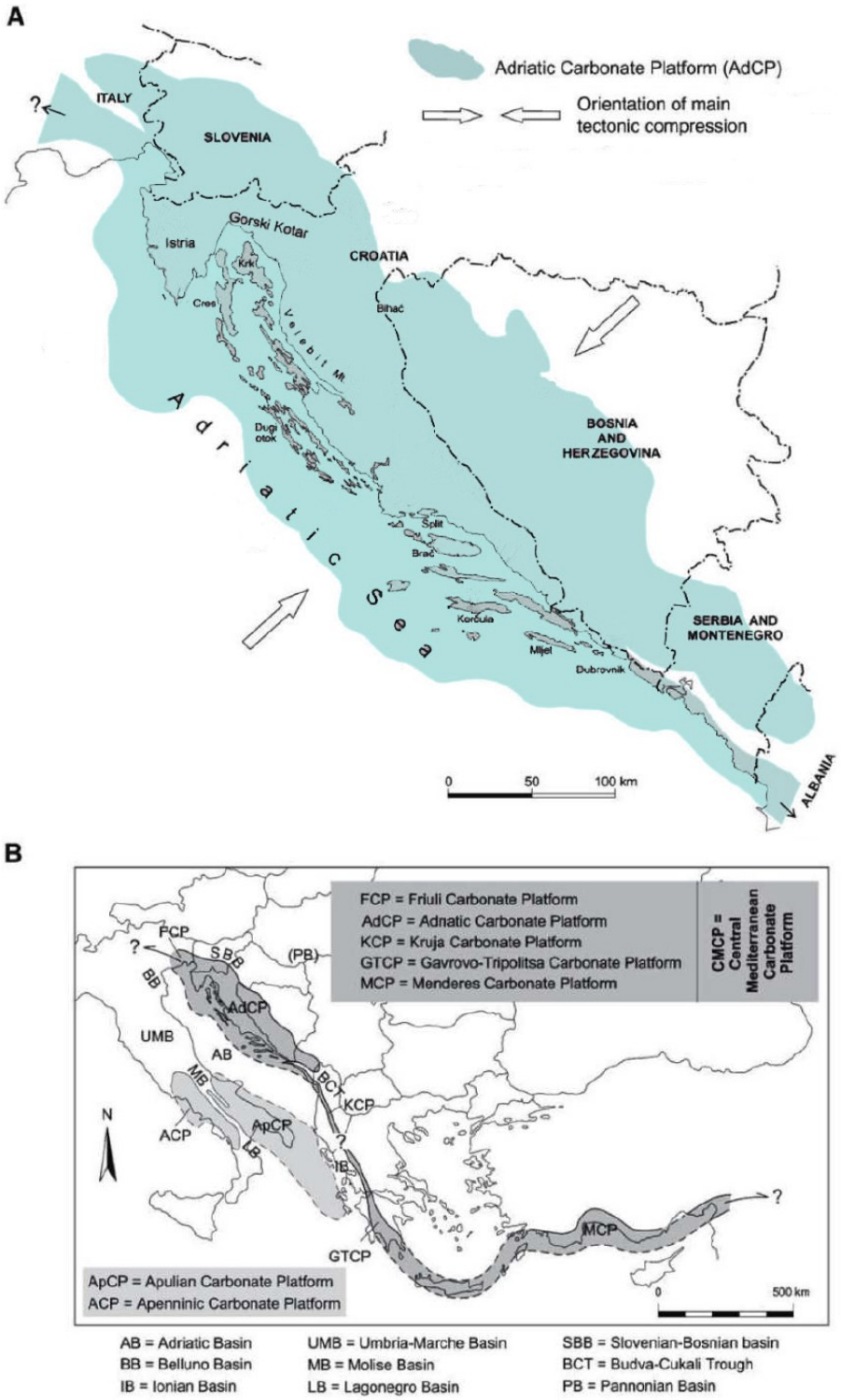

Figure 1.3 – (a) Map outline of Adriatic Carbonate Platform extension; (b) Recent carbonate deposits in the central Mediterranean (after Vlahović et al.,2005).

1.2.4 *Miocene to present-day stress field*

A comprehensive database of earthquake focal mechanisms and slip vectors produced by a high-sensitivity seismic monitoring network, borehole breakout analysis, in situ stress measurement and GPS measurement data in the area of the Circum-Mediterranean and the surrounding orogens, provides the possibility to address and understand the relationships between neotectonics, surface processes, and recent litospheric dynamics (**Figure 1.4**; Cloetingh et al., 2006; Bada et al., 2007).

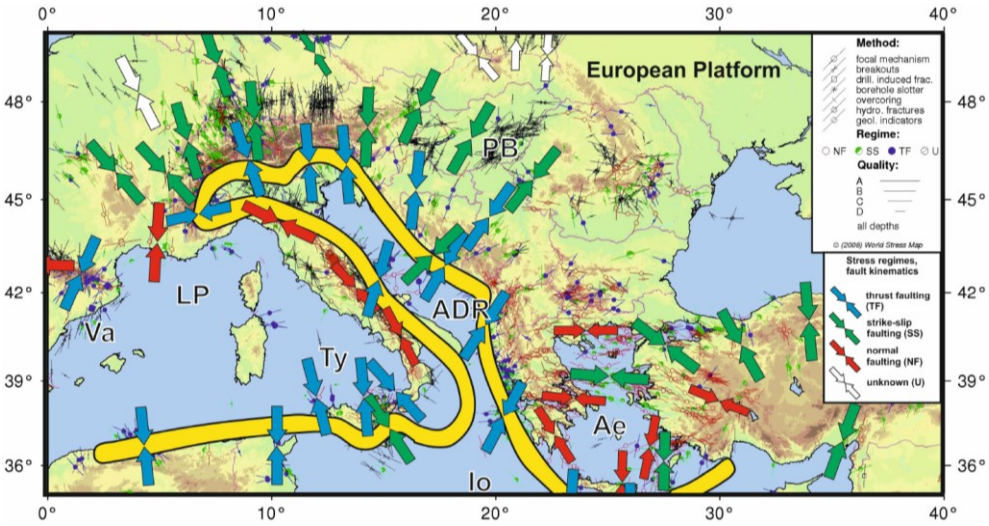

Figure 1.4 - Present-day maximum horizontal stress directions (Shmax) and tectonic regimes in the Europe-Africa subduction and collisional zone (after Reinecker et al., 2005; Bada et al., 2007; Heidbach et al., 2008). The yellow zone indicates the Adria Microplate (ADR) boundary. Abbreviations: Ae: Aegean sea, Io: Ionian Sea, Ty: Tyrrhenian basin, LP: Liguro-Provençal basin, Va: Valencia trough, PBS: Pannonian Basin.

The Europe-Africa subduction and collisional zones with their associated back-arc basins of the Mediterranean system represent a region of complicated short-scale stress perturbation (**Figure 1.4**, Bada et al., 2007). These horizontal stress field perturbations are caused by an active N-ward to NNE-ward directed convergence between stable Europe and the Adriatic Microplate, with convergence rates varying between 3 and 4.5 mm/year (**Figure 1.5**; Grenerczy et al., 2005). During Neogene and Quaternary times, the Adriatic Microplate behaved as a rigid block that is considered as a main driving force for horizontal shortening and seismic activity in deformation zones along its boundaries (Anderson and Jackson, 1987; Grenerczy et al., 2005; D'Agostino, 2008).

The total convergence between the Adria indenter and stable Europe, is partitioned in collisional zones of (**Figure 1.5**): (i) Adriatic Microplate-Eastern Alps and complementary Alpine-North Pannonian unit by 2-3 mm/yr, (ii) Adriatic Microplate and Central Dinarides by 1-1.5 mm/year near shore and 2 mm/year spreading across the Dinarides and (iii) 1-2 mm/year is transferred as far-field intra-plate stresses within the weak Pannonian lithosphere (Grenerczy et al., 2005). Distribution of seismicity, inverted GPS site velocities, change in Euler vector, and earthquake slip vectors were used by D'Agostino et al. (2008) to suggest that the Adriatic Microplate is fragmented into a northern (Adria) and a southern (Apulia) section separated by the Gargano-Dubrovnik seismic zone (**Figure 1.5**).
The Pliocene - Quaternary tectonic evolution of the AdCP and surrounding Pannonian Basin System is characterized by compression and transpression (Horváth and Tari, 1999; Dolton, 2006), whereas build-up of intra-plate stresses within the Pannonian lithosphere is associated to the present NE-ward translation and counterclockwise rotation of the Adria Microplate that converged with the Alpine orogenic belt (Gerner et al., 1999; Márton et al., 2003; Márton et al., 2005; Grenerczy et al., 2005; Pinter et al., 2005; Jarosinski et al., 2006; Ustaszewski et al., 2008; Jarosinski et al., 2011). According to Bada et al. (2007) and Jarosinski et al. (2011), this is caused by complete consumption of the subducted lithosphere of the European foreland and the detachment of the subducting slab in the Carpathians, ultimately caused the PBS to become locked and subjected to a compressional stress field with varying stress orientations.

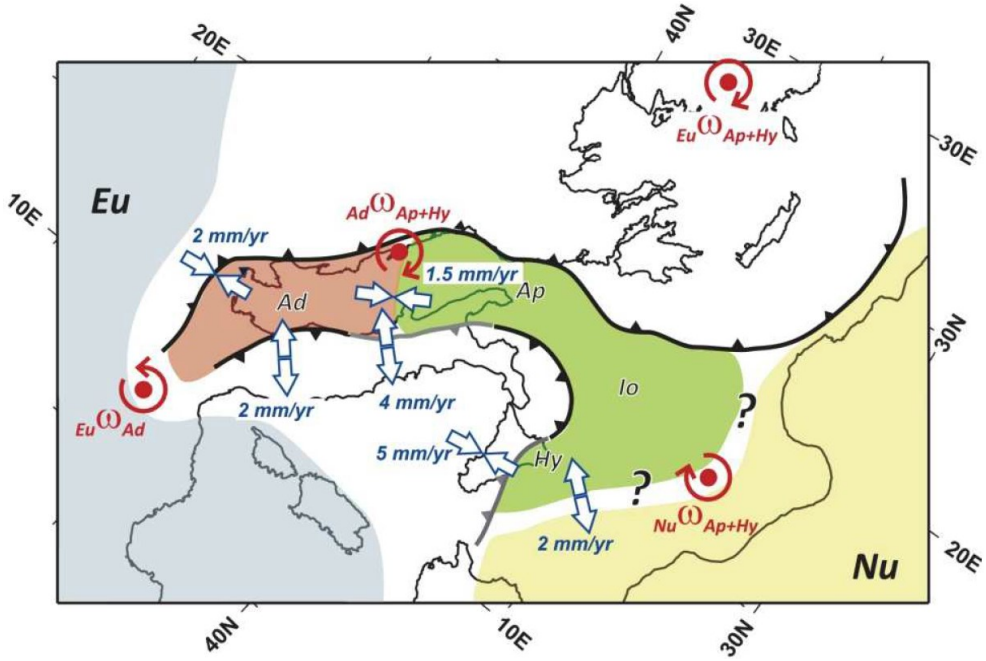

Figura 1.5 - GPS velocities with respect to Eurasia (after D'Agostino et al. 2008).

The Euler pole of the counterclockwise rotating Adriatic Microplate located in the Western Alps by e.g. Anderson and Jackson (1987), Calais et al. (2002), Oldow et al., (2002) has been confirmed by Weber et al. (2010) as 45.03°N and 6.52°E that is furthermore characterized by angular velocity vectors of 0.297 ± 0.116°/Ma. Besides those stresses that directly propagate from Adria through the Dinarides far into the PBS, significant stress transfer occurred due to "Adria push", which was achieved by dextral strike-slip motions and pure thrusting south of the Periadriatic Line and Mid-Hungarian fault zone. This process resulted in the Pliocene and Quaternary structural inversion of the inherited structural trends in the PBS (Grenerczy et al., 2005; Reinecker et al., 2005; Bada et al., 2007; D'Agostino et al., 2008).

The present-day horizontal stress pattern (SHmax) in the PBS is shown by heterogeneous stress indicators, mainly through borehole breakout and fault plane solutions data, which suggest that the alignment of compression and the trend of the principal maximum stress axis changes gradually from NNW-SSE to N-S in the Southern, central - Eastern Alps, respectively, and finally into NNE - SSW to NE - SW in the Dinarides and SW part of the PBS (**Figure 1.6**).

The patterns of Miocene deformation mapped across the central and south-eastern Dinarides partly fit the overall framework of Adriatic indentation studies (**Figure 1.6**, e.g., Handy et al., 2010; Pinter et al., 2005 and Van Unen et al., 2019). The overall N-S to NNE-SSW directions of compression derived from kinematic analysis in the southern part of the External Dinarides belt, proposed by Van Unen et al. (2019), is in general agreement with the N- to NE- ward direction of movement derived by GPS studies in the Dinarides by taking as a reference a stable European framework (**Figure 1.6**, e.g., D'Agostino et al., 2008; Grenerczy et al., 2005; Métois et al., 2015). While GPS movement vectors are oriented more N-wards in the NW Dinarides and the neighbouring Southern Alps, this movement gradually changes to NNE and NE towards the Pannonian Basin and the central and south-eastern part of the Dinarides (**Figure 1.6**). Across the Adriatic Sea, GPS studies indicate a N- to NE-ward movement of the Apennines along trajectories that can be generally connected with the ones observed in the Dinarides, Pannonian Basin, and Southern and Eastern Alps (**Figure 1.6b**). The situation changes in the Ionian domain, located to the SE, starting with the Albanides that record a ~1-5 mm/yr motion towards the NW in their external and towards the SE in their internal parts. The Hellenides record much larger motions of ~10-36 mm/year, gradually rotating from S- to SW-ward following the structural vergence of the orogen in the overall direction of the Aegean slab-roll back (Kahle et al., 2000).

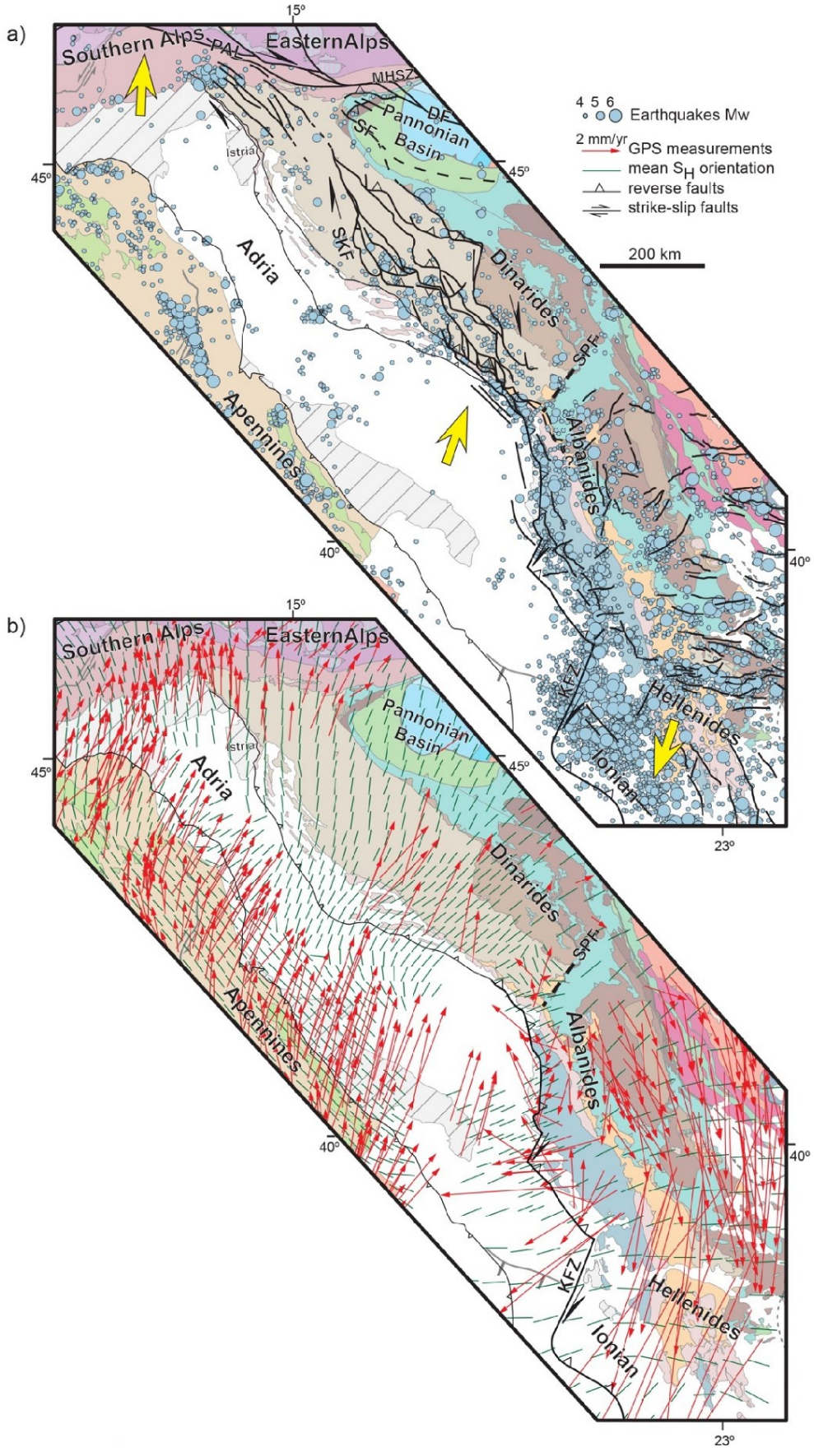
a)
b)
15°
45°
40°
23°
Southern Alps
PAL
EasternAlps
MHSZ
DF
SF
Pannonian Basin
Istria
Adria
SKF
Dinarides
SPF
Albanides
Apennines
KFZ
Hellenides
Ionian
4 5 6
Earthquakes Mw
2 mm/yr
GPS measurements
mean S_H orientation
reverse faults
strike-slip faults
200 km

Figure 1.6 (*in the previous page*) – (a) Tectonic map of the Dinarides and neighboring orogens (adapted from Schmid et al., 2008, 2011, legend and conventions presented in Figure 1.2), showing Miocene major deformation structures and seismicity. The Miocene fault pattern in the Dinarides, Pannonian Basin, Southern and Eastern Alps is taken from previous studies (Heberer et al., 2017; Moulin et al., 2016; Tomljenovic et al., 2008; Ustaszewski et al., 2014; Vrabec and Fodor, 2006; Vrabec et al., 2006 and Van Unen et al., 2019). Only presently active seismogenic faults are displayed in the Albanides and Hellenides (Caputo et al., 2012; Pérouse et al., 2017). Only the orogenic front is displayed in the Apennines. Only earthquakes with magnitude greater than 4 are displayed, their location is taken from the USGS earthquakes catalog. SKF = Split - Karlovac Fault; KFZ = Kefalonia Fault Zone; SPF = Skutari – Pec Fault; PAL = Peri-Adriatic Lineament; SF = Sava Fault; DF = Drava Fault; MHSZ = Mid-Hungarian Shear Zone; (b) The same tectonic map as in Figure 1.2 overlaid by the present-day stress distribution and GPS horizontal motions. The GPS horizontal motions are displayed in an Eurasian fixed reference framework (D'Agostino et al., 2008; Grenerczy et al., 2005; Jouanne et al., 2012; Métois et al., 2015; Nocquet, 2012). The mean present-day maximum horizontal stress orientation (SH) is compiled from previous studies (Bada et al., 2007; Heidbach et al., 2007; Heidbach et al., 2010).

The N-S to NNE-SSW direction of compression derived from paleostress analysis (Van Unen et al., 2019) is also in general agreement with modeled averages of the present-day maximum horizontal stress (SHmax) field in the Dinarides (**Figure 1.6**). This modelled stress component indicates a gradual change from N-S orientations in the NW to NE-SW orientations in the SE Dinarides, which is compatible with the overall Adria indentation (Bada et al., 2007; Heidbach et al., 2007; Heidbach et al., 2010) and a transpressional evolution at least from Miocene times.

On the other hand, in the Hellenides this stress field rotates to more E-W directions, by a combined effect of a similarly oriented compression in external areas, and a perpendicular N-S to NNE-SSW oriented extensional deformation elsewhere, inferred to be the result of the S- to SSW-wards slab roll-back combined with gravitational spreading of the Aegean lithosphere (Heidbach et al., 2007; Konstantinou et al., 2017). A similar situation is observed in the Apennines (**Figure 1.6b**), where the NW-SE SH orientations are the result of a NE-SW oriented extension. To the NW of the Apennines, the SH orientation gradually changes to NE-SW in the Adriatic Sea, interpreted to be a combination between horizontal gradients of the gravitational potential energy, the long-wavelength of the Africa-Europe convergence zone, and the Adriatic indentation according to Métois et al. (2015).

To the NW (**Figure 1.6a**), a significant number of NW-SE to WNW-ESE oriented, large offsets dextral strike-slip faults, associated with E-W to ENE-WSW oriented reverse faults and smaller offset NE-SW to NNE-SSW oriented sinistral strike-slip faults, have been interpreted to be either latest Miocene – Quaternary or Pliocene - Quaternary features, or active neotectonic deformation features along the Peri-Adriatic Lineament or southwards in the NW-most part of the Dinarides (e.g., Heberer et al., 2017; Moulin et al., 2016; Tomljenović & Csontos, 2001; Tomljenovic et al., 2008; Ustaszewski et al., 2014; van Gelder et al., 2015; Vrabec & Fodor, 2006; Vrabec et al., 2006). The southern part of this fault system (immediately north of the Istria peninsula, **Figure 1.6a**) likely connects with or transfer deformation to Split-Karlovac (Van Unen et al., 2019). The larger strike-slip and thrusting offset in the external part of the High-Karst, Budva and Dalmatian units of the SE Dinarides seem to be connect with Miocene faults (Bega, 2015; Roure et al., 2004; Vilasi et al., 2009).

It's noteworthy to observe that the zone where the overall structural kinematics, GPS motions, present-day horizontal stress, and seismicity distributions change across the entire Dinarides - Albanides – Hellenides orogens is the Kefalonia Fault (**Figure 1.6a**). This fault system is interpreted to be the expression of an older transformant fault that separated the Mesozoic carbonate facies evolution (e.g., Aubouin & Dercourt, 1975; Velaj et al., 1999) and accommodated significant Miocene extensional offset caused by an increase in roll-back subduction to the SE (Schmitz et al., 2017) of a transitional Adriatic-Ionian continental lithosphere affected by significant normal faulting (Bega, 2015).

1.3 THE MECHANICAL STRATIGRAPHY CONCEPT

Mechanical stratigraphy is generally accepted as a subdivision of rock or rock units into discrete intervals, i.e., mechanical units, based largely on rheology and deformation behavior (Corbett et al., 1987; Cooke, 1977; Gross et al., 1995). In layered sequences, mechanical stratigraphy is defined by various parameters as the mechanical properties, the layer thickness and the nature of the layer interfaces (Shackleton et al., 2005; Tavani et al., 2008; Laubach et al., 2009; Savage et al., 2010; Barbier et al., 2012; Gale et al., 2014; Ferrill et al., 2016). Such mechanical properties (e.g., strength, viscosity, cohesion, primary porosity etc.) are directly related to rock texture and mineralogy, and may naturally evolve and change during progressive burial, tectonic deformations, or fluid-rocks interaction processes (Marin et al., 1993; Rijken et al., 2002; Fischer et al., 2003; Shackleton et al., 2005).

Diagenetic processes, such as dissolution, precipitation, compaction (i.e. physical and chemical), tend to dramatically modify the original composition and texture of rocks, producing important changes on their mechanical properties (Rijken et al., 2002; Laubach et al., 2009). For example, rock mass concentration can easily modify the tensile strength, elastic stiffness and brittleness (Rijken et al., 2002), influencing fracture attributes and distribution (Olson et al., 2007, 2009). Moreover, post-depositional processes and tectonic evolution can drive and vary the thickness of mechanical units, the character of interfaces, and the fracture mechanics, forming units prone to localize deformation and fracture development (Laubach et al., 2009).

Moreover, frictional properties of layer interfaces can often influence the deformation behavior of siliciclastic and carbonate rocks. Frictional strength and interface cohesion can be decreased by the concentration of organic matter and insoluble clay minerals along bedding surfaces or in zones between competent beds (i.e., paleosoils). Differently, rugose or sutured boundaries produced by primary emplacement or depositional processes, increase the resistance to frictional sliding between layers (Ferrill et al., 2016). Burial pressure solution processes, extremely common in carbonates, usually develop layer-parallel stylolites that tend to lock bedding planes and to increase frictional resistance of bedding. Moreover, sharp mechanical contrast and weak beds or laminae (i.e., intertidal sequences in platform carbonates) may localize bedding parallel slip, driving stress concentration and deformation localization at the unit boundaries. They may also cause abrupt changes in deformation behavior (e.g., Higgs et al., 1991; Ferril et al., 1998, 2007, 2012; Cooke & Underwood, 2001; Ogata et al., 2017).

1.4 FOLDING RELATED DEFORMATION IN FORELAND FOLD-AND-THRUST BELTS

Foreland fold-and-thrust belts are typically controlled by deformation structure networks including fault-related folds and high-angle tear-faults (Tavani et al., 2015). In fold-and-thrust belt studies, the use of deformation pattern templates in cylindrical folds have significantly contributed to improve knowledge of foreland basin systems (DeCelles & Giles, 1996; Engelder & Geiser, 1980; Marshak & Engelder, 1985; Price & Cosgrove, 1990; Srivastava & Engelder, 1990; Gray & Mitra, 1993; Ferrill & Groshong, 1993; Fischer & Jackson, 1999; Lacombe et al., 1999; Storti & Salvini, 2001; Bellahsen et al., 2006; Wennberg et al., 2006; Lacombe et al., 2006; 2011; Tavani et al., 2006; Evans, 2010; Savage et al., 2010; Shackleton et al., 2011; Tavani et al., 2011; Beaudoin et al., 2012; Tavani et al., 2012; Tavani et al., 2015).

Deformation patterns in fold-and-thrust belts usually results from a long-lived evolution, starting with foreland flexuring followed by layer-parallel shortening at the toe of thrust wedges, growth of thrust-related anticlines, and late-stage tightening (Ramsay, 1974; Engelder & Engelder, 1977; Turcotte & Schubert, 1982; Cooper et al., 1983; Williams & Chapman, 1983; Wiltschko et al., 1985; Evan & Dunne, 1988; Price & Cosgrove, 1990; Doglioni, 1995; Gutiérrez-Alonso & Gross, 1999; Lacombe & Mouthereau, 1999; Billi & Salvini, 2003; Mazzoli et al., 2005; Tavani et al., 2008; Lacombe et al., 2011; Langhi et al., 2011; Tavani et al., 2011; Beaudoin et al., 2012; Tavani et al., 2012; Tavani et al., 2015 and reference therein; **Figure 1.7**).

In the case of non-cylindrical long-lasting deformation, characterized by changing of stress field orientations during folding, progressive deformation patterns could be different. Moreover, lithologically-controlled switch between strike-slip or compressive stress field configurations during shortening, and stress channeling during folding, can cause increasing variability in deformation patterns (Chester et al., 1911; Tavani et al., 2015 and references therein). For example, high-value of the Young modulus implies the onset of a compression field whilst the stress configuration in the surrounding layers is still strike-slip (Eisenstadt & De Paor, 1987). Tavani et al. (2015) clearly show that thrust ramps can nucleate in a strike-slip stress field configuration where local compressional stresses can occur due to depth and lithological effects combinations.

The occurrence of tight anticlines in stiff rocks developed in the frontal part of thrust-wedges is not common. In such a case, fold architecture and structural assemblage developed during pre- to late-deformation stages could be more complex than expected. Combined effects of rheology, stress-field orientation and its possible changes during syn-orogenic evolution, and the presence of inherited structures could affect fold evolution and its 3D architecture. For example, thrust nucleation and propagation can be facilitated by the occurrence of inherited pre- and/or early-orogenic deformation structures, which provide sectors for stress accumulation (Berbauer & Pollard, 2004; Sassi et al., 2012), inducing buttressing, inversion and/or mixed behaviors (Coward et al., 1989).

Another interesting point its related to the depth of deformation. In fact, it is well known that depth and rheology can favor local compressional stress configurations facilitating fault-tip migration (Tavani et al., 2015, reference therein). Due to depth variations during syn-orogenic evolution (i.e., from burial to exhumation), different stress field configurations occur and imply stress-switch events.

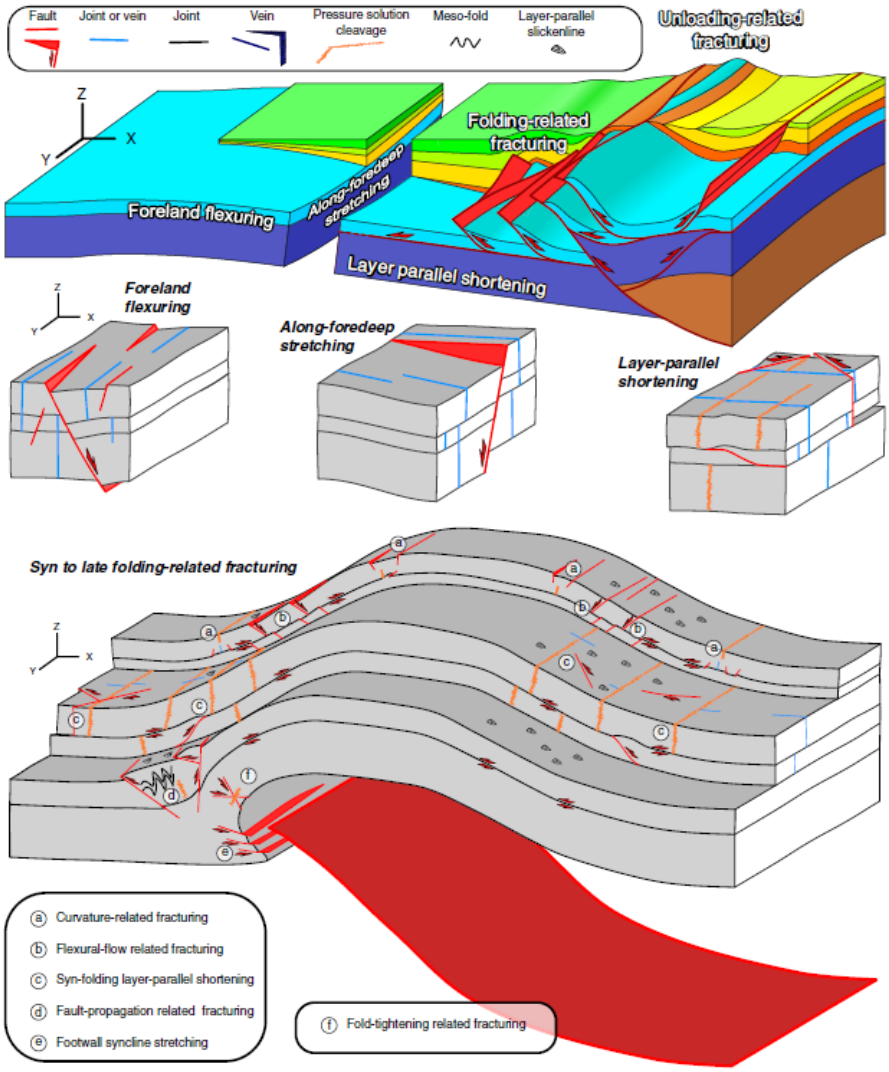

Figure 1.7 - 3D scheme showing the architecture of a foreland fold-and-thrust belt and the typical structural assemblages developing during five syn-orogenic deformation stages (from Tavani et al. ,2015).

In conclusion, while deformation patterns show a characteristic and well-known evolution in foreland thrust and fold belts, intrinsic changes and more complex fold architectures can develop at the near toe of thrust wedges as the result of multiple factors, including rheology (i.e., mechanical stratigraphy), deformation-depth, the presence of inherited deformation structures and their relative orientation, pore fluid pressure, and regional stress evolution.

CHAPTER 2.

GEOLOGICAL MAP OF THE PAG ANTICLINE

This chapter is presented in the form of a manuscript that is currently in production for being published in the *Geological Field Trip and Maps.* The manuscript describes the Geological map at 1:25,000 scale of the Pag anticline, its statigraphical and structural architecture and tectono-stratigraphic evolution.

PUBLISCHED ARTICLE

Geological and structural map of the southwestern Pag Island, Croatia: field constraints on the Cretaceous-Eocene evolution of the Dinarides foreland

Mittempergher, S., Succo, A., Bistacchi, A., Storti, F., Bruna, P-O., and Meda, M.

Geological Field Trip and Maps, 2019, Volume 11 (2.4), https://doi.org/10.3301/GFT.2019.06

GEOLOGICAL AND STRUCTURAL MAP OF THE SOUTHWESTERN PAG ISLAND, CROATIA: FIELD CONSTRAINTS ON THE CRETACEOUS-EOCENE EVOLUTION OF THE DINARIDES FORELAND

Silvia Mittempergher[1], Andrea Succo[2], Andrea Bistacchi[1], Fabrizio Storti[2], Pierre Olivier Bruna[3] & Marco Meda[4]

1. Dipartimento di Scienze dell'Ambiente e della Terra, Università Milano Bicocca, Piazza della Scienza 4, 20126 Milan, Italy

2. NEXT – Natural and Experimental Tectonics research group, Università di Parma, Dipartimento di Scienze Chimiche, della Vita e della Sostenibilità Ambientale, Parco Area delle Scienze 157/A, 43124 Parma, Italy

3. Department of Geoscience and Engineering, Delft University of Technology, Stevinweg 1, 2628 Delft, The Netherlands

4. Eni Spa, Upstream and Technical Services – Piazza Vanoni 1, 20097 San Donato Milanese - Italy

ABSTRACT

The sedimentary succession exposed in the Northern Dalmatia Islands mainly consists of Cretaceous to Neogene shallow water carbonates, folded and imbricated within the External Dinarides thrust belt. During Cretaceous times, carbonate sediments were deposed on a heterogeneous, tectonically-influenced carbonate platform, which was then uplifted and eroded, as evidenced by a regional unconformity embracing the Late Cretaceous and Paleocene. Sedimentation resumed during the Eocene, when the area was part of the foreland basin of the Dinaric belt. With our geological and structural map of the southeastern Pag Island at the 1:25,000 scale, we refined the stratigraphic and structural setting and the tectono-sedimentary evolution of the area.

2.1 INTRODUCTION

The hanging wall of the outermost Dinaric thrust is an imbricated belt of deformed Cretaceous to Neogene sediments (**Figure 2.1**; External Dinarides after Pamić et al., 1998), which recorded the transition from a long-lasting carbonate platform (the Adriatic Carbonate Platform, Vlahović et al., 2005) to a laterally heterogeneous Eocene – Oligocene foreland basin (e.g., Tari, 2001; Korbar, 2009; Vlahović et al., 2012). The large-scale tectono-sedimentary architecture of the region was well outlined since the earliest surveys conducted during the 19th century (Hauer, 1868), and the first geological map of the Pag Island at the 1:75,000 scale was published as early as the 1912 (Schubert and Waagen, 1913). The Basic Geological Map (Osnovna Geološka Karta) of Jugoslavia at the scale 1:100,000 (sheets Gospić, Zadar and Silba, Majcen et al., 1976; Mamužić and Sokač, 1973; Sokač et al., 1976) constitutes the most recent synthesis of the regional geology.

However, the sedimentary succession was surveyed with chronostratigraphic criteria and the structural setting, due to the small scale of representation and out-of-date interpretative concepts, is not fully reliable. In our new geological and structural map (**Attached 1** – Geological and structural map of the Pag anticline; see also **Figure 2.1** for map location), we mapped the area by identifying lithostratigraphic units correlated with the sedimentary formations at the regional scale, and surveyed in detail the tectonic structures. This allowed us to refine the stratigraphy and structural architecture of the folds outcropping in the area, and to document a pre-unconformity (thus pre-Eocene) tectonic stage.

2.2 METHODS AND TECHNIQUES

The geological and structural map of the southeastern Pag Island (**Attached 1** – Geological and structural map of the Pag anticline) is based on field surveys conducted between February 2017 and May 2018, integrated with the interpretation of high-resolution satellite images available from the Bing portal (https://www.bing.com/maps) and the geoportal of the Croatian Geodetic Service (https://geoportal.dgu.hr/). Field surveys were based on printed aerial photographs, or on GPS equipped tablets, mainly at the 1:5,000 scale, and locally at the 1: 2,000 scale. During the field surveys, we measured several stratigraphic columns across the area, and compared facies associations with published data, referring in particular to the megafacies described by Tišljar et al. (2002). Where no official formational names were available, we used the most commonly used names in the literature about the region (Gušić and Jelaska, 1990) and on the recently published geological maps at the 1:50,000 scale (e.g., Fuček et al,

2012). Structural data of fault kinematics were collected in selected locations along major fault zones. Since mapping was focused on the Meso-Cenozoic geological formations, the very limited Quaternary deposits were not surveyed in detail, and were only mapped as either Holocene loose deposits or Pleistocene cemented ones.

The map was digitized in UTM fuse 33N coordinates with WGS84 Datum with the GIS software ArcMap 10.6 and QGis 2.18.21. The background topographic map has been obtained by combining (i) 20 m-contours extracted, using the 3DAnalyst ArcGIS extension, from the photogrammetric Digital Elevation Model provided by the Croatian Geodetic survey, with (ii) topography elements (roads, perimeters of inhabited areas, salt ponds) downloaded from the OpenStreetMap® project and licensed under the Creative Commons Attribution-ShareAlike 2.0 license. The final printable map was obtained by editing the layouts from the GIS software with the vector graphics software Adobe Illustrator CS5®.

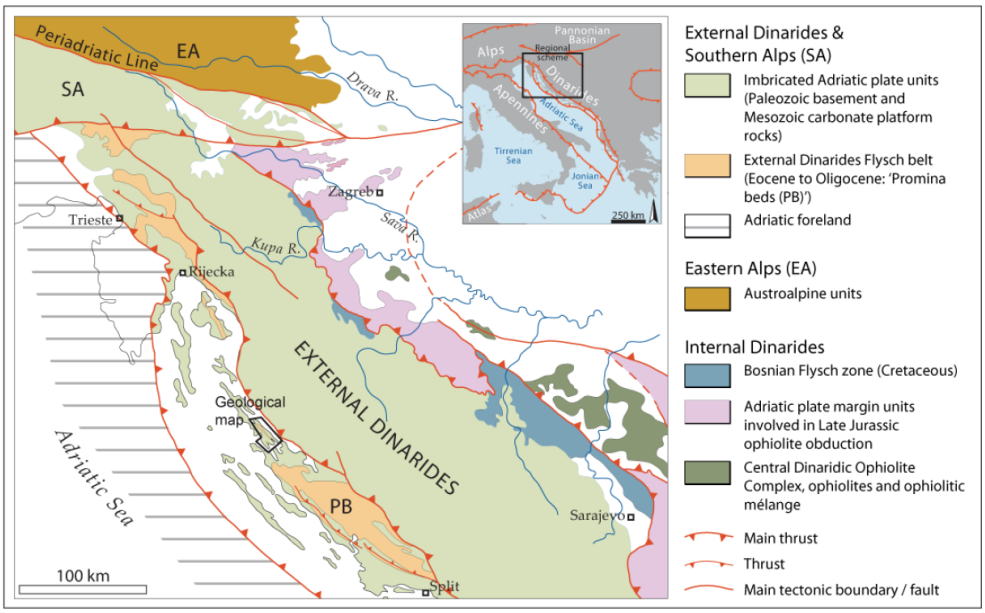

Figure 2.1 - Location of the map within a simplified regional scheme of the northern Dinarides (redrawn and simplified after Tomljenović et al., 2008; Ustaszewski et al., 2008; Korbar, 2009).

2.3 REGIONAL SETTING

The Northern Dalmatian islands are part of the External Dinarides, a belt of folded and thrusted sediments of Carboniferous to Neogene age (Pamić et al., 1998; Placer et al., 2010), forming the shallower part of the detached and highly deformed upper crust of the Adriatic plate (Korbar, 2009). This sector of the Adriatic plate was characterized by nearly continuous

deposition of shallow-water carbonates since Carboniferous times and, from the Lias to the Late Cretaceous, it was a well-defined paleogeographic domain known as the Adriatic Carbonate Platform, hereafter AdCP (Velić et al., 2002; Vlahović et al., 2002; Vlahović et al., 2005).

During Cretaceous times, the AdCP had a laterally heterogeneous facies distribution and underwent repeated subaerial exposures and episodic platform drownings (Tišljar et al., 2002; Vlahović et al., 2005). Relative sea level changes occurred due to the interplay between global eustatic variations and synsedimentary tectonics during the polyphasic convergence between Eurasia and Adria plates, which began in Late Jurassic times (Aubouin et al., 1970; Schmid et al., 2008) and is still active (Kastelic and Carafa, 2012; Kastelic et al., 2013). With the propagation of the orogenic front to the SW, the AdCP underwent dissection and emersion during a major event recorded by a regional unconformity surface, locally bearing bauxite (Vlahović et al., 2005; Kovačević Galović et al., 2012; Peh and Kovačević Galović, 2016). Sedimentation resumed in Early Eocene times, when the Northern Dalmatia constituted the foreland basin of the Dinarides. The foraminiferal limestone (Tišljar et al., 2002; Ćosović et al., 2004) was deposited on a carbonate ramp, interpreted as a retreating forebulge flank (Korbar, 2009; Babić and Zupanič, 2016; Ćosović et al., 2018). Shallow water carbonates were replaced during middle Eocene times by clastic hemipelagic sediments known as Dalmatian flysch (e.g., Babić and Zupanič, 2008), and by the upper Eocene-lower Oligocene regressive molasse sequence of the Promina Beds (Mrinjek, 1993; Tari Kovačić and Mrinjek, 1994; Vlahović et al., 2012; Zupanič and Babić, 2011), exposed some tens of kilometres to the southeast of the Pag Island. Sedimentological studies demonstrated that the Promina Beds were deposed during fold growth, thus constraining imbrication and folding in the southeastern part of the External Dinarides to Late Eocene-Oligocene times (Ćosović et al., 2018; Vlahović et al., 2012).

Another clastic body that characterizes the External Dinarides is the so-called Jelar breccia, a chaotic polymictic breccia of prevailing Jurassic to Cretaceous carbonate clasts and including also clasts of middle Eocene age (Pamić et al., 1998; Korbar, 2009; Vlahović et al., 2012). The origin of the breccia is still poorly understood because of its unclear structural position and intense younger tectonic deformation, and is interpreted as associated with gravitational collapse of early-stage anticlinal structures (Korbar, 2009; Vlahović et al., 2012). In Late Oligocene – Miocene times, an extensional tectonic event is recorded throughout the Dinaric chain (Ilić and Neubauer, 2005; van Unen et al., 2018), and in the same period a system of intramontane lakes developed, one of which is recorded by lacustrine

sediments preserved in the Pag Island (Bulić and Jurišić-Polšak, 2009; Jiménez-Moreno et al., 2009). After the late Miocene, a contractional to strike-slip tectonic setting resumed in consequence of the indentation and anticlockwise rotation of the Adria microplate (Ilić and Neubauer, 2005), which is still ongoing, as documented by GPS velocity studies and crustal stress patterns (e.g., Faccenna et al., 2014; Heidbach et al., 2016).

2.4 MAP DESCRIPTION

2.4.1 *Stratigraphy*

2.4.1.1 *The sedimentary succession of the Adriatic Carbonate Platform*

The Milna Formation (MI) of Cenomanian age consists of a sequence of shallowing upward cycles of intertidal limestones, including storm layers with large bioclasts, massive pelletal wackestones, intraformational breccias, paleosols and very abundant microbial laminae (**Figure 2.2a**). The laminites are locally deformed in meters to decametre-sized slumps (**Figure 2.2b**). Channelized and cross-laminated packstone-grainstone layers are subordinate to the peritidal facies (**Figure 2.2c**). During the deposition of the Milna Formation, the AdCP was covered by a shallow sea subjected to temporary sea level excursions, likely controlled by syn-sedimentary tectonics, as suggested by the occurrence of slumping structures, present also in other sectors of the AdCP (Korbar et al., 2012; Prtoljan et al., 2007).

The Milna Formation is sharply overlain by the Sveti Duh Formation (SD), consisting of nodular beds of whitish-yellowish wackestones and packstones rich in crinoids, foraminifera, sponge spicules and thin-shelled bivalves. The top of the Milna Formation is marked by a stained and burrowed surface, with the overlaying wakestone-packstone infilling the burrows, interpreted as a hard ground surface (**Figure 2.2d**). Between Cenomanian and Turonian times, several sectors of the AdCP were drowned with deposition of pelagic and ramp carbonate sediments (Gušić and Jelaska, 1993). The rise in relative sea level is correlated with the global Bonarelli anoxic event or OAE2 (e.g., Korbar et al., 2012), although areas which maintained a shallow marine sedimentation suggest that tectonic uplift locally overtake the sea level rise (e.g., Vlahović et al., 2002).

The Sveti Duh Formation passes transitionally to the shallow water carbonates of the Gornji Humac Formation (GH). The Gornji Humac Formation is characterized by high lateral and vertical facies variability, including banks of well-bedded peletoidal wackestones-packstones and microbial laminated limestones in shallowing-upward cycles, well sorted

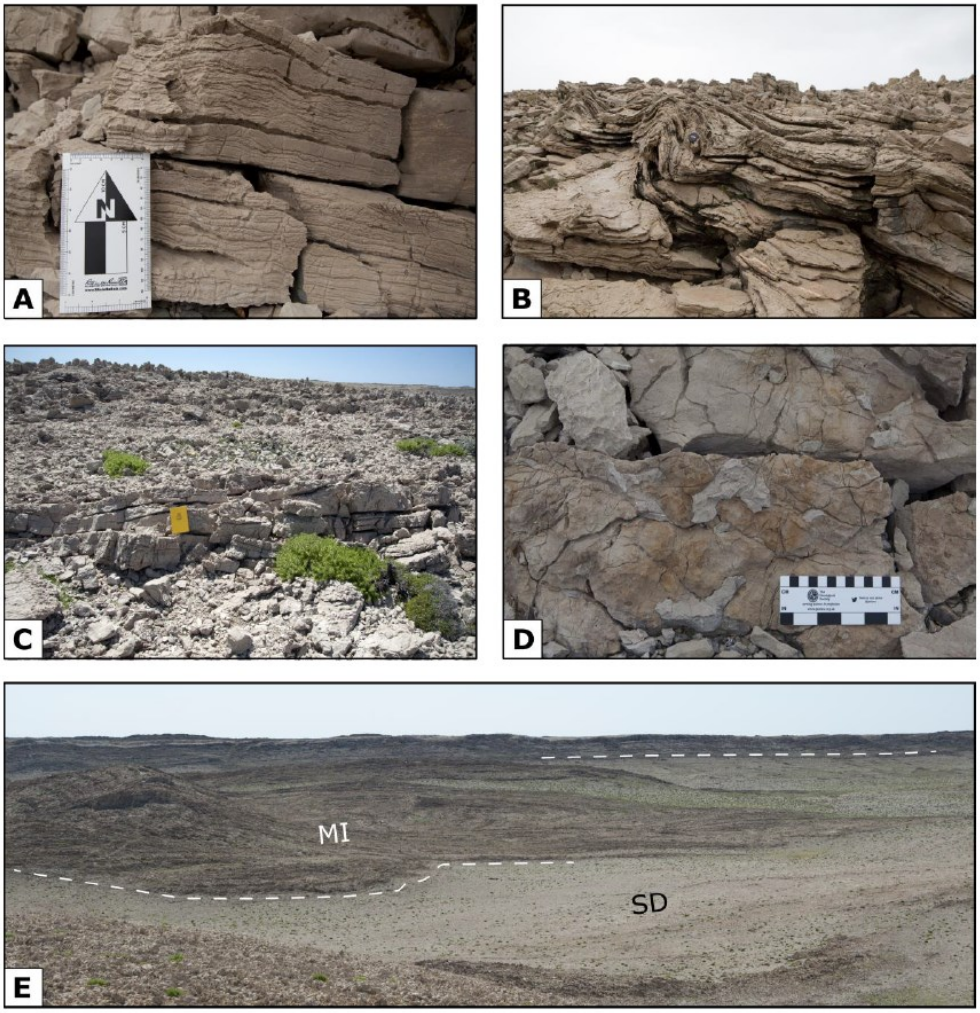

Figure 2.2 – Field pictures of the AdCP Milna and Sveti Duh Formations. (A) Detail of a stromatolite-rich interval. (B) Slumped laminated limestones. (C) Pinch-outs of channelized packstone-grainstone cross laminated interval within the Milna Formation. (D) The stained and burrowed surface at the interface between the Milna and Sveti Duh Formations. Plagues of light grey wackestone infill strata-parallel burrows. (E) Panoramic view of the sharp contact of the Sveti Duh Formation with the Milna Formation.

cross-laminated packstone-grainstones with channelized geometry and massive floatstone-mudstone layers (**Figures 2.2a, b**). Coarse clasts of rudists are very diffuse within the wackestone-packstone and mudstone banks (**Figure 2.3c**), and, especially in the upper part of the formation, rudstone beds of rudist shell fragments (coquinites) are widespread. The mudstone banks reach up to 3 m in thickness, in the lower part are composed of floatstone with large rudist fragments, and often terminate at the top with a thick (up to 40 cm) layer of centimetre-scale cavities filled by darker sediments and cemented by calcite, interpreted as bird's eyes structures.

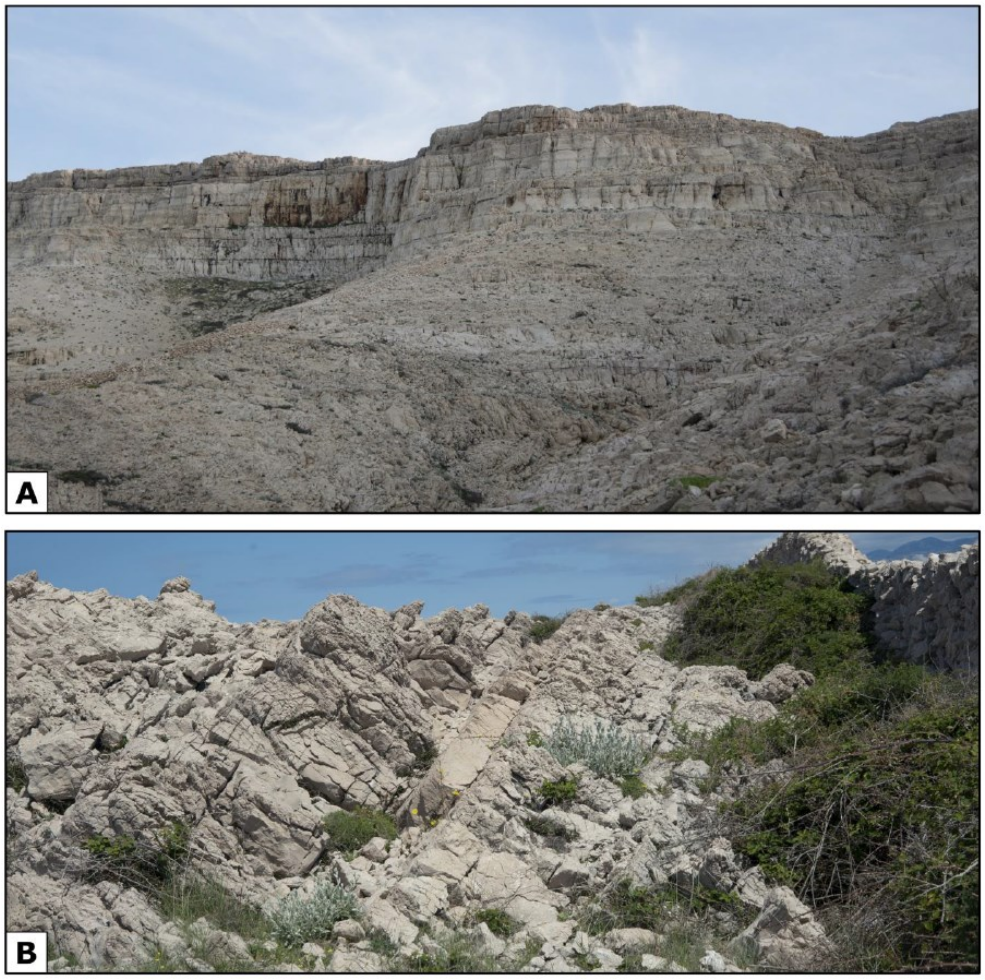

Figure 2.3 - Panoramic field pictures of the AdCP Gornji Humac Formation. (A) Panoramic view of the Gornji Humac Formation in the northern part of the Pag anticline. Meter-thick beds of white mudstone alternated with minor light brown packstone beds are the dominant facies association in this area. (B) View of the alternation of packstone, rudstone and mudstone banks having a prevailing brownish color, the dominant facies association in the central and southern sectors of the Pag anticline.

Mudstone-floatstone banks are the main lithology of the formation in the northwestern part of the area, while elsewhere cross-laminated packstone-grainstones are more abundant. Hectometric discordant bodies of coarse-grained, channelized carbonate breccias crosscut the strata of the Gornji Humac, Sveti Duh and Milna Formations (**Figures 2.4b, d**).

Bed parallel, lens-shaped dolomitized masses are common and are mostly de-dolomitized with precipitation of late-stage calcite crystals, forming recrystallized limestone bodies with whitish-pinkish colour in outcrop (**Figures 2.4a, c**). Dedolomitization is almost complete in the outcrops of the major anticline SE of the Pag village, while in the anticline

close to the village of Vlašići, dolostone is mostly preserved. A layer of whitish to pinkish recrystallized limestones also marks the upper 20 – 50 m of the Gornji Humac Formation, below the erosional surface truncating it (**Figure 2.3c**).

The erosive surface is lined by intraformational breccias, oxidized and vadose cement, and irregular cavities filled by brownish silty or sandy grainstone (**Figure 2.3d**). The Gornji Humac Formation is characterized by facies associated with shallow marine conditions, including both low energy environments as lagoons and peritidal/tidal flats, and high energy environments of shoreface and tidal bars. The overall abundance of rudist debris suggests a close proximity to reefal or perireefal areas. Synsedimentary tectonics is likely to have controlled the paleobatimetry of the platform, and the formation of fault escarpments associated with carbonate breccias deposits.

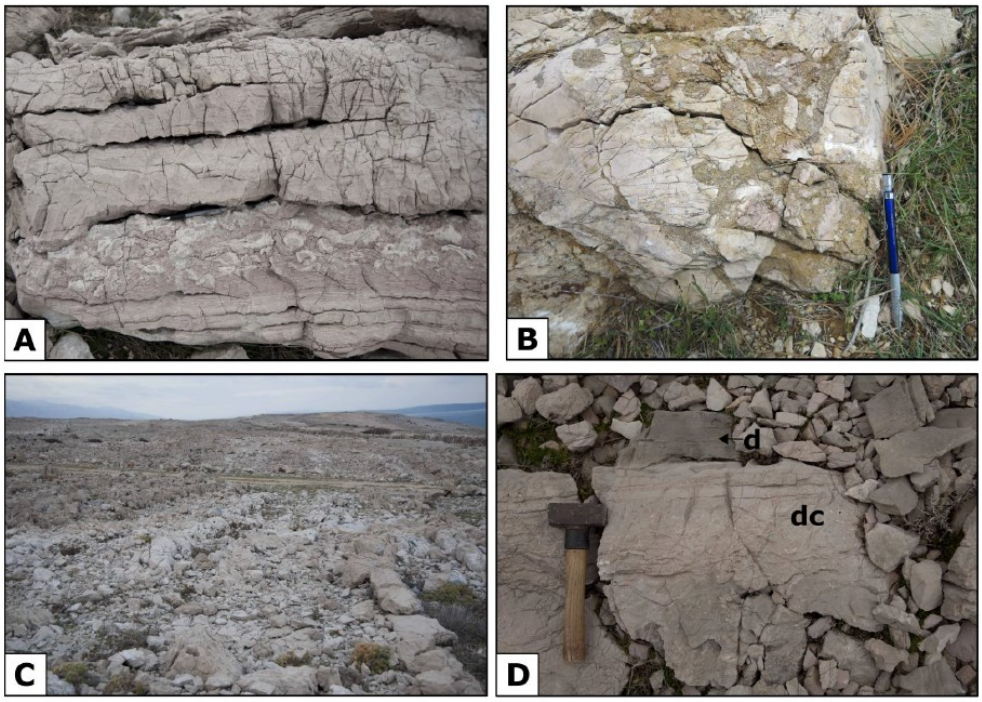

Figure 2.4 - Field pictures of the AdCP Gornji Humac Formation. (A) Detail of a storm layer rich in rudist shells, sharply overlying a stromatolite-rich bed. The pinkish color is typical of the recrystallized upper part of the formation, below the erosion surface. (B) Detail of the infilling of karst cavities along the erosional surface at the top of the Gornji Humac Formation. (C) Field picture of a couple of bed-parallel, white crystalline bodies of dedolomitized dolostone within the Gornji Humac Formation. (D) Detail of the transition of the late diagenetic greyish dolostone (d) to pinkish crystalline limestone (dc).

2.4.1.2 *The sedimentary succession of the Dinaric foreland basin*

In the Area of the Pag Island, the stratigraphic gap marked by the erosive surface atop of the Gornji Humac Formation lasted from Coniacian-Santonian to Ypresian times (Jelaska et al., 1994; Korbar, 2009). Sedimentation resumed with the deposition of benthic-foraminifera-rich carbonates with subordinate remnants of molluscs, echinoderms and bryozoans. These rocks, informally known in literature as 'foraminiferal limestone' (FL) (Tišljar et al., 2002; Ćosović et al., 2004), have an angular discordance on the order of 10° with bedding in the Gornji Humac Formation below the erosional surface, as visible in several outcrops (**Figure 2.5a**). The foraminiferal limestone includes Miliolids – rich wackestones-packstones, in undulating 20 – 30 cm thick beds (**Figure 2.5b**), and meter-thick cross-laminated banks of Alveolinid- and Nummulite-rich floatstones with packstone to grainstone matrix. The foraminiferal limestone, as described also in other sectors of the External Dinarides, is composed of facies typical of foraminiferal banks in an inner to middle carbonate ramp, alternating with mud-rich facies suggesting a more restricted lagoonal setting (Ćosović et al., 2004; 2018; Marjanac and Ćosović, 2000; Španiček et al., 2017). In the southern part of the mapped area, the top of the foraminiferal limestone consists of meter-thick banks of rudstones with abundant bioclasts of echinoderms and pluri-centimetric benthic foraminifera (**Figure 2.5c**), in sharp contact with the overlying hemipelagic pelites and marls of the Dalmatian flysch.

The top surface of the foraminiferal limestone is stained by iron oxydes and is intensely burrowed and bioturbated. Moreover, the uppermost layers of foraminiferal limestone below the stained surface bear glauconite. Accordingly, the top of foraminiferal limestone can be interpreted as a drowning surface. In the northern sector of the map, the foraminiferal limestone passes upward, with a fast transition, to a fining-upward sequence of marly limestones and greyish, glauconite-bearing marls (**Figure 2.5d**). The occurrence of planktonic foraminifera (Globigerinae) documents a significant deepening of the depositional environment to shelf or shallow bathyal conditions. Though only few tens of meters thick, this interval is recognized elsewhere in the region and referred to as '*transitional beds*' (Ćosović et al., 2004; Marjanac and Ćosović, 2000), which is locally found at the base of the Dalmatian flysch (DF), characterized by a sudden increase in the clastic over the carbonatic component.

In the Island of Pag, the Dalmatian flysch consists of a sequence of prevailing pelites and marls, with interbedded fine-grained sandstones and multimetric intervals of amalgamated sandstone beds. Pelites and marls have grey-blueish color and are interbedded with thin layers of fine-grained

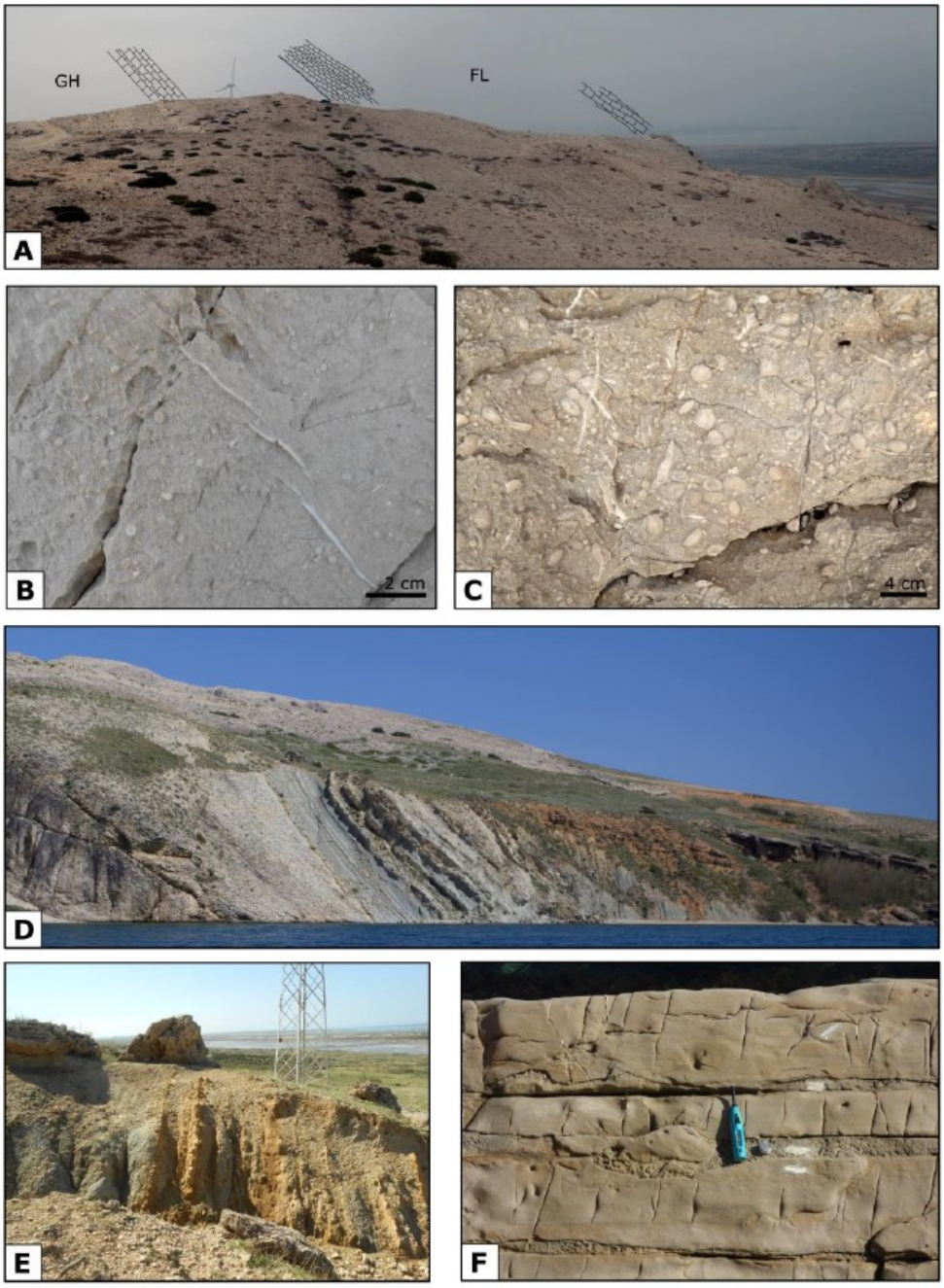

Figure 2.5 - Field pictures of the External Dinarides foreland units. (A) Panoramic picture taken along the southwestern limb of the Pag anticline north of the Pag town, looking to the SE. To highlight the angular unconformity of about 10° between the Gornji Humac Formation on the left and the foraminiferal limestone on the right, the strata are schematically drawn in section above the horizon line. The base of the foraminiferal limestone consists of mud-rich, well stratified inner ramp deposits, passing upward to a bar of coarse grained rudstone – packstone. (B) Mud-rich inner ramp limestone within the foraminiferal limestone. (C) Top layers of the foramniferal limestone, composed of thick beds of rudstone with packstone matrix, with abundant Nummulites, bivalve shells and echinoderms, associated with a deep, open carbonate ramp. (D) Panoramic view, along the coast north of

(*continued from the previous page*): the Pag town, of the sharp transition from foraminiferal limestone (on the left) to gray-blue, glauconitic marls and marly limestones of the transitional beds. (E) Outcrop of the Dalmatian flysch near the Stara Vasa village, consisting of dominant pelites and marls, with thin layers of fine-grained sandstone. The blocks on the top are disarticulated remnants of Pleistocene cemented deposits. (F) Detail of a bank of amalgamated sandstone within the Dalmatian flysch.

arenites, sometimes cross-laminated (**Figure 2.5e**). The amalgamated sandstones are made of banks of yellowish to grey, fine to very fine arenites, with at least 50% of non-carbonate component (**Figure 2.5f**), with erosive base, sometimes with mud chips and plane-parallel lamination in their lower part.

The association of facies of the Dalmatian flysch in the Island of Pag, as well as recent calcareous nannofossils data suggest a relatively shallow hemipelagic depositional environment under fluvial influence, in a shallow foredeep or thrust-top basin (Babić and Zupanič, 2008). The Dalmatian flysch exposed in the Island of Pag registered first a progradation of clastic units, culminating with the deposition of one (in the southern part of the mapped area) or more (in the northern sector) plurimetric banks of amalgamated sandstone, followed by a retrogradation with the reduction or cessation of coarse clastic input and the deposition of hemipelagic marls and pelites.

2.4.1.3 *Pleistocene to recent deposits*

Quaternary deposits are rare in the southeastern part of the Pag Island, where we mapped Pleistocene and Holocene strata. Pleistocene alluvial deposits contain angular, well sorted and cross-bedded subangular clasts, having reddish to yellowish color and cemented by vadose calcite. Cemented polymictic breccias with subrounded clasts also occur. Such cemented sediments were deposed in presence of a higher base level than the present-day one and are nowadays subject to erosion. They have been interpreted as deposed in glacial and periglacial conditions during the Middle Pleistocene (Marjanac and Marjanac, 2004; Marjanac, 2012; Marjanac and Marjanac, 2016). Holocene deposits consist mostly of (*i*) colluvial sediments produced by intense soil erosion, (*ii*) slope deposits in proximity of limestone cliffs, and (*iii*) lacustrine to marsh deposits in the larger valley floors.

2.4.2 *Tectonic features*

The tectonic structure of the Northern Dalmatia is dominated by NW-SE trending thrusts and folds (Mamužić and Sokač, 1973; Sokač et al., 1976). The mapped area includes a large anticline east of the Pag village, and a train of folds with lower amplitude in the surrounding of the Povljana village (**Figure 2.6**; see also **Attached 1** – Geological and structural map of the Pag anticline). The anticlines have box geometry with high-angle to overturned limbs and gently undulating crestal zones. The folds in the surroundings of Povljana are nearly symmetric, while the Pag anticline is asymmetric, and verges to the regional foreland in the southern sector **(section B-B'** in **Attached 1**), and to the hinterland in the northern sector (**section A-A'** in **Attached 1**). The change in polarity of the limbs asymmetry occurs through a major EW trending strike-slip fault, offsetting the fold in sinistral sense (**Figure 2.6**).

Due to the erosion and the high amplitude of the Pag anticline, the fold core is exposed and consists of a stack of thrust sheets that produces intense shortening of the detached laminated limestones of the Milna Formation (**Figure 2.7a**). The Pag anticline backlimb is structurally complex, with several undulations produced by backthrusts (**Figure 2.7b**) and out-of-the-syncline, foreland verging thrusts (Mitra, 2002). A triangle zone with oppositely verging thrusts is exposed along the northeastern Pag coast, juxtaposing the foraminiferal limestone on the overlying transitional beds (**Figure 2.7c**). The box geometry and the occurrence of oppositely verging thrusts crosscutting the fold limbs suggest that folds are the shallow expression of pop-up structures, and likely originated as detachment folds (e.g., Mitra, 2002).

Several subvertical strike-slip faults crosscut the folded sedimentary sequence (**Figures 3.6c**, **3.8**; see also **Attached 1** – Geological and structural map of the Pag anticline). The main sets strike NS, EW and NE. At the map scale, NS faults offset the sedimentary markers in dextral sense, EW faults in sinistral sense. However, field structural measurements demonstrate that most faults, including thrust faults, experienced a long-lasting activity with opposite strike-slip kinematics, and underwent buttressing. Most of the high-angle strike-slip faults are localized along the fold limbs dipping at high angle, produce offsets of less than 130 m, and their offsets decrease to vanish towards the fold axes (**Figure 2.6**).

According to the along-strike variability of limb dip in adjacent compartments, these faults acted as tear faults accommodating differential limb rotation during fold tightening. Few major fault zones separate fold domains having different structural architecture, thus suggesting that they

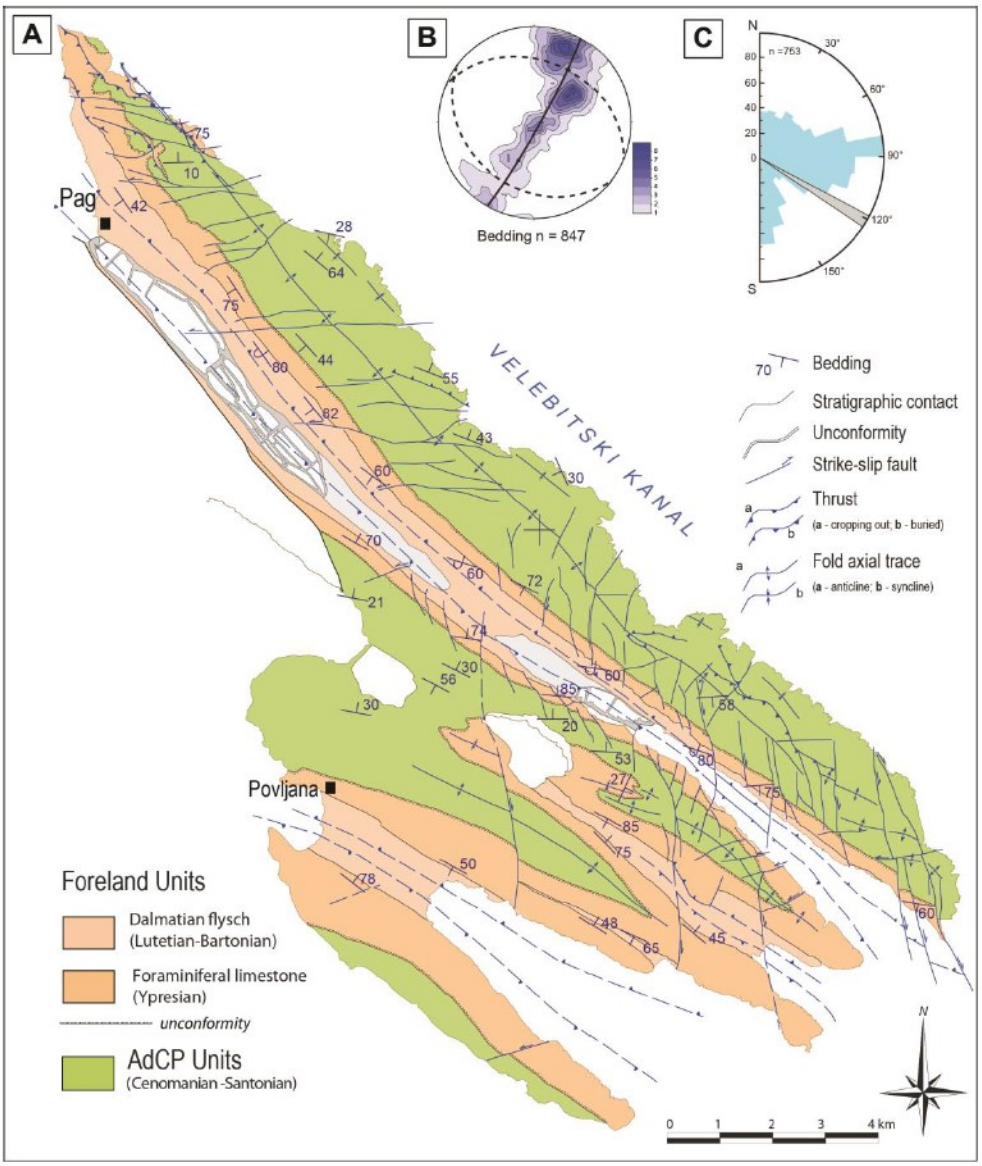

Figure 2.6 - Structural scheme and cumulative structural data. (A) Simplified structural scheme of the area. The geological sections A-A' and B-B' are in Attachment 1 - Geological Map of Pag. (B) Contoured stereoplot of the poles to bedding measured in the study area. Lower hemisphere, equal area projection (C) Rose diagram of the strikes of the main faults traced within the study area. The strike of the average fold axis is reported in grey

compartmentalized the folds since the early stages of fold growth (**Figure 2.6**) Major transversal faults crosscut all the structural elements of the folds thus indicating that strike-slip activity continued after folding.

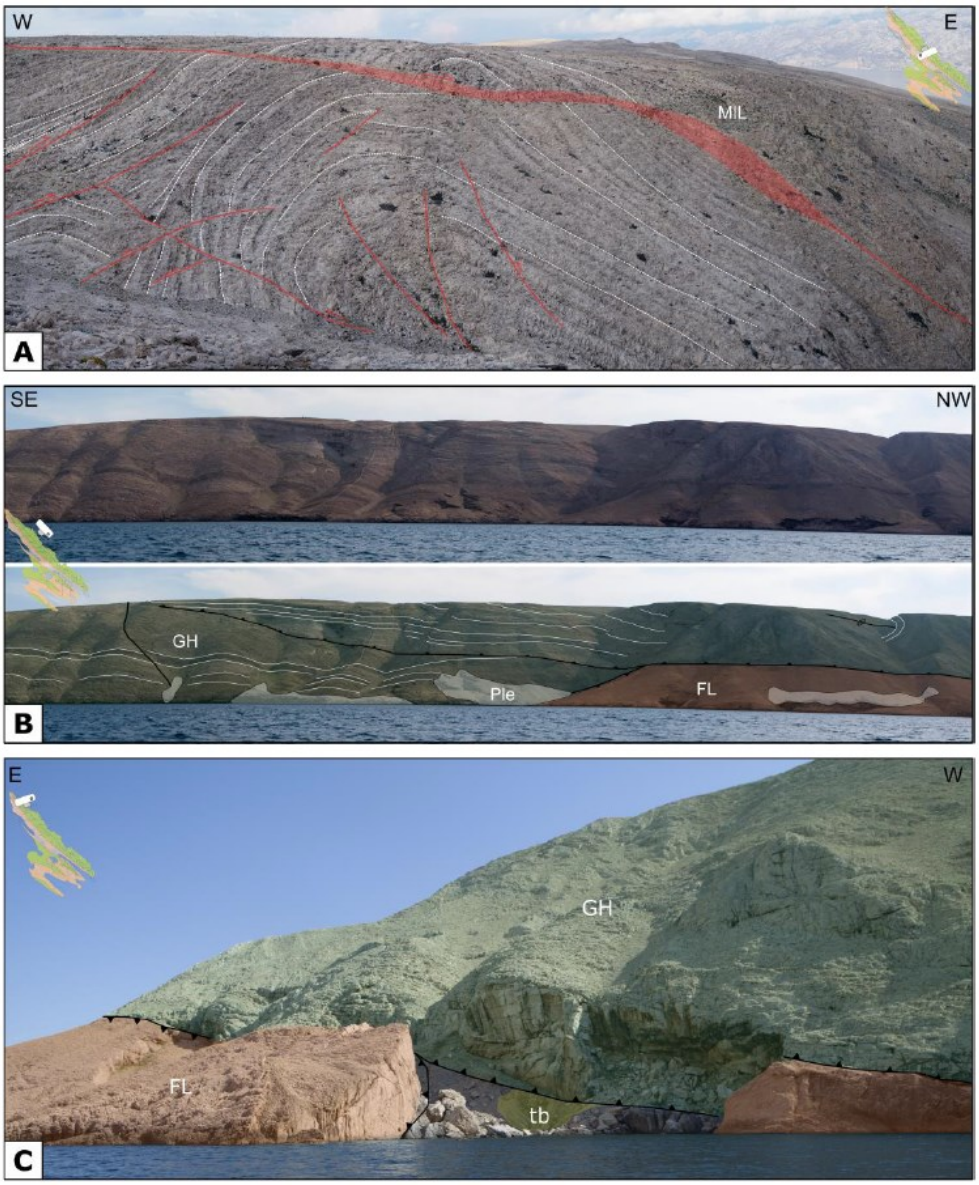

Figure 2.7 - Field pictures of tectonic structures. (A) A thrust stack in the nucleus of the Pag anticline. Faults are depicted in red, some of the strata are highlighted in dashed white. View to the NW. (B) Panoramic view of the backlimb of the Pag anticline, in its northern sector, and line drawing of the large scale tectonic structures. Picture taken looking to the SW from the Velebit Channel. (C) Detail of the triangle zone cropping out along the backlimb of the Pag anticline, at the contact between two oppositely verging thrusts. Picture taken looking to the SW from the Velebit Channel.

2.5 RELATIONS BETWEEN TECTONICS AND SEDIMENTATION

To explore the relations between tectonics and sedimentation, we restored the thicknesses of the individual formations continuously cropping out in the central sector of the forelimb of the Pag anticline (**Figure 2.6**), by assuming the drowning surface atop the foraminiferal limestone as horizontal (**Figure 2.8**). The thickness of the Gornji Humac Formation abruptly increases of about 100 m when crosscut by N-S striking faults in the surroundings of the village of Miškovići (**Figure 2.8**). The offset of the lower limit of the Gornji Humac Formation is not mimicked by the Cretaceous – Paleogene unconformity, which is roughly parallel to the top of the foraminiferal limestone (**Figure 2.8**).

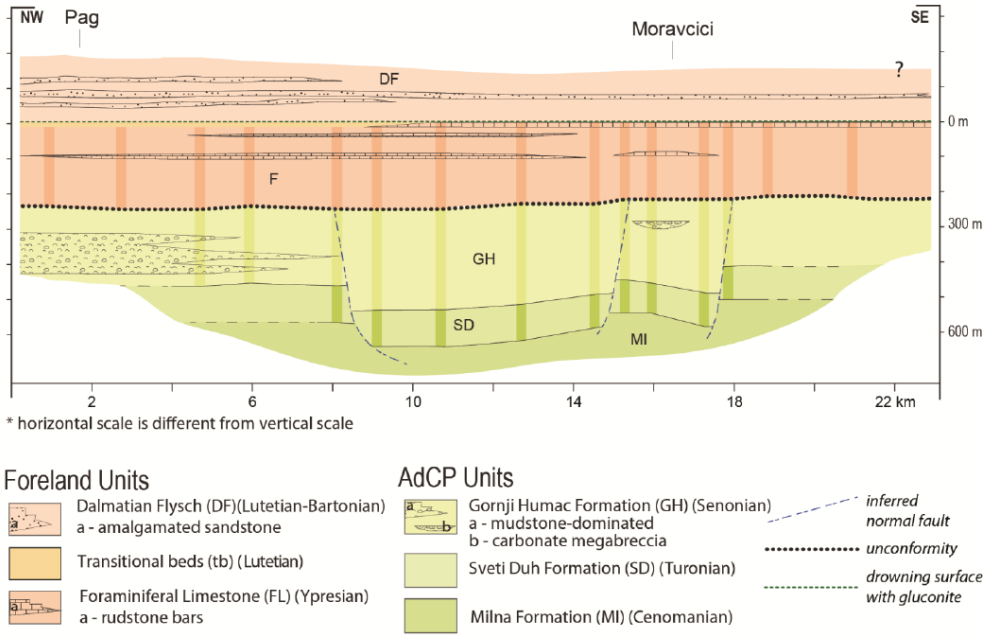

Figure 2.8 - Relations between faults and sedimentation. The thicknesses of the sedimentary formations as measured along the SW limb of the Pag anticline, restored to a horizontal top-foraminiferal limestone. Columns in darker colour are the projection of thicknesses measured on the map on a vertical section striking NW-SE. The variations in the facies associations is represented as well.

The same distribution of map-scale displacements, with higher values affecting strata below the unconformity, is found also along other N-S trending faults (**Attached 1** – Geological and structural map of the Pag anticline). This suggests that part of the displacement along the N-S-striking faults was accumulated before the unconformity, hence affecting the stratigraphic succession when still horizontal. Based on the cutoff angle between faults and bedding, when the sedimentary succession was

horizontal, the displacement caused by N-S trending faults was normal. We thus suggest that the sedimentary sequence was deformed by a system of normal faults before the Ypresian. It cannot be excluded that these faults were active also during the deposition of the AdCP formations, as it might be suggested by the lateral variations in the sedimentary facies associations (**Figure 2.8a**), reflecting a NW to SE variability in the paleobathimetry of the platform (**Figures 2.4b, d**).

2.6 DISCUSSION: IMPLICATION FOR THE TECTONO-SEDIMENTARY EVOLUTION OF THE REGION

The structural and stratigraphic data synthetized in our geological and structural map allowed us to refine the knowledge about the tectonic and sedimentary evolution of the area. Here, we summarize and discuss our findings in the framework of the regional geology, by recognizing the following evolutionary stages.

i. AdCP stage (Cenomanian – Santonian): during the Late Cretaceous, the area shared the large scale evolution of the AdCP, influenced by global sea-level variations and synsedimentary tectonics: deposition of intertidal limestones during the Cenomanian (Milna Formation), platform drowning during the Turonian (Sveti Duh Formation) and the restoration of a shallow marine environment during the Coniacian – Santonian (Gornji Humac Formation) (Tišljar et al., 1998; Vlahović et al., 2005). As described in other locations across the Dalmatian Islands, in the Pag Island synsedimentary tectonics produced emersion surfaces and slumping structures in the Milna Formation (Tišljar et al., 1998; Prtoljan et al., 2007; Korbar et al., 2012). In response to the global sea-level rise “Bonarelli event” (or OEA 2) (Korbar and Husinec, 2003; Husinec and Jelaska, 2006; Korbar et al., 2012), about 100 m of distal ramp limestones were deposed on a hard ground surface marking the drowning of the Milna Formation platform. Shallow water platform carbonate deposition was restored during the Coniacian-Santonian, on a laterally heterogeneous platform with rudist communities, closed lagoons, tidal flats, and shoreface bars, locally crosscut by channelized bodies of carbonate breccias. The lateral variability of depositional environment suggests that also during the Coniacian – Santonian the carbonate platform was subject to syn-sedimentary tectonics. Indeed, the Pag Island is very far from the AdCP platform margins located, to the SW, in the Adriatic Sea offshore the Dalmatian Islands and on the NE on the mainland around Karlovac

(Dragičević and Velić, 1994; Vlahović et al., 2002; Vlahović et al., 2012).

ii. Extensional faulting and regional unconformity (Santonian – Ypresian): by analyzing the displacement distribution on the well-exposed forelimb of the Pag anticline, we recognized normal faults offsetting the AdCP formations and truncated by the regional Late Cretaceous-Paleocene unconformity surface (**Figure 2.8**). The Santonian - Ypresian sedimentary hiatus registered at the Pag Island is among the longest in the Dalmatian Islands (Jelaska et al., 1994; Korbar, 2009), thus it is difficult to constrain the age and geodynamic context of the pre-unconformity faults.

iii. Dinaric foreland basin (Ypresian - Lutetian): the erosive surface truncating the Gornji Humac Formation constitutes the bedrock of the Eocene to Oligocene foreland basin of the Dinaric belt. Since the Ypresian, the study area underwent a marine transgression leading to the deposition of the ramp carbonates of the foraminiferal limestone in a shallow foredeep setting, with a paleobathimetry controlled by the retreating forebulge (Babić and Zupanič, 2016). The foraminiferal limestone is covered by the thick succession of the hemipelagic clastic deposits of the Dalmatian flysch. The transition from the foraminiferal limestone is sharp, marked by a glauconite-bearing drowning surface in the southern part of the mapped area, and by the glauconite-bearing marls of the transitional beds in the northern sector. Sedimentological and paleocurrent analyses suggest that the Dalmatian flysch of the Pag Island was deposed in river-fed distal pro-delta settings, in NW-SE trending basins compartmentalized by early structural deformation (Babić et al., 1993; Babić and Zupanič, 2008). Another evidence claiming for an early stage bathymetrically diversified proximal foreland basin is the persistency of contemporary (Lutetian) carbonate deposition on structural highs interpreted as the crest of growing anticlines (Ćosović et al., 2018).

iv. Tectonic shortening and thrust imbrication (Lutetian – Burdigalian): although the early stage propagation of blind thrusts controlled the physiography of the basin of the Dalmatian flysch, the main stage of folding and thrusting in the Pag Island postdates it, thus it is of post-Lutetian age. In the Ravni-Kotari peninsula, some tens of kilometres south-east of the study region, a Middle Eocene to Oligocene succession of neritic to terrestrial deposits (‘Promina beds’) was

accumulated in a ‘piggyback’ basin (Korbar, 2009) with a ridge-and-swale bathymetry controlled by blind-thrusts anticlines. Growth strata and migrating unconformable onlaps with the bedrock indicate that the Eocene Promina Beds were deposed during fold growth, and include clastic carbonates derived from the erosion of the anticline crests (Vlahović et al., 2012; Ćosović et al., 2018). The Oligocene upper part of the Promina beds is a ‘molasse’ sequence of orogeny-derived clastic deposits within fluvio-deltaic complexes progradating on the Dalmatian flysch (Korbar, 2009; Zupanič and Babić, 2011; Vlahović et al., 2012). The non-folded Early Miocene lacustrine deposits of the Island of Pag, north of the mapped area, constrain the upper age of folding to pre-Burdigalian times (Jiménez-Moreno et al., 2009).

ACKNOWLEDGMENTS

We are grateful to Roberto Fantoni and Giovanni Bertotti for insightful discussions about the geology of area. We thank Eni Spa for funding, reviewing and allowing us to publish the geological map. M. Martinelli is kindly acknowledged for support in the field and discussions. The constructive comments of the reviewer Tvrtko Korbar

CHAPTER 3.

CALCAREOUS NANNOFOSSIL BIOSTRATIGRAPHY

This chapter is presented in the form of a manuscript that is currently in production for being published in the *Geological Journal.* The manuscript describes the calcareous nannofossil biostratigraphy of the turbidites deposits of the Dalmatian Flysch outcropping in the Pag thrust-top basin, with the aim to redefine the age for constraint timing of folding and obtaining paleoenvironmental indications on the depositional environments.

PUBLISCHED ARTICLE

Calcareous nannofossil biostratigraphy of the External Dinarides Flysch (Vrčić-Staravasa Pag Island, Croatia): A key to an Eocene tectono-stratigraphic and paleoenvironmental interpretation

Persico, D., Succo, A., Mittempergher, S., Storti, F., Piccinini, E., and Villa, G.

Geological Journal, 2019, 1- 14, https://doi.org/10.1002/gj.3673

Accepted:7th October, 2019

CALCAREOUS NANNOFOSSIL BIOSTRATIGRAPHY OF THE EXTERNAL DINARIDES FLYSCH (VRČIĆ-STARAVASA PAG ISLAND, CROATIA): A KEY TO AN EOCENE TECTONO-STRATIGRAPHIC AND PALEOENVIRONMENTAL INTERPRETATION

Persico D. [1], Succo A. [1], Mittempergher S. [2], Storti F. [1], Piccinini E. [1] & Villa G.[1]

1. Università degli Studi di Parma, Dipartimento di Scienze Chimiche, della Vita e della Sostenibilità Ambientale, Parco Area delle Scienze 157/A, 43124, Parma, Italy

2. Università degli Studi di Milano Bicocca, Dipartimento di Scienze dell'Ambiente e della Terra, Piazza della Scienza 4, 20126 Milano, Italy

ABSTRACT

It is largely accepted that in the Dinaric shallow foredeep basin the onset of Cenozoic synorogenic sedimentation is diachronous along strike and shows orogen-parallel southward younging, creating a large uncertainty in the age of the Dalmatian Flysch. Calcareous nannofossil biostratigraphy was studied to investigate a turbiditic succession exposed in Pag Island (Croatia) with the main purpose of constraining its age, which is still a matter of debate. The age assignment for the turbiditic deposition bears important implications for better understanding of the geodynamic and paleoenvironmental evolution of the External Dinarides. We logged a well-exposed sedimentary section in the south-western limb of the Pag anticline and performed calcareous nannofossil quantitative analyses revealing a high species diversity and abundant assemblage. The age diagnostic species indicate CNE14-CNE15 biozones, suggesting that flysch deposition occurred in the Lutetian – Bartonian. This age can be further restricted to the CNE14 (42.37 – 40.51 Ma) by means of the lowest occurrence of *Reticulofenestra reticulata* and the highest occurrence of *Sphenolithus furcatolithoides*. Vertical facies variation and paleoecological indications suggest an increase in paleobathymetric depth during deposition. Our data support a post-Lutetian age of folding and thrusting for the Pag Island region and suggest a relatively short time span during the middle-late Eocene period for the main contractional stage in this sector of the External Dinarides. This result has important implications for the evolution of the Dinaride foreland basin system in Cenozoic times.

3.1 INTRODUCTION

The timing and geodynamic evolution of the frontal parts of orogens are preserved in the sedimentary records of foreland basin systems developed ahead of orogenic wedges (DeCelles & Giles, 1996).

The hanging wall of the External Dinaric thrust belt is an imbricated thrust system of deformed Cretaceous to Neogene sediments (**Figure 3.1**; External Dinarides after Pamić et al., 1998), which recorded the transition from a long-lived carbonate platform (the Adriatic Carbonate Platform, Vlahović et al., 2005) to laterally heterogeneous Eocene – Oligocene foreland basin (e.g., Korbar, 2009; Tari, 2001). In the Dinaric shallow foredeep basin (e.g. Babić & Zupanič, 2008a, b), a Lower Eocene marine transgression is marked by deposition of the ramp carbonates of the Foraminiferal Limestone, which records progressive water deepening in the depositional environment (Babić & Zupanič, 2016; Vlahović et al., 2012). Above the Foraminiferal Limestone, laterally-discontinuous glauconite-bearing marls "(i.e., the "transitional beds" of (Ćosović et al., 2004) testify to an abrupt relative sea-level rise and an abrupt increase in the sedimentary clastic component, with a rapid transition to the overlying hemipelagic to marginal-marine sediment of the Dalmatian Flysch (Babić et al., 2007; Ćosović et al., 2008; Marjanac & Ćosović, 2000; Vlahović et al., 2005; Vlahović et al., 2012). Eventually, clastic sedimentation is ended by a regressive molasses sequence infilling thrust-top basins in the region (i.e., Promina Beds, Tari- Kovačić & Mrinjek, 1994).

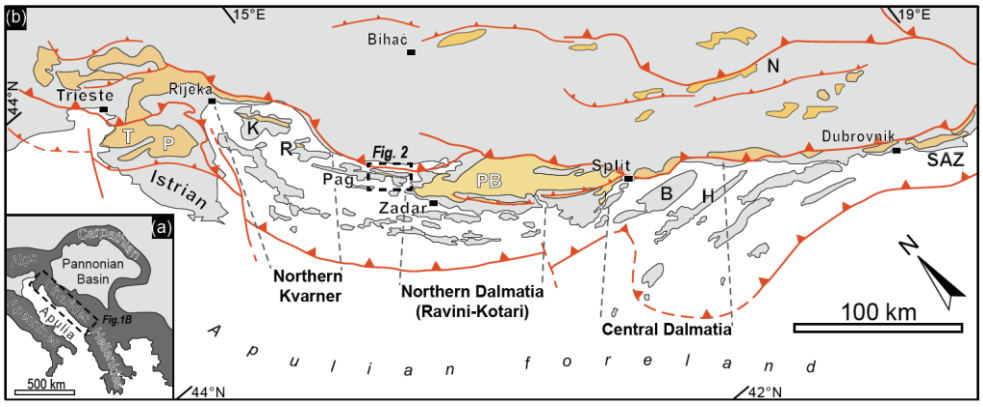

Figure 3.1 - (a) Position of the Dinarides within the Alpine orogeny (in dark grey). (b) Schematic tectonic map of the External Dinarides with the location of the main outcrop areas of the Cenozoic flysch and associated shallow marine sediments in the foreland basin system. Major thrusts after the Geological Map of Yougoslavia (Korbar, 2009; Mikes et al., 2008; Schmid et al., 2006; Tari, 2001). Abbreviations: B = Brac Island, H = Hvar Island, N = Nevesinjsko Polje, K = Krk Island, P = Pazin Basin, PB = Promina Beds Basin, R = Rab Island, SAZ = Southern Adriatic Zone, T = Trieste-Koper Basin. The broken rectangle indicates the position of the geological map in Figure 3.2.

Such a very simple scenario is affected by a large uncertainty in the age of the Dalmatian Flysch. It is largely accepted that the onset of Cenozoic synorogenic sedimentation in the Adriatic Apulian foreland is diachronous along strike and shows orogen-parallel southward younging (Piccoli & Proto Decima, 1969; Puškaric, 1987). An Eocene age of the older turbidite sediments in the northern and central Adriatic foreland basin system (i.e. Istrian Peninsula, Northern and Central Dalmatia; **Figure 3.1**) is well accepted (Babić et al., 2007; Ćosović et al., 2008; Grubić & Komatina, 1963; Marincic, 1981; Marjanac & Ćosović, 2000; Vlahović et al., 2012), whereas a Miocene age characterizes Central Dalmatia and the Southern Adriatic Zone and Ionian Zone (de Capoa & Radoicić, 1994a, b; de Capoa & Radoicić, 2002; de Capoa et al. 1995; Radoicić et al., 1989, 1991). However, recent studies question the previously proposed Paleogene sedimentation ages and extend to the Miocene the formation outcropping north, up to the Istrian Peninsula (Mikes et al., 2008).

Implications of the two alternative tectono-sedimentary scenarios on the geodynamic modeling of the complex interplay among the Dinaridic, Apenninic, and Southern Alpine belts are straightforward. With the aim of contributing to solving this conundrum, we carried out a biostratigraphic study by quantitative calcareous nannofossil analysis of the oldest Dalmatian Flysch sediments exposed along the southwestern coastal area of the island of Pag, Croatia (**Figures 3.1, 3. 2**). Our results favor a reappraisal of the Eocene age for the onset of foredeep turbidite sedimentation in the region and provide also palaeoecological information about the depositional environment.

3.2 GEOLOGICAL OUTLINE

The External Dinarides consists of a series of SW verging, carbonate imbricate thrust sheets produced by polyphase tectonics including underthrusting and right-lateral strike-slip faulting accommodating oblique convergence from Late Cretaceous to present-day times (e.g. Korbar, 2009; Tari, 2001). Progressive westward in-sequence thrust migration is supported by foredeep basins migration in Paleogene and Neogene times (Auboin et al., 1970; Handy et al., 2015; Pamić et al., 1998; Schmid et al., 2008; Tari, 2001). Several authors have proposed different Eocene foreland basin reconstructions ahead of the Dinaride thrust wedge, spanning from one long-lived basin (Herak, 1986; Marinčić, 1981; Marinčić et al., 1996), to different sub-basins (Babić et al., 2007; Babić & Zupanič, 1990; Marjanac, 1993; Marjanac & Ćosović, 2000; Sikic, 1964) separated by shallow-marine and marginal marine facies areas (Babić et al., 1993; Marinčić, 1981; Zupanič & Babić, 1991).

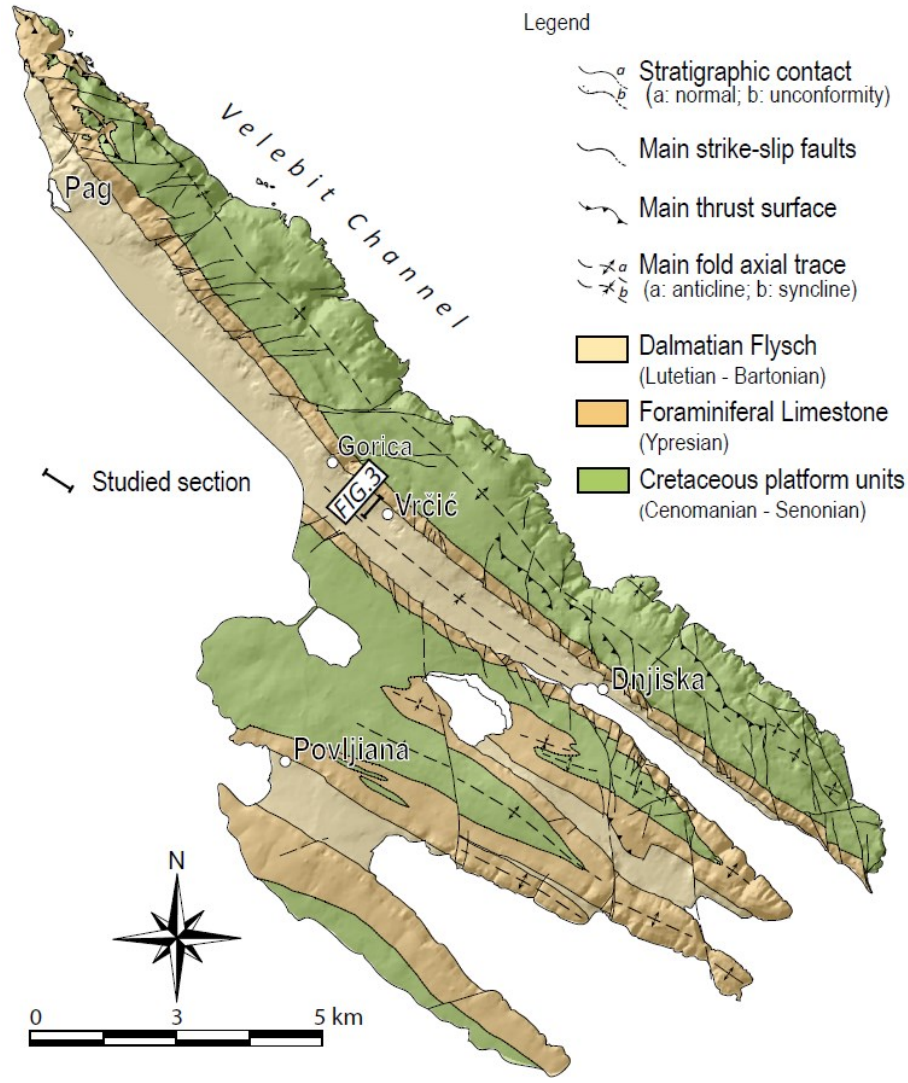

Figure 3.2 - Simplified geological map of the Pag Island, which exposes a train of NW-SE trending anticlines and synclines, dissected by axial-oblique fault zones. The studied section has been indicated by the black line adjacent to the label of Figure 3.3 (modified from Mittempergher et al., 2019).

In the island of Pag, the Dalmatian Flysch is exposed along the forelimb of a regional-scale anticline cored by Upper Cretaceous shallow-water carbonates, unconformably overlain by early Eocene Foraminiferal limestones, which pass upward to about 30 m of the transitional beds, consisting of marly limestones with benthic and planktonic foraminifera and echinoids (Mittempergher et al., 2019; Succo et al., 2018). They pass upward to alternating medium- to fine-grained sandstones and marls (Sokac et al., 1976; **Figures. 3.2, 3.3**), which were initially interpreted as belonging to the Proximal Flysch zone (Mamužić & Sokač, 1973; Marinčić, 1981) and then reinterpreted by Babić et al. (1993) as part of a delta-related shallow marine system. The Dalmatian Flysch is unconformably overlain by strongly-

cemented polymictic limestone breccias including Jurassic to Paleogene clasts, referred to as Jelar Formation (*sensu* Herak & Bahun, 1979).

3.3 STRATIGRAPHIC LOG

The studied stratigraphic section (337 m thick) is located 10 km SE from the Pag Bay (Latitude N44°38'88.5'' – Longitude E15°13'94.2'') and involves the upper portion of the transitional beds and the exposed flysch succession (**Figures 3.3, 3.4**).

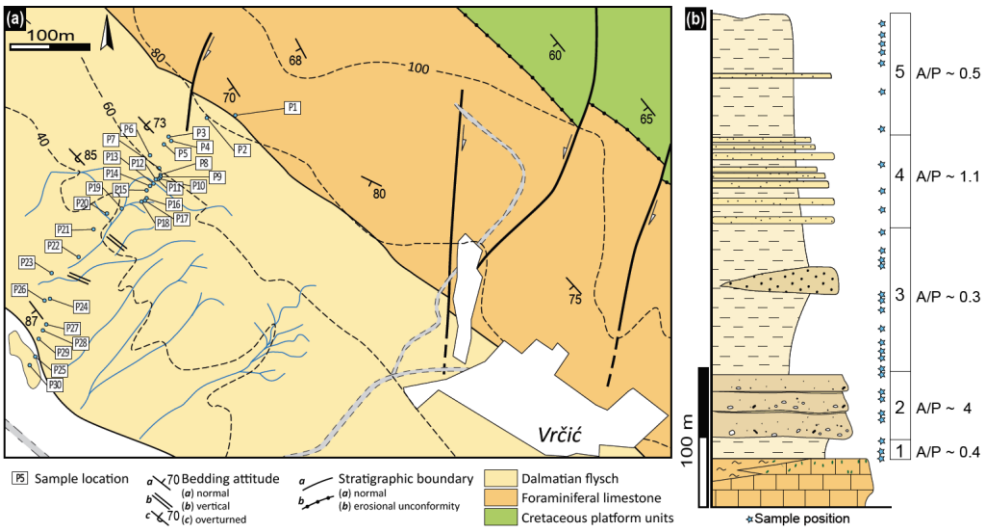

Figure 3.3 - (a) Geological map of the forelimb of the Pag anticline, showing the position of collected samples. Bedding dip is mostly subvertical to overturned, and no faults dissected the logged section. (b) Simplified stratigraphic log of the studied section. The numbered boxes from 1 to 5 indicate the main flysch portions characterized by different sandstone-pelite ratios. White stars indicate the sample positions.

Overall, the log shows a coarsening-up trend in the first part (up to about 100 m from the base), sharply followed by a fining-upward sequence with an increase of the sandstone-to-pelite ratio. The clear transition between the two sequences occurs as a c. 10-m-thick amalgamated massive-to-laminated sandstones showing an internal thickening-up cycle. In total, five sectors were identified, based on different sandstone-to-pelite ratios (**Figure 3.3b**). In more detail, the studied section starts with highly bioturbated marls and mud-rich pelites, followed by fine- to medium-grained sandstones, organized in 10-40 cm thick tabular beds, commonly amalgamated in metric, upward-thinning cycles (**Figure 3.4a**). Locally, parallel or gently inclined laminations occur in sandstones (**Figure 3.4b**), as well as dewatering structures in the

upper part of some beds. Intervals of massive micro-conglomerates with sharp, non-erosional to slightly erosional bases are commonly amalgamated with sandstone beds. Conglomerate clasts mainly consist of limestones and tests of benthic foraminifera. Quartz and sandstone clasts also occur but are less abundant. Quantitative petrographic analysis of sandstones on polished thin sections indicate a well-sorted, matrix-poor, carbonate-rich arenite to graywackes. Their composition typically consists of about 50% of carbonate grains, whereas the remaining particles consist of quartz, plant and rock fragments, and minor mud chips. In some sandstone beds, Nummulites occur and show an imbricated geometry, indicating northwestward flow directions of turbidites.

3.4 METHODS AND MATERIALS

Thirty-one samples were carefully collected from mudstones and pelite interlayers along the 337 meters of the studied section (**Figures 3.3a, b**; see also **Table ST3.1**). Calcareous nannofossils were analyzed using smear slides and standard polarized light-microscope techniques (1250X) (Bown & Young, 1998). A quantitative analysis was performed on all the fossiliferous samples by counting 300 specimens per sample, in variable number of fields of view (FOV), depending on the total abundance of nannofossils, whose preservation was estimated as Poor (P), Moderate (M), Good (G) and Excellent (X), following the ranking proposed by Bown and Young (1998). The biostratigraphic assignment was performed based on stratigraphic ranges of the taxa and their lowest (LO) to the highest (HO) occurrences. Cretaceous species were also classified as reworked but not counted.

To account for the strong reworking of older species that characterize turbidites, sedimentation ages were defined by the lowest occurrences or bottom of species, rather than the highest occurrences or top.

For the classification of Calcareous nannofossils at the species level, we followed Farinacci (1969-1989), Perch-Nielsen (1985), Bown (1998), Bown and Dunkley Jones (2012), and Agnini et al. (2014). The used chronostratigraphic scale was obtained by correlating the Paleogene biozonations of Agnini et al. (2014), Okada and Bukry (1980), Martini (1971), and the GPTS magnetostratigraphy. The age scale includes an integration of the orbitally-tuned time scale of Pälike et al. (2006), from top Oligocene to middle Eocene, and Cande and Kent (1995) in the interval from chrons C20n to C20r (Agnini et al., 2014).

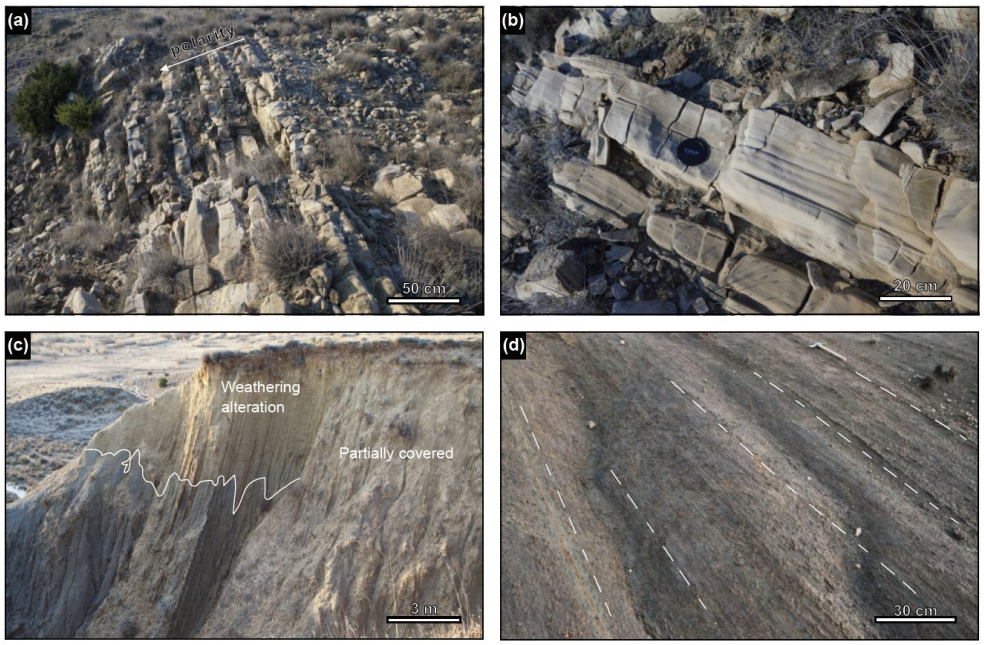

Figure 3.4 - Field pictures of the studied succession. (a) Lower portion of the succession, with fine-grained sandstone beds, 15-30 centimeters thick, interlayered with pelites and mudstones. The fining-upward trend is highlighted by the gradual decrease of sandstone bed thickness, towards a mud-dominated portion of the succession. (b) Detail of laminated turbidite beds in a thickening-upward sequence of the studied succession. Bedding is slightly overturned. (c) Fining-upward trend of thin brownish sandstone beds outcropping in the upper portion of the studied section; (d) Mud-rich portion of the succession, composed of locally laminated siltstones.

3.5 MICROPALEONTOLOGY

Of the 31 analyzed samples, only three were barren in nannofossils. The remaining ones have variable nannofossil abundances and preservation. A total of 69 Cenozoic species were identified, predominantly Middle Eocene in age, and the distribution of the recognized species is reported in the range chart (**Table ST4.2**).

The presence of *Clausicoccus vanheckiae* (Perch-Nielsen, 1986), *Discoaster wemmelensis* (Bown & Dunkley Jones, 2012), *Reticulofenestra wadeae* (Shepherd & Kulhanek, 2016), *Sphenolithus cuniculus* (Bown, 2005), *Sphenolithus furcatolithoides* (Agnini et al., 2014) and *Chiasmolithus solitus* (Perch-Nielsen, 1985), suggests an age not younger than the top of NP16 (Martini, 1971). A different stratigraphic position was determined for the HO of *S. cuniculus* by Agnini et al. (2014), with the event coinciding with the base of CNE12 (NP15/NP16 boundary Martini, 1971). Also the HO of *C. solitus* was considered uncertain by different authors (Agnini et al., 2014; Villa et al., 2008). A particular consideration is merited by *S. furcatolithoides*. This is a relatively small sphenolith with two parallel long spines diverging

at an acute angle. Agnini et al. (2014) proposed a subdivision of the species in two different morphotype named A and B in relation to the different extinction patterns. In our research, morphotype distinction was not possible due to poor preservation, therefore the overall range of distribution of *S. furcatolithoides* is derived from the data listed in **Table ST3.2** of Agnini et al. (2014).

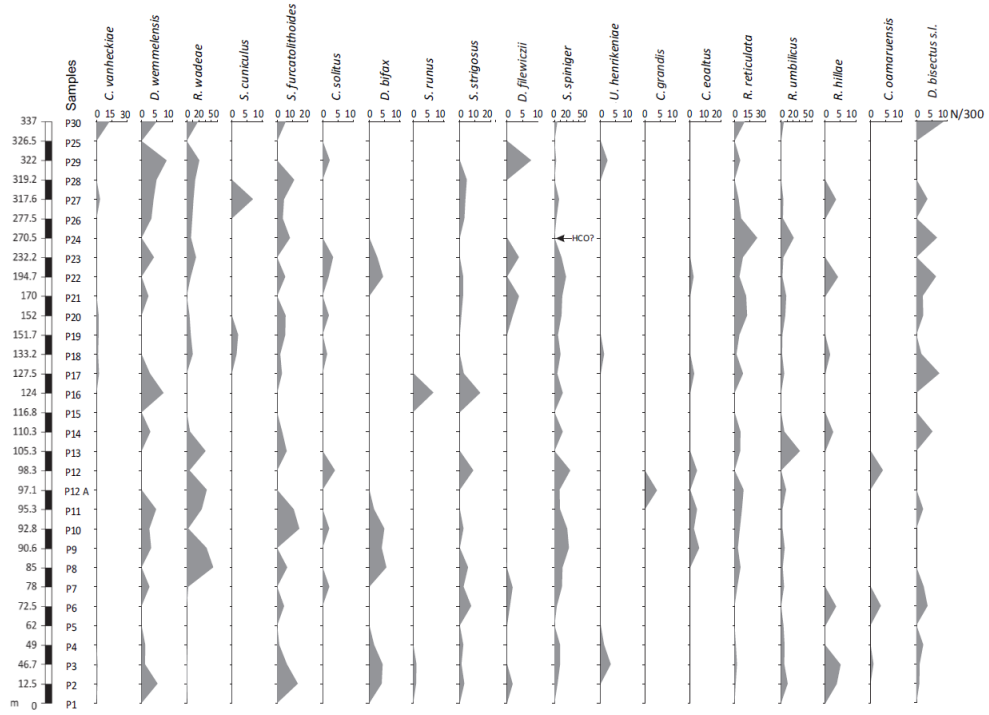

Figure 3.5 - Relative abundances (nannos/300 specimens) of the calcareous nannofossil marker species in the studied sequence of the Dalmatian Flysch exposed at Pag island.

Moreover, *Discoaster bifax*, *Sphenolithus runus* and *Sphenolithus strigosus* are exclusively distributed in CNE12-CNE15 Zones, with the lowest occurrences (LOs) and the HOs corresponding to the base of NP16 (within the CNE12) and the top of the NP16 biozone (within the CNE15). Lower Common Occurrence (LCO) of *Reticulofenestra reticulata* is the marker event identified by Agnini et al., (2014). This biostratigraphic datum that coincides with the CNE13-CNE14 boundary is more recent than the LO of Perch-Nielsen (1985) that correlates with the base of NP16. *Chiasmolithus eoaltus*, and *Reticulofenestra umbilicus* originated in CNE12 (base of NP16). In Agnini et al. (2014), the marker event of *R. umbilicus* is the LCO and coincides with the base of CNE13.

The LO of *Reticulofenestra hillae* is diachronous or uncertain (Bown & Dunkley Jones, 2012). In Agnini et al. (2014) and Fornaciari et al. (2010), the

LCO of *Sphenolithus spiniger* is defined at the base of CNE15. This species, continuously distributed in the Vrčić section, is the most important marker to narrow the biostratigraphic range. The HCO of *S. spiniger* has been correlated with the base of CNE15 (Agnini et al., 2014). The presence of *Umbilicosphaera henrikseniae* and *Chiasmolithus grandis,* which occurs up to the top of CNE16, constrains the upper boundary of the age of the studied section. The absence in the studied samples of *Isthmolithus recurvus* and *Chiasmolithus gigas* suggests a correlation of the stratigraphic sequence with the Middle Eocene interval into the CNE18 to CNE12 interval. The relative abundance of the recognized marker species is shown in **Figure 3.5**. No Oligocene or Neogene marker species were found (**Figures 3.6, 3.7 and 3.8**). On the other hand, Cretaceous reworked species have been found, namely *Arkhangelskiella* sp., *Micula decussata*, *Eiffellithus turriseiffelii*, *Microrhabdulus* sp. and *Watznaueria barnesae*. Few specimens of these species are distributed in all samples except the barren ones.

Despite the great thickness of the stratigraphic section, the nannofossil assemblage remains unchanged: most of the Eocene markers listed above are distributed, albeit rare, from the base to the top of the studied succession (**Figure 3.5**).

The lower part of the studied sequence, from samples P5 to P8, is characterized by the high concentration of ascidian spicules. In particular, we have quantitatively estimated a variable concentration of spicules from 5 to 25 specimens per FOV. Bown (2005) describes similar specimens of spicules from Palaeogene of Kilwa and Lindi areas of coastal Tanzania. A high concentration of ascidian spicules is considered a proxy to coastal environments associated with carbonate banks (Bown, 2005).

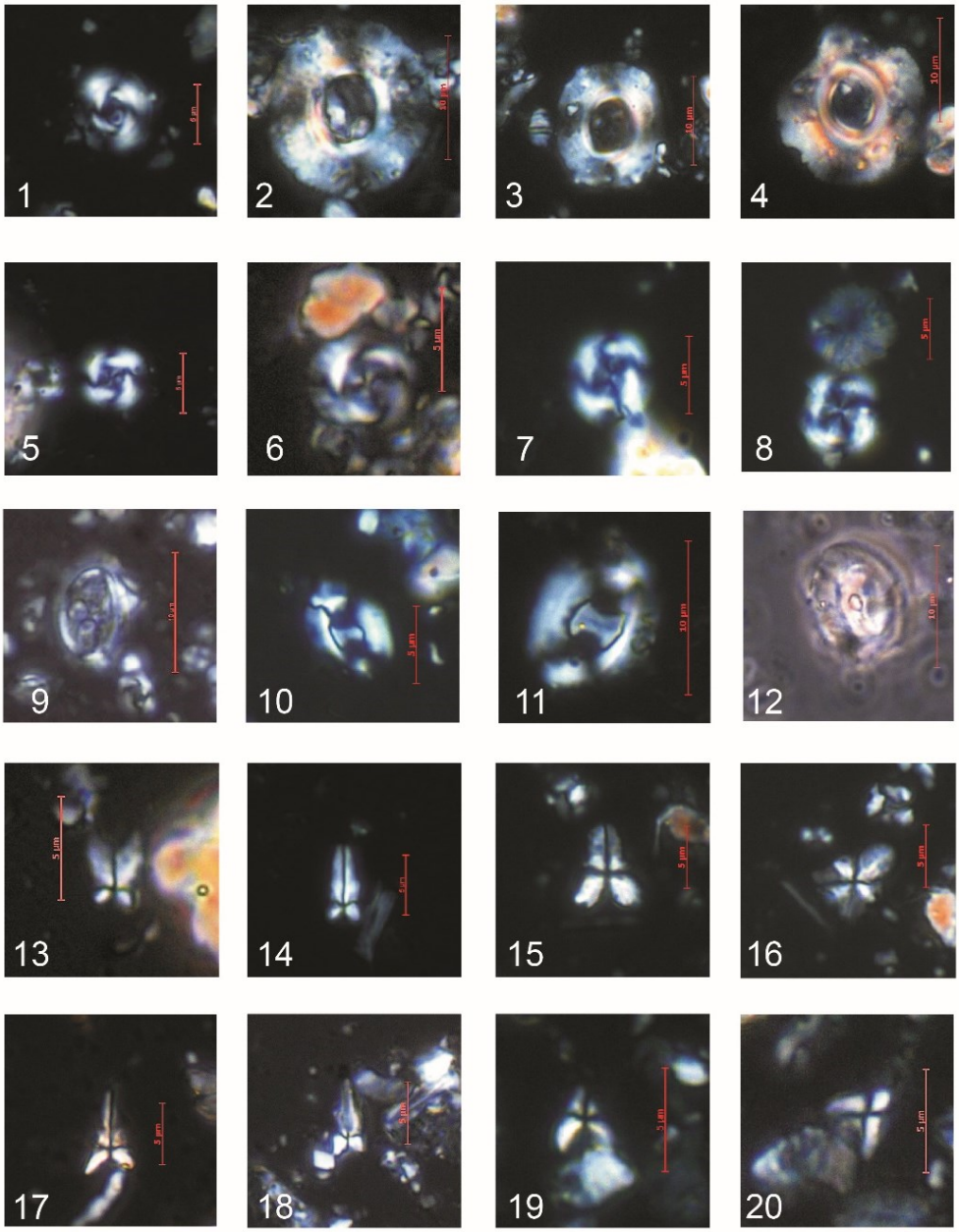

Figure 3.6 - Fig. 1. *Reticulofenestra laevis*; crossed nicols, 1250X, sample P22; Fig. 2. *Reticulofenestra umbilicus*; crossed nicols, 1250X, sample P3; Fig. 3. *R. umbilicus*; crossed nicols, 1250X, sample P13; Fig. 4. *Reticulofenestra hillae*; crossed nicols, 1250X, sample P13; Fig. 5. *Reticulofenestra reticulata*; crossed nicols, 1250X, sample P26; Fig. 6. *R. reticulata*; crossed nicols, 1250X, sample P19; Fig. 7. *R. reticulata*; crossed nicols, 1250X, sample P10; Fig. 8. *R. reticulata* and *Discoaster. wemmelensis*; crossed nicols, 1250X, sample P30; Fig. 9. *Clausicoccus vanheckiae*, crossed nicols, 1250X, sample P2; Fig. 10. *Helicosphaera bramlettei*; crossed nicols, 1250X, sample P13; Fig. 11. *H. bramlettei*; crossed nicols, 1250X, sample P13; Fig. 12. *Helicosphaera compacta*, phase contrast, 1250X, sample P20; Fig. 13. *Sphenolithus furcatolithoides*, crossed nicols, 1250X, sample P13; Fig. 14. *Sphenolithus spiniger* crossed nicols, 1250X, sample P28; Fig. 15. *Sphenolithus spiniger* (0°) crossed nicols, 1250X, Sample P3; Fig. 16. *S. spiniger* (45°); crossed

(*continued from the previous page*): nicols, 1250X, Sample P3; Fig. 17. *S. spiniger* (0°); crossed nicols, 1250X, Sample P14; Fig. 18. *Sphenolithus strigosus* (0°); crossed nicols, 1250X, Sample P20; Fig. 19. *S. spiniger* (0°); crossed nicols, 1250X, Sample P2; Fig. 20. *S. spiniger* (45°); crossed nicols, 1250X, Sample P2.

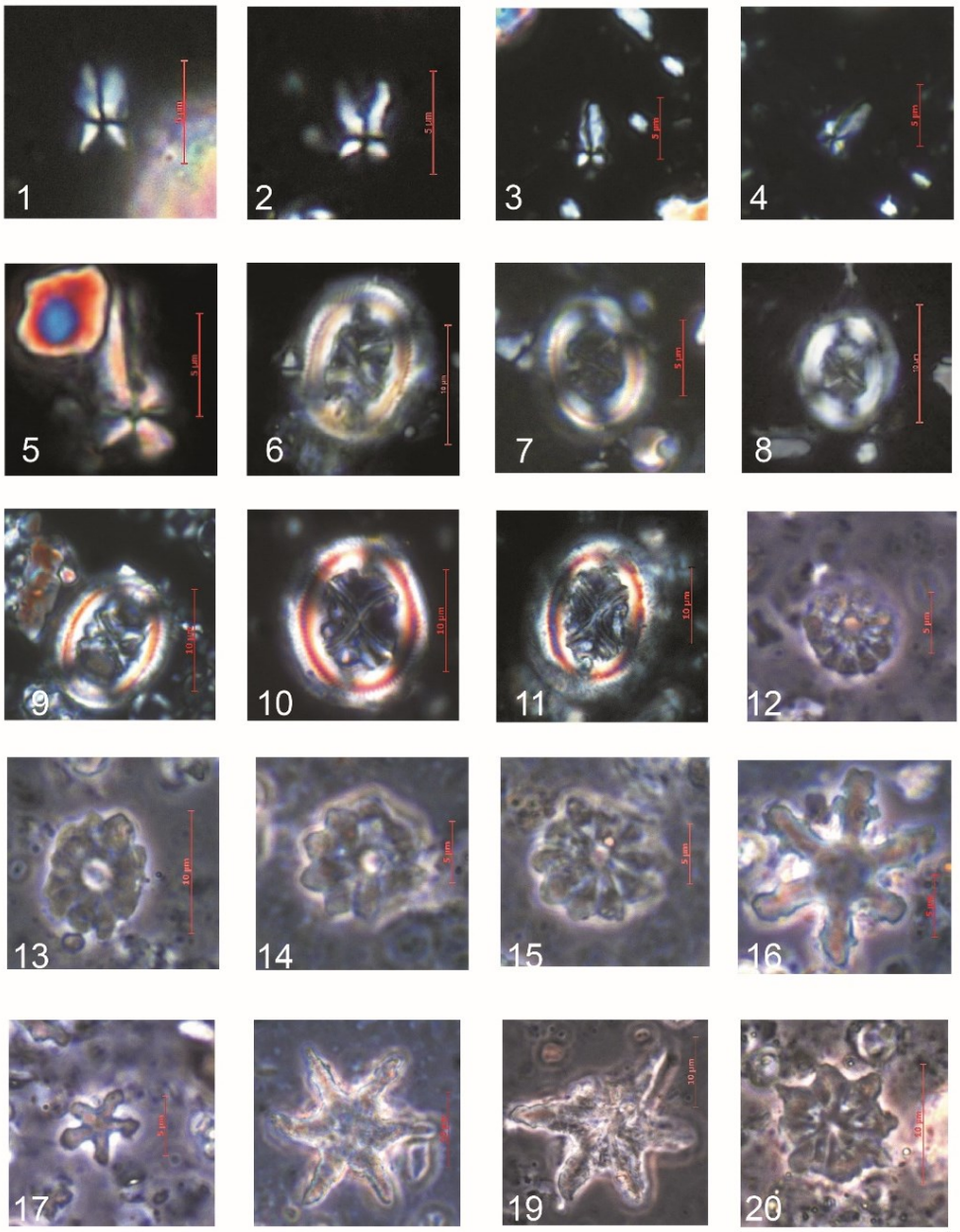

Figure 3.7 - Fig. 1. *Sphenolithus cuniculus*; crossed nicols, 1250X, sample P27; Fig. 2. *Sphenolithus perpendicularis*; crossed nicols, 1250X, sample P21; Fig. 3. *Sphenolithus runus* (0°); crossed nicols, 1250X, sample P3; Fig. 4. *S. runus* (45°); crossed nicols, 1250X, sample P3; Fig. 5. *Sphenolithus radians* crossed nicols, 1250X, sample P12; Fig. 6. *Chiasmolithus solitus*; crossed nicols, 1250X, sample P22; Fig. 7. *Chiasmolithus eoaltus*; crossed nicols, 1250X, sample P10; Fig. 8. *C. eoaltus*; crossed nicols, 1250X, sample P9; Fig. 9. *Chiasmolithus oamaruensis*; crossed nicols, 1250X, sample P12; Fig. 10. *Chiasmolithus grandis*; crossed nicols,

(*continued from the previous page*): 1250X, sample P6; Fig. 11. *C. grandis*; crossed nicols, 1250X, sample P2; Fig. 12. *Discoaster wemmelensis*; phase contrast, 1250X, sample P8; Fig. 13-15. *Discoaster bifax*; phase contrast, 1250X, sample P2; Fig. 16. *Discoaster binodosus*, phase contrast, 1250X, sample P22; Fig. 17. *Discoaster tani ornatus*; phase contrast, 1250X, sample P8; Fig. 18. *Discoaster lodoensis*; phase contrast, 1250X, sample P8; Fig. 19. *D. lodoensis*; phase contrast, 1250X, sample P27; Fig. 20. *Discoaster saipanensis*; phase contrast, 1250X, sample P8.

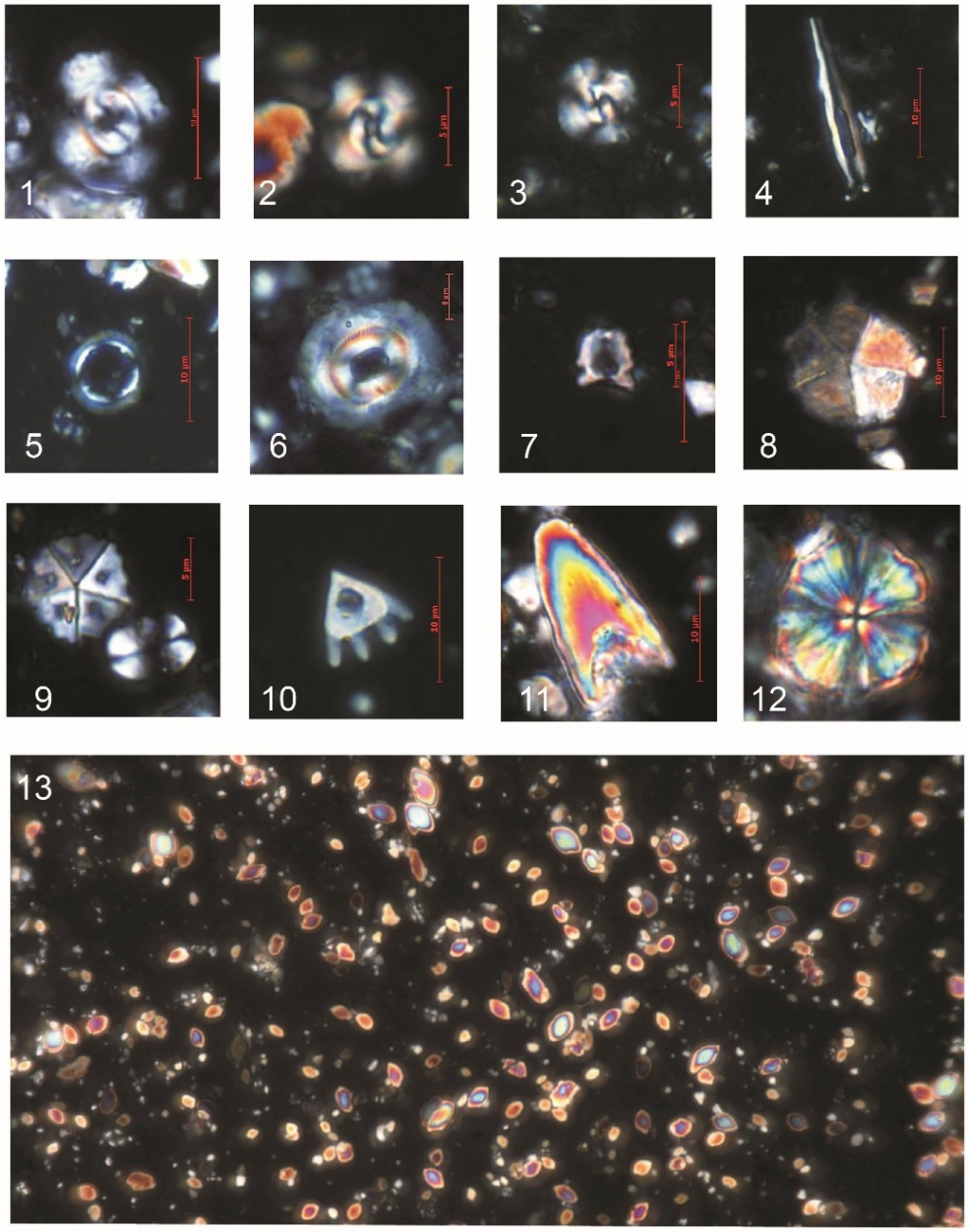

Figure 3.8 - Fig. 1. *Dictyococcites filewiczii*; crossed nicols, 1250X, Sample P10; Fig. 2. *Dictyococcites bisectus*; crossed nicols, 1250X, Sample P29. Fig. 3. *Dictyococcites bisectus*; crossed nicols, 1250X, sample P23; Fig. 4. *Blackites spinosus*; crossed nicols, 1250X, sample P29; Fig. 5. *Coronocyclus nitescens*;

(*continued from the previous page*): crossed nicols, 1250X, sample P3; Fig. 6. *Chiasmolithus eopelagicus*; crossed nicols, 1250X, sample P17; Fig. 7. *Blackites morionum*; crossed nicols, 1250X, sample P20; Fig. 8. *Braarudosphaera bigelowii*; crossed nicols, 1250X, sample P29; Fig. 9. *Pemma papillatum* and *Ellipsolithus macellus*; crossed nicols, 1250X, sample P23; Fig. 10. *P. papillatum*; crossed nicols, 1250X, sample 24; Fig. 11. Ascidian spicula; crossed nicols, 1250X, sample P5; Fig. 12. Ascidian spicula; crossed nicols, 1250X, sample P8; Fig. 13. High concentration of ascidian spicula, crossed nicols, 1250X, sample P5.

Ferreira et al. (2019) report similar results from Quaternary sediments in the Campos Basin (Brazil). This site shows low percentages of ascidian spicules in the nannofossil assemblages dominated by *Florosphaera profunda*, *Gephyrocapsa oceanica*, and *Emiliania huxleyi* was interpreted as having been transported from shelf to slope areas during periods of relative sea-level fluctuations in response to climate variations. The correlation between the low concentration of ascidian spicule and sedimentary processes indicates the ascidian spicule transport (Ferreira et al., 2019). In our case, the dominance of ascidian spicules in the calcareous microfossils assemblage suggests a coastal environment.

3.6 DISCUSSION AND CONCLUSIONS

Our results indicate that the nannofossil assemblage in the first 337 m of the Dalmatian Flysch exposed in Pag Island, Croatia, largely consists of Middle Eocene species. **Figure 3.5** shows the relative abundance diagrams of the middle Eocene species. The biostratigraphic scheme by Agnini et al. (2014) was here modified to correlate the stratigraphic sequence of Vrčić (**Figure 3.9**). In particular, the paleontological assemblage indicates a Lutetian - Bartonian age, thus supporting previous work from Benić (1975) rather than the Miocene Age indicated by Mikes et al. (2008). In fact, we did not find any Miocene species.

A possible explanation to this discrepancy lies in the use by Mikes et al. (2008) of *Reticulofenestra pseudoumbilicus*, *Reticulofenestra haqii*, *Coccolithus miopelagicus*, and *Calcidiscus premacintyrei*, to constrain the age of the sandstone succession in Pag. *Coccolithus miopelagicus* has ambiguous morphology that can be easily confused with Eocene forms of *Coccolithus eopelagicus*. Moreover, the *Reticulofenestra* group shows many taxonomical difficulties caused by similar morphologies but different shapes of the distal shield and central area and placolith length. *Reticulofenestra pseudoumbilicus* must have a total length >8 μm and could have been confused with *R. wadeae*. Our analyses were performed by applying the morphometric scheme proposed by De Kaenel (personal communication),

which allowed us to distinguish the following *Reticulofenestra* species: *R. caucasica* (Hay et al., 1966), *R. hillae*, *R. laevis* (Hay et al., 1967), *R. wadeae* (Bown, 2005), *R. rupeliensis*, *R. umbilicus* and *R. reticulata*. Additional sources of ambiguity are *Helicosphaera euphratis* and *C. premacintyrei*, which were both described by Mikes et al. (2008) but not found in our samples, where we recorded *Helicosphaera bramlettei* (NP14-NP15) together with the presence of *H. compacta* (NP16-NP24).

Following the original description (Hay et al., 1966) and the taxonomy from Persico et al. (2012), Bown and Dunkley Jones (2012), Fioroni et al. (2015) and Bown and Newsam, (2017), we include *D. bisectus* as specimens with lengths between 5 and 10 μm, labeling the specimens <10 μm and small central opening as *D. filewiczii* (Bown & Newsam, 2017) (**Figure 3.6**, Fig. 11). *Dictyococcites stavensis,* with size >10 μm, is not present in our samples. In Agnini et al. (2014), the name *D. bisectus* is used for specimens of *Dictyococcites* >10 μm with LO related to the upper part of the CNE14. The same authors referred to *Dictyococcites hesslandii* specimens <10 μm characterized by LO older than the specimens >10 μm. The LO of *D. bisectus,* from Agnini et al. (2014), shows in **Figure 3.9**, refers certainly to *D. stavensis* whose absence in our samples narrows the stratigraphic range.

The simultaneous occurrence, from the base to the top of the Vrčić sequence, of the *C. vanheckiae, D. wemmelensis, R. wadeae, S. cuniculus, S. furcatolithoides, C. solitus*, *D. bifax*, *S. runus, S. strigosus, D. filewichzii, S. spiniger*, together with long-ranging species such as *U. henrikseniae*, *C. grandis*, *C. eoaltus*, *R. reticulata*, *R. umbilicus*, *R. hillae*, *C. oamaruensis* and *D. bisectus* suggests a stratigraphic correlation with biozones CNE12-CNE16 (**Figure 3.9**). Moreover, the occurrence of *R. reticulata* and *S. furcatolithoides,* makes it possible to further constrain the stratigraphic range in correspondence to the CNE14. Babić et al. (2007) reported the same stratigraphic age (NP16, Martini, 1971) in Pazin Basin Flysch.

The *Chiasmolithus* genus also plays an important role in the biostratigraphic correlation of the flysch. In particular, the contemporaneous presence of *C. solitus*, *C. oamaruensis* and *C. eoaltus*, identifies a stratigraphic interval described by Persico and Villa, (2008), where the speciation event was correlated to the Lutetian stage. In Agnini et al. (2014) the stratigraphic distribution of *C. oamaruensis* contrasts with this hypothesis, showing the bottom of *C. oamaruensis* at the base of CNE17. According to Persico and Villa (2008), the origin of *C. oamaruensis* was phylogenetically related to *C. solitus* and *C. eoaltus* and the speciation event is stratigraphically

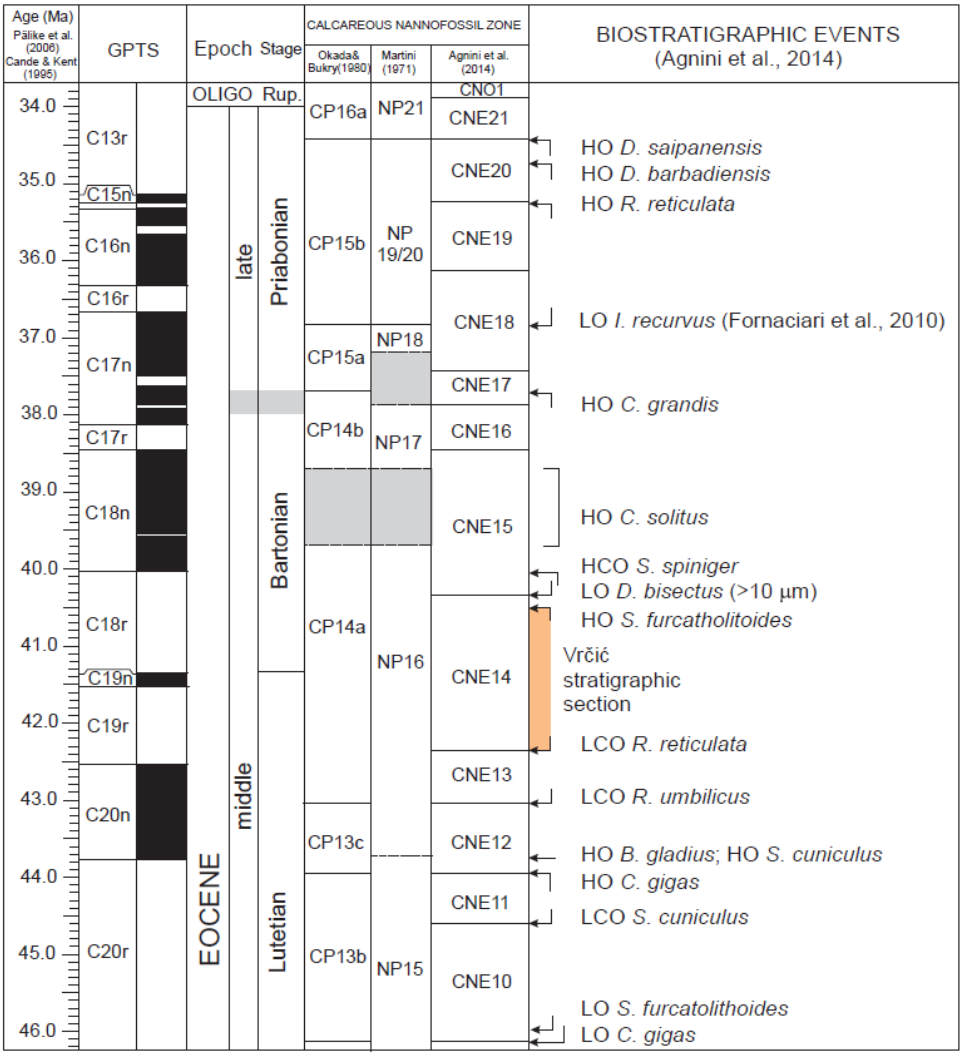

Figure 3.9 - Chronostratigraphic scheme, partly modified after Agnini et al. (2014), with Vrčić section biostratigraphic range correlated.

attributed to the CNE14, in the *R. reticulata* Biozone. All three species are contemporarily present in the Pag sequence.

The micropaleontological assemblage of the studied flysch, characterized by the presence of several age-diagnostic species all along the studied log, likely indicates a time interval from about 42.37, corresponding to the LO *R. reticulata*, to 40.51 Ma, corresponding to the HO *S. furcatolithoides* (**Figure 3.9**, orange band).

An interesting feature of our samples is the presence from the base to the top of the sequence of the nearshore species *Braarudosphaera bigelowii* and *Pemma papillatum* (Bown & Young, 2019) (**Table ST4.2**). Furthermore, a high concentration of ascidian spicules in the lower part of the section is significant. The small size of ascidian spicules, or their fragments, can be

observed under the polarizing microscope with the same magnification of calcareous nannofossils (**Figure 3.8**, Fig. 13). A particular abundance of ascidian remains indicates marine re-deposition close to littoral, estuarine or lagoonal environments (Bown & Young, 2019; Kemal Sagular et al., 2018). These paleoenvironmental indications for the source area of the sediments well agree with paleoenvironmental and paleogeographic reconstructions proposed by Babic and Zupanic (1990; 2008a), Babic et al. (1993) and Ćosović et al. (2008) for the Northern Dalmatia islands.

To sum up, results from our integrated biostratigraphic study indicate that in Middle Eocene time, for the Pag Basin included in the External Dinarides foreland system, progressive deepening of the depositional environment occurred, after the marine transgression and Foraminiferal Limestone deposition (Babić & Zupanič, 2016). The Ascidian assemblage, present at the base of the turbiditic succession, and on top of the Foraminiferal Limestone, suggest a shallow water source area environment, that feeds into the first stage of the turbiditic deposition. The sharp stratigraphic disappearance of the ascidian spicules after the P8 sample to the top of the sequence, combined with a progressive increase of the estimated pelite/arenaceous ratio (see **Figure 3.3b**), vertical facies variations and a general fining-upward trend can be interpreted as a progressive deepening of the Pag Basin. After the marine transgression, a relative sea-level rise and a sudden increase in the clastic component of sediments, likely due to the approaching orogenic front, marks the transition to the hemipelagic environment of the Dalmatian Flysch. Our data reject the hypothesis that such a major event in the Dinaric foreland basin system occurred at the beginning of the Middle Miocene, as proposed by Mikes et al. (2008).

Our data support a post-Lutetian age of folding and thrusting for the Pag Island region, in accordance with stratigraphic and sedimentological studies suggesting syn-folding Priabonian to Bartonian sedimentation in the area of the Promina Mount, some tens of kilometers south of the Pag anticline (Vlahović et al., 2012 and reference therein). Altogether, these data indicate a relatively short time span, of the order of about 10 Ma (Priabonian-Bartonian interval) for the main tectonic contractional stage, which led to folding the thrusting of the External Dinarides in this sector of the Northern Dalmatian islands.

ACKNOWLEDGMENTS

The authors wish to thanks Marco Meda from the ENI S.P.A and the entire SEFRAC group for their interest and insightful discussion. We are grateful to Giovanna Gianelli for preparing the smear slides, and to Cristian Cavozzi for technical support. Financial support from Eni Spa is kindly acknowledged. We extend our sincere thanks to Editor I. Somerville and the two reviewers for their constructive and thorough reviews, from which we have benefited greatly in revising our manuscript.

SUPPLEMENTARY MATERIALS

Sample	Locality	Latitude (N)	Longitude (E)
P1	Vrčić-Staravasa, 10 km SE Pag town	*44° 38' 88''*	*15° 13' 94''*
P2	Vrčić-Staravasa, 10 km SE Pag town	*44° 38' 87''*	*15° 13' 90''*
P3	Vrčić-Staravasa, 10 km SE Pag town	*44° 38' 86''*	*15° 13' 84''*
P4	Vrčić-Staravasa, 10 km SE Pag town	*44° 38' 86''*	*15° 13' 85''*
P5	Vrčić-Staravasa, 10 km SE Pag town	*44° 38' 85''*	*15° 13' 83''*
P6	Vrčić-Staravasa, 10 km SE Pag town	*44° 38' 84''*	*15° 13' 81''*
P7	Vrčić-Staravasa, 10 km SE Pag town	*44° 38' 84''*	*15° 13' 81''*
P8	Vrčić-Staravasa, 10 km SE Pag town	*44° 38' 83''*	*15° 13' 83''*
P9	Vrčić-Staravasa, 10 km SE Pag town	*44° 38' 82''*	*15° 13' 83''*
P10	Vrčić-Staravasa, 10 km SE Pag town	*44° 38' 82''*	*15° 13' 83''*
P11	Vrčić-Staravasa, 10 km SE Pag town	*44° 38' 82''*	*15° 13' 83''*
P12	Vrčić-Staravasa, 10 km SE Pag town	*44° 38' 82''*	*15° 13' 82''*
P12A	Vrčić-Staravasa, 10 km SE Pag town	*44° 38' 82''*	*15° 13' 82''*
P13	Vrčić-Staravasa, 10 km SE Pag town	*44° 38' 81''*	*15° 13' 82''*
P13	Vrčić-Staravasa, 10 km SE Pag town	*44° 38' 81''*	*15° 13' 81''*
P15	Vrčić-Staravasa, 10 km SE Pag town	*44° 38' 80''*	*15° 13' 81''*
P16	Vrčić-Staravasa, 10 km SE Pag town	*44° 38' 79''*	*15° 13' 81''*
P17	Vrčić-Staravasa, 10 km SE Pag town	*44° 38' 79''*	*15° 13' 81''*
P18	Vrčić-Staravasa, 10 km SE Pag town	*44° 38' 79''*	*15° 13' 80''*
P19	Vrčić-Staravasa, 10 km SE Pag town	*44° 38' 78''*	*15° 13' 77''*
P20	Vrčić-Staravasa, 10 km SE Pag town	*44° 38' 77''*	*15° 13' 77''*
P21	Vrčić-Staravasa, 10 km SE Pag town	*44° 38' 78''*	*15° 13' 75''*
P22	Vrčić-Staravasa, 10 km SE Pag town	*44° 38' 76''*	*15° 13' 73''*
P23	Vrčić-Staravasa, 10 km SE Pag town	*44° 38' 73''*	*15° 13' 70''*
P24	Vrčić-Staravasa, 10 km SE Pag town	*44° 38' 68''*	*15° 13' 70''*
P25	Vrčić-Staravasa, 10 km SE Pag town	*44° 38' 62''*	*15° 13' 64''*
P26	Vrčić-Staravasa, 10 km SE Pag town	*44° 38' 68''*	*15° 13' 69''*
P27	Vrčić-Staravasa, 10 km SE Pag town	*44° 38' 63''*	*15° 13' 66''*
P28	Vrčić-Staravasa, 10 km SE Pag town	*44° 38' 62''*	*15° 13' 66''*
P29	Vrčić-Staravasa, 10 km SE Pag town	*44° 38' 62''*	*15° 13' 65''*
P30	Vrčić-Staravasa, 10 km SE Pag town	*44° 38' 61''*	*15° 13°'63''*

Table ST 4.1 - Geographic position of sampling along the studied stratigraphic column. Coordinates are expressed in decimal degree and referenced system WGS84.

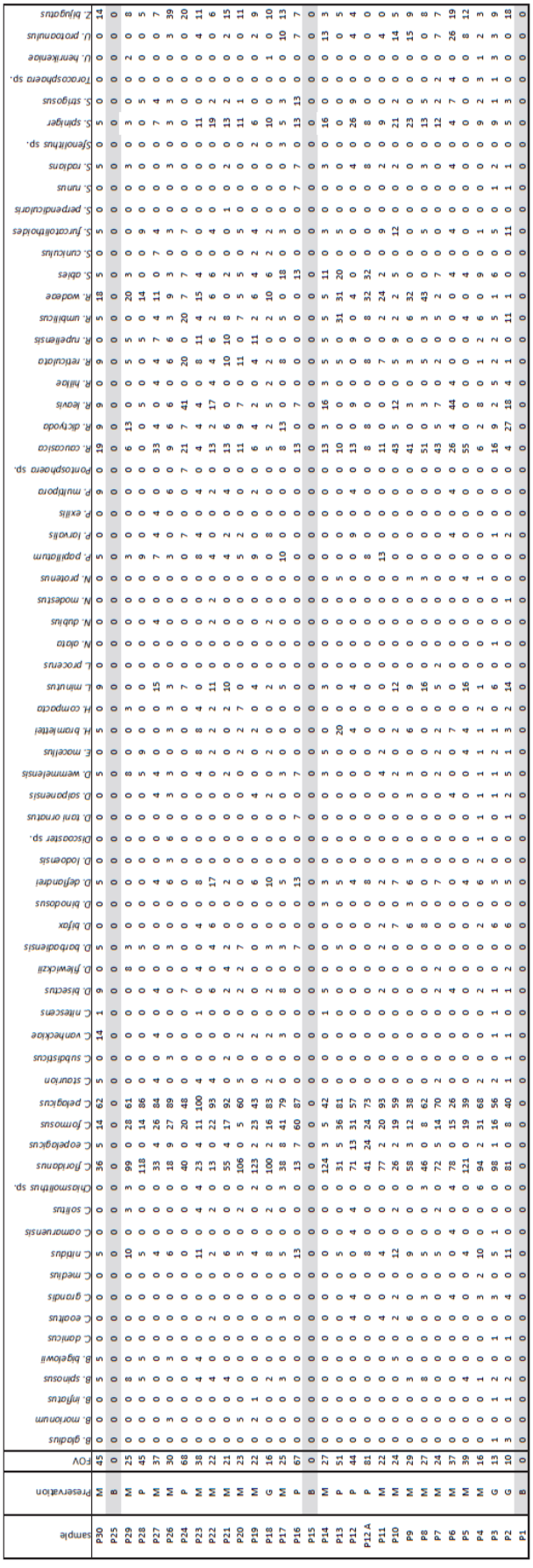

sample	Preservation	FOV	*B. gladius*	*B. morionum*	*B. inflatus*	*B. spinosus*	*B. bigelowii*	*C. danicus*	*C. eoaltus*	*C. grandis*	*C. medius*	*C. nitidus*	*C. oamaruensis*	*C. solitus*	*Chiasmolithus* sp.	*C. floridanus*	*C. eopelagicus*	*C. formosus*	*C. pelagicus*	*C. staurion*	*C. subdisticus*	*C. vanheckiae*	*C. nitescens*	*D. bisectus*	*D. filewickzii*	*D. barbadiensis*	*D. bifax*	*D. binodosus*	*D. deflandrei*	*D. lodoensis*	*Discoaster* sp.	*D. tani ornatus*	*D. saipanensis*	*D. wemmelensis*	*E. macellus*	*H. bramlettei*	*H. compacta*	*L. minutus*	*L. procerus*	*N. alata*	*N. dubius*	*N. modestus*	*N. protenus*	*P. papillatum*	*P. larvalis*	*P. exilis*	*P. multipora*	*Pontosphaera* sp.	*R. caucasica*	*R. dictyoda*	*R. leavis*	*R. hillae*	*R. reticulata*	*R. rupellensis*	*R. umbilicus*	*R. wadeae*	*S. abies*	*S. cuniculus*	*S. furcatolithoides*	*S. perpendicularis*	*S. runus*	*S. radians*	*Sfenolithus* sp.	*S. spiniger*	*S. strigosus*	*Toracosphaera* sp.	*U. henrikeniae*	*U. protoanulus*	*Z. bijugatus*
P30	M	45	0	0	0	5	5	0	0	0	0	5	0	0	0	36	5	14	62	5	0	14	1	9	0	5	0	0	5	0	0	0	0	5	0	5	0	9	0	0	0	0	0	5	0	0	9	0	19	9	9	0	9	0	5	18	5	0	5	0	0	5	0	5	0	0	0	0	14
P25	B	0	0	0	0	0	0	0	0	0	0	0	0	0	0	0	0	0	0	0	0	0	0	0	0	0	0	0	0	0	0	0	0	0	0	0	0	0	0	0	0	0	0	0	0	0	0	0	0	0	0	0	0	0	0	0	0	0	0	0	0	0	0	0	0	0	0	0	0
P29	M	25	0	0	0	8	0	0	0	0	0	10	0	3	3	99	0	28	61	0	0	0	0	0	8	3	0	0	0	0	0	0	0	8	0	0	3	0	0	0	0	0	0	3	0	0	0	0	6	13	0	0	5	5	0	20	3	0	0	0	0	3	0	3	0	0	2	0	8
P28	P	45	0	0	0	5	5	0	0	0	0	5	0	0	0	118	0	14	86	0	0	0	0	0	0	5	0	0	0	0	0	0	0	5	9	0	0	0	0	0	0	0	0	9	0	0	0	0	0	0	5	0	0	5	0	14	0	0	9	0	0	0	0	0	5	0	0	0	5
P27	M	37	0	0	0	0	0	0	0	0	0	4	0	0	0	33	4	26	84	4	0	4	0	4	0	0	0	0	4	0	0	0	4	4	0	0	0	15	0	0	4	0	0	7	4	4	0	0	33	4	0	4	4	7	4	11	0	7	4	0	0	0	0	7	4	0	0	0	7
P26	M	30	0	3	0	0	3	0	0	0	0	6	0	0	0	18	9	27	89	0	3	0	0	0	0	3	0	0	6	3	6	0	3	3	0	3	3	3	0	0	0	0	0	3	0	0	6	0	9	6	6	0	6	6	3	9	3	0	3	0	0	3	0	3	3	0	0	3	39
P24	P	68	0	0	0	0	0	0	0	0	0	0	0	0	0	40	0	20	48	0	0	0	0	7	0	0	0	0	0	0	0	0	0	0	0	0	0	7	0	0	0	0	0	0	7	0	0	7	21	7	41	0	20	0	20	7	7	0	7	0	0	0	0	0	0	0	0	0	20
P23	M	38	0	0	0	4	4	0	0	0	0	11	0	4	4	23	4	11	100	4	0	0	1	0	4	0	4	0	8	0	0	0	0	4	8	8	4	0	0	0	0	0	0	8	4	0	4	0	4	4	4	0	8	11	4	15	4	0	0	0	0	0	0	11	0	0	0	4	11
P22	M	22	0	0	0	4	0	0	2	0	0	2	0	2	0	13	0	22	93	4	0	0	0	6	0	4	6	0	17	0	0	0	0	0	2	2	2	11	0	0	2	2	0	4	0	0	2	0	13	2	17	4	4	6	2	6	6	0	4	0	0	0	0	19	2	0	0	0	6
P21	M	21	0	0	0	4	0	0	0	0	0	6	0	0	0	55	4	17	92	0	2	0	0	2	4	2	0	0	2	0	0	0	0	2	0	0	2	10	0	0	0	0	0	4	2	0	4	0	13	6	0	0	10	10	8	0	2	0	0	1	0	2	0	13	2	0	0	2	15
P20	M	23	0	5	0	0	0	0	0	0	0	5	0	2	0	106	0	5	60	5	0	2	0	2	2	7	0	0	0	0	0	0	0	0	2	2	7	0	0	0	0	0	0	5	2	0	0	0	11	9	7	0	11	0	7	5	5	0	5	0	0	0	0	11	1	0	0	0	11
P19	M	22	0	2	1	0	0	0	0	0	0	4	0	0	2	123	2	23	43	0	0	2	0	0	0	0	0	0	6	0	0	0	4	0	0	2	0	4	0	0	0	0	0	9	0	0	2	0	6	4	2	0	4	11	2	6	4	2	4	0	0	0	2	6	0	0	0	2	9
P18	G	16	0	0	0	2	0	0	0	0	0	8	0	2	0	100	2	16	83	2	0	2	0	2	0	3	0	0	10	0	0	0	2	0	2	0	0	2	0	0	2	0	0	0	8	0	0	0	5	2	5	2	2	0	2	10	6	2	2	0	0	0	0	10	0	0	1	0	10
P17	M	25	0	0	0	3	0	0	3	0	0	5	0	0	3	38	8	41	79	0	0	3	0	8	0	3	0	0	5	0	0	0	0	3	0	0	0	5	0	0	0	0	0	10	0	0	0	0	8	13	0	0	8	0	5	0	18	0	3	0	0	0	3	5	3	0	0	10	13
P16	P	67	0	0	0	0	0	0	0	0	0	13	0	0	0	13	7	60	87	0	0	0	0	0	0	7	0	0	13	0	0	7	0	7	0	0	0	0	0	0	0	0	0	0	0	0	0	0	13	0	7	0	0	0	0	0	13	0	0	0	7	7	0	13	13	0	0	7	7
P15	B	0	0	0	0	0	0	0	0	0	0	0	0	0	0	0	0	0	0	0	0	0	0	0	0	0	0	0	0	0	0	0	0	0	0	0	0	0	0	0	0	0	0	0	0	0	0	0	0	0	0	0	0	0	0	0	0	0	0	0	0	0	0	0	0	0	0	0	0
P14	M	27	0	0	0	0	0	0	0	0	0	0	0	0	0	124	3	5	42	0	0	0	1	5	0	0	0	3	3	0	0	0	0	3	5	0	0	3	0	0	0	0	0	0	0	0	0	0	13	3	16	3	5	5	5	5	11	0	3	0	0	3	0	16	0	0	0	13	3
P13	P	51	0	0	0	0	0	0	0	0	0	5	0	0	0	31	5	36	81	0	0	0	0	0	0	5	0	0	5	0	0	0	0	0	0	20	0	0	0	0	0	0	5	0	0	0	0	0	10	0	0	0	5	0	31	31	20	0	5	0	0	0	0	0	0	0	0	0	5
P12	P	44	0	0	0	0	0	0	4	4	0	0	4	4	0	71	13	31	57	0	0	0	0	0	0	0	0	0	4	0	0	0	0	0	0	4	0	4	0	0	0	0	0	0	9	0	4	0	13	0	9	0	0	9	0	4	0	0	0	0	0	4	0	26	9	0	0	4	4
P12 A	P	81	0	0	0	0	0	0	0	0	0	8	0	0	0	41	24	24	73	0	0	0	0	0	0	0	0	0	8	0	0	0	0	0	0	0	0	0	0	0	0	0	0	8	0	0	0	0	8	8	0	0	8	0	8	32	32	0	0	0	0	8	0	8	0	0	0	0	0
P11	M	22	0	0	0	0	0	0	4	0	0	4	0	0	0	77	2	20	93	0	0	0	0	2	0	2	2	0	2	0	0	0	0	4	2	0	0	0	0	0	0	0	0	13	0	0	0	0	11	0	0	0	7	0	2	24	2	0	9	0	0	2	0	9	0	0	0	4	0
P10	M	24	0	0	0	0	5	0	2	2	0	12	0	2	0	26	2	19	59	0	0	0	0	0	0	0	7	0	7	0	0	0	0	2	0	2	0	12	0	0	0	0	0	0	0	0	0	0	43	5	12	0	5	9	2	2	5	0	12	0	0	2	0	21	2	0	0	14	5
P9	M	29	0	0	0	3	0	0	6	0	0	9	0	0	0	58	3	12	38	0	0	0	0	0	0	0	6	3	6	3	0	0	3	3	0	6	0	9	0	0	0	0	3	0	0	0	0	0	41	0	3	0	3	0	6	32	0	0	0	0	0	0	0	23	0	0	0	15	9
P8	M	27	0	0	0	8	0	0	0	3	0	5	0	0	3	46	0	8	62	0	0	0	0	0	0	0	8	0	0	0	0	0	0	0	0	0	0	16	0	0	0	0	3	0	0	0	0	0	51	0	3	0	5	0	3	43	0	0	5	0	0	3	0	13	5	0	0	0	8
P7	M	24	0	0	0	0	0	0	0	0	0	5	0	2	0	72	5	14	70	2	0	0	0	2	2	0	0	0	7	0	0	0	0	2	2	2	0	5	2	0	0	0	0	0	0	0	0	0	43	5	7	0	2	0	5	2	7	0	0	0	0	0	0	12	2	2	0	7	7
P6	M	37	0	0	0	0	0	0	0	4	0	0	4	0	4	78	0	15	26	0	0	0	0	4	0	0	0	0	0	0	0	0	4	0	0	7	0	0	0	0	0	0	0	0	4	0	4	0	26	4	44	4	0	0	0	0	4	0	4	0	0	4	0	4	7	4	0	26	19
P5	M	39	0	0	0	4	0	0	0	0	0	4	0	0	0	121	0	19	39	0	0	0	0	0	0	0	0	0	4	0	0	0	0	0	4	4	0	16	0	0	0	0	4	0	0	0	0	0	55	0	0	0	0	0	4	0	4	0	0	0	0	0	0	0	0	0	0	8	12
P4	M	16	0	0	0	1	0	0	0	3	2	10	0	0	6	94	2	31	68	2	0	0	0	2	0	0	2	0	6	2	1	1	1	1	1	1	2	1	0	0	0	0	1	0	0	0	0	0	6	2	8	0	1	2	6	0	9	0	1	0	0	0	0	9	2	3	1	2	3
P3	G	13	1	0	1	2	0	1	0	3	0	5	1	0	0	98	1	16	56	2	0	1	1	1	0	0	6	0	5	0	0	0	1	1	2	1	0	6	0	1	0	0	0	0	1	0	0	0	16	9	2	5	2	2	5	1	6	0	5	0	1	2	0	9	1	1	3	3	9
P2	G	10	3	0	1	2	0	1	0	4	0	11	0	0	0	81	0	8	40	1	1	1	0	1	2	0	6	0	5	0	0	1	2	5	1	3	2	14	0	0	0	1	0	0	2	0	0	0	4	27	18	4	1	0	11	1	0	0	11	0	1	1	0	5	3	0	0	0	18
P1	B	0	0	0	0	0	0	0	0	0	0	0	0	0	0	0	0	0	0	0	0	0	0	0	0	0	0	0	0	0	0	0	0	0	0	0	0	0	0	0	0	0	0	0	0	0	0	0	0	0	0	0	0	0	0	0	0	0	0	0	0	0	0	0	0	0	0	0	0

Table ST 4.2 - Range chart of the calcareous nannofossil species counted in the Vrčić section.

CHAPTER 4.

INHERITED EXTENSIONAL FAULTS

This chapter is presented in the form of a manuscript that is currently been prepared for submission to *Geology*. The manuscript describes structural ad kinematic model of pre-folding inherited extensional fault zones passively rotated in the Pag anticline. This feature allowed us to investigate the role of thin-skin extensional features involved in contractional structures

ARTICLE IN PREPARATION

Folding thin-skinned listric extensional faults triggers fold compartmentalization

Succo, A., Mittempergher, S., Storti, F., Bistacchi, A, and Meda, M.

Article in preparation for submission to *Geology*

Status of manuscript: Awaiting approval by ENI for journal submission

Research activities in the Pag anticline were founded by ENI Spa and results are covered by a confidentiality agreement. Consequently, the manuscript in its present form is currently been reviewed by the Company and will be submitted to *Geology* upon approval.

.

FOLDING THIN-SKINNED LISTRIC EXTENSIONAL FAULTS TRIGGERS FOLD COMPARTMENTALIZATION

Succo A.*[1], Mittempergher S.[2], Storti F.[1], Bistacchi A.[2] and Meda M.[3]

1. NEXT, Natural and Experimental Tectonic Research Group, Department of Chemistry, Life Sciences and Environmental Sustainability, University of Parma, Parco area delle Scienze 11/a, 43124 Parma, Italy.

2. Department of Environmental and Earth Sciences, Università degli Studi di Milano Bicocca, Piazza della Scienza 4, 20126 Milano, Italy.

3. ENI Spa, Upstream and Technical Services – San Donato Milanese – Italy.

ABSTRACT

Although inherited fault zones are common features of thrust-related anticlines in most orogenic systems, reactivation of thin-skinned listric extensional faults and their role on tectonic evolution is actually poorly constrained and overlooked. Here, we document a new case study in which misoriented structural inheritance was folded during the growth of the Pag thrust-related anticline (External Dinarides, Croatia), promoting fold segmentation and preferential fluid migration and accumulation. Particularly, we describe the geometry and kinematics of the Dinjiška Fault supported by field-mapping and structural data. Stress inversion and slip-tendency analysis were performed to model the stress field conditions during the muti-stage fault re-activation. Multiple stages of fault reactivations and complex kinematic history characterize folded listric faults. We show that, during folding, fault-ramp segments triggered the nucleation and propagation of late-stage abutting tear faults, whose orientation and geometry are directly related to inherited fault geometry, while flat-segments promote stress concentration and buttressing. Our findings document that positive inversion is not the only mechanism that has to be taken into account for accommodating shortening, but also passively rotation and folding of thin-skinned extensional systems could provide an innovative template producing complex geometries and fold deformation patterns by transpressional or strike-slip tearing. The recognition of these structural features in fold and thrust belts (from outcrops to the subsurface) and their potential as preferential pathway for fluids, could be a new exploration target for future research in structural diagenesis and fault-fold interactions.

4.1 INTRODUCTION

Involvement of inherited extensional fault zones in thrust-related anticlines is a common feature in most orogenic systems (e.g. Bally, 1987; Gillcrist et al., 1987; Butler, 1989; Butler et al., 2006; Jammes et al., 2014; Scisciani, 2009; Tavani et al., 2018). Typically, pre-existing faults underwent positive inversion during contraction, to contribute accommodating shortening at different crustal levels (e.g., Bonini et al., 2012; Cooper et al., 1989; Sibson, 1985; Sibson & Scott, 1998; Turner & Williams, 2004; Williams et al., 1989). Multiple factors have been recognized to determine the efficiency of positive fault inversion (e.g. Turner & Williams, 2004; Bonini et al., 2012; Ruh & Vergés, 2018), including: (*i*) fault steepness, (*ii*) fault orientation compared to the compressional stress field, (*iii*) fault friction, and (*iv*) mechanical stratigraphy. Their combination produces a wide variety of positive inversion scenarios, involving total or partial re-activation and fault decapitation by thrust short-cut. Furthermore, earlier faults may also rotate during inversion giving rise to complex geometries (McClay et al., 1989; Tavarnelli et al., 1996; Scisciani, 2009).

Most templates of positive fault inversion describe structural architectures produced by both (*i*) fault-perpendicular compression and (*ii*) slip reversal along with basal detachment layers (e.g., McClay & Buchanan, 1992; **Figure 4.1A**). Reactivation of misoriented extensional faults produces more complex geometric and kinematic patterns of fold compartmentalization by transpressional or strike-slip tearing (**Figures 4.1B, C**). Basal detachment localization at greater depth during contraction is expected to inhibit fault inversion after a threshold difference of detachment depth. In this case, extensional faults can be passively folded rather than positively inverted, producing map patterns that depend on the relative orientation between structural inheritance and contractional stress field (**Figures 4.1D-F**).

Folded bedding-parallel extensional detachments provide layers of intense deformation where preferential fluid migration and accumulation is expected to occur, possibly enhancing metasomatic reactions suitable to dramatically modify rock petrophysical properties, such as limestone dolomitization (e.g. Sibson, 1995; Incerpi et al., 2019; Mozafari et al., 2019). Despite their role as potential hydrocarbon reservoirs or ore deposits, or even as preferential pathways for magmatic intrusions, bedding-parallel detachments are difficult to be imaged in reflection seismic data and thus are typically overlooked. On the other hand, folded fault ramp segments provide mechanical and stratigraphic discontinuities more easily identifiable in geophysical datasets, where they may appear as stratigraphically-confined deformation features **(Figures 4.1D-F**).

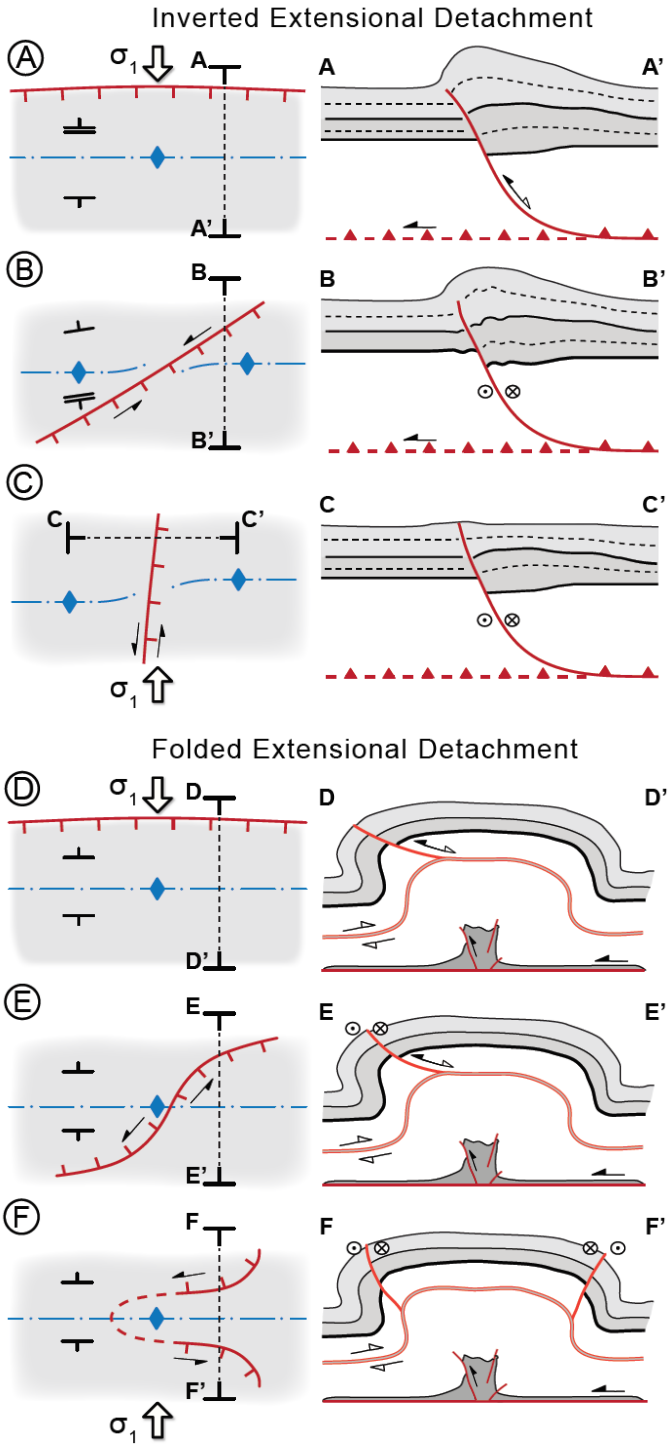

Figure 4.1 - Cartoon to illustrate in plane-view and cross-section a multiple scenario of geometry and deformation style of inverted extensional fault systems in function of the relative orientation of an extensional fault with respect to the contractional stress field (sub-parallel, oblique and sub-orthogonal to the maximum horizontal stress) and the reactivation (a, b, and c) or folding (d, e, and f) of inherited detachment layers. (a) Partially inverted extensional fault striking orthogonal to the maximum horizontal stress forming a thrust-related asymmetrical anticline; (b) re-activaton of a normal fault oblique to the maximum horizontal stress. Deformation

(*continued from the previous page*): is accommodating by folding and buttressing along the fault, plus a component of strike-slip reactivation; (c) reactivation of a normal fault sub-parallel to the maximum horizontal stress. Deformation is accommodated by sliding along the detachment, and the normal fault is reactivated as tear fault; (d)-(e)-(f) passively folded extensional detachment variously oriented respect to contraction. Depending on inherited fault orientation, multiple plane-view geometries can be formed. Pre-existing fault and relative detachment layer can be passively rotated and folded during fold growth, and in case of fault striking mostly orthogonal to the fold axis (sketch f), the extensional fault can be completely folded. Note how in these cases (d, e and f) fold geometry is not controlled by the inversion of the extensional system, but rather by the activation of a deeply rooted detachment layer and mechanical stratigraphy. Reactivation of extensional fault is depth-detachment dependent, and the presence of an extensional basal level (red line) higher than the detachment weak horizon controls the un-reactivation and subsequent folding of former faults, who come re-oriented during fold growth until an optimal orientation (a-c modified after Scisciani, 2009; Coward et al., 1991; Bonini et al., 2012). Red line, active faults. White arrowhead, normal fault developed during the first-phase extention; black arrowhead, inverted extensional fault (if associated with the white arrow), or thrust fault formed during inversion. Grey shading indicates the syn-sedimentary extensional fill.

Understanding that such fault segments may actually pertain to well-developed ramp-flat geometries dramatically increases interest on them as economic prospects, including aquifers. Moreover, fault ramp segments embedded in folded multilayers may provide weakness zones suitable to be exploited during folding as tears, which may propagate up- and down-section to eventually produce compartmentalization during fold tightening. Such tear fault propagation may occur by coseismic slip. It is thus very important to develop a comprehensive understanding of the appearance and kinematic architecture of folded listric extensional faults for their impact on fold evolution, seismic hazard, and economic potential.

In this paper we describe misoriented listric extensional fault zones cutting through Paleogene silicoclastic and carbonate rocks and flatting down into Upper Cretaceous platform carbonates, spectacularly exposed on the island of Pag, External Dinarides, Croatia. These fault zones were folded during the growth of the Pag anticline and their ramp segments triggered nucleation of late-stage tear faults that compartmentalized the anticlinal geometry. For this purpose, we used detailed geological and structural mapping, supported by high-resolution UAV photogrammetry. Moreover, normalized slip-tendency analysis (Morris et al., 1996; Lisle & Srivastava, 2004) was calculated for the studied fault segments, to verify the most suitable stress field conditions for re-activation.

4.2 GEOLOGICAL OUTLINE

The Pag anticline is located in the External Dinarides of Croatia, at the footwall of the Velebit major transpressional fault system (**Figure 4.2A**). The anticline involves about 2 km of Lower to Upper Cretaceous tight platform carbonates of the Adriatic Carbonate Platform (AdCP, Vlahović et al., 2005), unconformably overlain by an Eocene carbonate ramp and thrust-top basin succession (foraminiferal limestone and Dalmatian flysch, respectively; Mittempergher et al., 2019). Significant erosion during carbonate platform emersion in Late Cretaceous to Paleocene times is indicated by the long stratigraphic hiatus (**Figure 4.2B**) and widespread occurrence of karst features on top of the Cretaceous rocks (Jelaska et al., 1994; Korbar, 2009). Middle Eocene contraction and thrust imbrication led to the growth of the Pag anticline, which has an asymmetrical box-type geometry, with steeply-dipping to overturned limbs and a wide, flat crestal zone (Mittempergher et al., 2019; **Figure 4.2C**). A characteristic feature of the anticline is the pervasive occurrence on both fold limbs of two main sets of axial-oblique, sub-vertical left- and right-lateral strike-slip faults, striking E-W and N-S, respectively (**Figure 4.2A**). The best exposures occur on the forelimb, where structural data indicate that rotating bedding to the horizontal restores a set of conjugate NE-SW trending extensional faults (**Figure 4.2D**). In fact, the occurrence of a pre-unconformity extensional faulting, together with lateral facies and thickness variations along the aforementioned misoriented faults was recently described by Mittempergher et al. (2019), pointing out for the first time the existence of inherited faults pre-dating Eocene syn-tectonic deposition.

4.3 THE DINJIŠKA FAULT

In the following, we illustrate the representative case of the superbly exposed, passively rotated and reactivated Dinjiška Fault (DF hereafter). Two main fault strands are visible in the area, one striking approximately NS to NNW-SSE, crosscutting the bedding of the anticline forelimb at high angle, and a fault branch striking NW, at low angle to the bedding strike (**Figures 4.2A**, see also Supplementary material **S4.1** – **Attached 2**). The two faults share a NS-striking fault segment of about 200m (red and green line in **Figure 4.3A**). Based on the field data discussed below, we identify the DF as a listric normal fault confined within the Upper Cretaceous rocks, now visible in map view in the forelimb of the Pag anticline. The NS striking fault, partly reactivating the DF is a dextral strike-slip fault crosscutting and offsetting the folded sedimentary sequence up to Paleogene rocks (**Figure. 4.3A**).

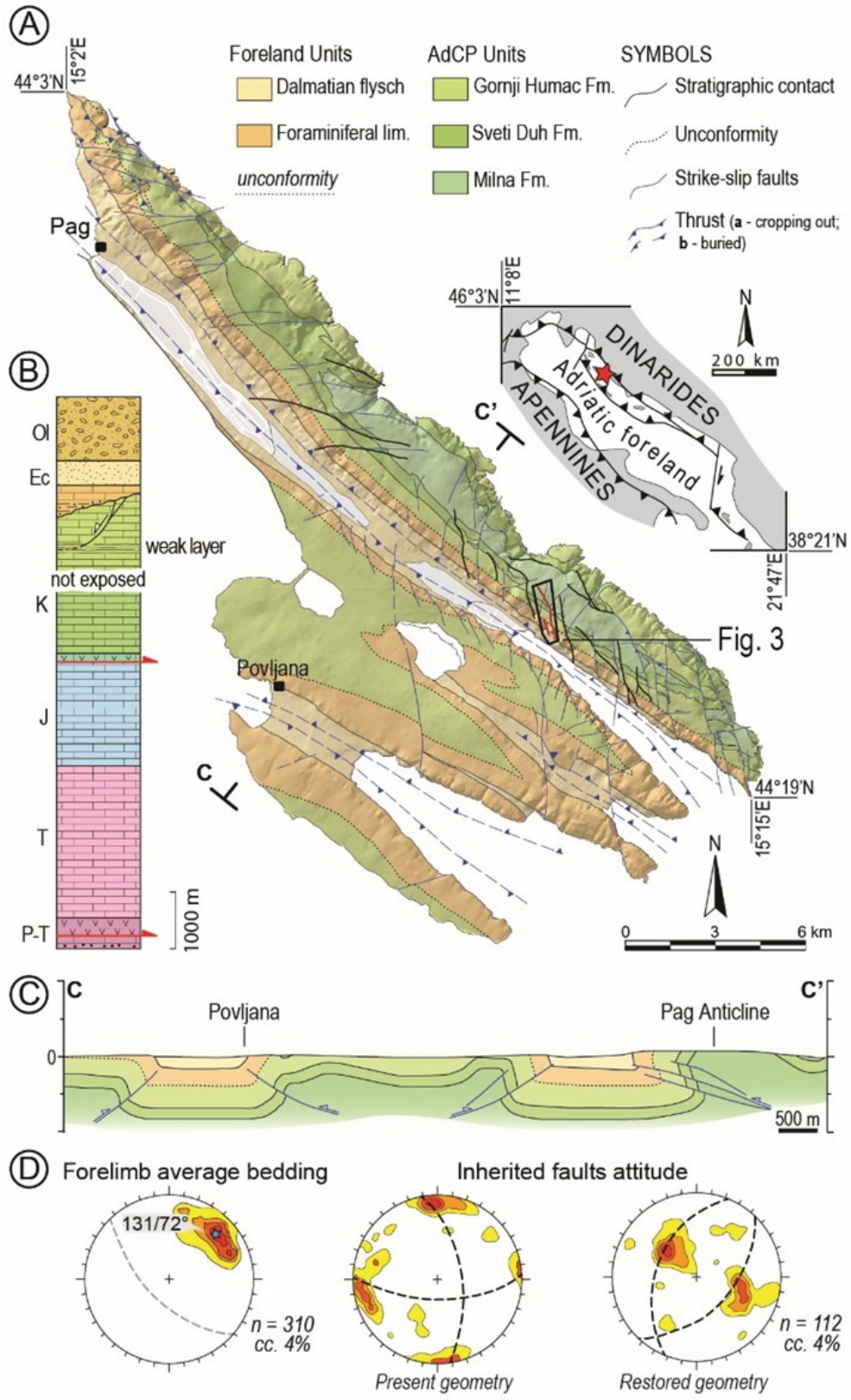

Figure 4.2 - Simplified geological map of Pag anticline. (a) Location of the Pag anticline in the Dinaric chain (red star) and structural map of the Pag anticline showing the lithostratigraphic units and position of the Dijniska Fault zone (in red;

(*continued from the previous page*): Figure 4.3a. Note how the anticline is extensively deformed by axial-oblique left-lateral and right-lateral strike-slip faults, striking E-W and N-S respectively. Modified from Mittempergher et al. (2019). Black lines are for field mapped inherited extensional faults; (b) stratigraphic column where the two main regional scale detachment levels are indicated (after Korbar, 2009). The extensional faults atop of the Late Cretaceous units have their detachment layer into a laminate-rich horizon within the Milna Formation. (c) simplified cross-section of the Pag anticline and minor folds near the Povljana village. After Mittempergher et al. (2019); (d) Stereoplot showing poles contouring and average plane (dotted line) for forelimb bedding, the N-S and E-W striking faults in Cretaceous platform units along forelimb of the anticline, in their present day attitude and restored to their pre-folding attitude. For the restoration surface has been used the average bedding attitude of base foraminiferal limestone unit in forelimb sector. A dark dotted great circle indicates the average fault plane. AdCP: Adriatic Carbonate Platform; P-T: Permo-Triassic; T: Triassic; J: Jurassic; K; Cretaceous; Ec: Middle Eocene; Ol: Oligocene.

Relative relationship between the cutoff angle with the bedding of the Cretaceous rocks, from NW to SE the Dinjiška normal Fault passes from a ramp to a flat, through a 100m long curved surface (**Figure 4.3A**). The ramp is sub-vertical, while the flat dips to the SW of 65°. When bedding is restored to horizontal through a rigid rotation of 75° around an axis oriented N310/5°, the Dinjiška normal Fault attains a NE-SW strike and a northwestward dip (pre-folding stage, **Figure 4.3C**). The flat consists of anastomosed N-S and NW-SE shear surfaces isolating moderately deformed lenses of limestone, where stylolites and shear surfaces arranged in S-C' arrays indicate dextral movement, corresponding to top to the NW transport in the pre-folding stage (**Figure S4.3**). Mechanical striations and rare calcite fibers occur on stylolite surfaces and indicate minor reverse reactivation (**Figure S4.3**). In the hangingwall, the transition between ramp and flat is marked by a volume of deformed limestone bearing evidence for soft-sediment deformation, including drag-folds, pinch-and-swells, dismembered beds, and fluid escape structures ('disrupted beds' in **Figures 4.3A**, **S4.3**). In the same location, the hangingwall is crosscut by EW striking low displacement faults and fractures, abutting against the normal fault plane and truncated by the major unconformity that separates Cretaceous from Paleogene rocks (**Figure 4.3A**). When restored to the pre-folding stage, these small-scale faults can be interpreted as antithetic high angle normal faults. The subvertical ramp segment is reactivated as a dextral strike-slip fault, with subhorizontal slickenlines (sites 2 and 3, **Figure 4.3A**). Within the Upper Cretaceous rocks, dolomitized and de-dolomitized bed-parallel bodies occur on both sides of the DF (**Figures 4.3A**, Supplementary material **S4.1** – **Attached 2**; **S4.2**).

The strike-slip fault is sub-vertical, bears nearly horizontal slickenlines and calcite shear fibers indicating dextral shearing (sites 1 – 3 and 8 – 9 in

Figure 4.3A). The bedding of the foraminiferal limestone and Dalmatian flysch, striking NW and dipping at 75 – 80° to the SW, are dragged coherently with dextral shearing approaching the fault zone. Towards the anticline nucleus, the strike-slip fault separates two dip domains of the Cretaceous succession, suggesting a different partition of fold tightening. The fault zone is formed of a complex network of anastomosing segments forming releasing and restraining bands, most of them being characterized by right steps with intense fracturing at their tips. The fault core rocks, consisting of red-to-yellow cataclasites, are foliated by intense fault-parallel pressure solution cleavage containing S-C structures coherent with dextral shearing and fault perpendicular buttressing (**Figure S4.3**).

The two fault segments are characterized by a distinct displacement-distance path. In particular, in noteworthy to observe that the ramp shows an abrupt separation step across the unconformity (**Figure 4.3B**). The distribution of the horizontal separation along fault strike confirms field and map observations, as the ramp of the rotated normal fault accumulated a separation which is the double of the separation accumulated by the strike-slip fault segments to the South and to the North of the ramp (**Figure 4.3B**). The distribution of the separation indicates also that the normal fault displacement affected only the Upper Cretaceous formations below the unconformity, while Paleogene rocks were crosscut and displaced only by the strike-slip fault (**Figure 4.3B**).

4.4 NORMALISED SLIP TENDENCY OF THE DINJIŠKA FAULT

Slip-tendency analysis provides an effective tool for rapid assessment of stress states and related potential fault activity (Morris et al. 1996). Normalized slip tendency analysis (Lisle & Srivastava, 2004; Bistacchi et al., 2012; Traforti et al., 2018) is calculated as:

$$NTs = \frac{Ts}{max(Ts)} = \tau\ tan\Phi/\sigma_n \quad (1)$$

where Ts is the slip-tendency defined as τ/σn (τ and σn are the tangential and normal stress, respectively), max(Ts) is the maximum slip tendency, attained when τ/σn = μ0, and μ0 = 0.7 is the average friction coefficient for carbonates rocks (Byerlee, 1978; Sibson, 1985; Lisle & Srivastava, 2004).

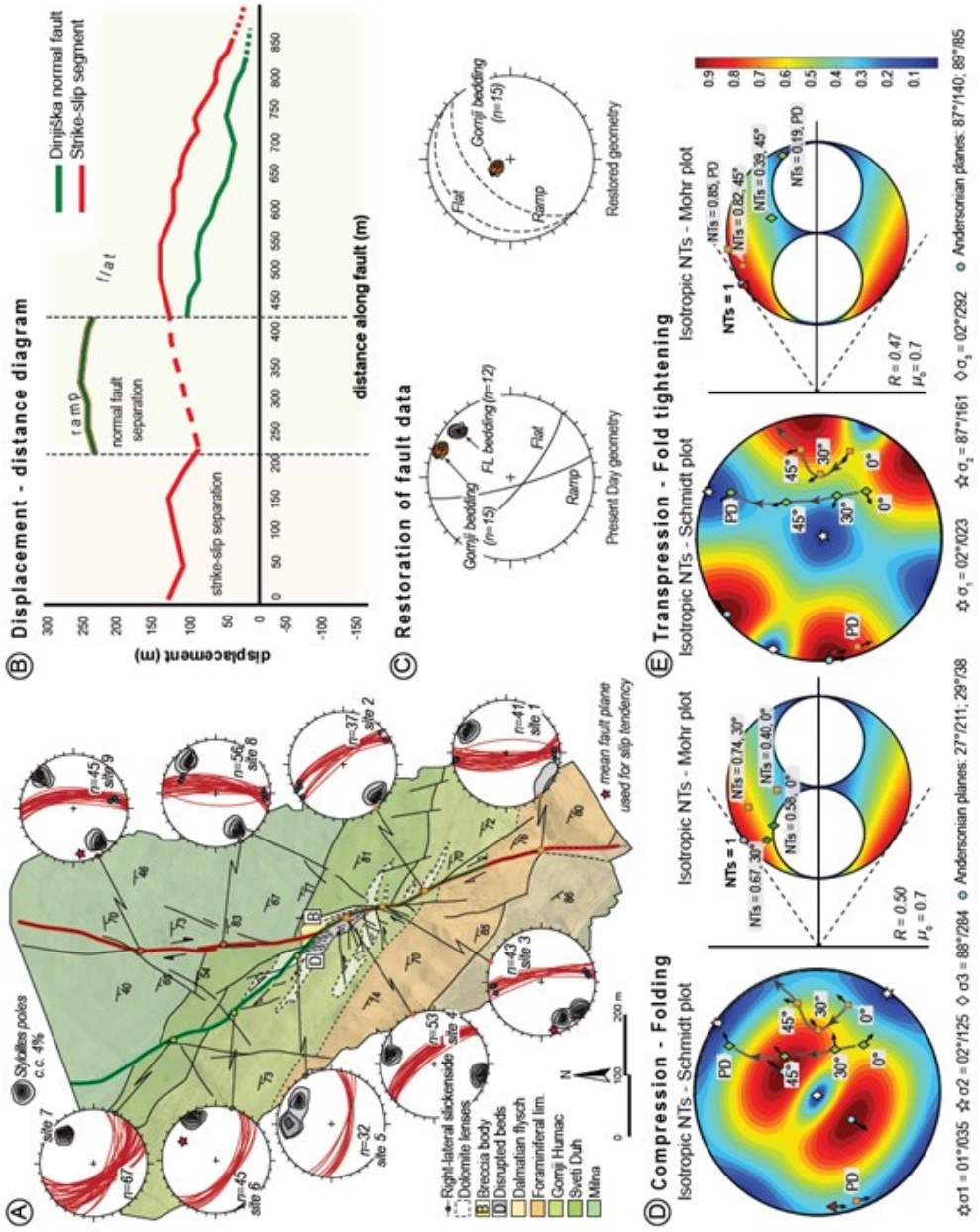

Figure 4.3 - Structural map, structural data and normalized slip tendency analysis results for the Dinjška Fault. (a) Line-drawing and structural map on drone orthophotograph of the Dijniska Fault zone (location of field sites is provided in Supplementary Material, ST1). In the stereonets, the red stars indicate the pole of the average fault planes used in the slip tendency analysis. In the map, the green line indicates the Dijniska normal fault flat segment, the red line indicates the strike-slip fault segment and the green-to-red line the Dijniska normal fault ramp segment that shows multiple reactivations. Stereonets are equal area projection, lower hemisphere. Base of the figure is a high-resolution (10cm/px) DEM obtain by photogrammetry (see S1 for full resolution droned area). PD: present day attitude; (b) displacement-distance diagram for the hanginwall of the Dijniska normal fault and of the western block of the strike-slip fault showing the separation of the units along the fault. Color coding as in Figure 4.3A. The former shows a complex

(*continued from the previous page*): displacement pattern while the abutting segment show a decreasing of displacement toward the crest of the anticline. Displacement along the abutting and re-activated ramp segment is comparable, indicating an amount of re-activation of about 120-130 meters. Restoring this dislocation, the inherited fault show, however, a positive extensional displacement. Note the abrupt displacement step crossing the unconformity; (c) restoration of bedding and fault data to the pre-folding orientation. When foraminiferal limestone (grey scale contour) is restored to horizontal, bedding in Cretaceous rocks (contoured poles) gently dips toward SE, while fault segments (ramp and flat) show a moderate di flat dipping toward NW; bedding data are FL: foraminiferal limestone; (d-e) estimation of the isotropic normalized slip tendency analysis performed for the two deformation stages, compression (d) and late-folding transpression (d), respectively. For each case, input parameters and the normalized slip tendency result plotted in the Schmidt and Mohr plot are reported. See the main text for detailed explanation and Supplementary Material, Section 3 for input parameters and stress inversion. The fault rotation path for each fault segment of the Dinjska fault, from rigid restoration to present-day attitude, is indicate by grey arrows. Note how ramp and flat segment followed different path and how the former is prone to right-lateral re-activation during the second stage. Black arrows on plotted data are indicative of predicted slip vectors.

When failure occurs on a fault, the relationship between its friction coefficient μ_f and μ_0 is expressed as:

$$\mu_f = NTs_f \, \mu_0, \tag{2}$$

$$NTs_f = \mu_f / \mu_0, \tag{3}$$

where NTs_f is the normalized slip-tendency of the fault master slip surface (Traforti et al., 2018).

Stress field orientation is an information necessary to calculate the slip-tendency. For this purpose, we performed a paleostress field inversion (see also Simón, 2019 and references therein) using vein, tectonic stylolite and conjugate thrust fault data collected in 21 structural analysis field sites along the anticline, properly restored to calculate the stress ellipsoid during layer-parallel shortening/early folding stage, and during late-stage fold tightening, respectively (Supplementary Material, **section 4.3**). The paleostress analysis was performed by applying the PBT-axes method implemented in the Win_Tensor software (Delvaux and Spencer, 2003; Delvaux, 2011). Stress inversion analysis provided a NE-SW oriented maximum principal axis of the stress ellipsoid (σ1 at 35/01° and σ3 at 292/88°) for the early folding stage, followed by a counterclockwise rotation of 12° (σ1 at 23/02°) and the shift

between the minimum (σ3) and intermediate (σ2) axes of the stress ellipsoid, which resulted in a transpressional stress field with a stress ratio R= (σ2-σ3)/(σ1-σ3) = 0.47 (Angelier, 1990).

The normalized slip-tendency analysis was performed on the Dinjiška Fault flat and ramp segments, respectively, for both contractional and transpressional stress fields. In contractional conditions, the slip-tendency of the flat segment is moderate in the pre-folding stage and increases during limb rotation, to attain its maximum value when the forelimb dip of the Pag anticline is about 45°. Further progression of folding causes a decrease of the slip-tendency, up to the very low value of the present-day attitude (**Figure 4.3D**). The slip tendency of the ramp segment shows a comparable pathway, where values increase with increasing bedding dip, up to a maximum when the forelimb dip is about 35°. Further limb rotation causes a decrease of the slip-tendency, up to the very low value of the present-day attitude. In transpressional stress field conditions, the slip-tendency of the flat fault segment is moderate in pre-folding conditions and then decreases with progressing limb rotation, up to the very low value of the present-day attitude (**Figure 4.3E**). The ramp segment has an opposite pathway, with stable moderate slip tendency values in the pre- to early folding stages, which then increase with increasing limb rotation up to the present-day attitude.

4.5 DISCUSSION AND CONCLUSIONS

Detailed field mapping supported by UAV photogrammetry, structural analysis, and unfolding of the structural fabric, indicate that the Cretaceous Dinjiška Fault, in the External Dinarides of Croatia, was a NE-SW striking listric extensional fault zone, partially eroded in Upper Cretaceous-Paleocene times, then sealed by Eocene silicoclastic sediments, and eventually passively folded during the growth of the Pag anticline, in Late-Eocene times (**Figure 4.4**). Upper Jurassic evaporites (Korbar, 2009) may have provided the shallower contractional décollement layer during thrusting and folding, which is much deeper in the folded stratigraphy than the extensional décollement layer, located in Cretaceous carbonates. This explains why the DF, as well as all the other extensional fault zones exposed on the island of Pag, were folded rather than undergoing inversion.

The first-order geometry of the DF consists of a ramp and flat main segments, which underwent different structural evolutions during folding because of their different orientations with respect to the evolving tectonic stress field. In particular, the flat segment underwent fault-parallel contraction that, according to the results from the normalized slip tendency analysis, likely occurred in the early stages of fold growth, under a contractional stress field. On the other hand, the fault ramp segment underwent a more complex

strike-slip re-activation history that, based on results from the normalized slip tendency analysis, may have started during forelimb rotation and should have continued in the late stages of folding, during tightening of the anticline under transpressional stress field conditions. Such a complex kinematic pathway helps to explain also the displacement-distance pattern of this fault segment.

The presence of the N-S trending right-lateral strike-slip fault zone, almost collinear to the ramp of the DF, strongly suggests a genetic relationship between the two. The evidence that the former (*i*) cuts through folded strata, (*ii*) has a "simple" path in the displacement-distance diagram, and (*iii*) fits almost perfectly with Andersonian faulting in the normalized slip tendency analysis under transpressional stress field conditions (**Figure 4.3E**), strongly supports a late-folding origin. In this view, the ramp of the Dinjška Fault may have provided a weakness zone that, combined with possible stress concentration in the curved sector passing to the flat segment (e.g. Griffith, 1924; Reches and Lockner, 1994), may have triggered nucleation of the N-S trending right-lateral strike-slip fault zone at the DF ramp-flat transition in the late stages of folding, during final tightening preceding fold locking (**Figure 4.4C**). This inference is supported by the location of the maximum displacement of the N-S fault zone in the linkage zone with the Dijnska Fault.

The evolutionary pathway proposed for the DF applies to the many other folded fault zones exposed in the Pag anticline that, after unfolding, restore to a NE-SW striking, near-symmetrical depocenter (**Figure 4.1**). The ramp segments of such a shallowly-detached extensional fault network provided effective nucleation sites for strike-slip tear fault zones that propagated towards the anticlinal crest from both fold limbs, resulting in effective, widespread fold compartmentalization during late-stage tightening (**Figure 4.4**). Accordingly, the position and orientation of inherited fault ramps exerted a fundamental control on fold geometry and evolution. Despite we are not aware of similar structural patterns described in the literature, the evidence that transverse extensional faults are abundant both in extensional (e.g. Destro, 1995) and contractional (e.g. Tavani et al., 2015) settings makes us confident that folded listric faults triggering segmentation of thrust-related anticlines by tear faulting should be a frequent feature at the toe of thrust wedges and in foreland basin systems. A reason for their apparent rarity might be possible overlooking as "simple" conjugate strike-slip fault arrays. Moreover, correct recognition in subsurface geophysical datasets is hampered by technical difficulties to properly image inherited extensional fault flat segments in fold limbs.

A seminal lesson from the geology of the Pag anticline is the widespread occurrence along folded extensional fault damage zones, of metasomatically-altered bodies of dolomitized and de-dolomitized carbonates with

petrophysical properties strongly different from pristine rocks. Near parallelism between sedimentary and tectonic surfaces in fault flat segments, and the common metasomatic replacement of cataclastic rocks, contribute to associating dolomitization and/or de-dolomitization to sedimentary diagenetic processes, thus neglecting possible contributions or even the dominant role of tectonically driven, localized fluid flow along bedding-parallel fault damage zones.

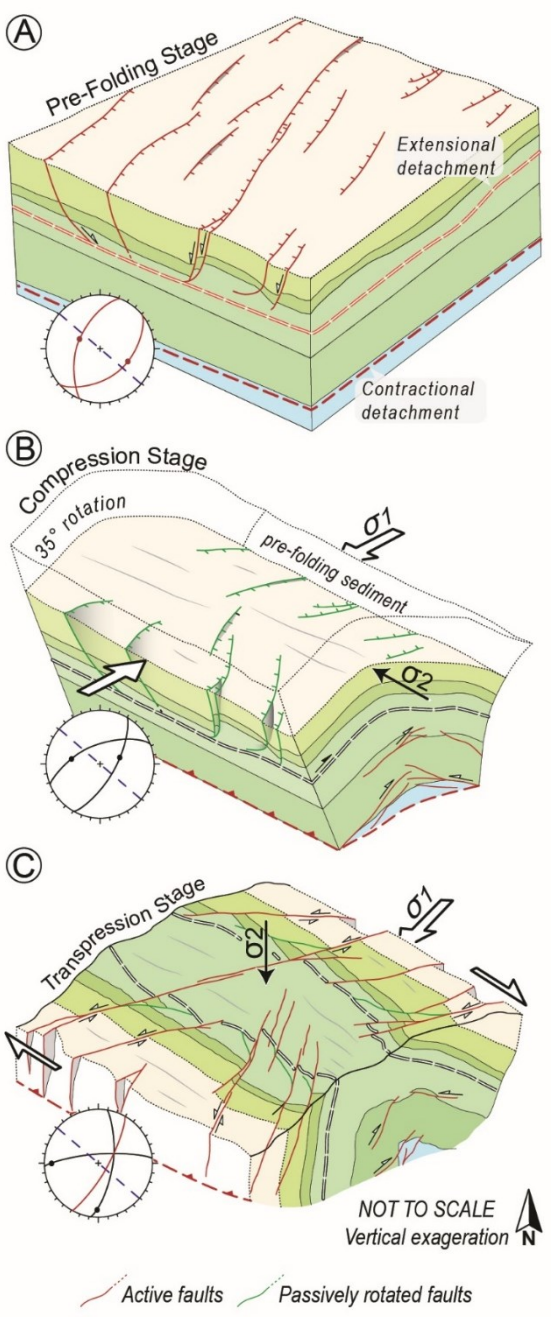

Figure 4.4 - Cartoon showing the proposed evolution models of passively folding faults and multiple-steps fold compartmentalization for the Pag anticline. Note how (continued from the previous page): inactive rotated faults (in green) promote strike-

slip fault formation striking in a not-common orientation respect to the fold axis. White-head arrows indicate active faults while black-head arrows indicate fault reactivations. Stereoplot graphically reported fault rotations during each step. Blue dotted line indicates axial trace, while block dots indicate slickenside on faults. Color code is the same of Figure 4.3. See text for details.

Significant volumes of such metasomatic carbonates and their economic impact as potential reservoirs suggest that specific attention should be deserved to better identify shallowly-detached, folded listric extensional fault zones in carbonates, both in the field, to improve our templates of structural diagenesis (Laubach et al., 2010), and in subsurface reflection seismic data, to exploit new plays in petroleum geology.

ACKNOWLEDGMENTS

Discussions with Fabrizio Balsamo, Alessio Lucca and Luigi Berio in the NEXT research group framework, are gratefully acknowledged. We are also indebted to Roberto Fantoni (Eni S.p.A.) for sharing his view on the tectonostratigraphic evolution of the External Dinarides. Technical support from Luca Barchi, Cristian Cavozzi, Andrea Comelli, and Enrico Selmo is gratefully acknowledged. Author's contribution: Fabrizio Storti and Andrea Succo ideated this study; Andrea Succo, Silvia Mittempergher and Fabrizio Storti collected most of the data and wrote the manuscript; Andrea Bistacchi developed and performed slip-tendency analysis and participated to some fieldwork, data discussion and tectonic interpretation and collect drone aerial ortophotograph; Marco Meda participated to some fieldwork and data discussion. We are grateful to Eni S.p.A. for funding this research and releasing the material for publication.

SUPPLEMENTARY MATERIALS

SECTION S4.1: *Drone aerial photo*

We built a high-resolution orthophotograph of the Dinjiška Fault from pictures collected with a DJI Mavic Pro drone. The 3D photogrammetric model was reconstructed with SFM (Structure From Motion) methodologies using Agisoft Photoscan ®. From the obtained point cloud, high-resolution meshes and orthophotos were extracted. The orthophoto has aground resolution of 10 cm, which was enough to recognize lithological boundaries and the main tectonic features. The acquired and interpreted data are provided in the plate: "**Attached 2 -** Inherited extensional fault drone orthophoto map**"**

In the following, we provide geographic coordinates for meso-structural field sites collected along the Dinjiška Fault (**Table ST4.1**)

TABLE ST1 - STRUCTURAL FIELD SITES

Fieldsite	Faults segments	Latitude (N°)	Longitude (E°)	Data number
SITE 1	Reactivated ramp	*44° 38' 88''*	*15° 13' 94''*	41
SITE 2	Reactivated ramp	*44° 38' 87''*	*15° 13' 90''*	37
SITE 3	Reactivated ramp	*44° 38' 86''*	*15° 13' 84''*	43
SITE 4	Reactivated ramp	*44° 38' 86''*	*15° 13' 85''*	53
SITE 5	Fault flat	*44° 38' 85''*	*15° 13' 83''*	32
SITE 6	Fault flat	*44° 38' 84''*	*15° 13' 81''*	45
SITE 7	Fault flat	*44° 38' 84''*	*15° 13' 81''*	67
SITE 8	NS strike-slip segment	*44° 38' 83''*	*15° 13' 83''*	56
SITE 9	NS strike-slip segment	*44° 38' 82''*	*15° 13' 83''*	45

Table ST4.1 - Compilation of field sites and their geographic position expressed in GCS_WGS_1984 coordinate system. The number of data for each field site is reported.

SECTION S4.2: *Fault related dolomitic and de-dolomitized fault-related bodies*

Figure S4.2 - Photographic chart of dolomitized and de-dolomitized bodies that occur on both sides of the Dinjiška Fault. (a) lens-shaped hectometric dolomitized body made of replacive grey dolomite sub-parallel to the bedding, preserved atop to the fault-ramp segment in the Cretaceous limestone of the Gornji Humac Fm. Photograph width is about 10m; (b) hectometric white plume of de-dolomitized limestone, dissected by right-lateral post-folding fault. Dolomite substitution entails a bleaching process, forming extremely recrystallized white to light-purple saccharoidal limestone. (d) detail of grey dolomite (D) affecting light-brown to purple wackestone bed. (d) detail of bleached re-cristallized limestone.

SECTION S4.3: *Fault-related deformation structures*

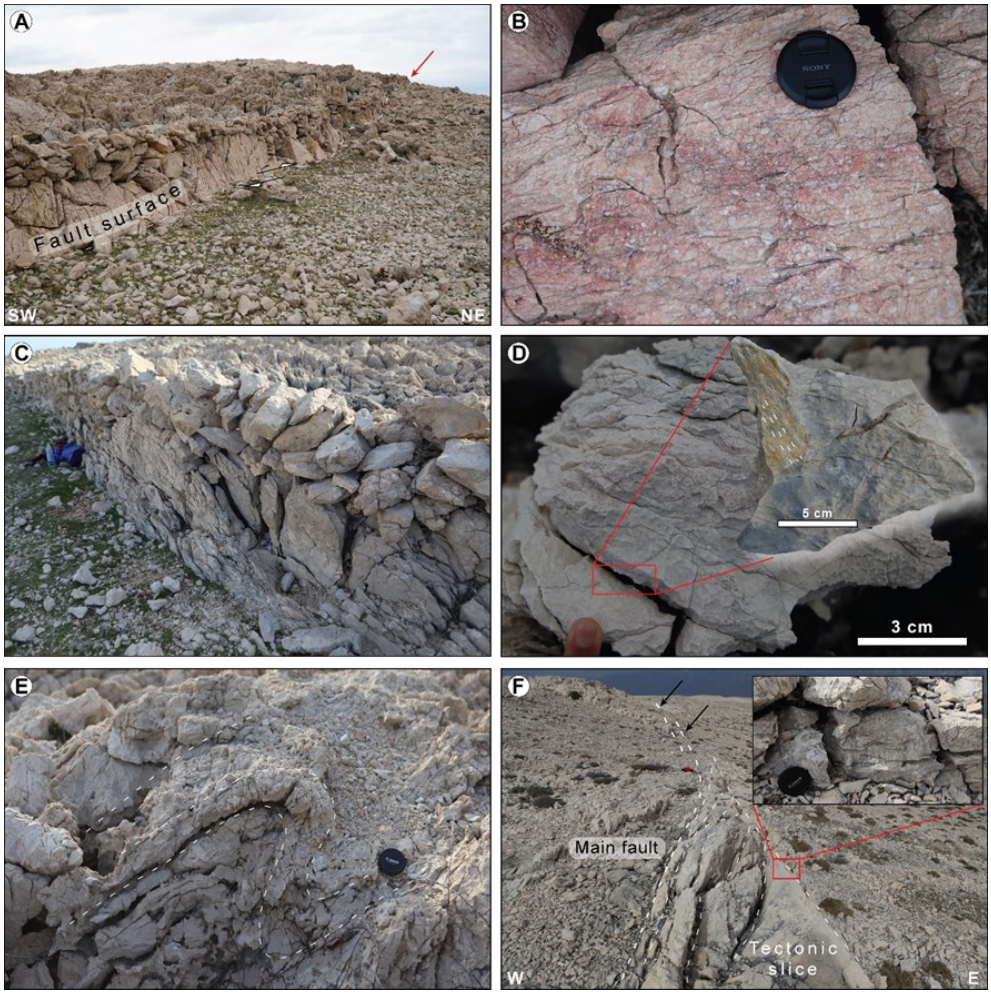

Figure S4.3. Photographic chart of some characteristical features of the Dinjiška Fault. (a) master slip surface in the ramp segment affecting the Gornji Formation. Fault surface forms a meter-high relief, due to highly-cemented fault rocks. Fault rocks in the ramp sector are red to yellow cataclastic to brecciated rocks. Fault-parallel tectonic stylolites form a pervasive fabric and crosscut high-angle NW-SE tectonic stylolites with associated minor veins. The penetrative fault-parallel stylolites affect fault core rocks (b) and fault damage zone, indicating stress concentration and buttressing against the fault zone; (b) details of cataclatics rock from the fault core in the ramp segment. Centimetric shear lenses formed by stylolitc array and shear plains in S-C type structures indicate right-lateral shear, are overprinted by another set of tectonics stylolite and associated veins, slightly parallel to the faults and by the pervasive fault-parallel stylolitc cleavage. Fault reactivation is here also indicated by strike-slip slickensides and striated calcite fibers along the master slip surfaces; (c) deformation in the flat segments. Deformation appears quite different from ramp reactivated segments. The NW-SE to NNW-SSE flat branch, with anastomosing to undulating trend and minor listric geometry, is characterized by a pervasive foliation arranged in S-C array giving a right-lateral (top-to-NW)

(*continued from the previous page*): transport direction (transtensive). Foliated breccia including rounded to elongated clasts in a micritic matrix is found along the fault surface, while cataclastic rocks cemented by calcite as those in the ramp segment are absent. The centimeter spaced cleavage of the fault core (d) is actually materialized by low-amplitude stylolites, which show minor dip-slip reverse component of reactivation, provided by striae and calcite-fibers on their surfaces (details in d); (e) example of soft-sediment deformation in hanging wall fault block. Together with a pluri-hectometric body of polymictic breccia and disrupted breccias only distributed along the fault surface, forms a tectono-sedimentary association that supports the shallow-depth activity of this inherited fault; (f) N-S right-lateral strike-slip fault, in the northern part of the Dinjiška Fault, forming the strike-slip folding-related segment. Fault architecture is characterized by multiple fault segments with overlapping bridges and restraining to releasing bands. Lens shaped tectonic slices, of highly-cemented fault rock characterize the plurimeter-thick fault core. Cataclastic rocks are preferentially concentrated along pluri-centimentric planes, and red o grey dilatation breccia delineates the master surfaces (red square details).

SECTION S4.4: *Paleostress inversion analysis*

Paleostress inversion techniques (Angelier, 1979; Etchecopar, 1984) allow to constrain the stress field causing slip on a fault plane by knowing fault-slip data parameters (fault plane orientation, slip direction and sense of movement). The inversion of these data allows the reconstruction of a reduced stress tensor. This tensor is defined by the orientation of the principal stress axes σ1, σ2 and σ3 (maximum, intermediate and least compression, respectively) and the Stress Ratio R = (σ2 - σ3)/ (σ1 - σ3). In this study, paleostress inversion was performed using the Win_Tensor program (see the detailed description of the Win_Tensor inversion approach in Delvaux and Sperner, 2003; Delvaux ,2011) on the basis of 315 structural elements including veins, tectonic stylolites, stylolite peaks and fault-slip data. These data were collected in 21 outcrops along the anticline and in correspondence of the major fault systems (**Table ST4.2**; **Figure S4.4**). Fold-related structural elements were collected in both limbs and crestal sectors and restored to their original position; because is out of the scope of this work, details fold kinematic evolution will be treated separately.

TABLE ST2 - SELECTED FIELD SITES FOR PALEOSTRESS ANALYSIS

Fieldsite	Dataset type	Latitude (N°)	Longitude (E°)	Data number
PG_A_001	Fold-related deformation pattern	44° 38' 88"	15° 13' 94"	18
PG_A_010	Fold-related deformation pattern	44° 38' 87"	15° 13' 90"	19
PG_M_002	Fold-related deformation pattern	44° 38' 86"	15° 13' 84"	24
PG_M_003	Fold-related deformation pattern	44° 38' 86"	15° 13' 85"	18
PG_H_005	Fold-related deformation pattern	44° 38' 85"	15° 13' 83"	16
PG_F_008	Fold-related deformation pattern	44° 38' 84"	15° 13' 81"	20
PG_E_011	Fault-related deformation pattern	44° 38' 84"	15° 13' 81"	22
PG_E_007	Fault-related deformation pattern	44° 38' 83"	15° 13' 83"	23
PG_E_020	Fault-related deformation pattern	44° 38' 82"	15° 13' 83"	15
PG_E_017	Fault-related deformation pattern	44° 38' 82"	15° 13' 83"	27
PG_C_003	Fold-related deformation pattern	44° 38' 82"	15° 13' 83"	20
PG_C_001	Fold-related deformation pattern	44° 38' 82"	15° 13' 82"	25
PG_C_004	Fold-related deformation pattern	44° 38' 82"	15° 13' 82"	26
PG_P_003	Fault-related deformation pattern	44° 38' 81"	15° 13' 82"	18
PG_P_004	Fault-related deformation pattern	44° 38' 81"	15° 13' 81"	21
PG_P_001	Fault-related deformation pattern	44° 38' 80"	15° 13' 81"	27
PG_I_002	Fault-related deformation pattern	44° 38' 79"	15° 13' 81"	22
PG_R_001	Fold-related deformation pattern	44° 38' 79"	15° 13' 81"	19
PG_R_004	Fault-related deformation pattern	44° 38' 79"	15° 13' 80"	21
PG_N_004	Fault-related deformation pattern	44° 38' 79"	15° 13' 77"	20
PG_B_001	Fault-related deformation pattern	44° 38' 79"	15° 13' 80"	27

Table ST4.2. Compilation of field sites and their geographic position expressed in GCS_WGS_1984 coordinate system. The number of data for each field site is reported.

For each field site stress inversion was applied, associating deformation elements, their geometry with the tectonic stages (Fig. S4). The paleostress inversion procedure was implemented on a merged dataset for the two tectonic stages (**Figures S4.5, S4.6**). In fact, fault-slip data from several outcrops evenly distributed over large areas can potentially be merged into a single dataset to reconstruct regional paleostress fields (Gushtenko, 1979; Saintot et al., 2011). However, it is worth to note that the use of merged datasets is reliable only if the stress field can be considered homogeneous at the scale of the study area. For this reason, we merged fold-related elements and fault-slip data that are ascribable to clearly internally coherent sectors of the analyzed fault zones.

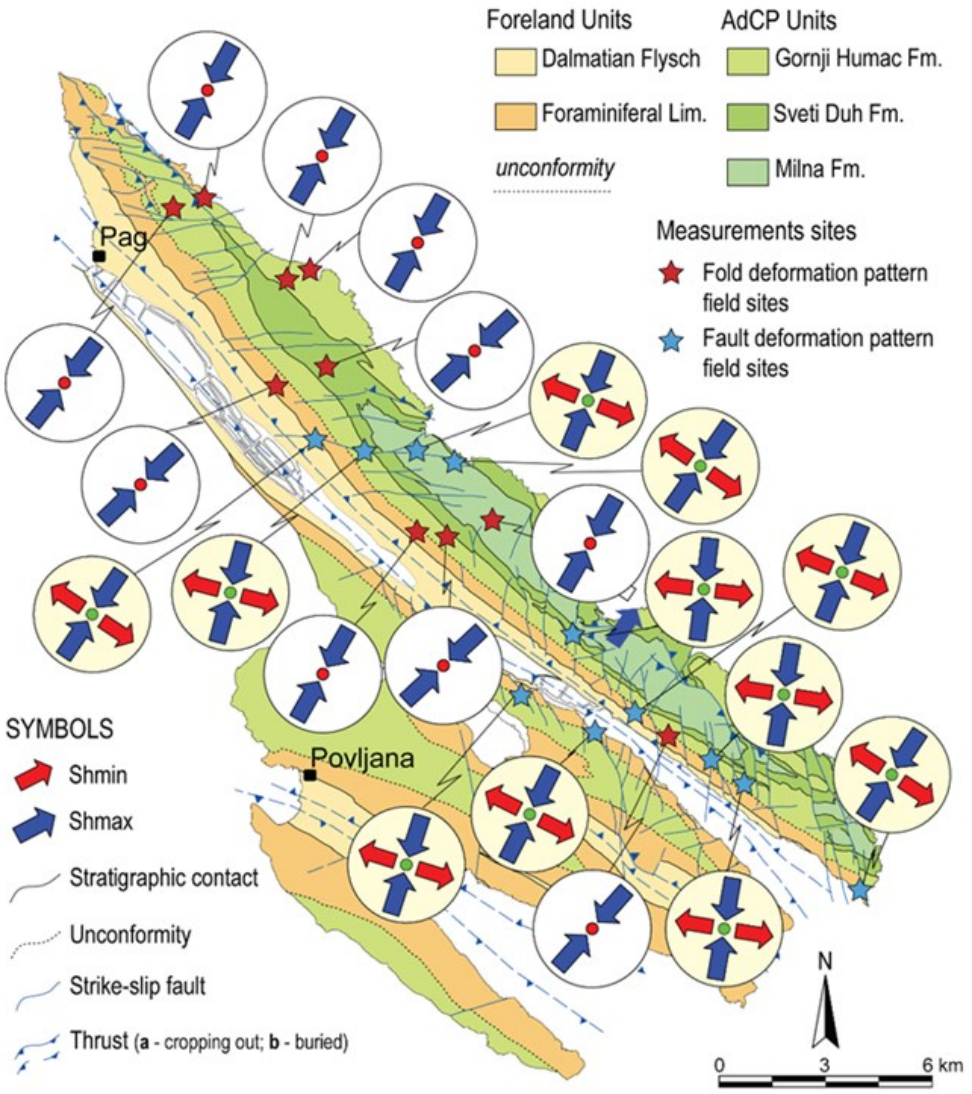

Figure S4.4 - Structural map showing the orientation of the reduced stress tensor and tectonic regime for each locality listed in Table ST2. Based on the field intersection relations, structural data were separated into fold-related and strike-slip related and processed separately. White circles indicate results of the inversion of fold related structures, pale yellow circles those of fault-related structures.

In the case of Pag anticline, we separated (*i*) fold-related elements in Cretaceous and Eocene units (i.e., bed-parallel veins, bed-perpendicular axial-parallel tectonic stylolites, conjugate thrust and backthrust and related deformation elements; **Figure S4.5**) form (*ii*) fault zones deformation patterns (i.e., fault-slip data) in sites structurally located in the fault zone hanging wall and footwall of the major N-S and E-W trending faults (**Figure S4.6**). Consistently, fault-slip data collected in the Cretaceous carbonate rocks were inverted by a fault-by-fault approach and merged together.

Stress inversion results are summarized in **Figures S4.5** and **S4.6**, where similarly oriented reduced stress tensors were associated with the same

deformation event, also accounting for geometric, mechanic and chronologic criteria derived from field observations. Its noteworthy to emphasize that, despite the small angular shift between compression and transpression σ1 stages (about 10°, compare **Figures S4.5**, **S4.6**), we need to take into account the Miocene rotation of the External Dinarides domain. In fact, considering paleomagnetic data, many authors (De Leeuw et al., 2012; Marton et al., 2003; Marton and Moro, 2009) pointed out a counterclockwise rotation of about 20° occurred in the Pag and Northern Dalmatia sectors, which should be added to the obtained relative stress field orientation. In addition, our results were evaluated against the available independent geological and chronological constraints on the deformation history of the External Dinarides. Paleostress results and stress field orientation agreement with what proposed by Van Unen et al. (2019), obtained in the southern Dalmatia sectors.

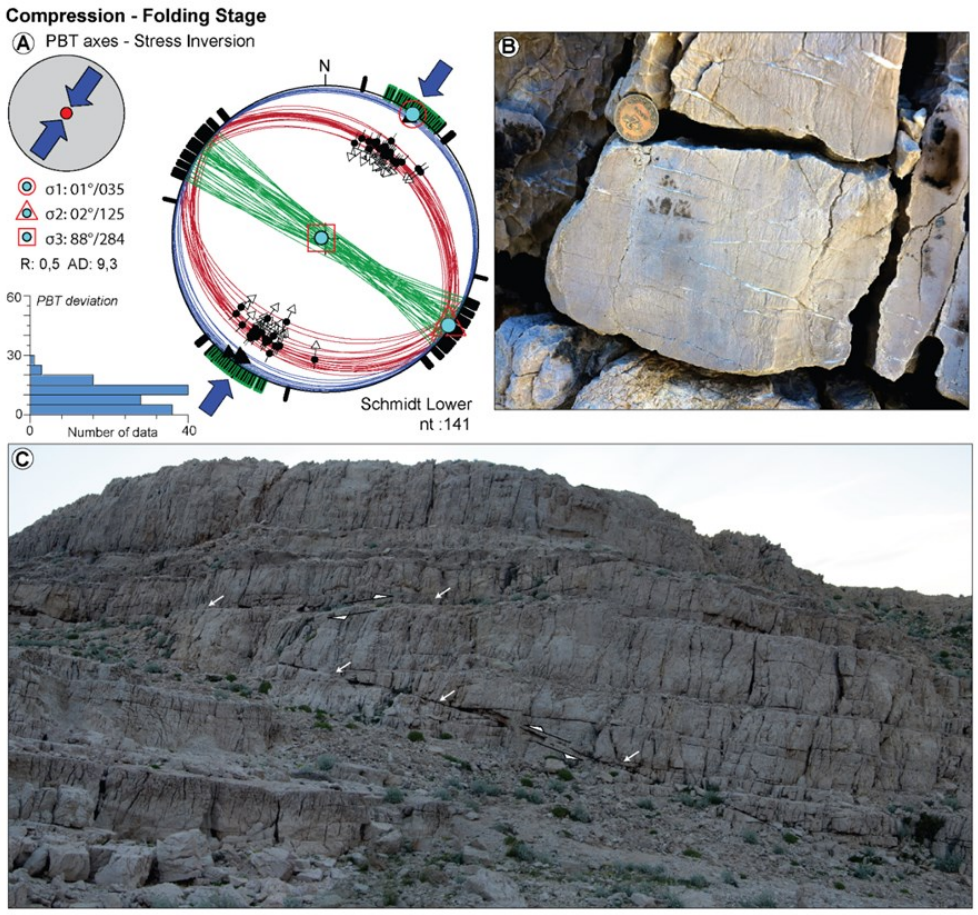

Figure S4.5 - (a) PBT axes methods and stress tensor reconstruction for folding tectonic stage. Stress tensor axes indicate a pure compression, with stress ratio R=0.5. Maximum stress axis (σ1) is oriented NE-SW with vertical σ3. Green great circles are tectonic stylolites, blue great circles veins and red is for thrust faults. Black triangles are for stylolite peaks. Some data are restored to the horizontal beds;

(*continued from the previous page*): (b) example of layer-perpendicular axial-parallel tectonic stylolites with associated layer-parallel veins formed in the early stage of compression. Closely associated with conjugate thrust pair, widespread outcropping in the flat crest (c) and in the fold limbs.

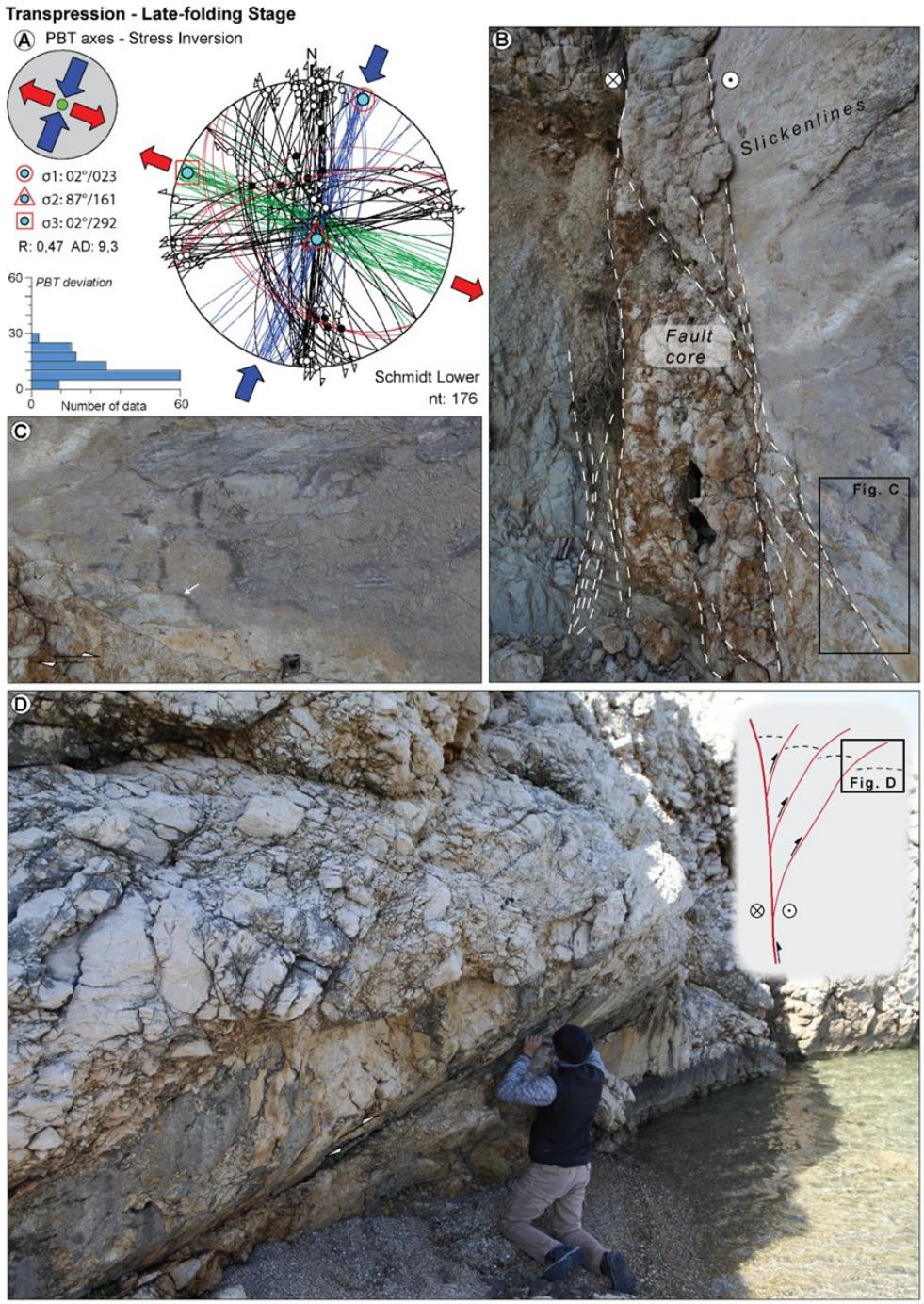

Figure S4.6 - (a) PBT axis methods, implemented on 176 faults, and obtained stress tensor for reconstructing the second tectonic stage. Stress tensor orientation indicates a NNW-SSE right-lateral transpression, with maximum stress axis (σ1) oriented (*continued from the previous page*): 23/02° and vertical σ2. Green great circles are

tectonic stylolites, blue great circle veins and black is for strike-slip faults with their respective slip-data (with dots and arrows). Red circle is for reverse faults; (b) example of fault core and well preserved striated fault slip surfaces (on the right) affect Formaminiferal Limestone (on the right) and marls (on the left) from the basal part of the Dalmatian flysch, formed by anastomosing shear surfaces. Photo width is about 1 m; (c) details of the mirror-like slip-surface, with striae, grooves and dark to white calcite-fibers, suggesting a right-lateral shearing; (c) example of low- to medium-angle reverse fault, associated to a positive right-lateral strike-slip flower, affecting the lower part of the foraminiferal limestone. Rocks were deformed by intense brecciation and a mirror-like slip-surfaces occur.

CHAPTER 5.

THE PAG ANTICLINE

This chapter is presented in the form of a manuscript that is currently been prepared for submission to *Tectonics*. It describes the structural architecture and kinematic evolution of the Pag thrust-related anticline, developed at the front of the External Dinarides thrust wedge (High Karst of Croatia). This case study includes (i) structural characterization of the anticline, (ii) multi-steps kinematic evolution in compression and transpression, and (iii) paleofluid evolution during syn- and post-tectonic folding.

ARTICLE IN PREPARATION

Structural inheritance, transpressional folding, and paleofluid evolution at the toe of the Dinaride orogenic belt: the Pag anticline, Croatia

Succo, A., Mittempergher, Lucca, A., Bistacchi, A., Meda, M., Storti, F.

Article in preparation for submission to *Tectonics*
Research activities in the Pag anticline were founded by ENI Spa and results are covered by a confidentiality agreement. Consequently, the manuscript in its present form is currently been reviewed by the Company and will be submitted to *Tectonics* upon approval

STRUCTURAL INHERITANCE, TRANSPRESSIONAL FOLDING, AND PALEOFLUID EVOLUTION AT THE TOE OF THE DINARIDE OROGENIC BELT: THE PAG ANTICLINE, CROATIA

Succo A.*[1], Mittempergher S.[2], Lucca A.[1], Bistacchi A.[2], Meda M.[3] and Storti F. [1]

1. NEXT, Natural and Experimental Tectonic Research Group, Department of Chemistry, Life Sciences and Environmental Sustainability, University of Parma, Parco area delle Scienze 11/a, 43124 Parma, Italy.

2. Department of Environmental and Earth Sciences, Università degli Studi di Milano Bicocca, Piazza della Scienza 4, 20126 Milano, Italy.

3. ENI Spa, Upstream and Technical Services – San Donato Milanese – Italy.

ABSTRACT

Understanding fold evolution at the toe of transpressional orogens bears important academic and economical implications. The Pag anticline, in the outer arc of the External Dinarides thrust-wedge, is located in the footwall of the major Velebit transpressional fault system. Accordingly, it provides a very appropriate field site for studying transpressional folding. We performed a structural and petrographical-geochemical study of the fold-related deformation pattern and faults zones associated with the development of this anticline. Our data show a complex non-cylindrical fold architecture and deformation pattern, both in space and time, characterized by the occurrence of intense faulting during folding and fold tightening, with the unusual occurrence of two sets of N-S right-lateral and E-W left-lateral strike-slip fault zones, respectively, which trend oblique to the NW-SE fold axial strike. Unfolding and stratigraphic evidence support interpretation of these strike-slip fault sets as derived from folding Late Cretaceous extensional faults detached at very shallow depth. Despite structural complexity and highly along-strike variability, folding-related deformation far from fault damage zones, shows a quite classical pattern, with bed-parallel veins preceding cross-folding veins and associated pressure-solution cleavage. This indicates a switch between minimum and intermediate stress axes during early-folding stages, when the maximum compressional axis trend was NE-SW. Re-opening of previously-formed deformation structures suggests axial bulging and along-axis dilation during late-stage folding and fold-tightening, when the maximum compressional axis trend was NNE-SSW. Field and geochemical data support the

fundamental role of inherited meteoric fluids, locally migrating during the initial stage of folding, and indicate intense fluid circulation along strike-slip fault zones, acting as conduct during fold-compartmentalization. We propose a kinematic evolutionary model for the Pag anticline, involving detachment along late-Jurassic evaporites layer, complex fault-fold interactions, initially partitioned transpression and consequent orthogonal folding, followed by transpressional tightening.

5.1 INTRODUCTION

Fold structural evolution and kinematics in shallow thrust-fold belts is driven by multiple factors, including the intimate interplay with underlying faults (e.g., Suppe, 1983; Tavani et al., 2006), the mechanical stratigraphy of the folded multilayer (Corbett et al., 1987; Gross, 1993; Fischer & Jackson, 1999; Wennberg et al., 2006; Lacombe, 2010), and the ratio between tectonic uplift and foreland syntectonic sedimentation rates (Storti & Salvini, 1996). In the frontal part of thrust-wedges, fold development may also involve further complexity provided by local variations of the geological and/or regional conditions (Macedo & Marshak, 1996), including the presence of inherited, pre- or syn-orogenic fault zones (e.g. Storti et al., 2018). Moreover, in orogenic salients, progressive forelandward migration of the deformation front and the arcuate shape are typically achieved by non-cylindrical deformations and partitioning between dip-slip and strike-slip faulting (Marshak, 1988; Tavani et al., 2015).

In case of transpressional folding of sedimentary successions involving structural inheritance, folding-related deformation patterns may significantly differ from classical distributions of deformation structures classically described in cylindrical thrust-related folds (Stearns, 1968; Cooper, 1992; Storti & Salvini, 1996; Lacombe et al., 2012; Tavani et al., 2006, 2008, 2015). In such cases, a better understanding of folding-related deformation patterns and their driving factors bears academic, economic, and societal implications. Accordingly, the availability of robust datasets from appropriate field analogues is certainly beneficial for better understanding transpressional fault-fold kinematics, reduce economical risks in hydrocarbon exploration, improve groundwater management, and mitigate seismic hazard.

Here we provide accurate descriptions of fold architecture, fault-fold interplay, and folding-related deformation structures exposed in the Pag anticline, in the northwestern sectors of the External Dinarides of Croatia. Moreover, microstructural, petrological, and isotopical characterization of vein networks provide useful constraints to their relative chronology of deformation structures and fold kinematic evolution. By such a

multidisciplinary approach including field and laboratory data, an evolutionary model is proposed for the Pag anticline, where layer-parallel shortening, early fold amplification, and strike-slip fold compartmentalization during fold tightening, contribute to the growth of this complex fault-fold structure.

5.2 GEOLOGICAL OUTLINE

The Pag anticline is located at the northwestern sector of the High Karst unit (i.e., External Dinarides, *sensu* Korbar, 2009), in the footwall of the southwestward-vergent deformation front of the Dinaric orogeny (**Figure 5.1**).

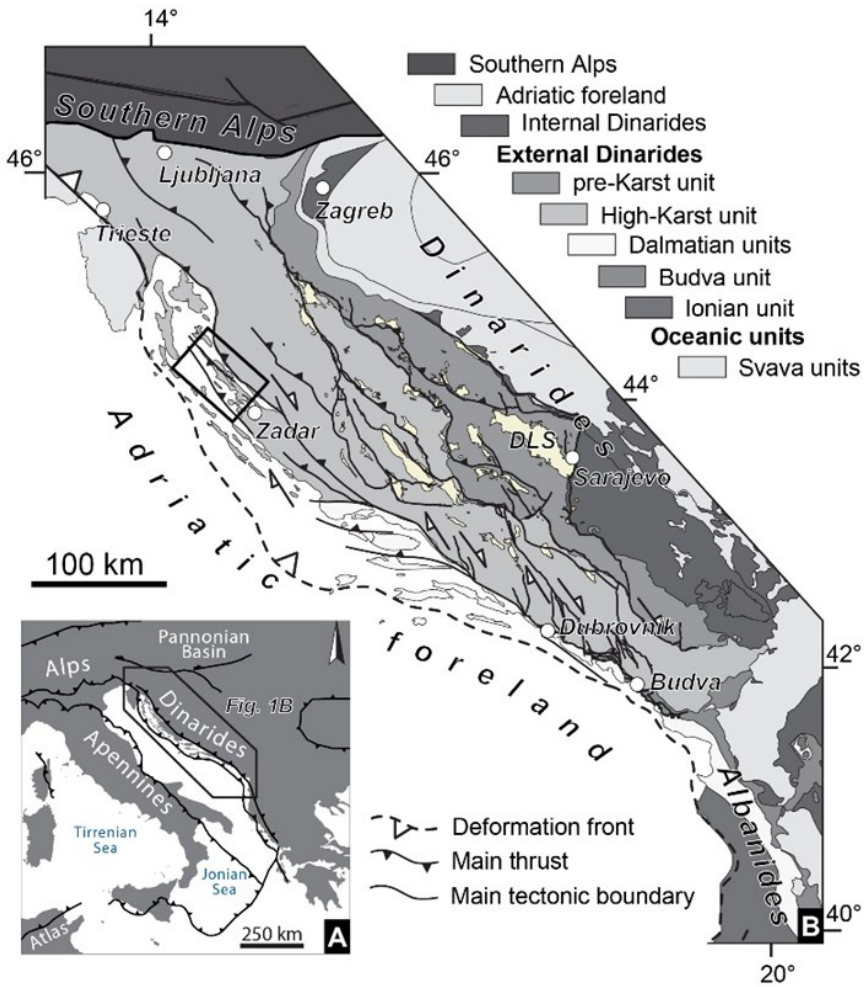

Figure 5.1 – (a) Location map in the Mediterranean geodynamic context; (b) Tectonic map of the external part of the Dinarides and Albanides (modified from Schmid et al., 2008, 2011; Vlahović et al., 2005; Korbar, 2009). Major thrust and strike-slip faults pattern is overlaid. DLS: Miocene age extensional basin of the Dinaric Lake System (after Mandic et al., 2012). The black rectangle indicates the location of the study area.

The stratigraphic succession in the High Karst nappes includes Permo-Triassic evaporites, carbonates, and volcanic rocks, sitting on a Paleozoic metamorphic basement and overlain by Mesozoic and Cenozoic platform carbonates with subordinate intra-platform basinal sediments (i.e., Budva unit, **Figure 5.1**). The Cenozoic succession includes Paleocene carbonates and Eocene to Miocene mixed carbonate-siliciclastic flysch (i.e., Dalmatian Flysch; Babić et a., 2008), overlain by Oligocene-Miocene conglomerates (i.e., Promina Beds, *sensu* Vlahović et al., 2005) (**Figure 5.2**). The presence of an Upper-Jurassic to Lower-Cretaceous evaporite layer has been suggested in the area of northern Dalamatia, Ravini-Kotari unit and Pag island (Tari-Kovačić and Mrinje, 1994; Korbar, 2009) and may support the inference that the basal thrust of the Pag and Ravini-Kotari units is localized within these low-friction rocks (Korbar, 2009).

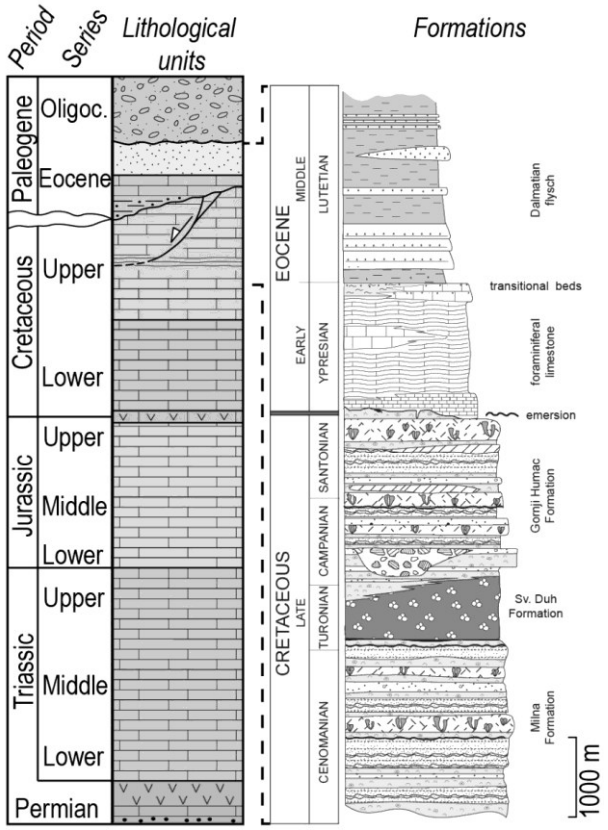

Figure 5.2 – Stratigraphic column of the High-Karst unit and detail of the Upper Cretaceous and Paleogene succession exposed in the Pag anticline. Modified from Mittempergher et al. (2019) and Van Unen et al. (2019).

The Pag island exposes an about 25 km long, 5 km wide anticline (**Figure 5.3**) where the Upper Cretaceous rudist-bearing platform carbonates (Cenomanian to Senonian), and in particular the lithostratigraphic units of Milna Formation (Cenomanian), Sveti-Duh Formation (Cenomanian-

Turonian) and Gornji Humac Formation (Senonian) of the Adriatic Carbonate Platform (AdCP, Vlahović et al., 2012) are exposed (**Figures 5.2, 5.3**). The former mainly consists of a supratidal facies-dominates sequence, with stromatolite-rich beds, paleosoils and hard-ground surfaces. It overlies the intrashelf external carbonate ramp deposits of the Sveti Duh Formation, recording a regional drowning event (**Figure 5.4**; Korbar et al., 2012) and providing a useful key layer for stratigraphic correlations. The Gornji Humac Formation mainly consists of rudist-bearing platform carbonates, with wackestone and mudstone facies interlayered with rudist debris forming storm beds and tidal sandwaves (**Figure 5.4**). Its top is characterized by an erosional surface with evidence for karst dissolution, karst red-beds and, locally, bauxite deposits (**Figure 5.4**). Evidence for strong erosion during uplift is widespread along the High Karst and Dalmatia units, which produced a regional stratigraphic gap lasted from Coniacian-Santonian to Ypresian times (Jelaska et al., 1994; Korbar, 2009; Mittempergher et al., 2019; **Figure 5.2**). Sedimentation resumed with the depositions of the foraminiferal limestone ramp-carbonates, passing upward to hemipelagic pelites and the predominantly shallow marine clastic succession of the Dalmatian Flysch (Lutetian-Bartonian; Persico et al., 2019). The youngest sediments exposed in the Pag Island are the Early Miocene freshwater lacustrine deposits, which lay unconformably on the folded substrate and dip at about 20° to the North, testifying for post-Miocene tectonic deformation in the area (Bulić & Jurišić-Polšak, 2009).

The Pag anticline belongs to the Ravni Kotari tectonic unit of the External Dinarides (Mamužić & Sokač, 1973), deformed in an array of en-échelon folds with Dinaric (NW-SE) strike and crosscut by late- to post-folding strike-slip faults. The geological structure of the Pag island is characterized by the occurrence of a major NW-trending anticline, extending for almost 30 km along axis to the east and south-east of the Pag village (Pag anticline hereafter), and three smaller anticlines to the south-west, in the surroundings of the Povljiana village (**Figure 5.3**).

5.3 STRUCTURAL DATA

The hinge line of the Pag anticline strikes almost NW-SE (N300°), with axial plunging of about 5°-10° to the NW, except for some local variations (**Figures 5.3, 5.5**). The exposed cross-sectional fold shape is a very tight and markedly asymmetrical anticline, with important along-strike

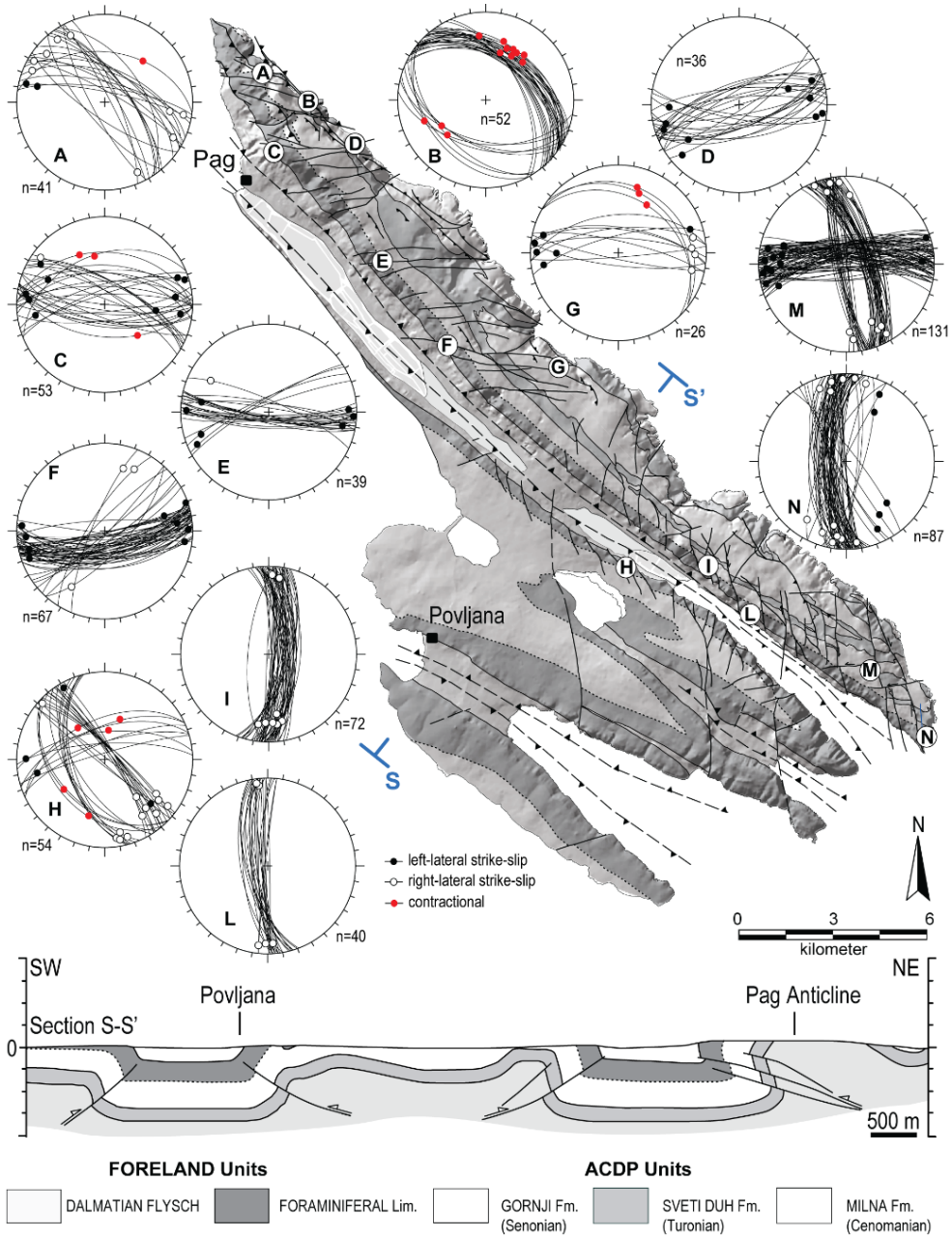

Figure 5.3 – Structural map of the Pag anticline showing the network of major fault zones mapped (modified from Mittempergher et al., 2019), and stereographic projections of fault data collected in the field localities A to N. The tip points of cross-section S-S' are indicated. In all figures, stereographic projections of planar surfaces are on the Wulff equal area net, lower hemisphere.

geometrical variations. In detail, the fold shows an asymmetrical close "box-type" geometry, with a large crestal zone and steeply dipping to overturned limbs (section in **Figure 5.3**). Fold kink-like hinges at the crest-limb transition show peculiar deformation structures, which depend on structural and stratigraphic positions. Their geometry and structural

architecture dramatically vary along the fold strike. Two axial surfaces, striking N293° and dipping about 40° to the NE, and N127° dipping 32°to the SW, respectively, were identified (**Figure 5.5**).

Figure 5.4 – Field pictures of the upper Cretaceous stratigraphic units exposed in Pag anticline. (a) Panoramic view of the medium part of the Gornji Humac Formation in the northern part of the anticline. Meter-thick beds of white mudstone-wackestone alternated with minor light brown packestone beds; (b) Brown-yellowich biolclastic wackestone of the Gornji Humac Formation exposed in the backlimb of the fold; (c) Panoramic view of the sharp contact of the Sveti

(*continued from the previous page*): Duh Formation and the underlying Milna Formation; (d) Detail of an intertidal sequence with laminated limestone in a stromatolite-rich interval of the Milna Formation; (E) Top of the Gornji Humac Formation with a detail of the infilling of karst cavities along the erosional surface that separate upper Cretaceous carbonate from lower Eocene carbonates. Karst features occur in a pluri-hectometric interval of the upper part of the Gornji formation, with metric and decametric cavities and neptunian dikes filled by red or brownish mixed carbonatic-siliciclastic sediments and calcite druse.

A characteristic structural feature of the anticline is the presence of linked N-S and E-W right- and left-lateral strike-slip faults, respectively (**Figures 5.3, 5.5**). The latter are concentrated in northern sectors of the fold, where a peculiar asymmetry toward NE occurs, while the former mainly developed in the southern part of the anticline.

These high-angle strike-slip fault zones have an oblique trend with respect to the fold strike (**Figure 5.3, 5.5**) and opposite kinematics. Moreover, most of them are localized along limbs and crest-limb transition zones, producing major offsets of about 100-150m that typically decrease to vanish toward the fold axes. As a whole, according to the along-strike variability of the limb dip in adjacent fault-compartmentalized blocks, the fault network creates general right-lateral block-rotation and tearing accommodating differential limb rotation. Moreover, the presence of inherited fault zones oriented NNW-SSE to N-S and ENE-SSW (Mittempergher et al., 2019) increases the structural complexity of the fault network.

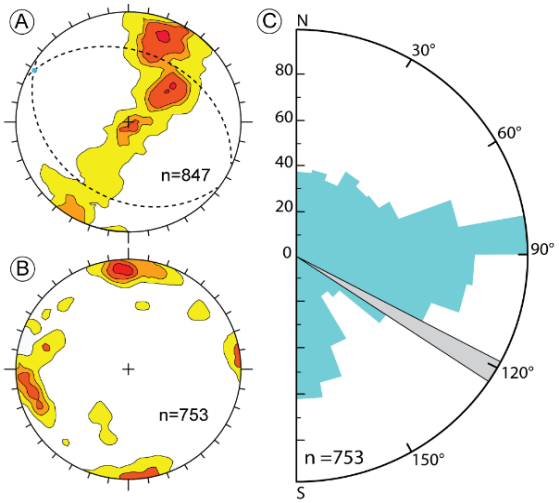

Figure 5.5 – (a) Stereographic projection of contoured poles to bedding planes collected along the Pag anticline. The light-blue dot indicates the fold axis, while dotted ciclographic circles provide the geometry of the two axial planes; (b) Contoured poles of fault data collected at several field localities along the Pag anticline, which show prevalent N-S and E-W strikes; (c) Rose diagram of the

(*continued from the previous page*): strikes of main faults traced within the study area. The strike of the average fold axis is reported in grey. Stereographic projections on the Schmidt equal area net, lower hemisphere, contouring at 4% intervals.

5.3.1 *Fold cross-section*

Seismic line interpretation (Miljus, 1971) indicates a series of open SW-vergent thrust-ramp anticlines flatting down in the Jurassic and Triassic units at about 5 km depth, up to the Velebit mountains, which constitute the backstop of the fold train. The presence of an Upper Jurassic-Lower Cretaceous evaporite layer is suggested by Tari-Kovačić and Mrinje (1994). The authors proposed interpretation of a seismic line located about 10 km southward of the Pag anticline, in which a series of SW-vergent duplexes detached in the upper Jurassic rocks. Evaporites are reported in the Northern Dalmatia subsurface (Durasek et al., 1981; Korbar, 2009) which show stratigraphic and sulfur isotope signatures typical of an Upper Permian-Middle Triassic age (Korbar, 2009), and constitute the regional detachment horizon. The presence of the aforementioned Upper Jurassic–Lower Cretaceous evaporites in the area of the Pag anticline, (i.e., Evaporite Complex of Tari-Kovačić and Mrinje, 1994), with a variable stratigraphic thickness ranging from 200 m to 1000 m, could explain the along strike differences in the tectonic style and major fold pattern observed in the region, which could be mostly related to the pre-orogenic distribution and stratigraphic position and thickness of the weakest evaporite horizons (Korbar, 2009).

We propose a NE-SW trending cross-section through the Pag, Povljana, and Vis anticlines (**Figure 5.6**), to investigate on the detachment depth and the role of the Evaporite Complex (*sensu* Tari-Kovačić and Mrinje, 1994) on the tectonic style of the Pag anticline. Cross-section construction was carried out in the MOVE software (Midland Valley Exploration, Scotland), combining information from geological map and stratigraphic sections analysis (Majcen et al., 1976; Mamužić and Sokač, 1973; Sokač et al., 1976).

The deformation style is characterized by detachement folds, which evolved into thrusted tight folds in their cores (Pag anticline, **Figure 5.6**). Fold shape is almost constant in terms of wavelength, with double-asymmetry and vergence. The upper Cenozoic sequence has a quite constant thickness through the section. Differently, post-Senonian units, which are composed of sediments related to the foreland basin stage, display major lateral thickness variations (**Figure 5.6**). Late-Eocene–Oligocene syntectonic deposits show thickness increasing toward SW.

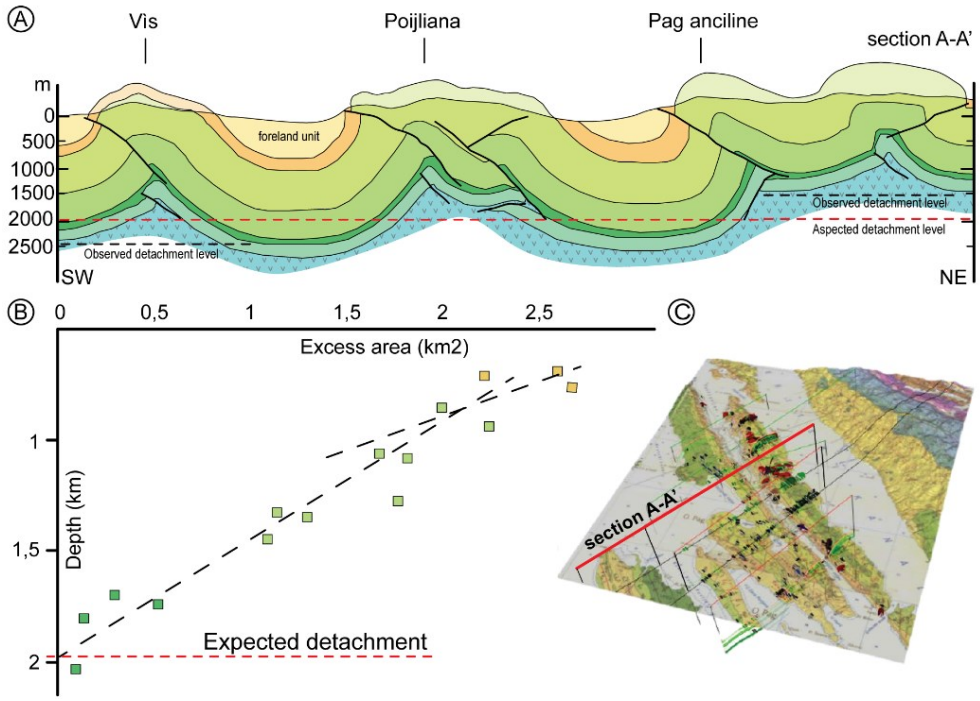

Figure 5.6 – (a) Cross-section of the through the Pag, Poijliana, and Vis anticlines. Color for units is in agreements with Majcen et al., 1976, and stratigraphic thicknesses are from Mamužić and Sokač, 1973; Mittempergher et al., 2019; Sokač et al., 1976; Korbar, 2009 and Tari-Kovačić and Mrinje, 1994; (b) Excess area – depth plot diagram, showing the ubication of the expected detachment at 2 km depth; (c) section location on a 3D DEM surface overlain by geological map at 100.000 scale and field data (in black).

To obtain constraints on the depth-to-detachment, we applied the excess area method proposed by Epard and Groshong (1993). The slope of the regression line in the plot of the excess area in cross-section versus the depth of the reference layer for several stratigraphic horizons intercepts the depth axis at the detachment depth, where the excess area is equal to zero. The calculated detachment depth is at about 2 km, not far from what obtained from our cross-section reconstruction based on geological and stratigraphic data (**Figure 5.6**). In the north-eastern part of the section the décollement layer minimum depth is about 500 m shallower than what expected from depth-to-detachment calculations. On the other hand, in the south-western segment of the section, the detachment is inferred to be deeper of about 400m with respect to what expected from depth-to-detachment calculations.

5.3.2 *Fold structural architecture and deformation structures*

Despite its apparent simple geometry at a first sight, the Pag anticline revels a very articulate and composite fold architecture, where the deformation style changes progressively along strike as a function of structural and stratigraphic position. In the north-western sector of the Pag anticline, a km-long periclinal termination (**Figures 5.3, 5.7**) is exposed and characterized by a progressive rotation of bedding up to strike perpendicular to the fold axis. To reconstruct the fold architecture, detailed fieldwork and analysis of serial cross-sections have been performed. Fold geometry changes and first-order deformation structures are synthesized in the 3D-block diagram of **Figure 5.7**.

The fold forelimb is very continuous along strike, and its characterized by bed dipping 60°-70° to the SW in the northern sector of the island, passing gradually to vertical and overturned beds towards the southern sectors. In the central sector of the anticline, the presence of a blind forethrust (**Figures 5.3, 5.7**) controls forelimb geometry with high-angle to overturned strata. In contrast, the backlimb shows a higher structural variability (**Figures 5.3, 5.7**).

The occurrence of a major forethrust is also suggested by outcropping subsidiary low-angle reverse fault splays, well exposed in the central sectors for about 2-3 km, which crosscut the vertical forelimb in the Foraminiferal limestone with metric displacement (**Figure 5.8**). Calcite slickenfibers and S-C cleavage are locally present along the thrust planes. In the central sector, the transition from the forelimb to the crestal plateau is marked by a series of sharp dip-domains. The major one is located in the Sveti Duh Formation, which is highly-deformed by small scale thrusting. Locally, also calcite-cemented dilatation breccias occur. The hinge line sector, well exposed in the Milna Formation, is characterized by a complex interplay of pluri-hectometric, asymmetric to symmetric folds and thrust faults (**Figure 5.9**). Due to the fold axis dip of about 10° toward the NE, a gradual bedding rotation to strike sub-perpendicular to the fold trend is observed. Here (see also **Figures 5.3, 5.7** for locations), multiple symmetric close to open folds deform the Milna multilayer, with associated minor out-of-sequence thrusts typically located in organic matter-rich or paleosoil layers (**Figure 5.9**). In this area, a well-exposed section of the deeper part of the anticline crops out, revealing the presence of a recumbent fault-propagation fold associated with disharmonic folding and a NE-verging, low-displacement passive-roof thrust (**Figure 5.10**, see also **Figure 5.7** for location). In the Milna Formation, deformation structures are partitioned between white mudstone layers, which tend to develop cataclastic breccias, and the more coherent brownish laminated-wackestone beds, which deform by pressure solution

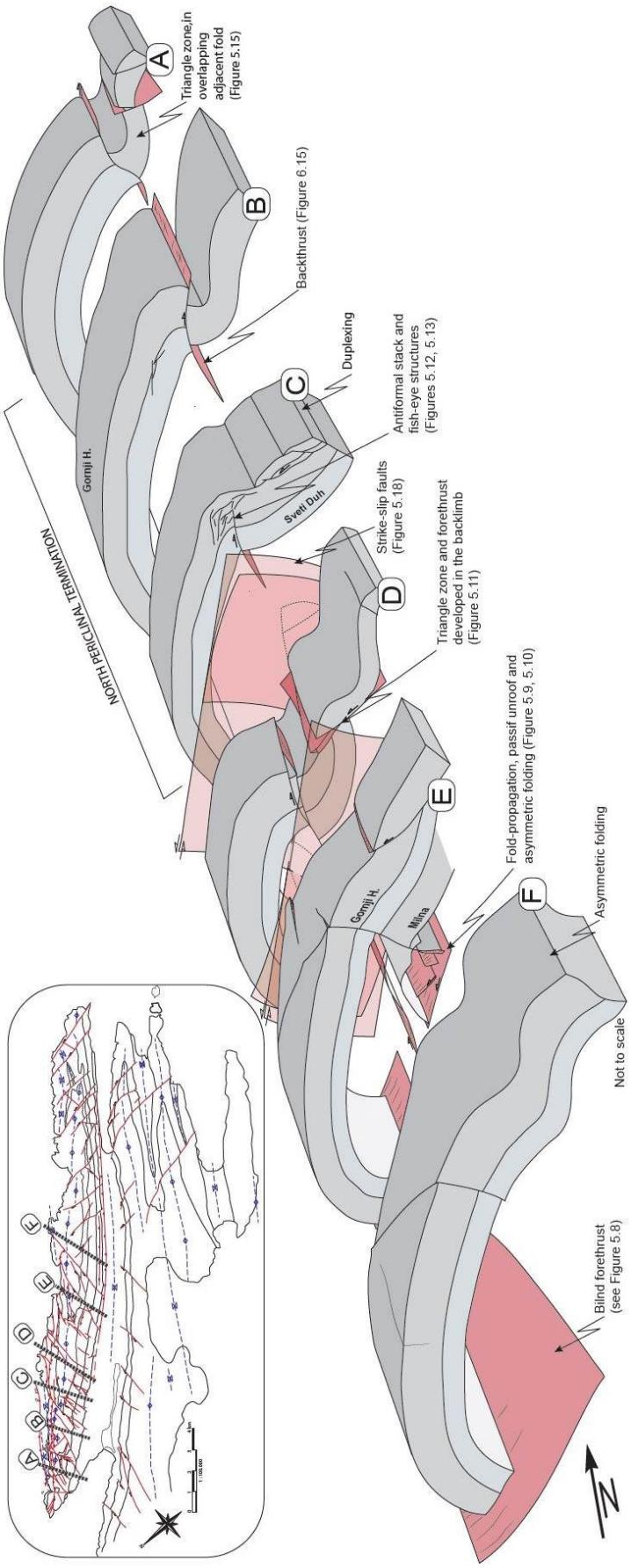
A
Triangle zone,in overlapping adjacent fold (Figure 5.15)
B
Backthrust (Figure 6.15)
C
Duplexing
Antiformal stack and fish-eye structures (Figures 5.12, 5.13)
Swell Dun
Strike-slip faults (Figure 5.18)
D
Triangle zone and forethrust developed in the backlimb (Figure 5.11)
E
Fold-propagation, passif unroof and asymmetric folding (Figure 5.9, 5.10)
Gomji H.
Milha
F
Asymmetric folding
Not to scale
Blind forethrust (see Figure 5.8)
N
NORTH PERICLINAL TERMINATION
Gomji H.
A
B
C
D
E
E
F

Figure 5.7 – (*from previous page*) Cartoon showing the along strike-variability, fold geometry changes, and the transition from a backthrust-dominated to forethrust dominated fold geometry. Section blocks A, B and C are in the periclinal fold sectors, while D, E, and F in the central north-eastern part of the anticline. Relative section position id provided in the black box. Ubication of figures 5.8, 5.9, 5.10, 5.12, 5.15 and 5.15 is provided. See the text for details on the relative sections.

cleavage and minor veining. Bedding dips toward north, with an axial plunge of about 10°. Meso-scale deformation structures consist mostly of tectonic bed-perpendicular stylolites, striking sub-parallel to the fold axis (TS hereafter; **Figure 5.10**). Minor bed-parallel veins (V0 hereafter) are present in laminated limestone, along the limbs and hinge of the pluri-decameter fault-propagation fold. Tectonic stylolites and bed-parallel veins are overprinted by the younger set of E-W veins, largely developed and localized along E-W to ENE-WSW right-lateral strike-slip fault zone. In the central sector of the Pag anticline, the backlimb domain show near-constant bedding dip values of 50°-55°, locally dissected by W-SW verging thrust faults. The crest-to-backlimb transition, where the Milna Formation is exposed, is dominated by a hectometric triangle zone in the footwall of a subsidiary backthrust (see sections D, E in **Figure 5.7**); the latter is associated with an overturned footwall syncline in the well-layered highly-cemented packstone-wackestone of the Milan Formation. Moving to the north, the backlimb geometry is dominated by the occurrence of a major forethrust, dipping northeastward by 40°-45° and cross-cutting Gronji strata with bedding dip values of 50°-55°. The thrust-fault is characterized by multiple ramp-flat geometries (**Figure 5.11**), with associated meter-scale duplexes and shear lenses, enveloped by tectonic stylolites arranged in S-C arrays in the hangiwall and footwall of this thrust zone (**Figure 5.11**). Minor splay thrust faults also occur. The thrust damage zone contains abundant tectonic stylolites and veins (VT, hereafter) that are arranged in high-angle (65°-70°) NW-SE trending and low-angle at about 30° with respect to the master slip surface, respectively (**Figure 5.11**).

Tectonic stylolites typically overprint bed parallel styolites. Moreover, in the vertical bedding at the footwall of the thrust, sub-vertical bed-parallel stylolites are displaced by younger sub-horizontal tectonic stylolites (for further details see also **Figure 5.17d**). Thin white calcite bed-parallel veins (i.e., V0) are widespread in the deformed strata. Their distribution depends on the stratigraphic facies; rudist-bearing wackestones are more pervasively affected by veining compared to the mudstone beds. The angle between thrust-damage zone veins (VT) and bed-parallel veins (V0) observed in the thrust footwall, is about 15°-20° (**Figure 5.11**).

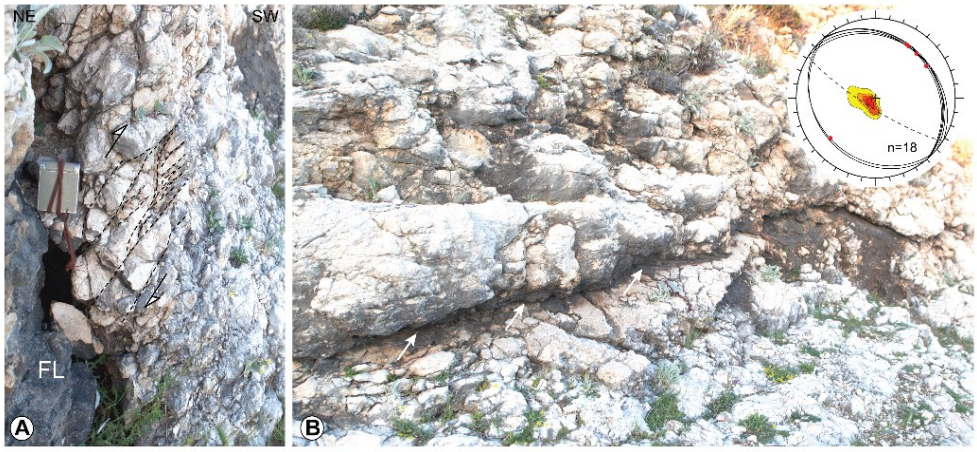

Figure 5.8 – (a) Footwall of the pluri-decameter thrust splay deforming the foraminiferal limestone (FL). Pressure solution shear planes in S-C array giving a top-to-SW transport direction; (b) Frontal view of a meso-scale thrust fault (white arrows). Stereographic projection of thrust plane geometry, slickenside along fault plane, and contoured poles to shear planes. Dotted ciclographics indicate the mean bedding attitude. Schmidt projection, lower hemisphere, contouring at 4% intervals.

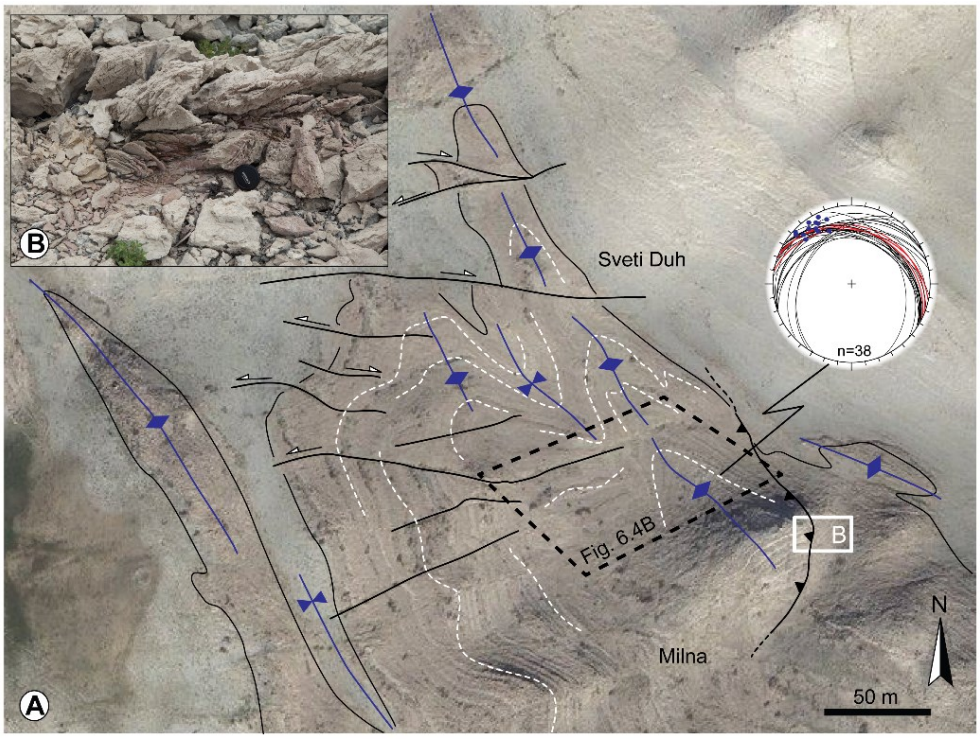

Figure 5.9 – (a) Drone-view map of the hinge line of the Pag anticline in its central sector. Milna and Sveti Duh formations crop out (see Figure 5.3 for locations), and are extremely deformed by multiple parasitic folds (trace of axial surfaces are indicated in blue). Most of them show symmetric geometries and were cross-cut by high-angle E-W to NE-SE strike-slip faults. The stereographic projection indicates bed attitude (black line), thrust surface (red line) e fold axis (light-blue dots) data

(*continued from the previous page*): collected in the field. Schmidt equal area, lower hemisphere; (b) Field detail of a backthrust surface, nucleated in a red paleosoil horizon in the Milna Formation. The abundant presence of organic- or laminated-rich layers and paoleokarst, forming a weak mechanical boundary, strongly influenced thrust faults localization.

The thrust fault zone is dissected at the fold scale by high-angle strike-slip faults, roughly oriented E-W, and teared by minor hectometric scale NE-SW trending strike-slip faults, accommodating differential slip-propagation and limb rotation (**Figure 5.7**, sections C, D). To the north, this important thrust fault zone dies out through a series of hectometric-scale low-displacement duplexes, involving pluri-decametric packages of the lower Gronji Formation (**Figure 5.7**, section C). Here, and in the surrounding area, the crest-to backlimb transition is described by a sharp dip-domain boundary (**Figures 5.12, 5.13**), in which in less than 30-35 meters, bedding is turned from sub-horizontal to about 55° dip. Deformation is expressed by conjugate dip-slip thrust fault pairs and associated diffuse veining in their damage zones. Kinematic data from calcite slikenfibers and thrust near-parallel veins (VT) indicates dip-slip reverse shearing towards the fold hinge (**Figure 5.12**). Thrust-related fabrics overprint earlier bed-parallel veins and bed-parallel stylolites, but clear cross-cutting relationship between bed-parallel veins i.e., V0, and thrust-related ones (VT) were not observed. In the Gornji Formation, and in particular in its lower part, weak-mechanical interlayers are lacking between meter thick mudstone and rudist-bearing packestone-rudstone. As a consequence, conjugate reverse faults flatting down into deformed strata and associated with fish-tails structures, producing intense brecciation and cataclastic flow structures (**Figure 5.13**). The previously described structure and meso-scale deformation elements (i.e., VT, axial-parallel tectonic stylolites, and bed-parallel veins) were cross-cut by sub-vertical calcite veins striking almost perpendicular to the fold strike (V1), and closely associated with sub-vertical stylolites (**Figure 5.14;** see also paragraph 6.3.3). In this forelimb fold sector, bedding dips toward southwest at about 60° and is mostly deformed by E-W strike-slip faults and subsidiary fault splays with left-lateral displacement (**Figure 5.3**, locality E).

Differently from the previously described area, in the northern fold periclinal sector the presence of a first-order backthrust fault zone (**Figures 5.3, 5.7** section A and B), exposed along the E-limb for about 4 km along strike, strongly influences the fold geometry, producing a northeastern fold asymmetry.

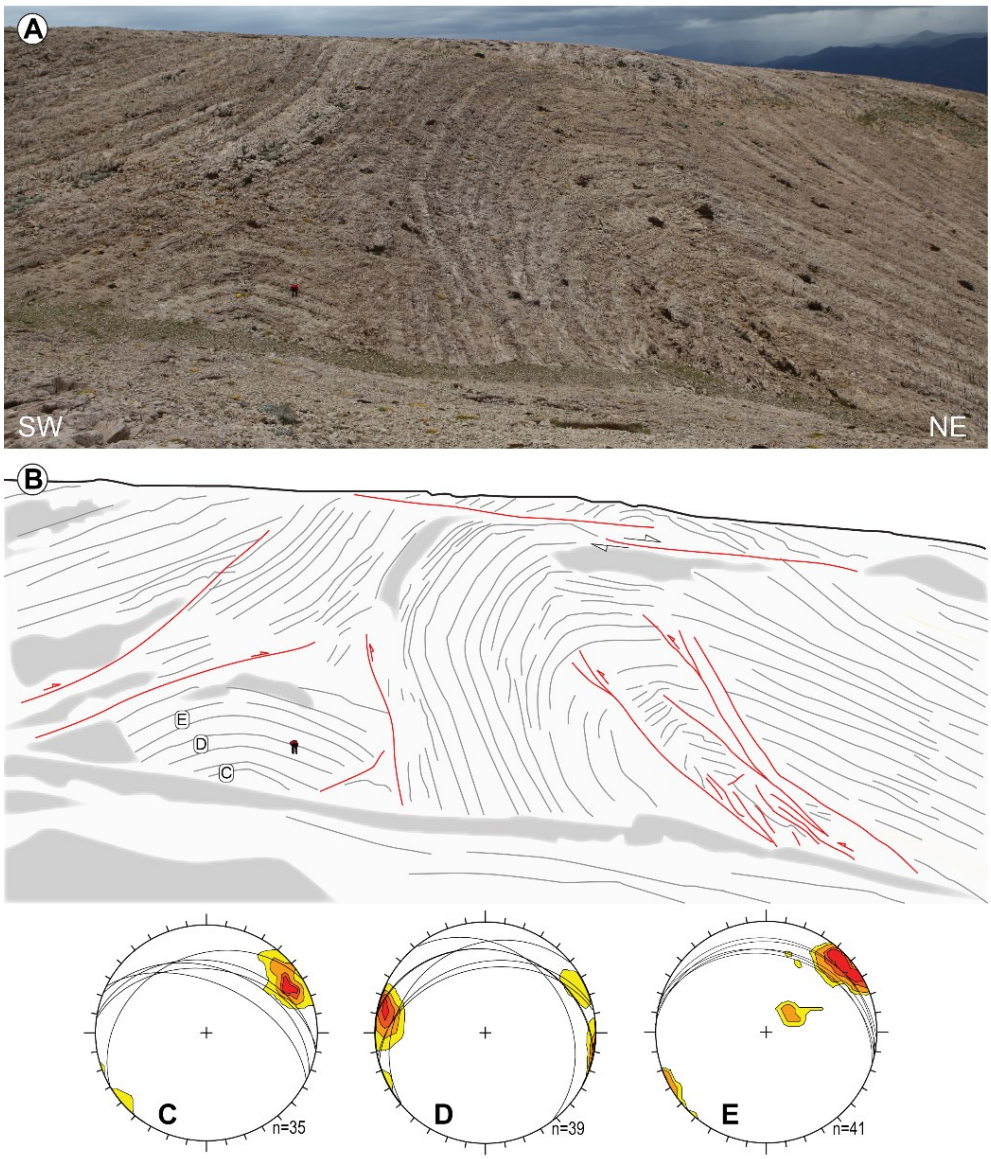

Figure 5.10 – (a) Panoramic view of the outcrop located northward of the field locality G (see Figure 5.3 for location), where Milna Formation limestone is exposed, showing a spectacular pluri-decametric fault-propagation fold at the core of the Pag anticline. Alessio Lucca for scale. (b) Line drawing of the same image; (c), (d), (e) Stereographic projections of bedding (black lines) and contoured poles of tectonic stylolites (interval at 4%) data, collected ahead of the fault-propagation anticline. Note how the attitude of bed-perpendicular axial parallel stylolites were refracted depending on the strata-facies where they were collected. Laminated wackestone (D) tends to refract stylolites with a clockwise rotation of about 20°, while meter-thick light-brown massive mudstone-wackestone imprint an anti-clockwise rotation of about10°-15°.

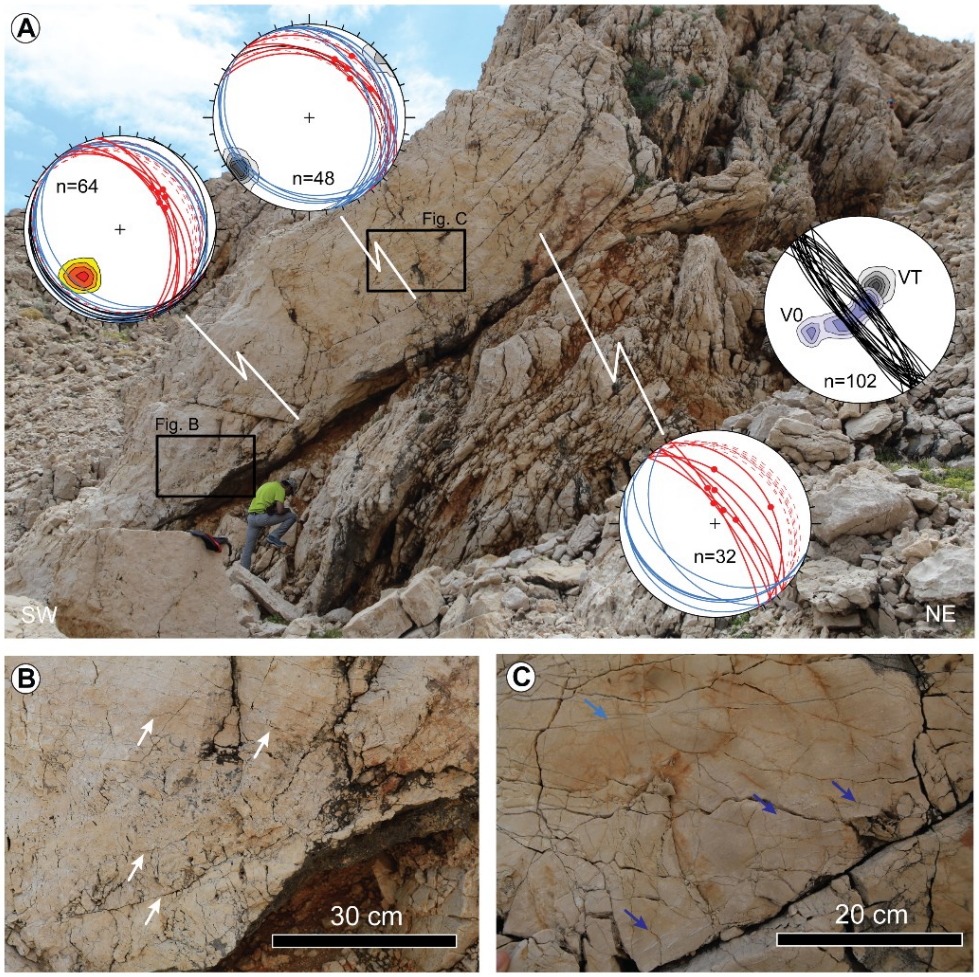

Figure 5.11 – (a) Photographic view of the SW-dipping thrust fault zone outcropping in the backlimb of the Pag anticline. The thrust forms ramp-flat geometry, with intense deformation exposed in its footwall, where highly-intensely deform shear lenses and duplex forms a meter-thick deformation zone, in which bedding in sheared and bent, indicating top-to- the hinge shear. Thrust fault core is characterizing by the occurrence of shear lenses and foliated cataclasites. On the master slip surfaces, slickenfibers and striae indicate contractional kinematic. Plots show, master fault surface data (thick red line), and minor splay faults (dotted red lines); thrust-damage zone veins (blue), and contouring of tectonic stylolites in shear lenses and in the thrust damage zone. A cumulative plot is also provided, showing attitude of tectonic stylolites (black line), pole contouring of bed parallel veins V0, and thrust-related veins VT, showing a mismatch of about 15°; (b) detail of slickolites lenses formed in a restraining sector of the hangingwall thrust; white arrows indicate calcite veins formed by dilation of bedding-parallel stylolites; (c) detailed view of the hangingwall damage zone showing the slightly difference in orientation between bel parallel veins (V0, dark blue arrows) and sub-horizontal thrust-related veins (VT, light blue arrow).

In fact, in this area, the forelimb dips more gently, and it has a very regular along strike geometry, characterized by three major dip domains having mean dip values of 60°-70°, 50°-40°, and 35°-20°, respectively, moving towards the crest. Such a fold geometry differs from the previously described one, in the central sector, (i.e., the area of overlap between backthrust and forethrust), which is characterized by overturned forelimb and a backlimb dipping 60°-65° to the NE. In the overlapping area between backthrust-dominated and forethrust-dominated architectures, deformation is mainly expressed by sub-vertical strike-slip faults compartmentalizing adjacent fold sectors, which underwent block rotation about vertical axes

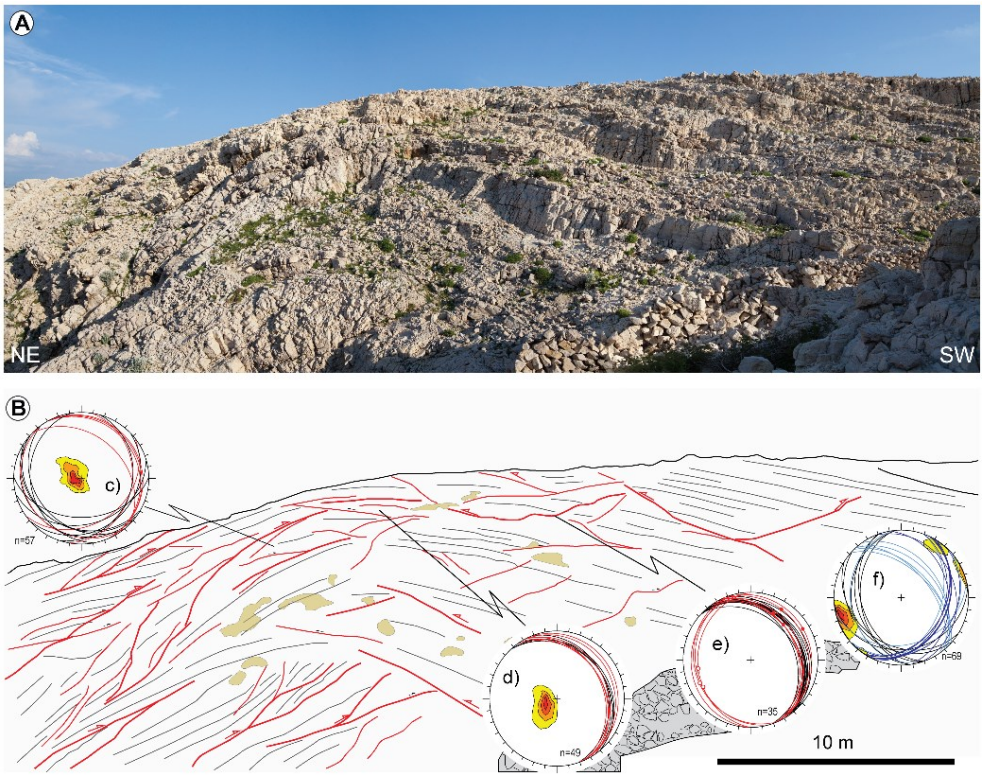

Figure 5.12 – (a) Panoramic view of the deformation style at the crest-to-backlimb transition in the deformed lower part of the Gornji Formatiom, few meters to the boundary with the Sveti Duh Formation. Grainstone to packestone limestone and dolomitic limestone are deformed by multiscale triangle zones and antiformal stacks. Low-angle thrusting, and reactivation of the bed surfaces occur. Bedding dip, from SW to NE, gradually changes from sub-horizontal to medium-angle in a sharp dip-domain boundary; (b) Line drawing of the same photo; (c), (d), (e) stereographic projections of bed attitude (dark lines), thrust surfaces (red lines) and contoured poles of thrust-damage zone veins (VT), close to thrust fault zones; (f) cumulative stereographic projection of bedding (black line), bed-parallel veins (light-blue), and thrust-related veins (VT, dark blue) data. Contoured poles to tectonic near bed-perpendicular, fold-parallel stylolites are also provided.

(*continued from the previous page*): Note that in this fold sector, deformation structures and bedding strike start to gradually rot**ate** with respect to the average fold axis attitude (N310°, **Figure 5.5**).

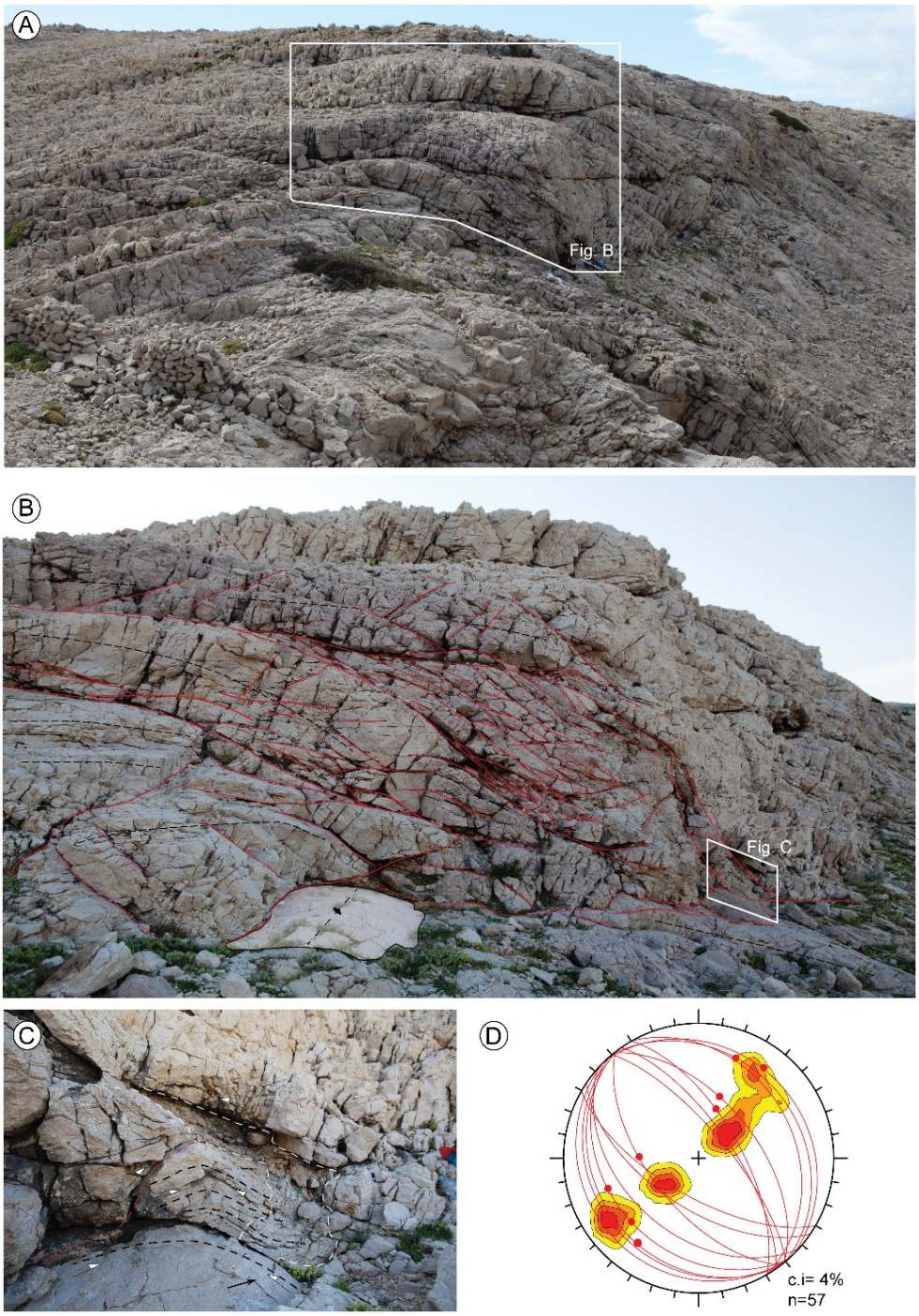

Figure 5.13 – (a) Panoramic view of the crest-to-backlimb transition to the north of the site in Figure 5.12. Dip domain transition is formed by meter-thick duplexing and fish-tail structures and indentation of carbonate bed packages; (b) Detail of the fish-tails structures accommodating hinge deformation. White area indicates bed

(*continued from the previous page*): surface with trend of the fold axis (in black); (c) Details of bed-parallel buffered cataclastic flow and bedding reactivation in the core of the antiformal stack; (d) Stereographic projection indicating thrust surfaces (red line), kinematic data, and contoured poles to bedding. Contour interval at 4%.

In the periclinal terminations, a narrow triangle zone (**Figure 5.15**, **5.7** section A) involves the stiff Gorgnji Formation (meter-thick mudstone-wackestone beds interlayered with decimeter-thick packstone-wackestone) thrusted onto weak marls and foraminiferal fimestone (inner ramp massive packstone). Moving southward, the crest-to-backlimb transition occurs through a major backthrust with minor thrust splays (section B in **Figure 5.7**). There, the Gornji Formation is thrusted onto foraminiferal limestone (**Figure 5.15**).

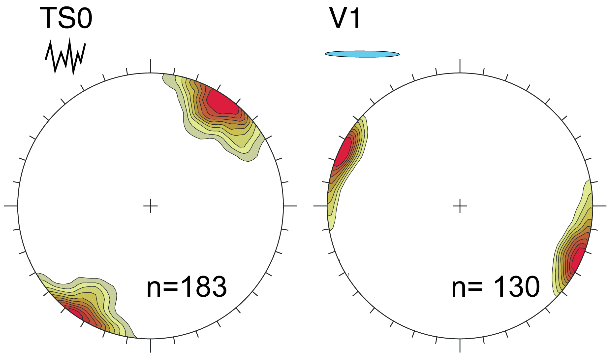

Figure 5.14 – Cumulative stereographic projection of cross-bed, mostly strike-parallel to the fold axis, on the left, and NE-SW high-angle cross-fold veins, on the right in Cretaceous limestone. Data were collected in 9 field sites in the crestal and forelimb domain. Data from the forelimb were restored to horizontal bedding. Schmidt projection, lower hemisphere, contouring interval at 7%.

In the hangingwall, the fold hinge is narrow, with sharp transition from low-angle to sub-vertical dip domains (**Figure 5.15**). Differently, in the footwall, bedding is sub-vertical to overturned and deformed by kink bands with sub-horizontal to low-angle axial planes. The occurrence of multiple slickenfibers and striae indicate polyphasic activity; calcite fiber and sub-horizontal calcite veins indicating top-to-NE shear predate a second striae generation, which indicates top-to-N motion. Earlier generation thrust-related veins and stylolites are compatible with a top to the NE motion, i.e., perpendicular to the fold axis. Thrust fault damage zones contain abundant fault-parallel thin veins, usually up to 5-8 cm long. Their distributions vary depending on the facies. Typically, calcite veins are scarce in white thick mudstone, compared to the brownish wackestone and packstone. Abundant veins occur in correspondence of pale purple beds, highly-cemented with bird-eyes structures. In the inner sector, moving toward the hinge line of the

Pag anticline, bed dips at low-angle to the norh – northeast. Here, in the hangingwall of the major backthrust, a well-developed conjugate pair of hectometric thrusts occur, with ramp-flat geometry dissecting the Gronji Formation and the boundary with the underlying Sveti Duh Formation (**Figure 5.16**). Similarity, to what previously described, deformational elements in the damage zones of the thrusts consists of sub-parallel calcite veins, typically in close associations with fault-perpendicular tectonic stylolites. Outward of damage zones, bed-parallel calcite veins (V0) occur and abutting relationships indicate that they pre-dated thrust-associated veins (VT). The formers, were displaced by cross-fold, bed perpendicular grey to white calcite veins (V1). V1 veins locally form en-échelon arrays indicating either dextral or sinistral sense of shear. Locally, such arrays form proto-fault zones. The same deformational structures (i.e., conjugate thrust pairs) occur in the folded and/or overturned strata in the footwall of the major backthrust down to the south. As for V0 veins, in the Gornji Formation V1 cross-fold veins tend to abut stratigraphic boundaries i.e., laminated limestone, rudist bioclast, or debris level in stormed beds. In the Milna Formation, cross-fold vein development was typically bed- or facies-confined by the laminated limestone and at their boundary with rudist-bearing storm beds or coarsening limestone (**Figure 5.17G**). Bed parallel veins, conjugate sets of subsidiary reverse faults, together with bed-perpendicular, axial-parallel tectonic stylolites (TS) and sub-horizontal calcite veins (VT) and cross-fold veins (V1) are abundant deformation structures in the fold limb and crestal area. Their cross-cutting relationships are well evident in the field (**Figure 5.17)**. When bedding is restored to the horizontal, bed-perpendicular stylolites (TS) become near vertical and mostly strike-parallel to the fold hinge. V1 bed-parallel veins become near vertical, striking perpendicular to the anticlinal axis, i.e. NE-SW. Shear veins striking ENE-WSW and forming left-lateral en-echelon shear bands cross-cutting and abutting the NE-SW sets were also observed. When Andersonian conjugate thrust system and reverse faults are restored to the horizontal, their geometry is compatible with a NE-SE compression, accordingly with deformation structures observed in the crestal domain. Outward of thrust damage zones the intensity of VT and associated stylolites decreases and bed-parallel vein scattering increases (**Figure 5.18**).

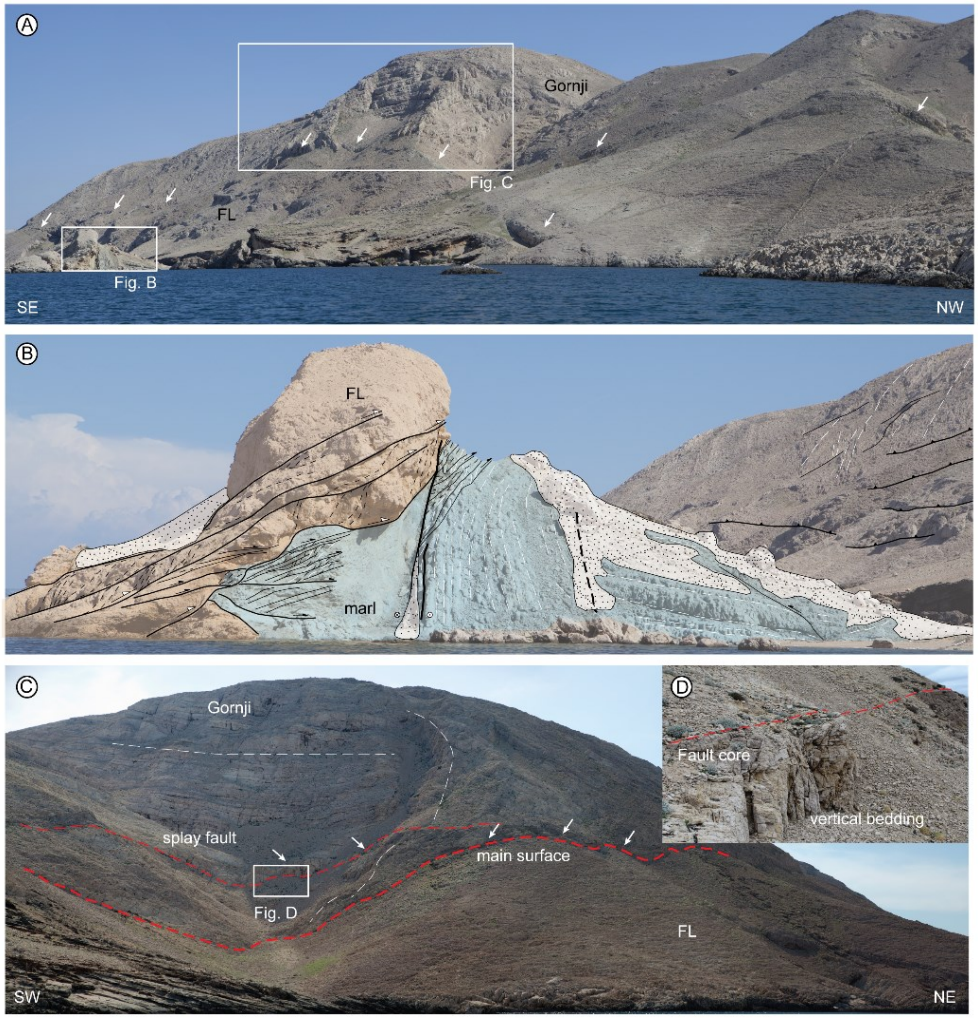

Figure 5.15 – (a) Panoramic view of the northern tip of the Pag anticline, where a fold-scale triangle zone control fold architecture. White arrows indicate the position of the master surfaces of the backthrust. The forethrust is exposed at the sea level in the small island on the left side of picture (b); (b) Detail of the forethrust bounding the triangle zone to the NE; Eocene marls (in blue) are overthrusted by foraminiferal limestone packstone rocks (in orange), and deformed by multiple thrust sufaces with SW transport direction. Shear fabric with S-C structure is well develop into weak marls. Thrust planes are displaced by a NW-trending high-angle strike-slip fault, with right-lateral sense of shear; (c)Panoramic view of the major backthrust and thrust-related anticline, developed in the Gornji Formation, which is thrusted onto Foraminiferal limestone wackestone (FL). The inner part of the fold is intensively deformed by multiple thrusting and indentation structures, quite similar to those described in Figure 5.13a. The footwall of the thrust shows vertical bedding (d) with minor asymmetrical kink fold, indicating top-to the NNE transport direction; (d) detail of the thrust fault splay surfaces, with a half-meter thick fault core made of coarse fault breccia and narrow cataclasite stripes.

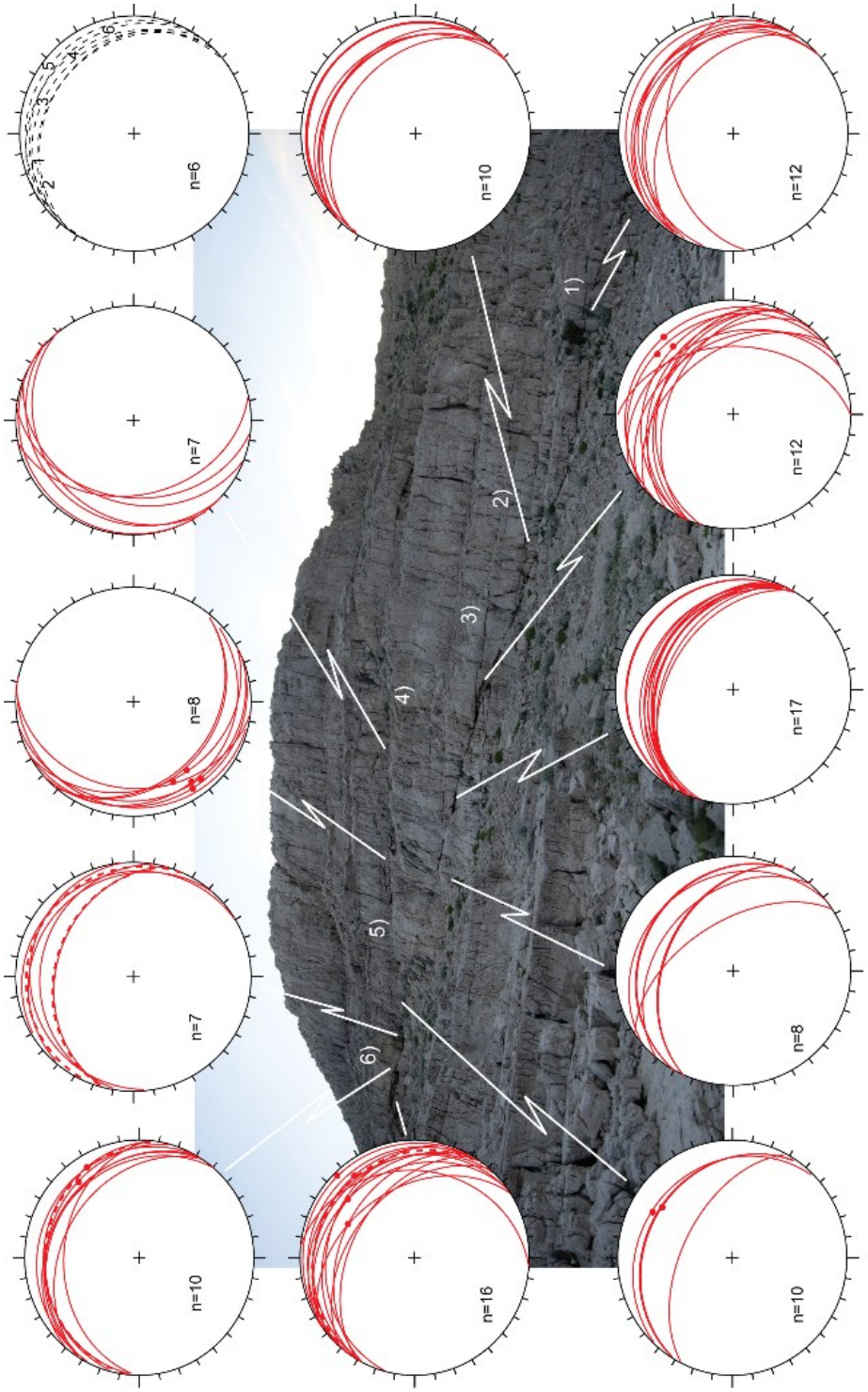

Figure 5.16 – Conjugate thrust pairs, dipping toward southwest and northeast respectively. Stereographic projections indicate fault attitude and kinematic data measured along thrust planes (red line) at each site. The dotted red lines indicate the geometry of the master slip surfaces, which show ramp-flat geometry, involving stiff and highly-cemented rudist-bearing weakestone of the Gornji Formation. The stereographic projection with dotted black circles displays bedding attitude at the relative measurement sites indicated by numbers on the photo.

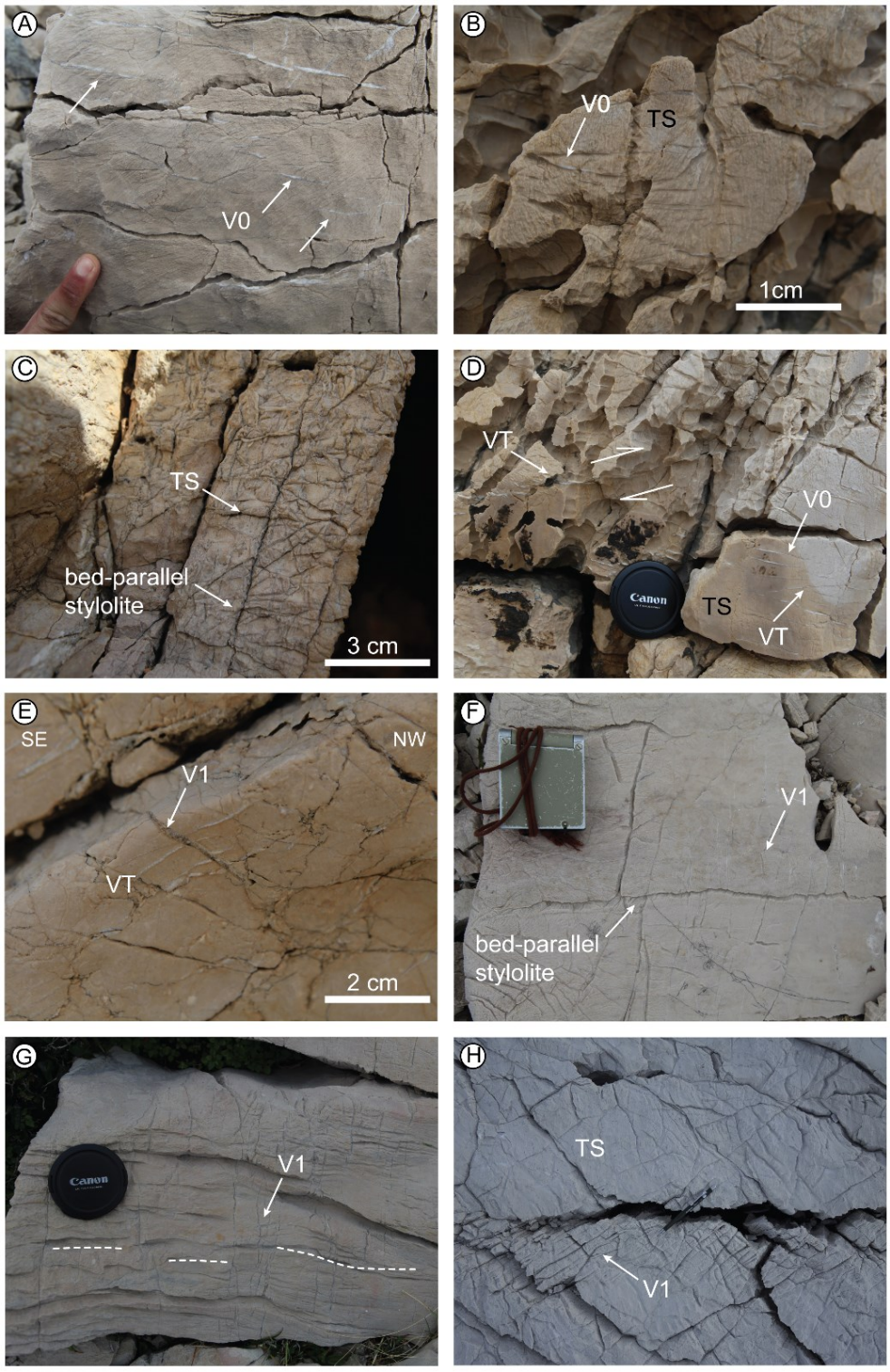

Figure 5.17 – (a) Bed-parallel veins (white arrows) developed in pale-yellowish wackestone of the Milna Fomation; (b) Details of thin bed-parallel veins (V0) and closely-spaced near-vertical tectonic stylolites in the hinge sector of the anticline, in the Gornji H. Formation. (c) Overturned beds, underlined by bed-parallel stylolites, overprinted by bed-perpendicular tectonic stylolites. The latter are reopened and filled by calcite cements. (d) Detail of a thrust footwall damage zone,

(*continued from the previous page*): in which thin V0 bed parallel veins and associated sub-vertical tectonic stylolites are present; (e) detail of the cross-cutting relationships between bed-parallel veins VT, overprinted by ENE-WSW striking cross-fold veins at high-angle to bedding; (f) Plane view of relations between thin grey calcite vein V1, overprinting bed parallel stylolites in a subvertical bed of the Gornji Formation; (g) Detail of V1 cross-fold veins in the hinge sector. Dotted white line indicates bed attitude; (h) detail of V1 veins and associate bed-perpendicular tectonic stylolites TS in the periclinal sector of the fold.

5.3.3 *Fault pattern and kinematics*

The illustrated complexity of the background deformation in the Pag anticline, in terms of fold geometry, deformational style, and deformation structures, is further increased by the presence of multiple sets of fault zones. Faults dissecting the anticline are widespread and occur in two main sets with strike-slip kinematics (**Figures 5.3, 5.5**). They clearly cross-cut the folded succession. The particularity of the fault pattern in Pag is the misorientation of the two strike-slip fault sets with respect to the fold axis: (*i*) one set strikes almost N-S and has right-lateral displacement; (*ii*) the other set strikes roughly E-W to ESE-WNW and shows left-lateral kinematics (**Figures 5.3, 5.5**). Acute angles varying between 85° and 90° indicate their non-Andersonian geometry. Field data collected in the Crikzna outcrop of late Miocene age lacustrine sediments, which were studied for stratigraphic and palaeomagnetic purposes by De Leuuw et al. (2011), indicate the presence of sub-vertical E-W to ESE-WNW left-lateral strike-slip faults (**Figure 5.18**).

Strike-slip E-W and N-S fault damage zones in Cretaceous carbonates are formed by minor splay faults and fractures trending sub-parallel to the master faults. They contain diffuse veins that are frequently arranged in sub-parallel or slightly oblique (35°-45°) sets with respect to the main surfaces (**Figure 5.18**). Two vein generations vein were recognized near-fault cores of both fault sets. The older set (V2) is filled by dark-grey calcite and reopened by V3 brownish to reddish calcite, which is extremely abundant in fault cores, where the orientation of stylolites is compatible with shear senses indicated by calcite veins. Moreover, abundant fault parallel tectonic stylolites also occur in both fault sets. The major observed offset is about 250-300m. Striae and slickensides along master fault planes suggest a multiple reactivation history and support left and right lateral movements, respectively, for both fault set (**Figure 5.18**). In N-S strike-slip faults, and in particular along those exposed in the southern part of the anticline, lens-shaped dolomitic bodies, ranging from plurimetric to hectometric scale, occur. The two fault sets cross-cut Eocene units (**Figure 5.18**) and when

they pass from stiff Cretaceous rocks to the Eocene ones, they locally change their geometry (**Figure 5.3**).

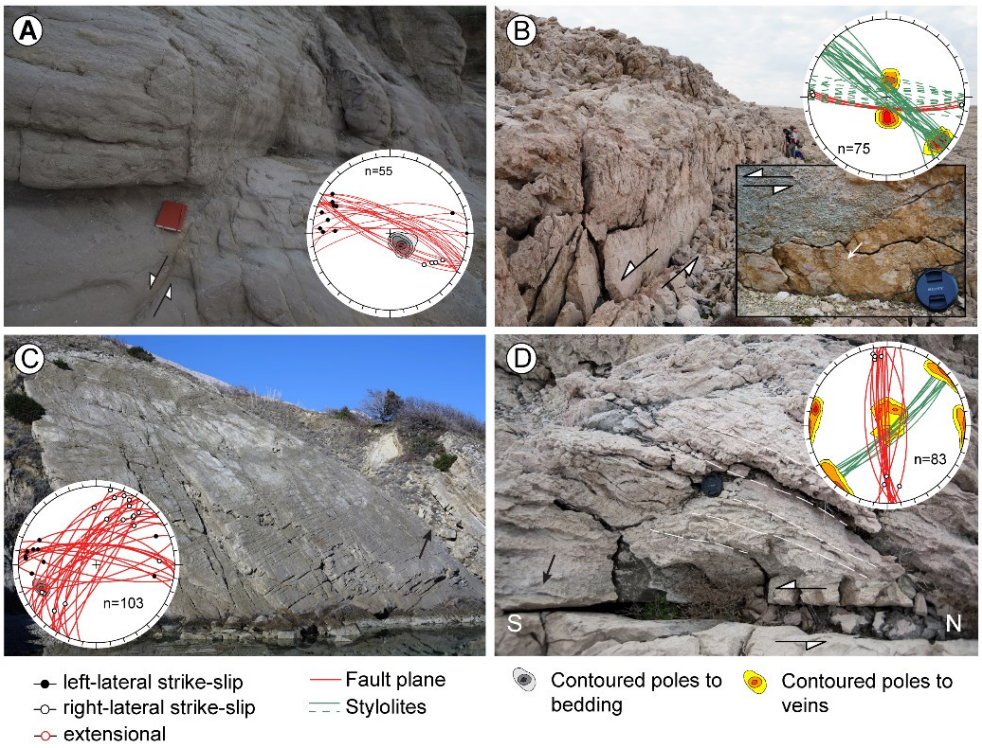

Figure 5.18 – (a) Example of left-lateral E-W small-scale fault interesting the lacustrine deposits at the Crikzna bay. The stereonet shows fault geometry (red) and contoured poles to bedding; (b) Panoramic view of an E-W strike-slip left lateral fault, and detail of striae along the fault plane; the stereographic projection shows fault geometry (red lines), stylolites in the fault core (green lines) and contoured poles to veins, striking almost parallel to the fault plane and near perpendicular to stylolites; (c) Example of the fault pattern in sub-vertical to high-angle turbiditic sandstone beds, displaced by a tear scissor-like fault (black arrow); (d) Fault core and related data from a N-S striking right-lateral fault. Although fault displacement and slikenlines indicate a dextral sense of shear, meso-scale fault analysis reveals a more-complex history, including left-lateral movements according to shear lenses and stylolites attitude in the fault core.

Intriguing relationships occur in zones accommodating shearing by the contemporaneous activity of both fault sets (see locality M in **Figure 5.3**), where cross-cutting relationships indicate that N-S trending stylolites and veins were mutually cross-cut and/or abutted by E-W trending ones (**Figure 5.19**). A minor fault set consists of NE-SW striking strike-slip faults that typically cross-cut Eocene units, with little right- and left-lateral displacements (**Figure 5.18**). They are well developed only along the vertical to steeply dipping limbs of the anticline, around Povljana and up the Pag village.

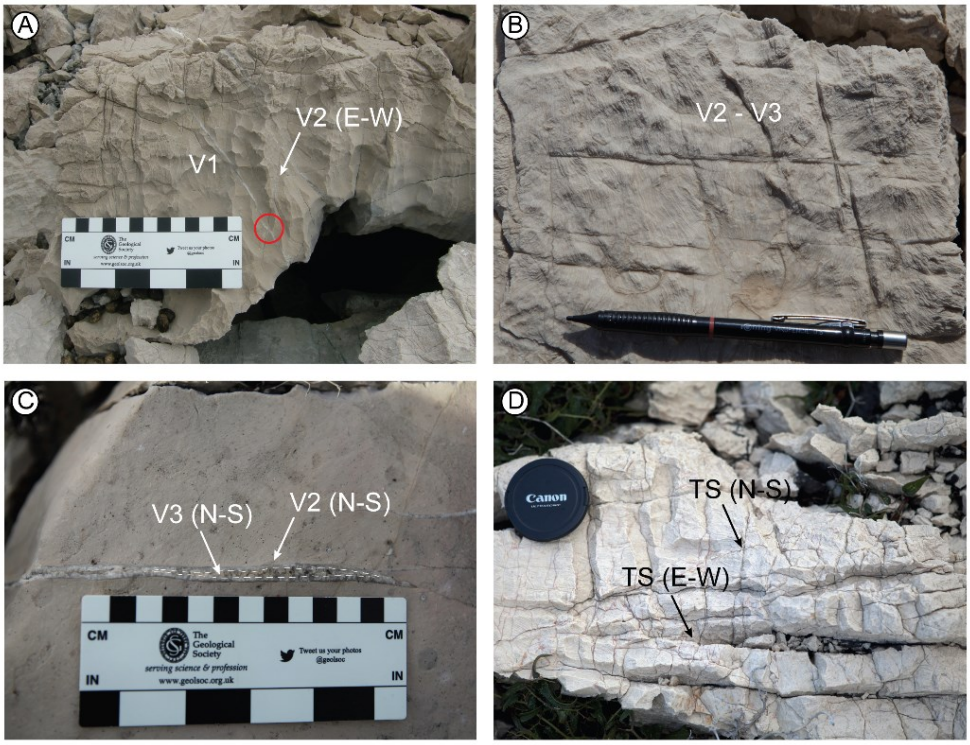

Figure 5.19 – (a) Cross-cutting relationships between V1 and V2 fault-related veins; (b) Thick white and brownish calcite V2-V3 vein arranged in N-S and E-W array with mutually cross-cutting relationships; the pencil is E-W oriented; (c) V3 veins reopening early V2 veins in E-W fault damage zone developed in the Foraminiferal limestone; (d) Mutual cross-cutting relationships between stylolites, mostly reopened and arranged in E-W and N-S trending arrays in a sector of overlapping E-W and N-S strike-slip fault damage zones.

5.3.4 *Deformation structures in Eocene units*

Understanding the relative timing of the deformation elements in the Eocene units is crucial for unravelling the evolution of the Pag anticline. The structural fabric observed in the Eocene units, outcropping mainly along the forelimb of the fold, is quite simple when compared to what we described in Cretaceous rocks. Except for local complexity, foraminiferal limestone were mainly affected by sub-vertical cross-fold veins filled by white calcite, and frequently forming en-énchelon conjugate left-lateral and right-lateral en-énchelon arrays. Bed-perpendicular pressure solution cleavage is closely associated with those veins. Such a fold parallel cleavage is particularly abundant in the external folds, near the Povljana village, where it constitutes the dominant deformation structures. When bedding is rotated to the horizontal, bed-perpendicular stylolites become near-vertical and veins remain sub-vertical, striking NW-SE. On the other hand, in turbiditic sandstone, particularly far from strike-slip fault damage zones, deformation structures consist of thin compaction bands, striking near

parallel to the bedding strike. Axial parallel joints and cross-bed conjugate shear joints also locally developed. Strike-slip E-W and N-S fault damage zones increase the deformation pattern complexity and overprint the older structural elements.

5.4 STRUCTURAL DIAGENESIS

The above described structural fabrics, in the background, in fault damage zones and within fault cores, were systematically sampled for petrographic, microstructural and geochemical analyses, to better unravel the kinematic evolution of the anticline and paleo-fluid circulation.

5.4.1 *Methods*

A total of 115 thin sections were cut from rock specimens sampled in the Pag anticline. Each sample was cut in two slabs, one of which was stained with Alizarin Red S and potassium ferricyanide to discriminate the different carbonate minerals including calcite and dolomite and their iron-rich equivalents (Dickson, 1966). The remaining slab was used to obtain a 30 µm thick thin section. Petrographic optical analyses were performed with a Zeiss Axioplan 2 microscope. Moreover, cold cathodoluminescence (CL) microscopy was performed by a Technosyn 8200 Mark II cold CL stage, mounted on a LEICA DM2700P optical microscope, at 10 kV and 256 µA gun current. Qualitative compositional maps of selected samples were acquired on four thin sections with a Zeiss Gemini 500 Scanning Electron Microscope. Operating conditions were 20 kV and 1.2 nA, 60 µm aperture, 8 mm distance and a 300-600 s counting time.

Following petrography and cathodoluminescence analyses, oxygen and carbon stable isotope ratios were determined on 253 selected samples of host rocks and cements. Stable isotope ratios are reported in %-notation relative to the V-PDB standard (Vienna Pee Dee Belemnite). 210 sub-samples of cements and host rocks were drilled directly from thin sections with an ESI New Wave Research Micromill with sub-micron step resolution and a milling chuck speed ranging from 1,200 rpm to 35,000 rpm. An additional of 43 sub-samples were drilled from rock slabs using a dental drill with 500 µm of width drill bits. For the geochemical analysis of each sample, 150-200 µg of carbonate powder was loaded into a GasBenchII autosampler, interspaced with three different reference materials (NBS18, NBS19 and MAB99). After helium flushing, 100% orthophosphoric acid was added at 25 °C and reacted at 72°C. Resulting gases were analysed automatically using a Thermo Finnigan Delta V+ mass spectrometer. A total of 40 peaks, in 10 steps, were measured for each sample. Each sample was

analyzed twice so the data uncertainty is ±0.10‰ and ±0.15‰ for δ13C and δ18O, respectively

5.4.2 *Petrography and microstructural data*

The Milna Fm. is composed of low-energy peritidal and lagoonal limestones deposited in a restricted platform environment (**Figure 5.19A**; Korbar, 2009; Korbar et al., 2012). Pseudoprimary, planar-E to porphyrotopic dolomites formed in peritidal limestone facies. Dolomites were later calcitized and are composed of micritic to microsparitic calcite cement. Calcitized dolomites and host rock limestone matrix show dull red luminescence in CL (**Figure 5.19B**).The Sveti Duh Fm. deposited in an open shelf environment. It is mainly made of mudstones and wackestones (Davey & Jenkyns, 1999; Korbar et al., 2012). Host rocks limestone matrix luminescence is orange and homogeneous in CL. The Gornji Humac Fm. is characterized by grainstones, packstones and subordinate wackestones (Korbar et al., 2012; Brlek & Glumac, 2014). The host rocks display dull purple to dull red colour in CL. Intergranular cement is granular mosaic calcite while rare fenestrae and moulds are occluded by drusy calcite cement. They show intense twinning Type I and are non-luminescent in CL.

Bed-parallel veins (V0) are up to a centimetre thick, no more than some centimetres long and made of “milky white” calcite. Calcite crystals are blocky, show high-intensity twinning Type I (Burkhard, 1993) and are non-luminescent in CL (**Figures 5.19C-D**). Thrust-fault damage zone (VT) veins, oriented parallel to bedding as V0 veins or at low angle to it but they show pluri-centimetric lengths. They occur along duplex systems and thrust fault zones. Calcite crystals display comparable twinning intensity and luminescence color of V0 veins (**Figures 5.19E-F**). Differently, V1 cross-fold veins are generally oriented normal to the axial plane of the Pag anticline and cut V0 veins. Calcite cement in V1 veins is made of granular mosaic calcite crystals showing dull orange colors in CL (**Figure 5.19D**). Rims of the veins composed by V1 calcite show solid inclusions zones with dolomitic habit that have a purplish color in CL and are clearly recognizable in transmitted light. Dolomites are planar-E, fracture filling (**Figures. 6.19G-H**). Type I twinning occurs in both purple and orange calcite cements but is less intense than in V0 calcite. Instead, V2 veins are organized in en-echelon arrays oriented N-S and E-W, associated with early strike-slip faulting deformation. They are generally less than 2 mm thick and less than 10 cm long. They are composed of a non-equigranular calcite cement, non-luminescent in CL and with rare Type I twinning (**Figure 5.19I**). V3 veins are associated with late-stage faulting and occur both along thrusts and strike-slip faults. They are composed of calcite cement showing non-

luminescent, yellow and orange growth zones in CL (**Figures 6.19B-F-H**). Where V3 calcite cement precipitated along re-opened stylolites, calcite crystals show smaller dimensions, rounded habit and a marked yellowish to reddish halo in transmitted light. Type I twinning occurs only locally.

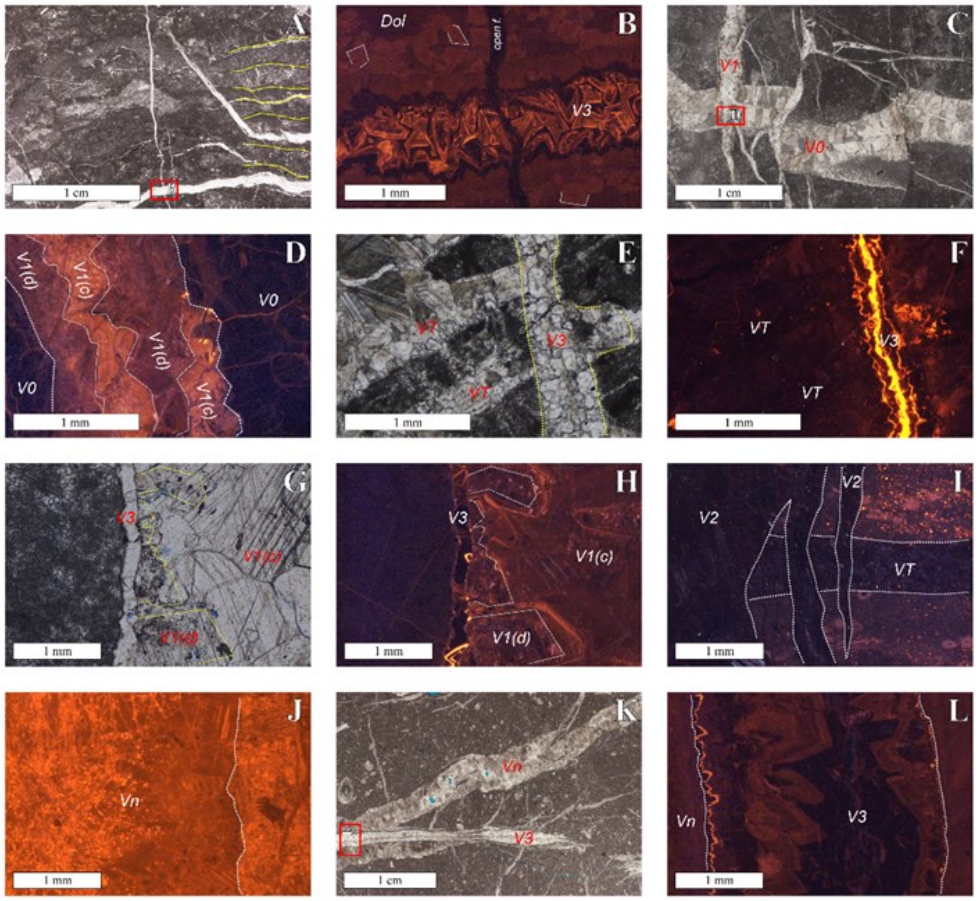

Figure 5.19 - (A) TSS of Milna Fm. limestone showing wavy laminated layers (yellow) including peloids and cyanobacteria. (B) Enlargement of A in CL illustrating calcitized idiotopic matrix dolomite crystals and V3 vein formed by calcite crystals with well evident non-luminescent and yellow growth zones. (C) TSS of Gornji Fm. showing crosscutting relationships between V0 and V1 veins; V0 shows extremely twinned calcite crystals, V1 is characterized by rims with solid inclusions zones and dissolution halos. (D) CL detail of C illustrating non-luminescent, highly-twinned V0 calcite crosscut by V1 which is composed by a purplish calcite cement (V1(d)), replacing euhedral fracture-filling dolomites and by orange calcite cement overgrowths (V1(c)). (E) PPL and (F) CL images of VT veins, filled by intensely-twinned non-luminescent calcite, crosscut by a non-twinned V3 vein. (G) PPL and (H) CL microphotographs illustrating well preserved dolomite habit in V1(d), overgrown by V1(c) and later antitaxial fracturing of V3 non-luminescent and yellow calcite cement. (I) CL image showing part of V2 en-echelon vein crosscutting VT Figure 5.19 vein; both are characterized by non-luminescent calcite cements. (J) CL detail of a VN vein in the

(*continued from the previous page*): foraminiferal limestones; they are cemented by elongate-blocy to fibrous calcite with twinning Type I and have the same CL color of the host rock (right); (K) TSS of the foraminiferal limestones including a VN syntaxially re-opened by a V3. (L) Detail of K showing the CL colors of V3, which appear dark orange and dull but preserve the well-evident growth zones. TSS stands for thin section scan; PPL for plane-polarized; XPL for cross-polarized light; CL for cathodoluminescence.

Eocene foraminiferal limestones wackestones and rudstones show a dull red to purple luminescence and an orange luminescence, respectively. They host VN veins, which show various calcite cement textures. Blocky, dogtooth, fibrous and microsparitic calcite cements fill VN veins and are characterized by different Type I twinning. However, in CL they all share the same color, according to their encasing host rocks. Therefore, VN veins in wackestones show dull red to purple colours while those that cut through rudstones are orange (**Figures 5.19J-K-L**). The Dinaric Flysch Fm. hosts VF veins in sandstone beds, mostly occurred in the strike-slip fault damage zone. They are composed of calcite cement, with rare Type I twinning, showing orange color in CL as the intergranular calcite cements. Notably, V3 veins, related to fault zones in the Gornji Humac Fm. cut also the Milna, Sveti Duh and Eocene Foraminiferal Limestones Formations and show the same textural features and similar CL patterns (**Figures. 6.19B-F-H-L**).

5.4.3 *Geochemistry*

Results of carbon and oxygen stable isotopes analyses are illustrated in **Figure 5.20** and in **Table T1**, where ranges, mean values and standard deviations are reported. $\delta\ ^{18}O$ and $\delta\ ^{13}C$ values are expressed in ‰ deviations relative to the Vienna Pee Dee Belemnite standard (V-PDB). The squared area indicates the range of $\delta\ ^{18}O$ and $\delta\ ^{13}C$ values of limestones precipitated in equilibrium with Late Cenomanian to Early Coniacian seawater (Veizer et al., 1999).

$\delta\ ^{18}O$ values of Cretaceous limestone host rocks, namely Milna, Sveti Duh and Gornji Humac Fms., show a similar range comprised between -6‰ and -3.5‰, excluding an outlier with a value of +1.9‰. Their $\delta\ ^{13}C$ values show slightly different ranges of -0.3‰ to +3.1‰, +1.9‰ to +3.4‰ and -0.8‰ to +2.5‰, respectively from bottom to top. Host rock fragments involved in cataclastic fault cores of late-stage strike-slip faults show lower $\delta\ ^{18}O$ and $\delta\ ^{13}C$ values up to -6‰ and -3.3‰ in the Sveti Duh and to -5.8‰ and -4.9‰ in the Gornji Humac for oxygen and carbon, respectively.

Cement type	$\delta^{18}O$‰ (V-PDB)			$\delta^{13}C$‰ (V-PDB)		
	Range	Mean	St. dev. (±1σ)	Range	Mean	St. dev. (±1σ)
Flysch V	-3,8 / -3,2	-3,57	0,16	-1,1 / -0,3	-0,51	0,26
Flysch HR	-5,3 / -4,0	-4,83	0,40	-0,6 / +1,9	+0,15	0,86
Nummulitic V	-9,3 / -4,2	-5,92	1,14	-1,2 / +2,5	+0,91	0,95
Nummulitic HR	-4,6 / -2,5	-3,43	0,56	-0,8 / +2,1	+1,16	0,77
V3 (late strike-slip)	-7,0 / -4,6	-5,66	0,58	-7,3 / +0,3	-3,96	1,76
V2 (early strike-slip)	-8,6 / -5,5	-7,25	0,76	-3,8 / +1,6	-0,87	1,55
V1 (cross-fold)	-9,0 / -5,6	-7,48	0,87	-4,4 / +2,2	-1,94	2,33
VT (thrusting)	-6,9 / -4,5	-5,82	0,69	-0,5 / +1,5	+0,57	0,52
V0 (bed-parallel)	-6,6 / -5,4	-5,93	0,37	-9,6 / +0,2	-4,71	3,56
Gornji HR	-6,2 / -1,9	-4,60	0,89	-4,9 / +2,5	+0,39	1,68
Sveti Duh HR	-6,1 / -3,8	-5,37	0,80	-3,3 / +3,4	+0,40	2,48
Milna HR	-5,5 / -3,5	-4,14	0,62	-0,3 / +3,1	+1,66	1,02

Table T1 – Cement type and related δ 18O and δ 13C range, mean and standard deviation value.

V0 bed parallel veins are filled by calcite cements which have $\delta^{18}O$ values in the range -6.6‰ to -5.4‰ but show large $\delta^{13}C$ shifts, from a minimum of -9.6‰ to a maximum of +0.2‰. VT veins, which are characterized by calcite cement similar to V0, have a comparable $\delta^{18}O$ range from -6.9‰ to -4.5‰ but a narrower cluster of $\delta^{13}C$ values, comprised between -0.5‰ and +1.5‰. Calcites in V1 veins in the Gornji Humac Fm. have $\delta^{18}O$ and $\delta^{13}C$ values comprised between -9‰ and -6.4‰ for $\delta^{18}O$ and between -4.4‰ and -1.6‰ for $\delta^{13}C$ while in the Milna Fm. these values are less depleted showing a $\delta^{18}O$ range of -8.1‰ to -5.6‰ and a $\delta^{13}C$ range of +0.7‰ to +2.2‰. Similar to calcite in V1 veins, calcite in V2 veins show $\delta^{18}O$ ranging from -8.6‰ to -5.5‰ and $\delta^{13}C$ from -3.8‰ and +1.6‰. V3 veins have a $\delta^{18}O$ range of -7.0‰ to -4.6‰ and of -7.3‰ to +0.3‰ for $\delta^{13}C$, similarly to eo-diagenetic, fenestral and V0 calcite cements. The most depleted V3 $\delta^{18}O$ values correspond to dedolomitized and calcitized areas.

The Eocene foraminiferal limestones host rocks range between -4.6‰ and -2.5‰ $\delta^{18}O$ and between -0.8‰ and +2.1‰ $\delta^{13}C$. Instead, VN veins in the foraminiferal limestones have $\delta^{13}C$ values similar to the host rocks, comprised between -1.2‰ and +2.5‰. $\delta^{18}O$ values of VN veins, conversely, show a large range from -9.3‰ to -4.2‰. The Dinaric Flysch Fm. calcite intergranular cement shows $\delta^{18}O$ values ranging from -5.3‰ to -4.0‰ and $\delta^{13}C$ values from -0.6‰ to +1.9‰, while calcite in a VF vein, hosted in the Flysch, shows a $\delta^{18}O$ range of -3.8‰ to -3.2‰ and a $\delta^{13}C$ range of -1.1‰ to -0.3‰.

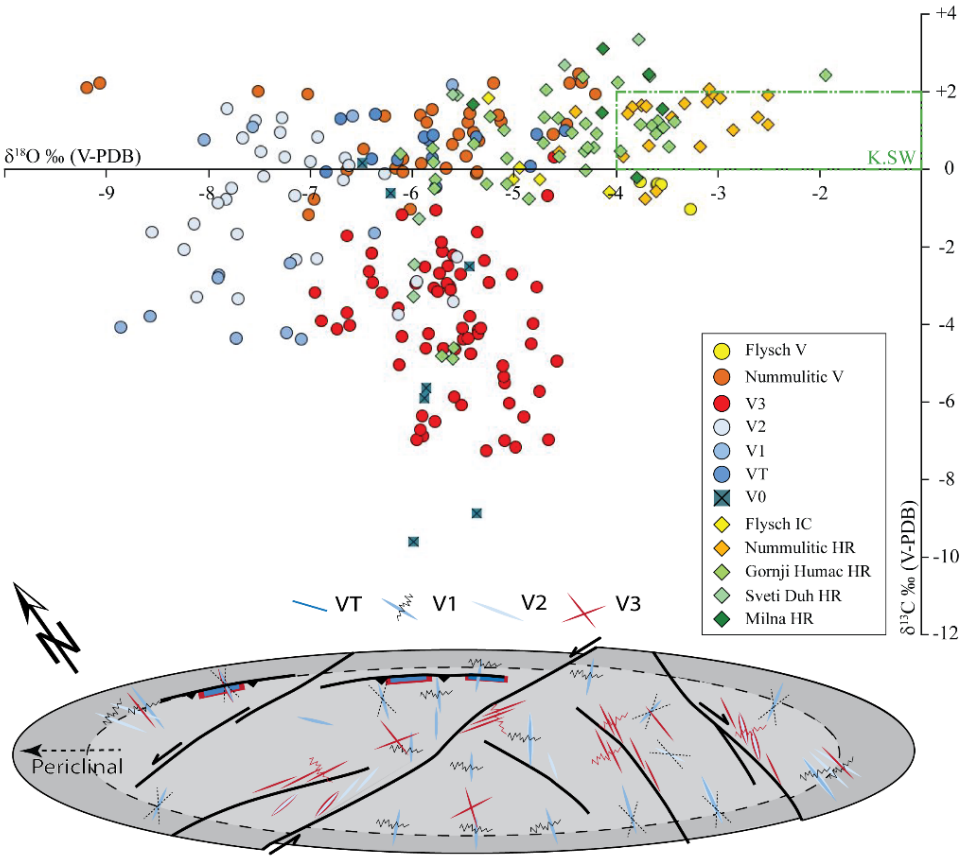

Figure 5.20 -Plot illustrating results of $\delta^{18}O‰$ vs. $\delta^{13}C‰$ of analyzed calcite cements. See legend in the plot for cement types. V are veins, HR are host rocks and IC is intergranular cement. Dashed green box indicated with K.SW shows the range of values of limestones which precipitated in equilibrium with Cenomanian to Coniacian seawater. In the lower part, cartoon illustrating orientation, relative position and type of cement for the described deformation structures. Color coding is the same in figures and isotope diagram. Cartoon oversimplified the folds, and Eocene units were not represented.

5.5 DISCUSSION

5.5.1 *Inferences on the depth to detachment*

Our data show that Pag and the adjacent folds to the SW are possibly detached at about 2000-2500 m depth (**Figure 5.6**). This depth is in agreement with that recently proposed by Korbar (2009) for the younger detachment localized in Upper Jurassic –Lower Cretaceous units where an evaporite layer occurs. Along strike differences in tectonic styles are mostly related to the pre-orogenic distribution and stratigraphical position of the weakest horizons, acting as detachments. Noteworthy, the significant role of Mesozoic evaporite horizons is recognized also by Merlini et al. (2002) in the NW part of the NE Adriatic region (Friuli).

5.5.2 *Relative chronology of deformation structures*

The combination of structural, petrological and geochemical data allows us to propose the relative chronology of deformation structures that is illustrated and described in **Figure 5.21**. Cartoon showing the proposed evolutionary steps for the deformation pattern of the Pag anticline. Bed parallel veins (V0) forms prevalently in laminated or mud-rich strata suggesting low burial and incipient conjugate thrust pairs with associated thrust-related veins (VT) and tectonic stylolites striking parallel to the fold axis. Continuing contraction caused lateral thrust propagation and the switch of sigma 2 from sub-horizontal to sub-vertical, triggering the nucleation of V1 veins and associated stylolites. V1 veins form en-chelon arrays that locally formed small scale proto faults and were overprinted by V2 veins, mostly localized along strike-slip N-S and E-W faults zone, that incipiently started to propagate at this stage. The orientation of sigma 1 changed at this stage, rotating counterclocwise; (**Figure 5.21**) the V3 pattern developed and reopened earlier structures (bed-perpendicular stylolites and veins, and V2. It prevalently localized along strike-slip fault zones, but also along transpressionally-reactivated thrust faults

5.5.3 *Diagenetic environments of cement precipitation*

Cenomanian to Coniacian limestone host rocks show depleted $\delta^{18}O$ compared to what should be expected from limestones that precipitated in equilibrium with seawater (Veizer et al., 1999; Gradstein et al., 2012). Light $\delta^{18}O$ values have been extensively documented to occur in Cretaceous limestones of the Adriatic Carbonate Platform and have been interpreted as proof of limestone precipitation in coastal and lagoon environments influenced by freshwater dilution (Vlahović et al., 2005; Korbar, 2009; Brlek & Glumac, 2014). At the top of the Gornji Humac Fm., $\delta^{18}O$ reaches values of -6‰. The Eocene foraminiferal limestones show $\delta^{18}O$ values comparable to other Eocene foraminiferal limestone sections in the Tethyan area (Holail, 1994; Dinçer, 2016). Slightly depleted $\delta^{18}O$ suggest influx of meteoric waters into the limestones after deposition. Host rocks $\delta^{13}C$ is in the range of marine waters of their depositional age.

V0 and then VT veins were the first to precipitate during layer parallel shortening and incipient thrusting (see **Figure 5.22**). They have $\delta^{18}O$ values slightly depleted (around 1.5‰) compared to their host rocks indicating that connate fluids were slightly heated or mixed with meteoric fluids at precipitation (Muchez et al., 1995; Hoefs, 1997).

Strikingly different $\delta^{13}C$ values in V0 and VT veins, which become progressively lighter moving up to the top of the Gornji Humac Fm., suggest they are most likely inherited from meteoric phreatic eodiagenesis

that occurred during the subaerial exposure of the Adriatic Carbonate Platform from Late Cretaceous to Paleocene (Brlek and Glumac, 2014). If this assumption is correct, lighter oxygen values are the result of syn-tectonic precipitation temperatures some degrees higher than seawater during primary carbonate precipitation. V1 and V2 veins, which precipitated during the main folding phase and the early re-activation of the pre-compressional N-S and E-W strike-slip faults (**Figure 5.22**), respectively, are characterized by the most depleted $\delta^{18}O$. V1 and V2 show $\delta^{18}O$ values up to 3‰ lighter than the lightest host rocks values, indicating that the diagenetic fluid precipitated at temperatures up to maximum 50 °C or that it was interested by a higher degree of mixing with meteoric waters, assuming equilibrium precipitation (Friedman & O'Neil, 1977). $\delta^{13}C$ still shows lighter values at the top of the Gornji Humac Fm. as for V0 and VT.

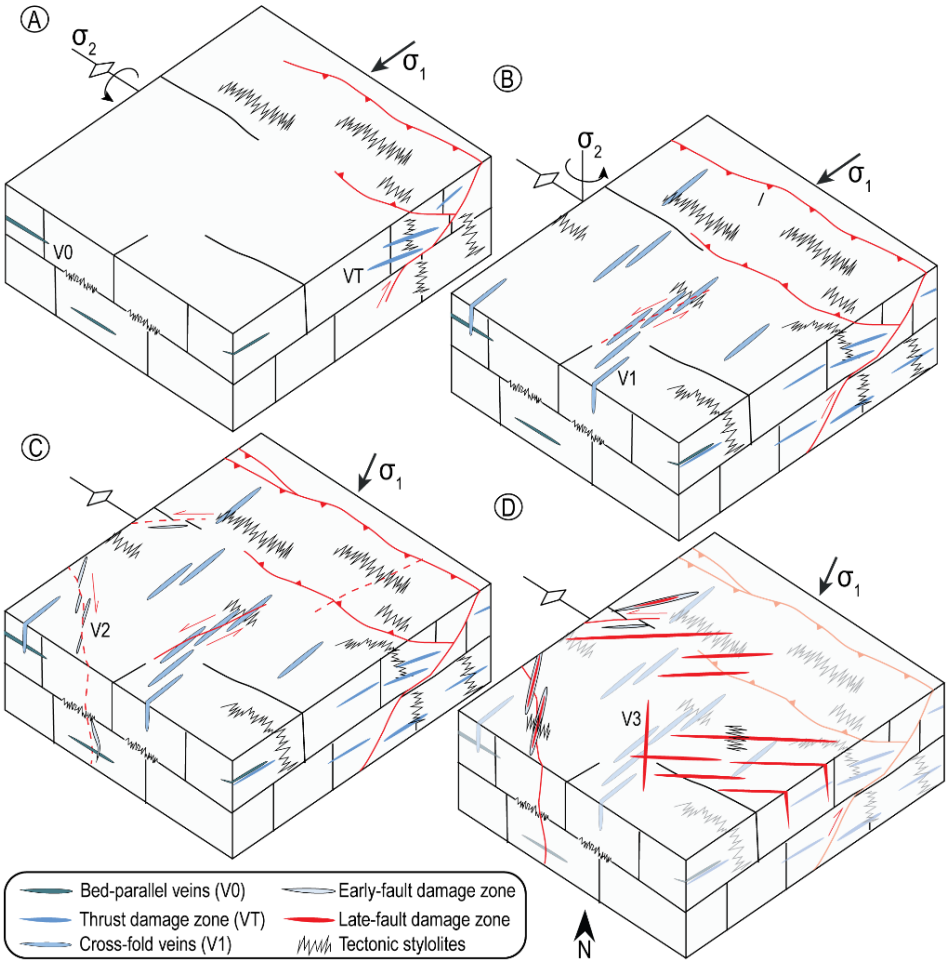

Figure 5.21 – Cartoon showing the proposed evolutionary steps for the deformation pattern of the Pag anticline. (a) Schematic representation of the nucleation of bed parallel veins (V0) and incipient conjugate thrust pairs with associated thrust-related veins (VT) and tectonic stylolites striking parallel to the fold axis; (b) Progressive contraction caused lateral thrust propagation and the

(*continued from the previous page*): switch of sigma 2 from sub-horizontal to sub-vertical, triggering the nucleation of V1 veins and associated stylolites. V1 veins form en-échelon arrays that locally formed small scale proto faults; (C) Veins V1 were overprinted by V2 veins, mostly localized along strike-slip N-S and E-W faults zone, that incipiently started to propagate at this stage. The orientation of sigma 1 changed at this stage, rotating counterclocwise; (d) the V3 pattern developed prevalently localized along strike-slip fault zones, and reopened earlier structures (bed-perpendicular stylolites and veins, and V2) cemented also along transpressionally-reactivated thrust faults.

Therefore, it is logical to conclude that the carbon source for calcite cements V0, VT, V1 and V2 was locally sourced by the encasing limestone strata, which $\delta^{13}C$ depends on the eodiagenetic overprint.

VN veins show lighter $\delta^{18}O$ values compared to their host rocks, generally depleted by a 3‰, but up to 5‰ (**Figure5.20**). Since the temperature effect on the fluid $\delta^{18}O$ has to be less pronounced than in the underlying Cretaceous limestones, the lighter values indicate that meteoric fluids certainly mixed at different degrees with marine connate fluids prior to precipitation. The $\delta^{13}C$ values of VN veins are similar to their encasing host allowing us to exclude major carbon sources external to the foraminiferal limestones.

V3 veins are associated with the re-activation of pre-compressional N-S and E-W strike-slip faults in the late fold tightening phase. They are characterized by $\delta^{18}O$ values similar to V0 and VT veins (**Figure 5.20**). Distinctly from older calcite cements, all $\delta^{13}C$ values are depleted compared to their host rocks. Lighter $\delta^{13}C$ ratios could be the result of meteoric fluids infiltrating from the surface along strike-slip faults and carrying in solution ^{12}C deriving from organic matter (Allan and Matthews, 1982; James and Choquette, 1990). Therefore, $\delta^{18}O$ ratios of the cementing fluid are reasonably depleted by the ingress of meteoric fluids, conversely to the older V0 and VT low-angle veins.

Intergranular calcite cement (IC) and calcite veins (VF) in the Dinaric Flysch show the heaviest $\delta^{18}O$ values amongst the studied cements. This could be both the result of a temperature effect, being the Flysch the shallowest studied unit, or due to a higher contribution of marine fluids during syntectonic precipitation.

Overall, we can infer that syntectonic fluids are sourced at a local scale (bed to bedset) from the layer parallel shortening phase up to the incipient re-activation of pre-compressional strike-slip faults. As soon as these inherited lineaments increased their permeability, fluid mixing between bedsets and also between units occurred. Moreover, as they propagated

towards the surface in the late fold tightening and tearing phase, they allowed infiltration of meteoric fluids.

5.5.4 *Fold kinematic evolution*

The proposed kinematic model (**Figure 5.22**) combines meso- and micro-structural data, and isotopic and geochemistry data on veins cements. A pre-folding, layer parallel shortening stage marks the onset of NE-SW-directed contraction in the area. Structural association of bed-perpendicular stylolites, layer-parallel veins and axial-perpendicular veins are all structures formed during this pre-folding stage and then passively rotated with bedding. The two coeval vein sets indicate that contractional and strike-slip (transpression) stress regimes occurred during LPS. Increasing the vertical load by sedimentation of the proximal turbidites in a thrust-top basin, as indicated by cartographic growth strata in the upper part of the flysch unit, is expected to have caused the switch from thrust to strike-slip stress fields. Syn-folding deformation events during fold amplification and major thrusting are recorders by vein growth in arrays perpendicular and parallel to the fold axis, respectively, and by contemporaneous re-working of previous deformation structures. Both vein sets were cemented by the second generation of calcite (V2) that shows a non-luminescent character in cathodoluminescence, similar to the host rock, thus suggesting local fluid circulation. Stable isotopes data for pre-to syn folding cements suggest a rock-buffered circulation in the Cretaceous rocks.

At the end of this stage, fold tightening was facilitated by the passive rotation of the inherited normal faults, which also caused fold compartmentalization and tearing. Fold tightening was recorder by formation of new deformation elements oriented obliquely to the fold axis and by re-activation of previously-formed deformation structures in a right-lateral transpression regime (thrusts and oblique faults). New conjugate strike-slip faults nucleated and newly-formed segments connected inherited fold-related deformation structures (**Figure 5.22**).

During fold evolution, the interconnection of deformation structures and cementation of host rock and veins strongly influenced the paleo-fluid flow and paleo-permeability. During layer-parallel shortening and early folding, the permeability of the fracture network was essentially controlled by transversal fractures, bed parallel veins and by the onset of larger-scale deformation feature (thrust, fish-tails structure).

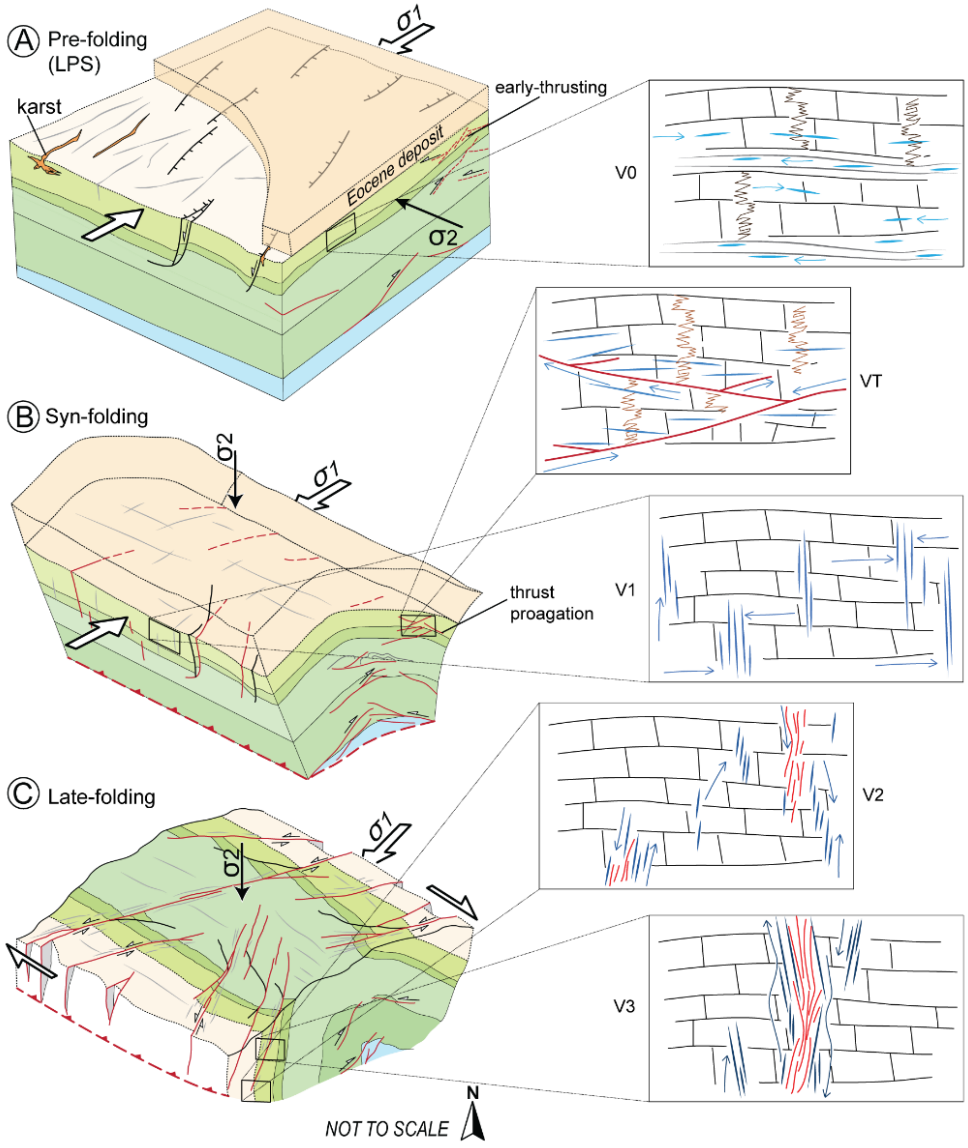

Figure 5.22 – Cartoon showing the proposed kinematic evolutionary model for the Pag anticline.

Poor connectivity of small scale deformation structures is documented, and scattered crack-seal events are recorded. Bed-confined veins, strongly influenced by bed facies, caused an increase in porosity and poor permeability for vertical fluid migration. During fold amplification and progressive tightening and compartmentalization, the paleo-fluid system progressively changed with evolving deformation. Re-activation of well-oriented inherited faults as tear faults, and newly formed ones connected fold limbs and produced effective conduits for fluid flow at this stage. At the same time, layer-parallel flow was inhibited by early pre-to-syn folding cemented veins.

5.6 CONCLUSIONS

We performed a structural and petrograhical-geochemical study of the structural architecture and deformation structures exposed in the Pag anticline, in the external sector of the External Dinarides, Croatia. Field and laboratory data have been integrated with geological mapping and cross-section reconstructions in the central and periclinal sectors of the fold. The results of our work can be summarized in the following points:

1. Despite its position near the toe of the Dinaride belt, the Pag anticline shows a high structural complexity, including a non-cylindrical box fold geometry dissected by a major overstepping, conjugate thrust and backthrust pair, and strongly compartmentalized by high-angle to vertical strike-slip fault zones trending roughly E-W and N-S, respectively.

2. Deformation style is in agreement with a detachment fold. The detachment level governing fold geometry and evolution is ubicated in the Upper Jurassic-Lower Cretaceous units at a depth of about 2000-2500 m.

3. In the north-western sector of the Pag anticline, a km-long periclinal termination is exposed and characterized by a progressive rotation of bedding up to strikes perpendicular to the fold axis. In the central sector of the anticline, a blind forethrust controls forelimb geometry with steeply-dipping to overturned strata. Subsidiary low-angle reverse fault splays outcrop in this sector, crosscutting the vertical forelimb with metric displacement. In the northern fold tip area, the presence of a first-order backthrust fault zone strongly influences fold geometry, producing a northeastern fold asymmetry. In fact, in this area the forelimb dips more gently and has a very regular along strike geometry, characterized by three major dip domains having mean dip values of 60°-70°, 50°-40°, and 35°-20° respectively, moving towards the crest. In the central sector

of the fold, the area of overlap between backthrust and forethrust is characterized by a tighter fold geometry: the forelimb gradually becomes vertical to overturned and the backlimb reaches a dip of 60°-65° and is affected by a higher structural complexity with subsidiary thrust faults forming an articulated and anastomosed hectometric-wide deformation zone in map view. In the transition area between backthrust-dominated and forethrust-dominated architectures, deformation is mainly expressed by sub-vertical strike-slip faults compartmentalizing adjacent fold sectors, which underwent block rotation about vertical axes.

4. Strike-slip faults crosscutting also Miocene deposits are present in the mapped area, and might be correlated with NNE to NE directed shortening after the Oligocene to Late Miocene extensional phase associated with the development of the Dinaric lake system. Such a contractional regime, which is still active, is associated with the anticlockwise rotation of the Adria plate since Miocene time.

5. Mechanical stratigraphy strongly influenced the deformation pattern in the folded and faulted sedimentary succession, despite all the exposed rocks formed in a carbonate platform environment. This indicates that the primary control on deformation patterns in platform carbonates is exerted at the facies level.

6. Evidence from structural diagenesis supports the evolution from a “bed-confined” fluid system to an open one only during late-stage fold tightening. Such a switch in fluid circulation was favored by development of strike-slip faults dissecting the anticline. This implies that particular attention should be paid in reservoir structural characterization to the presence of late-stage, low-displacement strike-slip faults because of their role of effective conduits for fluid flow. Moreover, we remark the role of inherited diagenetic fluid during the earlier stage of deformation for controlling cement precipitation and changing in mechanical properties of the involved succession.

7. This work indicates that despite the complex fold architecture of the Pag anticline, developed in shallow condition of deformation, a quite classical background fold-related deformation pattern formed. However, conventional templates for folding-related fracturing do not predict the coexistence of folding-related thrusts and misoriented strike-slip faults. Similar atypical fault and fold pattern could be expected also in structures at the toe of other thrust wedges, where inherited pre-folding extensional faults frequently occur. We consequently stress the importance of studying appropriate field analogues for fault-related folds constrained by

a multiscale and multidisciplinary approach, for understanding the timing of the fault, fold and fracture system growth.

ACKNOWLEDGMENTS

Discussions with Fabrizio Balsamo and Luigi Berio in the NEXT research group framework, are gratefully acknowledged. We are also indebted to Roberto Fantoni (Eni S.p.A.) for sharing his view on the tectonostratigraphic evolution of the External Dinarides. We are grateful to Paola Iacumin and Enrico Selmo for providing carbon and oxygen isotope data and discuss their significance. We are indebted with Andrea Comelli for providing thin sections. Technical support from Cristian Cavozzi and Luca Barchi is gratefully acknowledged. We are grateful to Eni S.p.A. for funding this research and releasing the material for publication.

CHAPTER 6.

GENERAL CONCLUSIONS

Folding-related deformation patterns in foreland thrust-and-fold belts bear important academic implications for better understanding the evolution of orogenic systems, and also economic ones for optimizing hydrocarbon exploration and production in foreland basin system plays. For these reasons, such a subject is well studied and a large amount of specific literature is available and contributed to developing “classical” templates of deformation patterns in cylindrical folding. These templates and conceptual models contribute to driving the distribution of synthetic fracture attributes in reservoir models. However, multiple factors, including rheology (i.e., mechanical stratigraphy), strain rate, deformation-depth, the presence of inherited deformation structures, and their relative orientation, pore fluid pressure, and external driving stresses, typically contribute to determining folding-related deformation patterns, which can significantly deviate from what expected in “classical” cylindrical folding, particularly in case of transpressional tectonic regimes.

To further investigate on major factors controlling deformation patterns associated with folding and faulting at the toe of transpressional orogens, we performed a structural, petrographic-geochemical, and biostratigraphic study of the Pag anticline, in the External Dinarides of Croatia, where folded carbonate platform rocks are extremely well exposed. By combining field and photogrammetric techniques, we performed geological mapping at 1:25,000 scale of the Pag island, which allowed us recognizing an extensional faulting event atop of the Upper Cretaceous carbonate rocks, pre-dating the regional Santonian-Ypresian unconformity. Constraints on the age of folding were obtained by combing field and paleontological data on the well-exposed Dalmatian Flysch, outcropping along the coast of the Pag island. New nannofossil biostratigraphic data from the basal part of the turbiditic succession exposed in the Pag Island allowed us to reject the previously proposed Miocene age for the turbiditic succession and to support a Lutetian – Bartonian age for the Dalmatian Flysch. Moreover, our biostratigraphic study indicates that progressive deepening of the depositional environment occurred after marine transgression and Foraminiferal limestone deposition. A relative shallow water depositional environment near an estuarine to deltaic source area is suggested for the Dalmatian Flysch by paleontological and stratigraphic evidence, well-fitting into stratigraphic and paleoenvironment reconstructions proposed by previous authors for the surrounding areas. Although the early stages of fold growth controlled the morphology and distribution of the turbiditic basin, the main stage of folding and thrusting of the Pag anticline postdated turbidite deposition. Accordingly, we propose a post-Lutetian to pre-Burdigalian age for the main folding stage, based on field evidence and biostratigraphic data.

Our geological map documents folding of the pre- Santonian-Ypresian extensional faults, which are misoriented with respect to the hinge line of the Pag anticline. Actually, they are near almost perpendicular to the fold axial strike. Detailed structural analyses supported by UAV photogrammetric techniques, stress inversion, and slip tendency analyses, were carried out one of these pre-folding fault zones, i.e. the very well exposed Dinjiška Fault, which clearly shows the interaction between the inherited fault zone segment and a newly formed one cutting also through the Dalmatian Flysch. The evolutionary pathway proposed for the Dinjiška Fault applies to all the folded Late Cretaceous fault zones exposed in the Pag anticline. According to our data, the position and orientation of inherited fault ramps exerted a fundamental control on fold geometry and evolution. Actually, the ramp segments of such a shallowly-detached extensional fault network provided effective nucleation sites for strike-slip tear fault zones that propagated towards the anticlinal crest from both fold limbs, resulting in effective, widespread fold compartmentalization during late-stage tightening. Despite we are not aware of similar structural patterns described in the literature, the evidence that transverse extensional faults are abundant both in extensional and contractional settings, makes us confident that folded listric faults triggering segmentation of thrust-related anticlines by tear faulting should be a frequent feature at the toe of thrust wedges and in foreland basin systems. A reason for their apparent rarity might be possible overlooking as “simple” conjugate strike-slip fault arrays. Moreover, correct recognition in subsurface geophysical datasets is hampered by technical difficulties to properly image inherited extensional fault flat segments in fold limbs. Passive rotation and folding of thin-skinned extensional faults may provide an innovative template to produce complex fault arrays and related deformation patterns during late-stage fold tightening. The recognition of these structural features in fold and thrust belts and their potential as preferential pathways for fluid-flow could be a new exploration target for future research in structural diagenesis and fault-fold interactions.

The structural architecture and paleofluid evolution of the Pag anticline were investigated by a multidisciplinary study combining field analyses with microstructural, petrological and isotopical data, providing vein network characterization and constraints on the relative chronology of deformation structures and fold kinematic evolution. The anticline shows a high structural variability along strike, mostly controlled by the occurrence of a major overstepping conjugate thrust and backthrust pair. The tight fold geometry, the along-strike fold asymmetry variation, and the deformation style suggest a detachment fold kinematics, with the sole thrust located in the Upper Jurassic-Lower Cretaceous rocks, at about 2000-2500 m depth.

Along-strike variability, deformation style, and related deformation pattern were strongly influenced by mechanical stratigraphy, despite all exposed rocks formed in a carbonate platform environment. The pre-folding deformation pattern formed in two stages of layer-parallel shortening, respectively dominated by horizontal and then vertical σ_2. We interpret this shift of the intermediate principal stress axis as the result of an increase of the sedimentary/tectonic load during the layer-parallel-shortening stage. The major folding stage occurred under transpressional stress conditions, produced by counterclockwise rotation of σ_1, which continued during late folding stages. In particular, the syn- to late-folding deformation pattern developed under N-S right-lateral transpression superimposed on the older network of veins and stylolites that formed in response to a NE-SW compression. During fold evolution, N-S and E-W strike-slip faults underwent multiple reactivations with opposite shear senses.

In terms of structural diagenesis, isotopic signatures of pre-folding and syn-folding calcite-filled veins suggest a dissolution-re-precipitation process occurred in a bedset confined hydromechanic system. Inherited diagenetic fluids controlled cement precipitation and mechanical property changes of the folded succession. On the other hand, isotopic values of syn- to late-folding veins and fault cements on reactivated faults indicate meteoric fluid percolation through conduits produced by effective fracture networks affecting the entire deformed succession.

As a general conclusion, despite the complex fold architecture of the Pag anticline, a quite classical background folding-related deformation pattern formed. The fundamental perturbation that added significant complexity to such a background fracture pattern was provided by the Late Cretaceous, inherited extensional faults, which triggered the development of misoriented strike-slip faults and related damage zones. Similar atypical fault and fold patterns are be expected to occur also at the toe of other thrust wedges, where inherited pre-folding extensional faults frequently occur. We consequently stress on the importance of studying appropriate field analogues for fault-related folds, constrained by a multiscale and multidisciplinary approach, for understanding the timing of faulting and folding, folding-related deformation patterns, and paleofluid evolution.

The results of this Ph.D. Thesis bear scientific and industrial implications, providing insights into folding processes and fold architecture development in tight carbonate rocks. Understand folding-related processes is a fundamental step for obtaining fracture network templates from outcrop analogues, which are essential to fill the gap between seismic and well log or core scales.

BIBLIOGRAPHY

Agnini, C., Fornaciari, E., Raffi, I., Catanzariti, R., Pälike, H., Backman, J. & Rio, D. (2014). Biozonation and biochronology of Paleogene calcareous nannofossils from low and middle latitudes. *Newsletters on Stratigraphy*, v. 47, p. 131–181.

Anderson, H. & Jackson, J. (1987). Active tectonics of the Adriatic region. *Geophysical Journal International*, v. 91, p. 937–983.

Andrić, N., Sant, K., Matenco, L., Mandic, O., Tomljenović, B., Pavelić, D., Hrvatović, H., Demir, V. & Ooms, J. (2017). The link between tectonics and sedimentation in asymmetric extensional basins: Inferences from the study of the Sarajevo–Zenica Basin. *Marine and Petroleum Geology*, v. 83, p. 305-332, doi: 10.1016/j.marpetgeo.2017.02.024.

Angelier, J. (1979). Determination of the mean principal directions of stresses for a given fault population. *Tectonophysics*, v. 56, no. 3-4, p. T17-26, doi: https://doi.org/10.1016/0040-1951(79)90081-7.

Angelier, J. (1990). Inversion of field data in fault tectonics to obtain the regional stress. A new rapid direct inversion method by analytical means. *Geophysical Journal International*, v. 103, no. 2, p. 363–376, doi: https://doi.org/10.1111/j.1365-246X.1990.tb01777.x.

Aubouin, J., Blanchet, R., Cadet, J.P., Celet, P., Charvet, J., Chorowicz, J. & Rampnoux, J.P. (1970). Essai sur la geologie des Dinarides. *Bulletin de la Société Géologique de France*, S7–XII (6), 1060–1095, doi : https://doi.org/10.2113/gssgfbull.

Babić L. & Zupanič J. (2008a). Evolution of a river-fed foreland basin fill: the North Dalmatian flysch revisited (Eocene, Outer Dinarides). *Natura Croatica*, v. 17, no. 4, p. 357-365.

Babić L. & Zupanič J. (2016). The youngest stage in the evolution of the Dinaric carbonate platform: the Upper Nummulitic Limestones in the North Dalmatian foreland, Middle Eocene, Croatia. *Natura Croatica*, v. 25, no. 1, p. 55–71, doi: https://doi.org/10.20302/NC.2016.25.3.

Babić L., Zupanič J. & Crnjaković M. (1993). An association of marine tractive and gravity flow sandy deposits in the Eocene of the NW part of the Island of Pag (Outer Dinarides, Croatia). *Geologia Croatica*, v. 46, no. 1, p. 107–123.

Babić, L. & Zupanič, J. (1990). Progradacijski slijedovi u paleogenskom klastičnom bazenu Vanjskih Dinarida, od sjeverne Dalmacije do zapadne Hercegovine. *Rad Jug. akad. znan. Umj*, v. 449, no. 24, p. 319-343. [In Croatian]

Babić, L. & Zupanič, J. (2008b). Major events and stages in the sedimentary evolution of the Paleogene Promina basin (Dinarides, Croatia). *Geologia Croatica,* v. 16, no. 4, p. 215-232.

Babić, L., Hernitz-Kučenjak, M, Corić, S. & Zupanič, J. (2007). The Middle Eocene age of the supposed late Oligocene sediments in the flysch of the Pazin Basin (Istria, outer Dinarides). *Natura Croatica*, v. 16, p. 83–103.

Bada, G., Horvath, F., Dovenyi, P., Szafian, P., Windhoffer, G. & Cloetingh, S. (2007). Present day stress field and tectonic inversion in the Pannonian basin. *Global and Planetary Change*, v. 58, p. 165-180.

Bally, A.W., (1987). Balanced Sections and Seismic Reflection Profiles Across the Central Apennines, Italy. *Huston Geological Society Bulletin*, v.29, no. 8, p. 11-12.

Barbier, M., Hamon, Y., CAllot, J-P., Floquet, M. & Daniel, J.M. (2012). Sedimentary and diagenetic controls on the multiscale fracturing pattern of carbonate reservoir: The Madison Formation (Sheep Mountain, Wyoming, USA), *Marine and Petroleum Geology*, v. 29, p. 50-67.

Beaudoin, N., Leprêtre, R., Bellahsen, N., Lacombe, O., Amrouch, K., Callot, J.P., Emmanuel, L. & Daniel, J.M. (2012). Structural and microstructural evolution of the Rattlesnake Mountain Anticline (Wyoming, USA): new insights into the Sevier and Laramide orogenic stress build-up in the Bighorn Basin. *Tectonophysics*, v. 576, p. 20–45.

Bega, Z. (2015). Hydrocarbon Exploration Potential of Montenegro - a Brief Review, *Journal of Petroleum Geology*, v. 38, no. 3, doi: 10.1111/jpg.12613.

Bellahsen, N., Fiore, P. & Pollard, D.D. (2006). The role of fractures in the structural interpretation of Sheep Mountain Anticline, Wyoming. *Journal of Structural Geolology*, v. 28, no. 5, p. 850–867.

Benić, J. (1975). Calcareous nannoplankton from the Eocene flysch on Pag Island. *Geolos˘ki vjesnik*, v. 28, p. 19–23.

Bergbauer, S. & Pollard, D.D. (2004). A new conceptual fold-fracture model including prefolding joints, based on the Emigrant Gap anticline, Wyoming. *Geological Society of America Bulletin*, v. 116, p. 294–307.

Billi, A. & Salvini, F. (2003). Development of systematic joints in response to flexure-related fibre stress in flexed foreland plates: the Apulian forebulge case history, Italy. *Journal of Geodynamics*, v. 36, no. 4, p. 523–536.

Bistacchi, A., Massironi, M., Menegon, L., Bolognesi, F. & Donghi, V. (2012). On the nucleation of non-Andersonian faults along phyllosilicate-rich mylonite belts. *Journal of the Geological Society* [London], Special Publications, v. 367, p. 185-199, doi: https://doi.org/10.1144/SP367.13.

Bonini, M., Sani, F., & Antonelli, B. (2012). Basin inversion and contractional reactivation of inherited normal faults: A review based on previous and new experimental models. *Tectonophysics*, v. 522-523, p. 55-88, doi: https://doi.org/10.1016/j.tecto.2011.11.014.

Bown, P.R. & Dunkley Jones, T. (2006). New Paleogene calcareous nannofossil taxa from coastal Tanzania: Tanzania Drilling Project Sites 11 to 14. *Journal of Nannoplankton Research*, v. 28, no. 1, p. 17-34.

Bown, P.R. & Dunkley Jones, T. (2012). Calcareous nannofossils from the Paleogene equatorial Pacific (IODP Expedition 320 Sites U1331-1334). *Journal of Nannoplankton Research*, v. 32, no. 2, p. 3-51.

Bown, P.R. & Newsam, C. (2017). Calcareous nannofossils from the Eocene North Atlantic Ocean (IODP Expedition 342 Sites U1403–1411). *Journal of Nannoplankton Research*, v. 37, no. 1, p. 25–60.

Bown, P.R. & Young, J. R. (2019). The fossil record of coastal coccolithophores. *Journal of Nannoplankton Research,* Special Issue, v. 4, p. 73-80.

Bown, P.R. & Young, J.R. (1998). Introduction - calcareous nannoplankton biology. In: Bown, P.R. (eds.), *Calcareous nannofossil biostratigraphy*. British Micropalaeontological Society Publication Series. Chapman and Hall, pp. 1-15.

Bown, P.R. (2005). Palaeogene calcareous nannofossils from the Kilwa and Lindi areas of coastal Tanzania (Tanzania Drilling Project 2003-4). *Journal of Nannoplankton Research,* v. 27, no. 1, p. 21-95.

Bown, P.R. (Editor), (1998). Calcareous nannofossil biostratigraphy. *British Micropalaeontological Society Publication Series*, Chapman and Hall, Cambridge, 328 pp.

Brlek, M. & Glumac, B. (2014). Stable isotopic (δ 13 C and δ 18 O) signatures of biogenic calcretes marking discontinuity surfaces: a case study from Upper Cretaceous carbonates of central Dalmatia and eastern Istria, Croatia. *Facies*, v. 60, no. 3, p. 773-788.

Bulić J. & Jurišić-Polšak Z. (2009). Macropalaeontology and stratigraphy of lacustrine Miocene deposits at Crnika beach on the Island of Pag (Croatia). *Geologia Croatica*, v. 62, no. 3, p. 135–155, doi: https://doi.org/10.4154/gc.2009.16.

Burkhard, M. (1993). Calcite twins, their geometry, appearance and significance as stress-strain markers and indicators of tectonic regime: a review. *Journal of structural geology*, v. 15, p. 351-368.

Butler, R.W.H. (1989), The influence of pre-exiting basin structure on thrust system evolution in the Western Alps. *Journal of the Geological Society* [London], Special Publications, v. 44, no. 1, p. 105-122, doi: https://doi.org/10.1016/j.jsg.2006.09.006.

Butler, R.W.H., Tavarnelli, E. & Grasso, M. (2006). Structural inheritance in mountain belts: an Alpine-Apennine perspective. *Journal of Structural Geology*, v. 28, no. 11, p.1893-1908, doi: https://doi.org/10.1016/j.jsg.2006.09.006.

Byerlee, J.D. (1978). Friction of rocks. *Pure and Applied Geophysics*, v.116, p. 615–626.

Calais, E., Nocquet, J. M., Jouanne, F. & Tardy, M. (2002). Current strain regime in the Western Alps from continuous global positioning system measurements, 1996–2001. *Geology*, v. 30, p. 651–654.

Cande, S.C. & Kent, D.V. (1995). Revised calibration of the geomagnetic polarity time scale for the Late Cretaceous and Cenozoic. *Journal of Geophysical Research,* v.100(B4), p. 6093–6096, doi:10.1029/94JB03098.

Caputo, R., Chatzipetros, A., Pavlides, S. & Sboras, S. (2012). The greek database of seismogenic sources (GreDaSS): State-of-the-art for northern greece. *Annual of Geophysical*, v. 55, p. 859-894.

Chester, J.S., Logan, J.M. & Spang, J.H. (1991). Influence of layering and boundary conditions on fault-bend and fault-propagation folding. *Geological Society of America Bulletin,* v. 103, no. 8, p. 1059–1072.

Cloetingh, S., Bada, G., Matenco, L., Lankreijer, A., Horvath, F. & Dinu, C. (2006). Modes of basin (de)formation, lithospheric strength and vertical motions in the Pannonian–Carpathian system: inferences from thermo-mechanical modeling. *Journal of the Geological Society* [London], Memoirs, v. 32, p. 207–221.

Cooke, M., L. (1997). Predicting fracture localization in folded strata from mechanical stratigraphy and fold shape: Case study of east Kaibab monocline: Proceedings of 36th U.S. Rock Mechanics Sumposium: *International Journal of Rock Mechanics and Mining Sciences*, Special Issue, v. 34, no. 3/4, p. 351.

Cooke, M.L. & Underwood, C.A. (2001). Fracture termination and step-over at bedding interfaces due to frictional slip and interface open. *Journal of Structural Geology*, v. 23, p. 223-238.

Cooper, M. (1992). The analysis of fracture systems in subsurface thrust structures from the Foothills of the Canadian Rockies. Thrust tectonics 391–405.

Cooper, M.A., Williams, G.D., de Graciamsky, P.C., Murphy, R.W., Needham, T., de Paor, D., Stoneley, R., Todd, S., P., Turner, J.P. & Ziegler, P.A. (1989). Inversion tectonics – a discussion. In: Cooper, M.A., Williams, G.D., (eds.), Inversion Tectonics: *Journal of Geological Society* [London], Special Pubblications, v. 44, p. 335-347.

Corbett, K., Friedman, K. & Spang, J. (1987). Fracture development and mechanical stratigraphy of Austin Chalk, Texas. *American Association of Petroleum Geosciences*, v. 71, p. 17-28.

Corbett, K., Friedman, M. & Spang, J. (1987). Fracture development and mechanical stratigraphy of Austin Chalk, Texas, *American Association of Petroleum Geologist Bulletin*, v. 71, p. 17-28.

Ćosović V., Mrinjek E., Nemec W., Španiček J. & Terzić K. (2018). Development of transient carbonate ramps in an evolving foreland basin. *Basin Research*, v. 30, no. 4, p. 746–765, doi: https://doi.org/10.1111/bre.12274.

Ćosović, V., Drobne, K. & Moro, A. (2004). Paleoenvironmental model for Eocene foraminiferal limestones of the Adriatic carbonate platform (Istrian peninsula). *Facies*, v. 50, p. 61-75, doi: https://doi.org/10.1007/s10347-004-0006-9.

Ćosović, V., Drobne, K., Ogorelec, B., Moro, A., Koić, M., Šoštarko, I., Tarlao, A. & Tunis, G. (2008). Decastronema barattoloi (de Castro), characteristic fossil of the Palaeocene and the Eocene peritidal sediments from the Adriatic Carbonate Platform. *Geologia Croatica,* v. 61, p. 321-332, doi: https://doi.org/10.1111/bre.12274, [In Croatian].

Coward, M.P., Gillcrist, R. & Trudgill, B. (1991). Extensional structures and their tectonic inversion in the Western Alps. In: Roberts, A.M., Yielding, G., & Freeman, B. (eds.), The Geometry of Normal Faults: *Journal of Geological Society* [London], Special Pubblication, v. 56. p. 93–113.

D'Agostino, N., Avallone, A., Cheloni, D., D'Anastasio, E., Mantenuto, S. & Selvaggi, G. (2008). Active tectonics of the Adriatic region from GPS and earthquake slip vectors. *Journal of Geophysical Research*, v. 113, p. B12413, doi: 10.1029/2008JB005860.

Davey, S. D. & Jenkyns, H. C. (1999). Carbon-isotope stratigraphy of shallow-water limestones and implications for the timing of Late Cretaceous sea-level rise and anoxic events (Cenomanian-Turonian of the peri-Adriatic carbonate platform, Croatia). *Eclogae Geologicae Helvetiae*, v. 92, no. 2, p. 163-170.

De Capoa, P. & Radoicić, R. (1994a). Calcareous nannoplankton biostratigraphy of Tertiary sequences of the Cukali-Budva Basin (Montenegro, External Dinarides, Yugoslavia). *Rivista Espanola de Micropaleontologia*, v. 26, p. 101–116.

De Capoa, P. & Radoicić, R. (1994b). Tertiary nannoplankton biostratigraphy of the Zeta Intraplatform Furrow (Montenegro). *Palaeopelagos*, v. 4, p. 289–294.

De Capoa, P. & Radoicić, R. (2002). Geological implications of biostratigraphic studies in the external and internal domains of the Central-Southern Dinarides. *Memorie della Società Geologica Italiana*, v. 57, p. 185–191.

De Capoa, P., Radoicić, R. & D'argenio, B. (1995). Late Miocene deformation of the External Dinarides (Montenegro and Dalmatia): New biostratigraphic evidence. *Memorie di Scienze Geologiche,* v. 47, p. 157–172.

De Leeuw, A., Mandic, O., Krijgsman, W., Kuiper, K. & Hrvatović, H. (2012). Paleomagnetic and geochronologic constraints on the geodynamic evolution of the Central Dinarides. *Tectonophysics*, v. 530-531, p. 286-298, doi: https://doi.org/10.1016/j.tecto.2012.01.004.

DeCelles, P.G. & Giles, K.A. (1996). Foreland basin systems. *Basin research,* v. 8, p. 105-123.

Delvaux, D. & Spencer, B. (2003). New aspects of the tectonic stress inversion with reference to the TENSOR program. In: Nieuwland, D.A., (eds.), New insight into Structural Interpretation and Modelling. *Journal of the Geological Society*

[London], Special Publications, v. 212, p. 75-100, doi: https://doi.org/10.1144/GSL.SP.2003.212.01.06.

Delvaux, D. (2011). Win-Tensor, an interactive computer program for fracture analysis and crustal stress reconstruction: *Geophysical Research Abstract*. In: Proceedings, EGU General Assembly, 2011, v.13, EGU2011-4018, Vienna.

Destro, N. (1995). Release fault: A variety of cross fault in linked extensional fault systems, in the Sergipe-Alagoas Basin, NE Brazil. *Journal of Structural Geology*, v. 17, no. 5, p. 615-629, doi: https://doi.org/10.1016/0191-8141(94)00088-H.

Dickson, J. A. D. (1966). Carbonate identification and genesis as revealed by staining. *Journal of Sedimentary Research*, v. 36, no. 2, p. 491-505.

Dimitrijević, M. D. (1997). Geology of Yugoslavia. 2nd edition, *Geoinstitute, Belgrade*, Serbia.

Dimitrijević, M. D. (2001). Dinarides and the Vardar Zone: a short review of the geology. *Acta Vulcanologica*, v. 13, no. 1-2, p. 1-8, doi: 10.1400/19061.

Doglioni, C. (1995). Geological remarks on the relationships between extension and convergent geodynamic settings. *Tectonophysics*, v. 252, no. 1, p. 253–267.

Eisenstadt, G. & De Paor, D.G. (1987). Alternative model of thrust–fault propagation. *Geology*, v. 15, no. 7, p. 630–633.

Engelder, T. & Engelder, R. (1977). Fossil distortion and decollement tectonics of the Appalachian Plateau. *Geology*, v. 5, no. 8, p. 457–460.

Engelder, T. & Geiser, P. (1980). On the use of regional joint sets as trajectories of paleostress fields during the development of the Appalachian Plateau, New York. *Journal of Geophysical Research*, v. 85, no. 11, p. 6319–6341.

Etchecopar, A. (1984). Étude des états de contrainte en tectonique cassante et simulations de déformations plastiques: approche mathématique [Ph.D. thesis]: Univeisry of Science and Technique du Languedoc, Montpellier, 272 p.

Evans, M.A. & Dunne, W.M. (1991). Strain factorization and partitioning in the North Mountain thrust sheet, central Appalachians, USA. *Journal of Structural Geology*, v. 13, no. 1, p. 21–35.

Evans, M.A. (2010). Temporal and spatial changes in deformation conditions during the formation of the Central Appalachian fold-and-thrust belt: Evidence from joints, vein mineral paragenesis, and fluid inclusions. From Rodinia to Pangea: The Lithotectonic Record of the Appalachian Region 206, p. 477.

Faccenna, C., Becker, T. W., Auer, L., Billi, A., Boschi, L., Brun, J.-P., Capitanio, F. A., Funiciello, F., Horvath, F., Jolivet, L., Piromallo, C., Royden, L., Rossetti, F. & Serpelloni, E. (2014). Mantle dynamics in the Mediterranean. *Reviews of Geophysics*, v. 52, no. 3, p. 283-332. doi: 10.1002/2013RG000444.

Farinacci, A. (1969-1989). Catalogue of calcareous nannofossils. *Tecnoscienza*, Roma.

Ferreira E. P., Alves, C. F., Sanjinésa, A. E. S. & Alves, M. C. (2019). Ascidian spicules of Quaternary sediments from the lower slope of the Campos Basin (Brazil). *Quaternary International*, v. 508, p. 116-124.

Ferril, D.A., Morris, A.P. & McGinnis, R.N. (2012). Extensional fault-propagation folding in mechanically layered rocks: the case against the frictional drag mechanism. *Tectonophysics*, v. 577, p. 78-85.

Ferril, D.A., Morris, A.P. & Smart, K.J. (2007). Stratigraphic control on extensional faulting propagation folding: Big Brushy Canyon monocline, Sierra del Carmen, Texas. In: Jolley, S., Barr, D., Walsh, J.J. & Knipe, R.J. (eds.), Structurally Complex Reservoirs. *Journal of the Geological Society* [London], Special Publication, v. 292, p. 203-217.

Ferril, D.A., Morris, A.P., Jones, S.M. & Stamatakos, J.A. (1998). Extensional layer parallel shear and normal faulting. *Journal of Structural Geology*, v. 20, p. 355-362.

Ferrill, D.A. & Groshong, R.H. (1993). Kinematic model for the curvature of the northern Subalpine Chain, France. *Journal of Structural Geology*, v. 15, no. 3, p. 523–541.

Ferrill, D.A., Morris, A.P., Wigginton, S.S., Smart, K.J., McGinnis, R.N. & Lehrmann, D. (2016). Deciphering thrust fault nucleation and propagation and the importance of footwall synclines. *Journal of Structural Geology*, v. 85, p. 1-11.

Fioroni, C., Villa, G., Persico, D. & Jovane, L. (2015). Middle Eocene-Lower Oligocene calcareous nannofossil biostratigraphy and paleoceanographic implications from Site 711 (equatorial Indian Ocean). *Marine Micropaleontology*, v. 118, p. 50-62.

Fischer, M.P. & Jackson, P.B. (1999). Stratigraphic controls on deformation patterns in faultrelated folds: a detachment fold example from the Sierra Madre Oriental, northeast Mexico. *Journal of Structural Geology*, v. 21, no. 6, p. 613–633.

Fischer, M.P. & Jackson, P.B. (1999). Stratigraphic controls on deformation patterns in fault related folds: a detachment fold example from the Sierra Madre Oriental, northeast Mexico. *Journal of Structural Geology*, v. 21, no. 6, p. 613–633.

Fornaciari, E., Agnini, C., Catanzariti, R., Rio, D., Bolla, E.M. & Valvasoni, E. (2010). Mid- Latitude calcareous nannofossil biostratigraphy and biochronology across the middle to late Eocene transition. *Stratigraphy*, v. 7, no. 4, p. 229-264.

Friedman, I., & O'Neil, J. R. (1977). Compilation of stable isotope fractionation factors of geochemical interest, Vol. 440, US Government Printing Office.

Fuček, L., Matičec, D., Vlahović, I., Oštrić, N., Prtoljan, B., Korbar, T. & Husinec, A (2012) - Osnovna geološka karta Republike Hrvatske M 1:50 000: list Cres 2, (417/2). - Hrvatskigeološki institut (Zavod za geologiju), 1 list, Zagreb, ISBN: 978-953-6907-26-7.

Gale, J.F.W., Laubach, S.E., Olson, J.E., Eichubl, P. & Fall, A. (2014). Natural fractures in shale: a review and new observations, *American Association of Petroleum Geologist Bulletin*, v. 98, no. 11, p. 2165-2216, doi: 10.1306/08121413151.

Gerner, P., Bada, G., Dövenyi, P., Müller, B., Oncescu, M., Cloetingh, S. & Hórvath, F. (1999). Tertiary extension within the Alpine Orogen. In: Seranne, M. (eds.), Recent tectonic stress and crustal deformation in and around the Pannonian Basin: data and models: the Mediterranean basins. *Journal of the Geological Society* [London], Special Publications, v. 156, p. 269–294.

Gillcrist, R., Coward, M. & Mugnier, J-L. (1987). Structural inversion and its controls: examples from the Alpine foreland and the French Alps. *Geodinamica Acta*, v. 1, p. 5-34, doi: 10.1080/09853111.1987.11105122.

Gray, M.B. & Mitra, G. (1993). Migration of deformation fronts during progressive deformation: evidence from detailed structural studies in the Pennsylvania Anthracite region, USA. *Journal of Strctural Geology*, v. 15, no. 3, p. 435–449.

Grenerczy, G., Sella, G., Stein, S., & Kenyeres, A. (2005). Tectonic implications of the GPS velocity field in the Northern Adriatic region, Geophysical Research Letters, 32(L16311), 1-4. doi: 10.1029/2005GL022947.

Griffith, A.A. (1924). The theory of rupture. In: Biezeno, C.B. & Burgers, J.M. (eds.), First International Congress on Applied Mechanics, Delft, J. Waltman, pp. 55–63.

Gross, M.R. (1993). The origin and spacing of cross joints: examples from the Monterey Formation, Santa Barbara Coastline, California. *Journal of Structural Geology*, v. 15, no. 6, p. 737–751.

Gross, M.R., Fischer, M.P., Engelder, T. & Greenfield, R.J. (1995). Factors controlling joint spacing in interbedded sedimentary rocks: integrating models with field observations from the Montery Formation, USA. In: Ameen, M.S. (eds.), Fractography: Fracture Topography as a Tool in Fracture Mechanics and Stress Analysis. *Journal of the Geological Society* [London], Special Pubblication, v. 92, p. 215-233.

Grubić, A. & Komatina, M. (1963). Properties of the Eocene-Oligocene Flysch between Split and Makarska. *Sedimentologija*, v. *2–3*, p. 21–38.

Gušić I. & Jelaska V. (1993). Upper Cenomanian-lower Turonian sea-level rise and its consequences on the Adriatic-Dinaric carbonate platform. *Geologisches Rundschau*, v. 82, no. 4, p. 676–686, doi: https://doi.org/10.1007/BF00191495.

Gutiérrez-Alonso, G. & Gross, M.R. (1999). Structures and mechanisms associated with development of a fold in the Cantabrian Zone thrust belt, NW Spain. Journal of Structural Geology, v. 21, no. 6, p. 653–670.

Handy, M.R., Ustaszewski, K. & Kissling, E. (2015). Reconstructing the Alps–Carpathians–Dinarides as a key to understanding switches in subduction polarity, slab gaps and surface motion. *International Journal of Earth Sciences*

(Geologisches Rundschau), v. 104, no. 1, doi: https://doi.org/10.1007/s00531-014-1060-3.

Harzhauser, M., Mandic, O., Latal, C. & Kern, A. (2011). Stable isotope composition of the Miocene Dinaride Lake System deduced from its endemic mollusc fauna. *Hydrobiologia*, v. 682, p. 27-46.

Hauer F. R. Von. (1868). Geologische Übersichtskarte der Österreichischen Monarchie. Jahrb. d. k. k. Geol. R. A. Bd, 3(431).

Hay, W.W., Mohler, H.P. & Wade, M.E. (1966). Calcareous nannofossils from Nalchik (northwest Caucasus). *Eclogae Geologicae Helvetiae*, v. 59, p. 379-399.

Hay, W.W., Mohler, H.P., Roth, P.H., Schmidt, R.R., & Boudreaux, J.E. (1967). Calcareous nannoplankton zonation of the Cenozoic of the Gulf Coast and Caribbean-Antillean area, and transoceanic correlation. *Transactions of the Gulf Coast Association of Geological Societies*, v. 17, p. 428-480.

Heberer, B., Reverman, R.L., Fellin, M.G., Neubauer, F., Dunkl, I., Zattin, M., Seward, D., Genser, J. & Brack, P. (2017). Postcollisional cooling history of the Eastern and Southern Alps and its linkage to Adria indentation. International Journal of Earth Sciences, v. 106, p. 1557-1580.

Heidbach, O., Custodio, S., Kingdon, A., Mariucci, M. T., Montone, P., Müller, B., Pirdominici, S., Rajabi, M., Reinecker, J., Reiter, K., Tingay, M., Williams, J. & Ziegler, M. (2016). Stress Map of the Mediterranean and Central Europe 2016. GFZ Data Services, 45. https://doi.org/10.5880/WSM.EUROPE2016.

Heidbach, O., Rajabi, M., Cui, X., Fuchs, K., Muller, B., Reinecker, J., Reiter, K., Tingay, M., Wenzel, F., Xie, F., Ziegler, M.O., Zoback, M.-L. & Zoback, M. (2018). The World Stress Map database release 2016: Crustal stress pattern across scales. *Tectonophysics*, v. 744, p. 484-498.

Heidbach, O., Reinecker, J., Tingay, M., Muller, B., Sperner, B., Fuchs, K. & Wenzel, F. (2007). Plate boundary forces are not enough: Second- and third-order stress patterns highlighted in the World Stress Map database. *Tectonics*, v. 26, p. 486-497.

Herak, M. & Bahun, S. (1979). The role of the calcareous breccias (Jelar Formation) in the tectonic interpretation of the High Karst Zone of the Dinarides. *Geologia. Vjesnik,* v. 31, p. 49-59.

Herak, M. (1986). A new concept of geotectonics of the Dinarides. *Acta Geologica*, v. 16, no. 1, p. 1-42.

Higgs, W.G., Williams, G.D. & Powell, C.M. (1991). Evidence for flexural shear folding associated with extensional faults. *Geological Society of America Bulletin*, v. 103, p. 710-717.

Holail, H. (1994). Carbon and oxygen ratios of Middle Eocene dolomite, Gebel Ataqa, Egypt. *Neues Jahrbuch für Geologie und Paläontologie. Abhandlungen*, v. 191, no. 1, p. 111-124.

Hrvatović, H. (2006). Geological Guidebook through Bosnia and Herzegovina (ISBN: 9958-9351-3). Sarajevo, Bosnia and Herzegovina: Geological Survey of Federation Bosnia and Herzegovina.

Husinec A. & Jelaska V. (2006) . Relative Sea-Level Changes Recorded on an Isolated Carbonate Platform: Tithonian to Cenomanian Succession. *Southern Croatian Journal of Sedimentary Research*, v. 76, no. 10, p. 1120–1136, doi: https://doi.org/10.2110/jsr.2006.099.

Ilić A. & Neubauer F. (2005). Tertiary to recent oblique convergence and wrenching of the Central Dinarides: Constraints from a palaeostress study. *Tectonophysics*, v. 14, p. 465–484, doi: https://doi.org/10.1016/j.tecto.2005.02.019.

Incerpi, N., Martire, L., Manatschal, G., Bernasconi, S. M., Gerdes, A., Czuppon, G., Palcsu, L., Karner, L.D., Johnson, C.A. & Figueredo P.H. (2019). Hydrothermal fluid flow associated to the extensional evolution of the Adriatic rifted margin: Insights from the pre- to post-rift sedimentary sequence (SE Switzerland, N Italy). Basin Research, *online version*, doi: https://doi.org/10.1111/bre.12370.

Jammes, S., Huismans, R.S. & Muñoz, J.A. (2014). Lateral variation in structural style of mountain building: controls of rheological and rift inheritance. *Terra Nova*, v. 26, no. 3, p.201-207, doi: https://doi.org/10.1111/ter.12087.

Jarosinski, M., Beekman, F., Bada, G., Cloetingh, S. (2006): Redistribution of recent collision push and ridge push in Central Europe: insights from FEM modelling. Geophys. J. Int., 167, 860–880.

Jarosinski, M., Beekman, F., Matenco, L. & Cloetingh, S. (2011). Mechanics of basin inversion: Finite element modeling of the Pannonian Basin System. *Tectonophysics*, v. 502, no. 1-2, p. 121-145.

Jelaska, V., Gušić, I., Jurkovšek, B., Ogorelec, B., Ćosović, V., Sribar, L. & Toman, M. (1994). The Upper Cretaceous geodynamic evolution of the Adriatic-Dinaric carbonate platform, *in* Proceedings, Perimediterranean carbonate platforms, First International Meeting: France, Marseille, 5-8 September 1994, Volume 21, p. 89–91.

Jiménez-Moreno G., de Leeuw A., Mandic O., Harzhauser M., Paveli, D., Krijgsman W. & Vranjković A. (2009). Integrated stratigraphy of the Early Miocene lacustrine deposits of Pag Island (SW Croatia). Palaeovegetation and environmental changes in the Dinaride Lake System. *Palaeogeography and Palaeocology*, v. 280, no. 1–2, p. 193–206, doi: https://doi.org/10.1016/j.palaeo.2009.05.018.

Jonas, B. & Vergés, R. J. (2018). Effects of reactivated extensional basement faults on structural evolution of fold-and-thrust belts: Insights from numerical modelling applied to the Kopet Dagh Mountains. *Tectonophysics*, v. 746, p. 493-511, doi: https://doi.org/10.1016/j.tecto.2017.05.020.

Jouanne, F., Mugnier, J.L., Koci, R., Bushati, S., Matev, K., Kuka, N., Shinko, I., Kociu, S. & Duni, L. (2012). GPS constraints on current tectonics of Albania. *Tectonophysics*, v. 554-557, p. 50-62.

Kahle, H.G., Cocard, M., Peter, Y., Geiger, A., Reilinger, R., Barka, A. & Veis, G. (2000). GPS-derived strain rate field within the boundary zones of the Eurasian, African, and Arabian Plates. *Journal of Geophysical Research - Solid Earth*, v. 105, p. 23353-23370.

Kastelic V. & Carafa M.M.C. (2012). Fault slip rates for the active External Dinarides thrustand-fold belt. *Tectonics*, v. 31, no. 3, doi: https://doi.org/10.1029/2011TC003022.

Kastelic V., Vannoli P., Burrato P., Fracassi U., Tiberti M. M. & Valensise G. (2013). Seismogenic sources in the Adriatic Domain. *Marine Petroleum Geology*, v. 42, p. 191–213, doi: https://doi.org/10.1016/j.marpetgeo.2012.08.002.

Kemal-Sagular, E., Ünal Yümün, Z. & Meriç, E. (2018). New didemnid ascidian spicule records calibrated to the nannofossil data chronostratigraphically in the Quaternary marine deposits of Lake-Iznik (NW Turkey) and their paleoenvironmental interpretations. *Quaternary International*, v. 486, p. 143 – 155.

Konstantinou, K.I., Mouslopoulou, V., Liang, W.T., Heidbach, O., Oncken, O. & Suppe, J. (2017). Present-day crustal stress field in Greece inferred from regional-scale damped inversion of earthquake focal mechanisms. *Journal of Geophysical. Research - Solid Earth*, v. 122, p. 506-523.

Korbar T. & Husinec A. (2003). Biostratigraphy of Turonian to Coniacian Platform Carbonates : A Case Study from the Island of Cres (Northern Adriatic , Croatia). *Geologia Croatica*, v. 56, p. 173–186.

Korbar T., Glumac B., Tešović B. C. & Cadieux S. B. (2012). Response of a carbonate platform to the Cenomanian-Turonian Drowning and OAE 2: a case study from the Adriatic Platform (Dalmatia, Croatia). *Journal of Sedimentary Research*, v. 82, no. 3, p. 163–176, doi: https://doi.org/10.2110/jsr.2012/17.

Korbar, T. (2009). Orogenic evolution of the External Dinarides in the NE Adriatic region: a model constrained by tectonostratigraphy of Upper Cretaceous to Paleogene carbonates. *Earth-Science Reviews*, v. 96, no. 4, p.296–312, doi: https://doi.org/10.1016/j.earscirev.2009.07.004.

Korbar, T., Skelton, P.W., Tišljar, J., Moro, A., Vlahović, I., Velić, I. & Fuček, L. (2002). Middle to Upper Cenomanian transition: high-energy shoals with recumbent rudists to relatively low-energy environments with elevator rudists in southern Istria (Gomila, Tašalera and Fenoliga Islet). In: Vlahović, I. & Korbar, T. (eds.), 6th International Congress on Rudists, Rovinj, Abstracts and Excursion Guidebook, 111–122, Zagreb.

Kovačević Galović E., Ilijanić N., Peh Z., Miko S. &Hasan O. (2012). Geochemical discrimination of Early Palaeogene bauxites in Croatia. *Geologia Croatica*, v. 65, no. 1, p. 53–65, doi: https://doi.org/10.4154/gc.2012.04.

Lacombe, O. & Mouthereau, F. (1999). What is the real front of orogens? The Pyrenean orogen case. C. R. Acad. Sci. 329 (II), 889–896.

Lacombe, O. (2010). Calcite twins, a tool for tectonic studies in thrust belts and stable orogenic forelands. *Oil and Gas Science and Technology*, v. 65, no. 6, p. 809–838.

Lacombe, O., Bellahsen, N. & Mouthereau, F. (2011). Fracture patterns in the Zagros Simply Folded Belt (Fars, Iran): constraints on early collisional tectonic history and role of basement faults. *Geological Magazine*, v. 148, no. 5–6, p. 940–963.

Lacombe, O., Mouthereau, F., Deffontaines, B., Angelier, J., Chu, H.-T. & Lee, C.T. (1999). Geometry and quaternary kinematics of fold-and-thrust units of SW Taiwan. *Tectonics*, v. 18, no. 6, p. 1198–1223.

Lacombe, O., Mouthereau, F., Kargar, S. & Meyer, B. (2006). Late Cenozoic and modern stress fields in the western Fars (Iran): implications for the tectonic and kinematic evolution of central Zagros. *Tectonics*, v. 25, no. 1, TC1003.

Lacombe, O., Tavani, S. & Soto, R. (2012). An introduction to the Tectonophysics special issue “Into the deformation history of folded rocks”. *Tectonophysics*, v. 576–577, p. 1–3.

Langhi, L., Ciftci, N.B. & Borel, G.D. (2011). Impact of lithospheric flexure on the evolution of shallow faults in the Timor foreland system. *Marine Geology*, v. 284, no. 1, p. 40–54.

Laubach, S.E., Eichhubl, P., Hilgers, C. & Lander, R.H. (2010). Structural diagenesis. *Journal of Structural Geology*, v. 32, no. 12, p. 1866-1872, doi: https://doi.org/10.1016/j.jsg.2010.10.001.

Laubach, S.E., Olsen, J.E. & Gross, M.R. (2009). Mechanical and fracture stratigraphy, *American Association of Petroleum Geologist Bulletin*, v. 93, no. 11, p. 1413-1426.

Lisle, R.J., & Srivastava, D.C. (2004). Test of the frictional reactivation theory for faults and validity of fault-slip analysis. *Geology*, v. 32, no. 7, p. 569-572, doi: https://doi.org/10.1130/G20408.1.

Locker, S. (1967). Neue Coccolithophoriden (Flagellata) aus dem Alttertiar Norddeutschlands. *Geologie* (Berlin) *16*:361-364.

Macedo, J. & Marshak, S. (1999). Controls on the geometry of fold-thrust belt salients. *Geological Society of America Bulletin*, v. 111, no. 12, p. 1808-1822.

Majcen Ž., Korolija B., Sokač B., Nikler L. (1976) – Osnovna geološka karta SFRJ 1 : 100 000. Tumač za list Zadar L 33-139. Institut za geološka istraživanja, Zagreb, Savezni geološki zavod, Beograd [In Croatian].

Mamužić P., Sokač B. (1973) – Osnovna geološka karta SFRJ 1 : 100 000. Tumač za listov Silba L 33-126 i Molat L 33-138. Institut za geološka istraživanja, Zagreb, Savezni geološki zavod, Beograd [In Croatian].

Mandic, O., de Leeuw, A., Bulić, J., Kuiper, K. F., Krijgsman, W. & Jurišić-Polšak, Z. (2012). Paleogeographic evolution of the Southern Pannonian Basin: 40Ar/39Ar age constraints on the Miocene continental series of Northern Croatia. *International Journal of Earth Sciences*, v. 101, no. 4, p. 1033-1046, doi: 10.1007/s00531-011-0695-6.

Marin, B.A.S., Clift, H.S., Hamlin, H.S. & Laubach, S.E. (1993). Natural fractures in Sonora Canyon sandstone, Sutton County, Texas, *Society of Petroleum Engineers*, v. 258, p. 523-531.

Marinčić, S. (1981). Eocene flysch of the Adriatic area. *Geoloski vjesnik,* v. 34, p. 27–38.

Marinčić, S., Šparica, M., Tunis, G. & Uchman, A. (1996). The Eocene flysch deposits of the Istrian peninsula in Croatia and Slovenia: Regional, stratigraphic, sedimentological and ichnological analyses. *Annales*, v. 9, p. 139-156.

Marjanac L. & Marjanac T. (2004). Glacial history of the Croatian Adriatic and Coastal Dinarides. In: J. Ehlers & P. L. Gibbard (eds.), Quaternary Glaciations - Extent and Chronology (pp. 19–26). Elsevier B. V.

Marjanac L. (2012). Pleistocene glacial and periglacial sediments of Kvarner, northern Dalmatia and southern Velebit Mt. - Evidence of Dinaric glaciation. Doctoral thesis, University of Zagreb, Faculty of Science, Department of Geology.

Marjanac T. & Ćosović V. (2000). Tertiary Depositional History of Eastern Adriatic Realm. *Pancardi 2000*, Dubrovnik, Croatia, 1 – 3.10.2000, 93–103.

Marjanac T. & Marjanac L. (2016). The extent of middle Pleistocene ice cap in the coastal Dinaric Mountains of Croatia. *Quaternary Research*, v. 85, no. 3, p. 445–455, doi: https://doi.org/10.1016/j.yqres.2016.03.006.

Marjanac, T. (1993). Evolution of Eocene-Miocene flysch basin of Central Dalmatia, Croatia. PhD Thesis, University of Zagreb, 1-348.

Marshak, S. & Engelder, T. (1985). Development of cleavage in limestones of a fold–thrust belt in eastern New York. *Journal of Structural Geology*, v. 7, no. 3, p. 345–359.

Marshak, S. (1988). Kinematics of orocline and arc formation in thin-skinned orogens. *Tectonics*, v. 7, no. 1, p. 73-86.

Martini, E. (1971). Standard Tertiary and Quaternary calcareous nannoplankton zonation, in Proceedings of the Second Planktonic Conference Roma 1970, (ed. A. Farinacci), Edizioni Technoscienza, Rome, 2, 739-785.

Márton, E. & Moro, A. (2009). New paleomagnetic results from imbricated Adria: Its island and related areas. *Geologia Croatica*, v. 62, no. 2, p. 107-114, doi: 10.4154/gc.2009.09.

Márton, E., Drobne, K., Ćosovi ć, V. & Moro, A. (2003). Paleomagneteic evidence for Tertiary counterclockwise rotation of Adria. *Tectonophysics*, v. 377, p. 143-156, doi: https://doi.org/10.1016/j.tecto.2003.08.022.

Mazzoli, S., Pierantoni, P.P., Borraccini, F., Paltrinieri, W. & Deiana, G. (2005). Geometry, segmentation pattern and displacement variations along a major Apennine thrust zone, central Italy. Journal of Structural Geology, v. 27, no. 1, p. 1940–1953.

McClay, K. R. & Buchanan, P. G. (1992). Thrust faults in inverted extensional basins. In: McClay, K. R., (eds.), Thrust tectonics, Springer, Dordrecht, p. 93-104.

McClay, K.R. (1989). Analogue models of inversion tectonics. In: Cooper, M.A. & Williams, G.D. (eds.), Inversion tectonics: *Journal of the Geological Society* [London], Special Publications, v. 44, pp. 335-347.

Merlini, S., Doglioni, C. & Ponton, M. (2002). Analisi strutturale lungo un profilo geologico tra la linea Fella-Sava e l'avampaese adriatico (Friouli Venezia Giulia-Italia). Memorie della Società Geologica Italiana, v. 87, p. 31-40.

Microsoft (2019). Bing maps. [ONLINE] Available at: https://www.bing.com/maps. [Accessed 10 December 2018].

Mikes, T., Baldi-Beke, M., Kazmer, M., Dunkl, I. & von Eynatten, H. (2008). Calcareous nannofossil age constraints on Miocene flysch sedimentation in the Outer Dinarides (Slovenia, Croatia, Bosnia-Herzegovina and Montenegro). In: Siegesmund, S., Fügenschuh, B. & Froitzheim, N. (eds.), Tectonic Aspects of the Alpine-dinaride-carpathian System. *Journal of the Geological Society* [London], Special Publications, v. 298, pp. 335–363.

Mitra S. (2002). Fold-accommodation faults. *American Association of Petroleum Geologist Bulletin*, v. 4, no. 4, p. 671–693, doi: https://doi.org/10.1306/61EEDB7A-173E-11D7-8645000102C1865D.

Mittempergher, S., Succo, A., Bistacchi, A., Storti, F., Bruna, P. O. & Meda, M., (2019). Geological and structural map of the south-eastern Pag Island, Croatia: field constraints on the Cretaceous – Eocene evolution of the Dinarides foreland, *Geological Field Trips and Maps*, v. 11(2.4), doi: https://doi.org/10.3301/GFT.2019.04

Morris, A.P., Ferrill, D.A. & Henderson, D.B. (1996). Slip-tendency analysis and fault reactivation. *Geology*, v. 24, no. 3, p.275-278, doi: https://doi.org/10.1130/0091-7613(1996)024<0275:STAAFR>2.3.CO;2

Moulin, A., Benedetti, L., Rizza, M., Jamšek Rupnik, P., Gosar, A., Bourles, D., Keddadouche, K., Aumaitre, G., Arnold, M., Guillou, V. & Ritz, J.-F. (2016). The Dinaric fault system: Large-scale structure, rates of slip, and Plio-Pleistocene evolution of the transpressive northeastern boundary of the Adria microplate. *Tectonic*s, v. 35, p. 2258-2292.

Mozafari, M., Swennen, R., Balsamo, F., Desouky, H.E., Storti, F. & Taberner, C., (2019). Fault-controlled dolomitization in the Montagna dei Fiori Anticline (Central Apennines, Italy): record of a dominantly pre-orogenic fluid migration. *Solid Earth*, v.10, no.4, p.1355-1383, doi: https://doi.org/10.5194/se-10-1355-2019.

Mrinjek, E. (1993). Sedimentology and depositional setting of alluvial Promina Beds in Northern Dalmatia. *Geologia Croatica*, v. 46, no. 2, p. 243-261. Retrieved from https://hrcak.srce.hr/19915.

Muchez, P., Slobodnik, M., Viaene, W. A. & Keppens, E. (1995). Geochemical constraints on the origin and migration of palaeofluids at the northern margin of the Variscan foreland, southern Belgium. *Sedimentary Geology*, v. 96, no. 3-4, p. 191-200.

Nocquet, J.-M. (2012). Present-day kinematics of the Mediterranean: A comprehensive overview of GPS results. *Tectonophysics*, v. 579, p. 220-242.

Ogata, K., Storti, F., Balsamo, F., Tinterri, R., Bedogni, E., Fetter, M., Gomes, L. & Hatushika, R. (2017). Sedimentary facies control on mechanical and fracture stratigraphy in turbidites. *Geological Society of America Bulletin*, v. 129, p. 76-92, doi: 10.1130/B31517.1.

Okada, H. & Bukry, D. (1980). Supplementary modification and introduction of code numbers to the low–latitude coccolith biostratigraphic zonation (Bukry, 1973:1975). *Marine Micropaleontology*, v. *5*, no. 3, p. 321-325.

Oldow, J., Ferranti, L., Lewis, D., Campbell, J., D'Argenio, B., Catalano, R., Pappone, G., Carmignani, L., Conyi, P. & Aiken, C. (2002). Active fragmentation of Adria, the north African promontory, central Mediterranean orogen. *Geology*, v. 30, p. 779-782.

Olson, J.E., Laubach, S.E. & Lander, R.H. (2007). Combining diagenesis and mechanics to quantify fracture aperture distribution and fracture pattern permeability. In: Lorergan, R., Jolley, J., Sanderson, D.J. & Rawnsley, K. (eds.), Fractured reservoirs, *Journal of the Geological Society* [London], Special Pubblications, v. 270, p. 97-112.

Olson, J.E., Laubach, S.E. & Lander, R.H. (2009). Natural fracture characterization in thight gas sandstone: integrating mechanics and diagenesis. *American Association of Petroleum Geologist Bulletin*, v. 93, n. 11, p. 1535-1549, doi: 10.1306/08110909100.

Pälike, H., Norris, R.D., Herrle, J.O., Wilson, P.A., Coxall, H.K., Lear, C.H., Shackleton, N.J., Tripati, A.K. & Wade, B.S. (2006). The heartbeat of the Oligocene climate system. *Science,* v. 314, p. 1894–1898, doi: 10.1126/science.1133822

Pamić, J., Gušic, I. & Jelaska, V. (1998). Geodynamic evolution of the Central Dinarides. *Tectonophysics*, v. 297, p. 251–268.

Peh Z. &Kovačević Galović E. (2016). Geochemistry of Lower Palaeogene bauxites – unique signature of the tectonostratigraphic evolution of a part of the Croatian Karst. *Geologia Croatica*, v. 69, no. 2, p. 269–279, doi: https://doi.org/10.4154/gc.2016.24.

Perch-Nielsen, K. (1985). Cenozoic calcareous nannofossils. In: Plankton Stratigraphy (eds. H.N. Bolli; J.B. Saunders and K. Perch-Nielsen), Cambridge University Press, pp. 427-554.

Perouse, E., Sebrier, M., Braucher, R., Chamot-Rooke, N., Bourles, D., Briole, P., Sorel, D., Dimitrov, D. & Arsenikos, S. (2017). Transition from collision to subduction in Western Greece: the Katouna–Stamna active fault system and regional kinematics. *International Journal of Earth Sciences*, v. 106, p. 967-989.

Persico, D. & Villa, G. (2008). A new Eocene Chiasmolithus species: hypothetical reconstruction of its phyletic lineage. *Journal of Nannoplankton Research,* v. 30, no. 1, p. 23-33.

Persico, D., Fioroni, C., & Villa, G. (2012). A refined calcareous nannofossil biostratigraphy for the middle Eocene–early Oligocene Southern Ocean ODP sites. *Palaeogeography, Palaeoclimatology, Palaeoecology*, *335-336*, 12–23.

Persico, D., Succo, A., Storti, F., Piccinini, E. & Villa, G. (2019). Calcareous nannofossil biostratigraphy of the External Dinarides Flysch (Vrčić-Staravasa Pag Island, Croatia): A key to an Eocene tectono-stratigraphic and paleoenvironmental interpretation. *Geological Journal*, doi: 10.1002/gj.3673.

Piccoli, G. & Proto Decima, F. (1969). Ricerche biostratigrafiche sui depositi flyschoidi della regione Adriatica settentrionale e orientale. *Memorie degli Istituti di Geologia e Mineralogia dell'Università di Padova*, v. 27, p. 3–21.

Pinter, N., Grenerczy, G., Weber, J., Stein, S. & Medak, D. (2005). The Adria Microplate: GPS Geodesy, Tectonics and Hazards. *Nato Science Series IV Earth and Environmental Sciences*, v. 6, Dordrecht, The Netherlands: Springer.

Placer L., Vrabec M. & Celarc B. (2010). The bases for understanding of the NW Dinarides and Istria Peninsula tectonics. *Geologija*, v. 53, no. 1, p. 55–86, doi: https://doi.org/10.5474/geologija.2010.005.

Price, N.J. & Cosgrove, J.W. (1990). Analysis of Geological Structures.

Prtoljan B., Jamicic D., Tešovic B. C., Kratkovic I. & Markulin Ž. (2007). The influence of Late Cretaceous synsedimentary deformation on the Cenozoic structuration of the middle Adriatic, Croatia. *Geodynamic Acta*, v. 20, no. 5, p. 287–300, doi: https://doi.org/10.3166/ga.20.287-300.

Puškaric, S. (1987). Calcareous nannoplankton from clastic sediments of the Island of Hvar. RAD *Jugoslavenske akademije znanosti i umjetnosti,* v. 431, p. 7–16.

Radoicić R., De Capoa, P. & D'argenio, B. (1991). Middle-Late Miocenic age of the preorogenic sedimentation in the Dinaric carbonate platform domain of Herzegovina. *Annales Geologiques de la Peninsule Balkanique,* v. *55*, p. 1–21.

Radoicić, R., De Capoa, P. & D'argenio, B. (1989). Late rather than early Tertiary deformation of External Dinarides. Stratigraphic evidence from Montenegro. *Rendiconti dell'Accademia delle Scienze Fisiche e Matematiche Napoli*, v. 56, p. 41–59.

Ramsay, J.G. (1974). Development of chevron folds. *Geological Society of America Bulletin*, v. 85, no. 11, p. 1741–1754.

Reches, Z. & Lockner, D.A. (1994). Nucleation and growth of faults in brittle rocks: *Journal of Geophysical Research*, v. 99, p. 18159–18172.

Reinecker, J., Heidbach, O., Tingay, M., Sperner, B. & Müller, B. (2005). The Release 2005 of the World Stress Map. Available online: www.world-stress-map.org.

Rijken, P., Holder, J., Olson, J.E. & Laubach, S.E. (2002). Predicting fracture attributes in the Travis Peak Formation using quantitative mechanical modeling and structural diagenesis, Gulf Coast *Association of Geological Society Transactions*, v. 52, p. 837-847.

Roure, F., Fili, I., Najaz, S., Cadet, J.P., Mushka, K., & Bonneau, M. (2004). Kinematic Evolution and Petroleum Systems—An Appraisal of the Outer Albanides. In: K.R. McClay (eds.), Thrust tectonics and hydrocarbon systems. *American Association of Petroleum Geoscientist*, Memoir v. 82, pp. 474-493.

Sassi,W., Guiton, M.L.E., Leroy, Y.M., Daniel, J.M. & Callot, J.P. (2012). Constraints on bed scale fracture chronology with a FEM mechanical model of folding: the case of Split Mountain (Utah, USA). *Tectonophysics*, v. 576, p. 197–215.

Savage, H.M., Ryan Shackleton, J., Cooke, M.L. & Riedel, J.J. (2010). Insights into fold growth using fold-related joint patterns and mechanical stratigraphy. *Journal of Structural Geology*, v. 32, v.10,p. 1466–1475.

Schmid, S., Bernoulli, D., Fugenschuh, B., Matenco, L., Schefer, S., Schuster, R., Tischler, M., & Ustaszewski, K. (2008). The Alpine-Carpathian-Dinaridic orogenic system: correlation and evolution of tectonic units. *Swiss Journal of Geosciences*, v. 101, no. 1, p. 139-183. doi: 10.1007/s00015-008-1247-3.

Schmid, S.M., Bernoulli, D., Fugenschuh, B., Matenco, L., Schefer, S., Oberhansli, R. & Ustaszewski, K. (2014). Tracing the closure of Neotethys from the Alps to Western Turkey II: Similarities and differences between Dinarides, Hellenides and Anatolides-Taurides. *Geophysical Research Abstracts*, 13, EGU2011- 4000.

Schubert, R. J. & Waagen, L. (1913). Erläuterungen Geologischen Karte der Im Reichsrate vertretenen Königreiche und Länderder österr. – Ungar. Monarchie. SW-Oruppe Nr. 115 Pago. Verlag Der k. k. *Geologischen Reichsanstalt*.

Scisciani, V. (2009). Styles of positive inversion tectonics in the Central Apennines and in the Adriatic foreland: Implications for the evolution of the Apennine chain (Italy). *Journal of Structural Geology*, v. 31, no. 11, p. 1276-1294, doi: https://doi.org/10.1016/j.jsg.2009.02.004.

Shackleton, J.R., Cooke, M.L. & Sussam, A.J. (2005). Evidence of temporally changing mechanical stratigraphy and effects on joint-network architecture, *Geology*, v. 33, no. 2, p. 101-104.

Shackleton, J.R., Cooke, M.L., Vergés, J., Simó, T. (2011). Temporal constraints on fracturing associated with fault-related folding at Sant Corneli anticline, Spanish Pyrenees. Journal of Strctural Geology, v. 33, no. 1, p. 5–19.

Shamrock, J.L. & Watkins, D.K. (2009). Evolution of the Cretaceous calcareous nannofossil genus Eiffellithus and its biostratigraphic significance. *Cretaceous Research, v.* 30, no. 5, p. 1083-1102.

Shepherd, C. L. & Kulhanek, D. K. (2016). Eocene nannofossil biostratigraphy of the mid-Waipara River section, Canterbury Basin, New Zealand. J. *Nannoplankton Research,* v. 36, no. 1, pp.33–59.

Sibson, R.H. & Scott, J. (1998). Stress/fault controls on the containment and release of overpressured fluids: Examples from gold–quartz vein systems in Juneau, Alaska; Victoria, Australia and Otago, New Zealand: *Ore Geology Reviews*, v. 13, p. 293–306.

Sibson, R.H. (1985). A note on fault reactivation. *Journal of Structural Geology*, v. 7, no. 6, p. 751-754, doi: https://doi.org/10.1016/0191-8141(85)90150-6.

Sibson, R.H. (1995). Selective fault reactivation during basin inversion: potential for fluid redistribution through fault-valve action. In: Buchanan, J.G. & Buchanan, P.G. (eds.), Basin inversion. *Journal of the Geological Soci*ety [London], Special Publication, v. 88, pp. 3–19.

Šikic, D. (1964). Horizontalna kretanja u Dinaridima. Zbornik radova RGNF 1939-1964, 129-143, Zagreb.

Simón, J.L. (2019). Forty years of paleostress analysis: has it attained maturity?: *Journal of Structural Geology*, v. 125, p. 124-133, doi: https://doi.org/10.1016/j.jsg.2018.02.011.

Sokač, B., Šćavničar, B. & Velić, I. (1976). Osnovna geološka karta SFRJ 1: 100 000. Tumač za list Gospić L 33-127. Institut za geološka istraživanja, Zagreb, Savezni geološki zavod, Beograd.

Španiček J., Ćosović V., Mrinjek E. & Vlahović I. (2017). Early Eocene evolution of carbonate depositional environments recorded in the Čikola Canyon (North Dalmatian Foreland Basin, Croatia). *Geologia Croatica*, v. 70, no. 1, p. 11–25, doi: https://doi.org/10.4154/gc.2017.05.

Srivastava, D.C., Engelder, T., 1990. Crack-propagation sequence and pore fluid conditions during fault-bend folding in the Appalachian Valley and Ridge, central Pennsylvania.Geol. Soc. Am. Bull. 102 (1), 116–128.

Stampfli, G. M. & Borel, G. D. (2002). A plate tectonic model for the Paleozoic and Mesozoic constrained by dynamic plate boundaries and restored synthetic oceanic isochrones. *Earth and Planetary Science Letters*, v. 196, no. 1–2, p. 17-33, doi: 10.1016/S0012-821X(01)00588-X.

State Geodetic Administration of Croatia (2015) – Geoportal DGU. [ONLINE] Available at: https://geoportal.dgu.hr/. [Accessed 10 December 2018].

Stearns, D.W. (1968). Certain aspects of fracture in naturally deformed rocks. Rock Mechanics Seminar: Air Force Cambridge Research Laboratory, pp. 97–118.

Storti, F. & Salvini, F. (1996). Progressive rollover fault-propagation folding: a possible kinematic mechanism to generate regional-scale recumbent folds in shallow foreland belts. American Association of Petroleum Geosciences Bulletin, v. 80, no. 2, p. 174–193.

Storti, F. & Salvini, F. (2001). The evolution of a model trap in the Central Apennines, Italy: fracture patterns, fault reactivation and development of cataclastic rocks in carbonates at the Narni Anticline. *Jorunal of Petroleum Geology*, v. 24, n. 2, p. 171–190.

Storti, F., Balsamo, F., Mozafari, M., Koopman, A., Swennen, R. & Taberner, C. (2018). Syn-Contractional Overprinting Between Extension and Shortening Along the Montagna Dei Fiori Fault During Plio-Pleistocene Antiformal Stacking at the Central Apennines Thrust Wedge Toe. *Tectonics*, v. 37, no. 10, p. 3690-3720.

Succo A., Mittempergher S., Bistacchi A., Mozafari M., Bruna P.O., Balsamo F. & Storti F. (2018). Structural style and deformation pattern in folded carbonate platfom units: case study of Pag anticline, External Dinarides, Croatia. *Geophysical Research Abstracts*, *20*, EGU2018-16752-1, Wien.

Šumanovac, F. & Dudjak, D. (2016). Descending lithosphere slab beneath the Northwest Dinarides from teleseismic tomography. *Journal of Geodynamics*, v. 102, p. 171-184, doi: 10.1016/j.jog.2016.09.007.

Šumanovac, F., Markušić, S., Engelsfeld, T., Jurković, K. & Orešković, J. (2017). Shallow and deep lithosphere slabs beneath the Dinarides from teleseismic tomography as the result of the Adriatic lithosphere downwelling. *Tectonophysics*, v. 712, p. 523-54, doi: 10.1016/j.tecto.2017.06.018.

Suppe, J. (1983). Geometry and kinematics of fault–bend folding. *American Journal of Sciences,* v. 283, no. 7, p. 684–721.

Tari V. (2001). Evolution of the northern and western Dinarides: a tectonostratigraphic approach. In: Bertotti, G., Schumann, K. & Cloetingh, S. (eds.), Neotectonics and surface processes: the Pannonian Basin and Alpine/Carpathian System. *Stephan Mueller Special Publication Series*, v. 1, p. 223–236, doi: https://doi.org/10.5194/smsps-1-223-2002

Tari-Kovačić, V. & Mrinje, E. (1994). The role of Palaeogene clastics in the tectonic interpretation of Northern Dalmatia (Southern Croatia). *Geologia Croatica*, v. 47, no. 1, p.127–138.

Tavani, S., Parente, M., Vitale, S., Innace, A., Corradetti, A., Bottini, C., Morsalnejad, D. & Mazzoli, S. (2018). Early Jurassic rifting of the Arabian passive continental margin of the Neo-Tethys. Field evidence from the Lurestan

region of the Zagros fold-and-thrust belt, Iran: *Tectonic*s, v. 37, no. 8, p. 2586-2607, doi: https://doi.org/10.1029/2018TC005192.

Tavani, S., Storti, F., Bausà, J. & Muñoz, J.A. (2012). Late thrusting extensional collapse at the mountain front of the northern Apennines (Italy). *Tectonics*, v. 31, no. 4, TC4019.

Tavani, S., Storti, F., Fernández, O., Muñoz, J.A. & Salvini, F. (2006). 3-D deformation pattern analysis and evolution of the Anisclo anticline, southern Pyrenees. *Journal of Structural Geology*, v. 28, no. 4, p. 695–712.

Tavani, S., Storti, F., Lacombe, O., Corradetti, A., Muñoz, J.A, and Mazzoli, S. (2015). A review of deformation pattern templates in foreland basin systems and fold-and-thrust belts: Implications for the state of stress in the frontal regions of thrust wedges. *Earth-Science Reviews*, v. 141, p. 82-104, doi: https://doi.org/10.1016/j.earscirev.2014.11.013.

Tavani, S., Storti, F., Salvini, F. & Toscano, C. (2008). Stratigraphic versus structural control on the deformation pattern associated with the evolution of the Mt. Catria anticline, Italy. *Journal of Structural Geology*, v. 30, no. 5, p. 664-681.

Tavani, S., Storti, F., Soleimany, B., Fallah, M., Muñoz, J.A. Gambini, R. (2011). Geometry, kinematics and fracture pattern of the Bangestan anticline, Zagros, SW Iran. *Geological Magazine*, v.148, n. 5–6, p. 964–979.

Tavarnelli, E. (1996). Tethyan heritage in the development of the Neogene Umbria–Marche fold-and-thrust belt, Italy: a 3D approach. *Terra Nova*, v. 8, p. 470–478.

Tišljar J., Vlahović I., Velić I. & Sokac B. (2002). Carbonate platform megafacies of the Jurassic and Cretaceous deposits of the Karst Dinarides. *Geologia Croatica*, v. 55, no. 2, p. 139–170.

Tišljar J., Vlahović I., Velić I., Matičec D. & Robson J. (1998). Carbonate Facies Evolution from the Late Albian to Middle Cenomanian in Southern Istria (Croatia): Influence of Synsedimentary Tectonics and Extensive Organic Carbonate Production. *Facies*, v. 38, p. 137–152, doi: https://doi.org/10.1007/BF02537361.

Tomljenović B., Csontos L., Márton E. & Márton P. (2008). Tectonic evolution of the northwestern Internal Dinarides as constrained by structures and rotation of Medvednica Mountains, North Croatia. *Journal of the Geological Society* [London], Special Publications, v. 298, no. 1, p. 145–167, doi: https://doi.org/10.1144/SP298.8.

Traforti, A., Massironi, M., Bistacchi, A., Zampieri, D. &Viola, G. (2018). Slip-tendency analysis as a tool to constrain the mechanical properties of anisotropic rocks. *Journal of Structural Geology*, v. 117, p. 136-147, doi: https://doi.org/10.1016/j.jsg.2018.09.001.

Turcotte, D. & Schubert, G. (1982). Geodynamics. Wiley, New York.

Turner, J.P. & Williams, G.A. (2004). Sedimentary basin inversion and intra-plate shortening. *Earth-Science Reviews*, v. 65, n. 3-5, p. 277–304, doi: https://doi.org/10.1016/j.earscirev.2003.10.002.

Ustaszewski, K., Herak, M., Tomljenović, B., Herak, D. & Matej, S. (2014). Neotectonics of the Dinarides–Pannonian Basin transition and possible earthquake sources in the Banja Luka epicentral area. *Journal of Geodynamics*, v. 82, p. 52-68, doi: 10.1016/j.jog.2014.04.006.

Ustaszewski, K., Schmid, S. M., Fügenschuh, B., Tischler, M., Kissling, E. & Spakman, W. (2008). A map-view restoration of the alpine-carpathian-dinaridic system for the early Miocene. *Swiss Journal of Geosciences*, v. 101(SUPPL. 1), p. 273–294, doi: https://doi.org/10.1007/s00015-008-1288-7.

Van Gelder, I. E., Matenco, L., Willingshofer, E., Tomljenović, B., Andriessen, P. A. M., Ducea, M. N., Beniest, A. & Gruić, A. (2015). The tectonic evolution of a critical segment of the Dinarides-Alps connection: Kinematic and geochronological inferences from the Medvednica Mountains, NE Croatia. *Tectonics*, v. 34, p. 1952–1978, doi: 10.1002/2015TC003937..

Van Unen, M., Matenco, L., Nader, F.H., Darnault, R., Mandic, O., and Demir, V. (2019) Kinematics of Foreland-Vergent Crustal Accretion: Inferences From the Dinarides Evolution: *Tectonics*, v. 38, no. 1, p. 49-76, doi: https://doi.org/10.1029/2018TC005066.

Veizer, J., Ala, D., Azmy, K., Bruckschen, P., Buhl, D., Bruhn, F. & Jasper, T. (1999). 87Sr/86Sr, δ13C and δ18O evolution of Phanerozoic seawater. *Chemical geology*, v. 161, no. 1-3, p. 59-88.

Velaj, T., Davison, I., Serjani, A. & Alsop, I. (1999). Thrust Tectonics and the Role of Evaporites in the Ionian Zone of the Albanides. *American Association of Petroleum Geosciences Bulletin*, v. 83, p. 1408-1425.

Velić, I., Vlahović, I. & Matičec, D. (2002). Depositional sequences and paleogeograpgy of the Adriatic Carbonate Platform. *Memorie della Società Geologica Italiana*, v. 57, p. 141-151.

Velić, J., Malvić, T., Cvetković, M. & Velić, I. (2015). Stratigraphy and petroleum geology of the Croatian part of the Adriatic Basin. Journal of Petroleum Geology, v. 38, no. 3, p. 281-300, doi: 10.1111/jpg.12611.

Vilasi, N., Malandain, J., Barrier, L., Callot, J.-P., Amrouch, K., Guilhaumou, N., Lacombe, O., Muska, K., Roure, F. & Swennen, R. (2009). From outcrop and petrographic studies to basin-scale fluid flow modelling: The use of the Albanian natural laboratory for carbonate reservoir characterisation. *Tectonophysics*, v. 474, p. 367-392.

Villa, G., Fiorini, C., Pea, L., Bohaty, S. & Persico, D. (2008). Middle Eocene-late Oligocene climate variability: Calcareous nannofossil response at Kerguelen Plateau, Site 748. *Marine Micropaleontology*, v. 69, no. 2, p. 173-192.

Vlahović I., Tišljar J., Velić I. & Matičec D. (2005). Evolution of the Adriatic Carbonate Platform: Palaeogeography, main events and depositional dynamics. *Palaeogeography and Palaeocology*, v. 220, no. 3–4, p. 333–360, doi: https://doi.org/10.1016/j.palaeo.2005.01.011.

Vlahović I., Tišljar J., Velić I., & Matičec D. (2002). The Karst Dinarides are composed of relics of a single Mesozoic platform; facts and consequences. *Geologia Croatica*, v. 55, no. 2, p. 171–183. https://doi.org/10.4154/GC.2002.15.

Vlahović, I., Mandic, O., Mrinjek, E., Bergant, S., Ćosović, V., de Leeuw, A., Enos, P., Hratovic, H., Matičec. D., Miksa, G., Nemec, W., Pavelić, D., Pencinger V., Velić, I. & Vranjković, A. (2012). Marine to continental depositional systems of Outer Dinarides foreland and intra-montane basins (Eocene - Miocene, Croatia and Bosnia and Herzegovina). Field Trip Guide. *Journal of Alpine Geology*, v. 54, p. 405–470.

Vrabec, M. & Fodor, L. (2006). Late Cenozoic tectonics of Slovenia: structural styles at the northeastern corner of the Adriatic microplate. In: Pinter, N., Gyula, G., Weber, J., Stein, S. & Medak, D. (eds.), The Adria Microplate. *GPS Geodesy, Tectonics and Hazards*. Springer Netherlands, Dordrecht, 151-168.

Weber, J., Vrabec, M., Pavlovčič-Prešeren, P., Dixon, T., Jiang, Y. & Stopar, B. (2010). GPS derived motion of the Adriatic microplate from Istria Peninsula and Po Plain sites, and geodynamic implications. *Tectonophysics*, v. 483, no. 3-4, p. 214-222, doi: 10.1016/j.tecto.2009.09.001.

Wennberg, O.P., Svånå, T., Azizzadeh, M., Aqrawi, A.M.M., Brockbank, P., Lyslo, K.B. & Ogilvie, S. (2006). Fracture intensity vs. mechanical stratigraphy in platform top carbonates: the Aquitanian of the Asmari Formation, Khaviz Anticline, Zagros, SW Iran. *Petroleum Geosciences*, v. 12, no. 3, p. 235–246.

Wennberg, O.P., Svånå, T., Azizzadeh, M., Aqrawi, A.M.M., Brockbank, P., Lyslo, K.B. & Ogilvie, S. (2006). Fracture intensity vs. mechanical stratigraphy in platform top carbonates: the Aquitanian of the Asmari Formation, Khaviz Anticline, Zagros, SW Iran. *Petroleum Geosciences*, v. 12 , no. 3, p. 235–246.

Williams, G. & Chapman, T. (983). Strains developed in the hanging walls of thrusts due to their slip/propagation rate: a dislocation model. *Journal of Structural Geology*, v. 5, no. 6, p. 563–571.

Wiltschko, D.V., Medwedeff, D.A. & Millson, H.E. (1985). Distribution and mechanisms of strain within rocks on the northwest ramp of Pine Mountain block, southern Appalachian foreland: a field test of theory. *Geological Society of America Bulletin*, v. 96, no. 4, p. 426–435.

Zupanič J. & Babić L. (2011). Sedimentary evolution of an inner foreland basin margin: Paleogene Promina Beds of the type area, Mt. Promina (Dinarides, Croatia). *Geologia Croatica*, v. 64, no. 2, p. 101–120, doi: https://doi.org/104154/gc.2011.09.

Zupanić, J., & Babić, L. (1991). Cross-bedded sandstones deposited by tidal currents in the Eocene of the Outer Dinarides (Island of Rab, Croatia). *Geologia. vjesnik* v. 44, p. 235-245.

APPENDIX

Attached 1: Chapter 2 – Geological and Structural Map of the Pag Anticline

Attached 2: Chapter 4 – Inherited extensional fault drone orthophoto map

Geological Field Trips and Maps, Vol. 11(2.4) (2019) (https://doi.org/10.3301/GFT.2019.06)

GEOLOGICAL AND STRUCTURAL MAP OF THE SOUTHEASTERN PAG ISLAND (Northern Dalmatia, Croatia)

S. Mittempergher[1], A. Succo[2], A. Bistacchi[1], F. Storti[2], P. O. Bruna[3], M. Meda[4]

1 - Dipartimento di Scienze dell'Ambiente e della Terra, Università Milano Bicocca, piazza della Scienza 4, 20126 Milan, Italy
2 - NEXT – Natural and Experimental Tectonics research group, Università di Parma, Dipartimento di Scienze Chimiche, della Vita e della Sostenibilità Ambientale, Parco Area delle Scienze 157/A, 43124 Parma, Italy
3 - Department of Geoscience and Engineering, Delft University of Technology, Stevinweg 1, 2628 Delft, The Netherlands
4 - Eni Spa, Upstream and Technical Services – Piazza Vanoni 1, 20097 San Donato Milanese - Italy
* corresponding author: *silvia.mittempergher@unimib.it*

REGIONAL SETTING

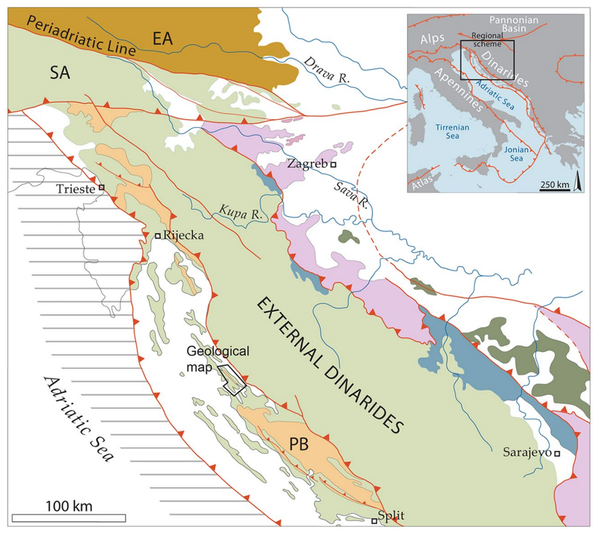

External Dinarides & Southern Alps (SA)
- Imbricated Adriatic plate margin units (Paleozoic basement and Mesozoic carbonate platform rocks)
- External Dinarides Flysch belt (Eocene to Oligocene, 'Promina beds (PB)')
- Adriatic foreland

Eastern Alps (EA)
- Austroalpine units

Internal Dinarides
- Bosnian Flysch zone (Cretacoeus)
- Adriatic plate margin units involved in Late Jurassic ophiolite obduction
- Central Dinaridic Ophiolite Complex, ophiolites and ophiolitic mélange

- Main thrust
- Thrust
- Main tectonic boundary / Fault

LEGEND

QUATERNARY DEPOSITS

Holocene deposits (Hol).

Colluvial and alluvial deposits.

Slope deposits.

Lacustrine, lagoon and marsh deposits.

Unconformity

Pleistocene deposits (Ple). Well sorted and cross stratified alluvial deposits, in alluvial fan complexes. Polymictic cemented breccias. Thickness: 0 - 50 m? (Middle Pleistocene).

Unconformity

UNITS OF THE DINARIC FORELAND

DF — **Dalmatian Flysch (DF).** Dominant grey-bluish pelites and marls, with interbedded fine-grained sandstones and plurimetric intervals of amalgamated banks of yellowish to grey, fine to very fine arenites. Arenite banks sometimes show normal gradation, have erosive base and include in their lower part mud chips, or layers of embricated Nummulite tests. Minimum thickness: 350 m. *(Lutetian)*

tb — **Transitional beds (tb).** Yellowish and blue-gray marls and marly limestone rich in glauconite. Thickness: 0 - 30 m. *(Ypresian – Lutetian?)*

FL — **Foraminiferal Limestone (FL).** Packstones – grainstones in wavy to nodular beds, mostly composed of the complete or fragmented tests of benthic foraminifera, with subordinate remnants of molluscs, echinoderms and bryozoans. The dominant biota are, from the bottom to the top of the formation, Miliolids, Alveolinids, Nummulites and Dyscocyclinids, indicating a progressive deepening and opening of the carbonate ramp. Thickness: 250 - 300 m. *(Ypresian)*

Unconformity

UNITS OF THE ADRIATIC CARBONATE PLATFORM

GH — **Gornji Humac Formation (GH).** Well-bedded pelletal wackestones-packstones alternated with microbial laminated limestones in shallowing-upward cycles, well sorted cross-laminated packstone-grainstones and massive floatstone-mudstone layers. Coarse grained rudist bioclasts are very common within the wakestone-packstone and mudstone banks, and, especially in the upper part of the formation, beds almost entirely composed of rudist shells (coquinites) are common. Locally, channelized bodies of coarse grained breccias composed of platform carbonate clasts are present. The upper part of the formation is characterized by late diagenetic dolostone bodies (GHUa) and crystalline limestones of dedolomitized dolostone (GHUb). The lower boundary with the Sveti Duh Formation is transitional. Thickness: 250 - 350 m. *(Campanian - Santonian)*

SD — **Sveti Duh Formation (SD).** Poorly defined and sometimes nodular, meter thick beds of whitish-yellowish wackestones and packstones. Bioclasts include crinoid fragments, foraminifera, sponge fragments and thin-shelled bivalves. The lower boundary with the Milna Formation is sharp and marked by a hard ground. Thickness: 100 - 150 m. *(Cenomanian –Turonian)*

MI — **Milna Formation (MI).** Peritidal limestones in shallowing upward cycles of up to 0.5 m thick banks of pelletal wackestones-packstones overlaid by biogenic laminated limestones. Often, the subtidal banks consist of floatstones including Chondrodonta and rudist fragments or, more rarely, of cross laminated grainstone layers. Paleosols and intraformational breccias are frequent. Slumped laminate layers are locally present. Thickness: > 300 m. *(Cenomanian)*

SYMBOLS

- Salt pond
- Quarry
- Stratigraphic boundary
- Unconformity
- Attitude of bedding a) upright; b) overturned
- Strike-slip fault a) outcropping; b) inferred
- Thrust fault a) oucropping; b) inferred
- Trace of fold axial plane a) syncline; b) anticline
- A — A' Trace of geological cross section

STRUCTURAL SCHEME

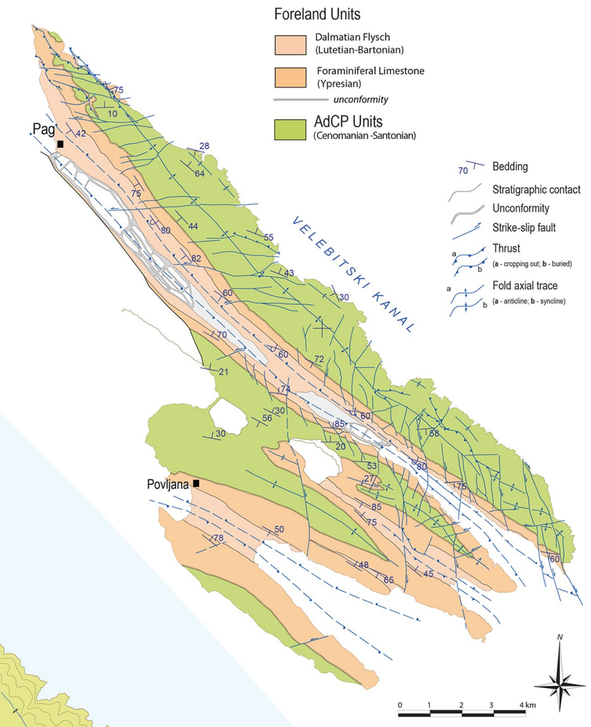

STRATIGRAPHIC COLUMN

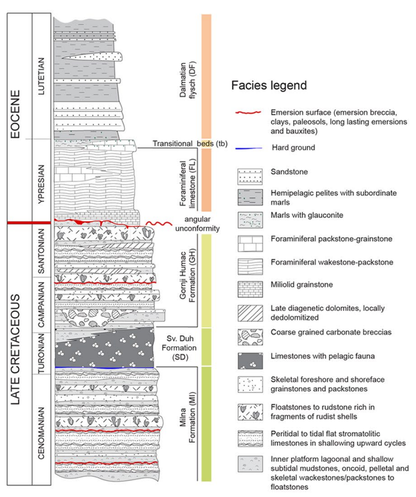

STRATIGRAPHIC SCHEME

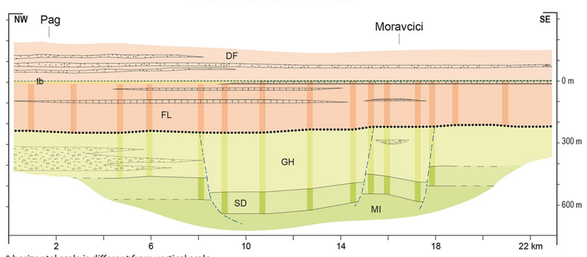

* horizontal scale is different from vertical scale

Foreland Units
- Dalmatian Flysch (DF)(Lutetian-Bartonian) a - amalgamated sandstone
- Transitional beds (tb) (Lutetian)
- Foraminiferal Limestone (FL) (Ypresian) a - rudstone bars

AdCP Units
- Gornji Humac Formation (GH) (Senonian) a - mudstone-dominated b - carbonate megabreccia
- Sveti Duh Formation (SD) (Turonian)
- Milna Formation (MI) (Cenomanian)

- *inferred normal fault*
- *unconformity*
- *drowning surface with gluconite*

Scale 1 : 25,000

m 250 0 500 1,000 1,500 2,000 2,500 m

Projection WGS 1984 UTM zone 33 N

Northing / Easting

Folding thin-skinned listric extensional faults triggers fold compartmentalization

Succo, A., Mittempergher, S., Storti, F., Bistacchi, A., and Meda, M.

Supplementary material S4.1 - Attached 2

"Inherited extensional fault drone orthophoto map"

UNIVERSITÀ DEGLI STUDI DI MILANO BICOCCA
DISAT
UNIVERSITÀ DI PARMA
NEXT Natural and EXperimental Tectonics research group

15°11'33"E 15°11'51"E 15°12'9"E

44°22'3"N 44°21'54"N 44°21'45"N 44°21'36"N 44°21'27"N 44°21'9"N

Milna Formation

Sveti Duh Formation

Gornji Humac Formation

Stromatolites level

Figure S4.2B

Figure S4.3A

Paleokarst deposit

Foraminipheral Limestone

Sveti Duh Formation

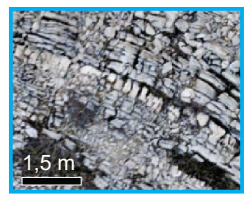

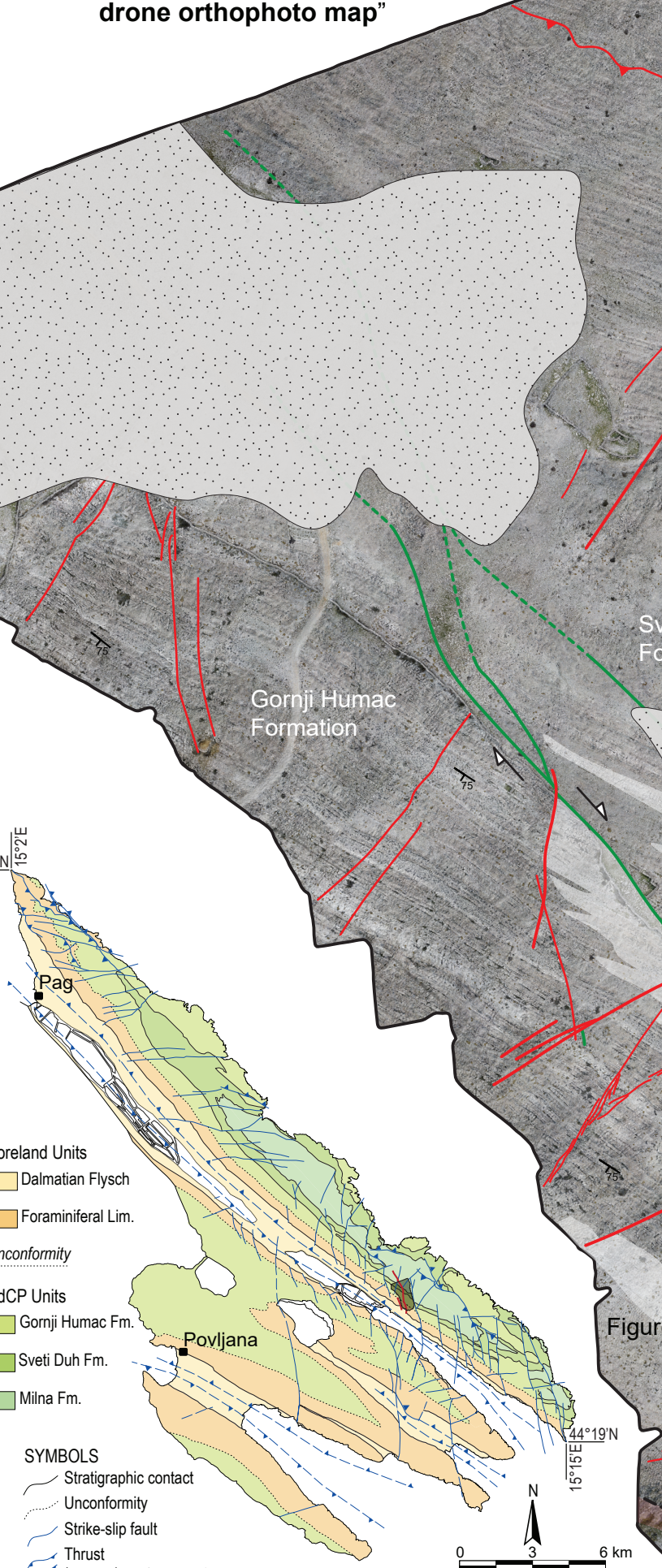

a
b
Inherited extensional fault
a: unreactivated segment
b: reactivated segment

Strike-slip faults

Unconfomity

Dolomitic and dedolomitic levels

Detritic cover

a
b
Kinematics
a: inherited extensional
b: strike-slip reactiovation

Poligenic breccia deposit

N

0 25 50 75 100 m

1 : 2.500

15°11'42"E 15°12'0"E